UNIVERSITY OF LIVERPOOL

Methionine Adenosyltransferase Structure and Function Studies: the Novel Role of a Gating Loop and a Disease-Causing Residue in Enzyme Catalysis

Thesis submitted in accordance with the requirements of the University of Liverpool for the degree of Doctor in Philosophy

By

Jiraporn Panmanee

May 2020

Abstract

Methylation is an underpinning process of life and provides control for biological processes such as DNA synthesis, cell growth and apoptosis. Methionine Adenosyltransferases (MAT) produce the cellular methyl donor, S-Adenosylmethionine (SAMe). Dysregulation of SAMe levels is a relevant event in many diseases including cancers such as hepatocellular carcinoma and colon cancer. In addition, MAT deficiency causes isolated persistent hypermethioninemia (IPH), resulting from mutations in MAT1A gene encoding MATαl (hepatic form). Most associated hypermethioninemic conditions are inherited as autosomal recessive traits, however dominant inheritance of hypermethioninemia is caused by Arg264His (R264H). Also, R264H mutation has been confirmed in a screening programme of newborns as the most common mutation in babies with IPH. Arg264 makes an inter-subunit salt bridge located at the dimer interface where the active site assembles. In mammals, MATα1/α2 and MATβV1/V2 are the catalytic and the major form of regulatory subunits, respectively. A gating loop comprising residues 113-131 is located beside the active site of the catalytic subunits (MATα1/α2) and provides controlled access to the active site. The gating loop adopts conformational changes during enzyme catalysis facilitating SAMe formation and controlling the catalytic efficiency. Mutations of a number of residues including MATα1 (Arg264) and MATα2 (Gln113, Ser114 and Arg264) led to partial or total loss of enzymatic activity demonstrating their critical role in SAMe formation. The enzymatic activity of the mutated enzymes is restored to varying degrees upon complex formation with MATβV1 or MATβV2 endorsing its role as an allosteric regulator of MATα2 in response to the levels of methionine or SAMe. The protein-protein interacting surface formed by the MATα1/2:MATβ complexes is explored to demonstrate that several quinolone-based compounds modulate the activity of MATα1/2 and its variants, providing a rational for chemical design/intervention responsive to the level of SAMe in the cellular environment.

Acknowledgement

First of all, I would like to thank DPST scholarship (Development and Promotion of Science and Technology Talents Project), Thailand for the financial support both tuition fee and living stipend. Thank the office of educational affairs, the royal Thai embassy for management of my annual tuition fee payment and providing PhD guidance throughout my study.

I would like to express my gratefulness to my supervisors, Prof. Samar Hasnain and Dr. Svetlana Antonyuk for continuing supports throughout my four years of study. I would like to deeply thank Prof. Samar Hasnain who is my primary supervisor to encourage me to think broadly and intensively guide me during my manuscript preparation; I truly appreciated. I would like to sincerely thank Dr. Svetlana Antonyuk for all of her helps and supports both in academic and PhD life. I thank Dr. Jill Madine and Dr. Lunnng Liu, my internal accessors, for their helpful suggestion and being very supportive during my 1st to 3rd-year viva.

My first protein purification and crystallisation, which are the main part of my project, were introduced and trained by Dr. Kangsa Amporndanai, so I would like to thank him very much for his kindness. I would like to thank Dr. Michael Capper for his X-ray crystallography lecture and helping me process my first X-ray data. I would like to thank Fernanda Sala, my colleague, for helping me with everything in the lab when I had just started my PhD. Thanks to Dr. Gareth Wright for helping me collect SAXS data and solving many technical problems. Thanks to Dr. Varunya Chantadul for her suggestion about DSF experiments. I thank Dr. Daisuke Sasaki and Dr. George Chiduza for the thoughtful discussion throughout my study. I would like to thank all staff and management of Diamond Light Source, UK and SOEIL, France for crystallographic facilities and their synchrotron centres.

I thank P. Fah, Gwen, Yin and Matthew for welcoming me very warmly in the UK and sharing their experiences with me. Thanks to P. Ploy, Pong, Kiang, P. Toey, P. Noon, N. Deaw, P. Oh,

P. Tong, Chai, P. May, Micky, Bookie and N. Tom for beautiful friendship and all of your supports. Being friend with you guys made my life here very happy and colourful; I greatly appreciated. Thank Chaba Chaba Thai Restaurant (J. Lee and Richard) for providing me an authentic Thai food. Thank Prof. Piyarat Govitrapong, Asst. Prof. Sujira Mukda and Dr. Chitikorn Nopparat for all of your kindly supports and encouraging me to study in the UK.

Finally, I would like to thank all of my beloved family and friends in Thailand who always support me continuously. Thank Mom and Dad for being very supportive and calling me every morning (keep me away from being homesick).

Table of Contents

List of Abbreviations

5-MTHF	5-methyltetrahydrofolate
Å	Ångström (10^{-10} meter)
ADO	Adenosine
ADP	Adenosine diphosphate
AMB	L-2-amino-4-methoxy-cis-but-3-enoic acid (methionine analogue)
AMP-PNP	Adenylyl-imidodiphosphate (non-hydrolysable ATP analogue)
ANK	Ankyrin
ANOVA	One-way analysis of variance
AP-1	Activator protein 1
ARF-GAP	N-terminal ARF-GTPase activating domain
ATP	Adenosine triphosphate
B-factor	Temperature factor
Bcl-2	B-cell lymphoma 2
BHMT	Betaine-homocysteine methyltransferase
BM	Bending magnet
c-Maf	Cellular muscular aponeurotic fibrosarcoma
c-Myb	Myeloblastosis viral oncogene homologue
c-Myc	Viral oncogene homologue
C/EBP	CCAAT enhancer binding protein
CC	Coiled coil
CCA	Cholangiocarcinoma
CREBP	Cyclic AMP response element binding protein
CryoEM	Cryogenic electron microscopy
CV	Column volume
DMSO	Dimethyl sulfoxide
DSF	Differential scanning fluorimetry
DTT	Dithiothreitol
E2F	E2F- and DP-like subunits
eMAT	*E. coli* MAT
FPKM	Fragments per kilobase of exon model per million mapped reads
GC	Glucocorticoid

GIT1	G-protein-coupled receptor kinase 1
GPCR	G-protein-couple receptor
GRE	Glucocorticoid response element
GSH	Glutathione
HCC	Hepatocellular carcinoma
Hcy	Homocysteine
HIF-1α	Hypoxia-inducible factor-1α
hMAT	*H. sapiens* MAT
HNF	Hepatocyte-enriched nuclear factor
HPLC	High performance liquid chromatography
ID	Insertion device
IL-6	Interleukin-6
IMAC	Immobilised metal ion affinity chromatography
IPH	Isolated persistent hypermethioninemia
IPTG	Isopropyl β-D-1-thiogalactopyranoside
ITC	Isothermal titration calorimetry
LcisAMB	L-2-amino-4-methoxy-cis-but-3-enoic acid
MAPK	Mitogen-activated protein kinase
MAT	Methionine adenosyltransferase
Met	Methionine
MR	Molecular replacement
MS	Methionine synthase
MT	Methyltransferase
NF-κB	Nuclear factor kappa B
NF1	Nuclear factor 1
NO	Nitric oxide
P300	E1A binding protein p300
PBS	Paxillin-binding site
PCR	Polymerase chain reaction
PDB	Protein data bank
PEG	Polyethylene glycol
Pi	Orthophosphate
PKC	Protein kinase C

PMSF	Phenylmethylsulphonyl fluoride
PPAR	Peroxisome-proliferator activated receptor
PPi	Pyrophosphate
PPNP	(Diphosphono)aminophosphonic acid
PPPi	Tripolyphosphate
PPRE	Peroxisome-proliferator activated receptor response element
PVDF	Polyvinylidene difluoride
RF	Radiofrequency
rMAT	*R. norvegicus* MAT (rat liver MAT)
RMSD	Root Mean Square Deviation
RO	Reverse osmosis
SAE	S-adenosylethionine
SAH	S-adenosylhomocysteine
SAMe	S-adenosyl-L-methionine
SDS-PAGE	Sodium dodecyl sulphate polyacrylamide gel electrophoresis
SEC	Size exclusion chromatography
SEC-SAXS	Size exclusion chromatography-small angle X-ray scattering
SEM	Standard Error of Mean
SENP2	Sentrin-specific protease 2
SHD	Spa2-homology domain
Sp1	Specificity protein 1
SsMAT	*S. solfataricus* MAT
STAT	Signal transducers and activators of transcription
SUMO	Small ubiquitin modifier
TCA	Trichloroacetic acid
TCEP	Tris(2-carboxyethyl)phosphine)
TEV	Tobacco etch virus
TGF-β1	Transforming growth factor beta 1
THF	Tetrahydrofolate
TkMAT	*Thermococcus kodakarensis* MAT
Tm	Melting temperature
TNF-α	Tumour necrosis factor-alpha
Ubc9	Ubiquitin-conjugating enzyme 9

v-Myb	Avian myeloblastosis viral oncogene homologue
XRD	Single-crystal X-ray diffraction
β-ME	β–mercaptoethanol

List of Figures

List of Tables

Chapter I

Introduction to methionine adenosyltransferase and X-ray crystallography

1.1 Methionine adenosyltransferases

Methionine adenosyltransferase (MAT) or S-adenosylmethionine synthetase (EC 2.5.1.6) catalyses S-adenosyl-L-methionine (SAMe, SAM or AdoMet) from methionine (Met) and adenosine triphosphate (ATP). This enzyme is found in all living organisms excepting some intracellular parasites gaining SAMe from their host [1]. Normal cellular function and survival requires SAMe as a versatile molecule ranging its roles from methylation, gene expression to membrane fluidity [2-4].

In mammalian cells, MAT1A, MAT2A and MAT2B genes encode MATα1, MATα2 and MATβ, respectively. MATα1 and MATα2 are the catalytic subunits of MAT enzymes [5, 6], while MATβ is the regulatory subunits co-expressing with MATα2 proteins in extrahepatic tissues [7]. MATβ has four variants (MATβV1, MATβV2, MATβV2a and MATβV2b), the major isoforms of which are MATβV1 and MATβV2 [8-10]. MATα1 forms two homo-oligomeric states, a dimer or a tetramer, and it is mainly found in the adult liver [11, 12]. MATα2 functions as a hetero-oligomer forming the hetero-complex with the regulatory subunit, MATβ, in 2:1 ratio [10, 13]. One subunit of MATβV2 interacts with one MATα2 dimer at the dimeric interface as reported in structural studies of $MAT(\alpha2)_4(\beta V2)_2$ complexes (PDB: 4KTT, 4NDN and 4KTV) [13]. MATα1 can also interact with MATβ, but both of them are not co-expressed in the same tissue [13]. The oligomeric states of MAT isoforms are illustrated in Fig 1.1A. The catalytic subunits of MAT revealed by structural and phylogenetic study are shown to be conserved from eubacteria to mammal with 30 % sequence identity [1],

while about 20 % sequence similarity is found among archaeal bacteria, *S. solfataricus*, to *E. coli* and human [14]. In addition, the protein structures of MAT catalytic isoforms are found to be conserved though evolution at secondary (β-sheets, α-helices, etc.) and tertiary (protein folding) structural levels (Fig.1.1B). Three domains of β-sheets are folded at the interface necessary for dimer formation, while the α-helices are located at the solvent-exposed surface.

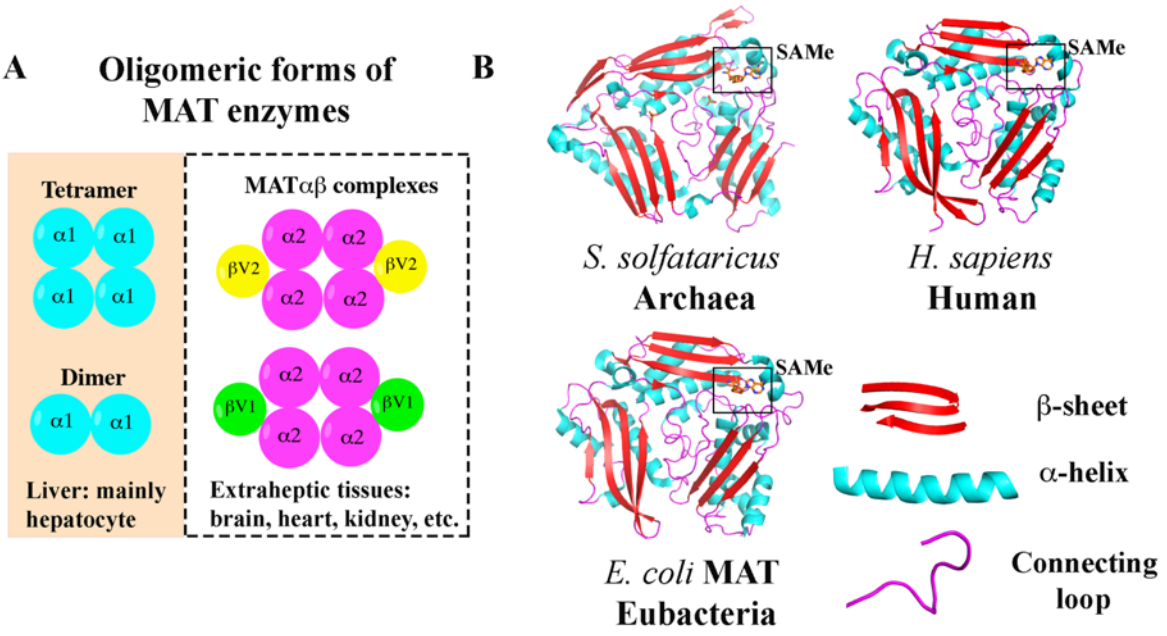

Fig. 1.1 Catalytic and regulatory subunits of human MAT enzymes. (A) MATα1 is mainly localised in the adult liver as a homo-tetramer or a homo-dimer. MATα2 is found in extrahepatic tissues and it forms the hetero complex with the regulatory subunit, MATβV1 or MATβV2. **(B)** The structures of a *S. solfataricus* MAT (PDB: 4L7I), a human MATα2 (PDB: 5A1I) and an *E. coli* MAT (PDB: 1RG9) monomer show the same pattern of three-dimensional protein folding. The conserved patterns are found at secondary and tertiary structures. SAMe molecules are represented as sticks (carbon, nitrogen and oxygen atoms are shown in orange, blue and red colour, respectively). The figure (1.1B) was modified from reference [14].

1.1.1 Expression and similarity of MATs

MATα1 and MATα2 are encoded by MAT1A and MAT2A genes located in chromosome 10 (cytoband, q22) [15] and chromosome 2 (cytoband, p11.2) [16], respectively. They encode 395 amino acids in length for both isoforms. MATα1 has 84 % similarity to MATα2 [17], despite their distinct kinetic properties and tissues of gene expression.

MATα2 is expressed in several organs including heart, brain, kidney and fetal liver, while MATα1 is highly expressed in the adult liver (mainly in hepatocytes) where MATα2 is expressed at very low levels [18]. Liver and colon tumour cells show the increase in MATα2 expression, whilst MATα1 expression is down-regulated [19-22]. Under normal condition, methionine metabolism in liver mainly depends on MATα1 function. Methylation reactions (84 %) and methionine metabolism (48 %) take place in the liver, suggesting its role in regulation of blood methionine levels [23, 24]. MATα1 and MATα2 tissue-specific expressions are shown in Fig.1.2 [25].

The MAT2B gene encoding the regulatory subunit, MATβ, is located on chromosome 5 (cytoband, q34) [8]. Among the four variants of the regulatory subunits (MATβV1, MATβV2, MATβV2a and MATβV2b), MATβV1 and MATβV2 are the two predominant isoforms which have 334 and 323 amino acids, respectively. MATβ proteins are expressed ubiquitously in extrahepatic tissues including kidney, lymph node, heart, brain and thyroid [10]. The pattern of MAT2B gene expression is shown in Fig. 1.3 [25]. MATβV1 and MATβV2 differ in their first 20 amino acids residues of the N-terminus as a result of differences in a transcriptional initiation site. Regarding the expression levels of the other two MATβ variants (MATβV2a and 2b), their expressions are very low in comparison with MATβV2 [10]. Available functional data have been studied mainly on the V1 and the V2 isoform. Therefore, the information on

V2a and V2b variants associating with the catalytic MATα2 subunits and how they regulate MATα2 is still lacking to date. The detail of MATβ expressions in different human tissues and hepatocellular carcinoma (HCC) was studied by Yang H et al., (2008) [10]. The difference in gene expression pattern of these two main variants (V1 and V2) was found in human healthy tissues (Fig. 1.4A). The MATβV1 isoform was highly expressed in thyroid, lung, prostate and brain, while MATβV2 was mainly expressed in heart and kidney (Fig. 1.4A). In human HCC, the mRNA levels of MAT2A and the two major variants of MAT2B (V1 and V2) were elevated, while MAT1A gene expression was silenced (Fig. 1.4B).

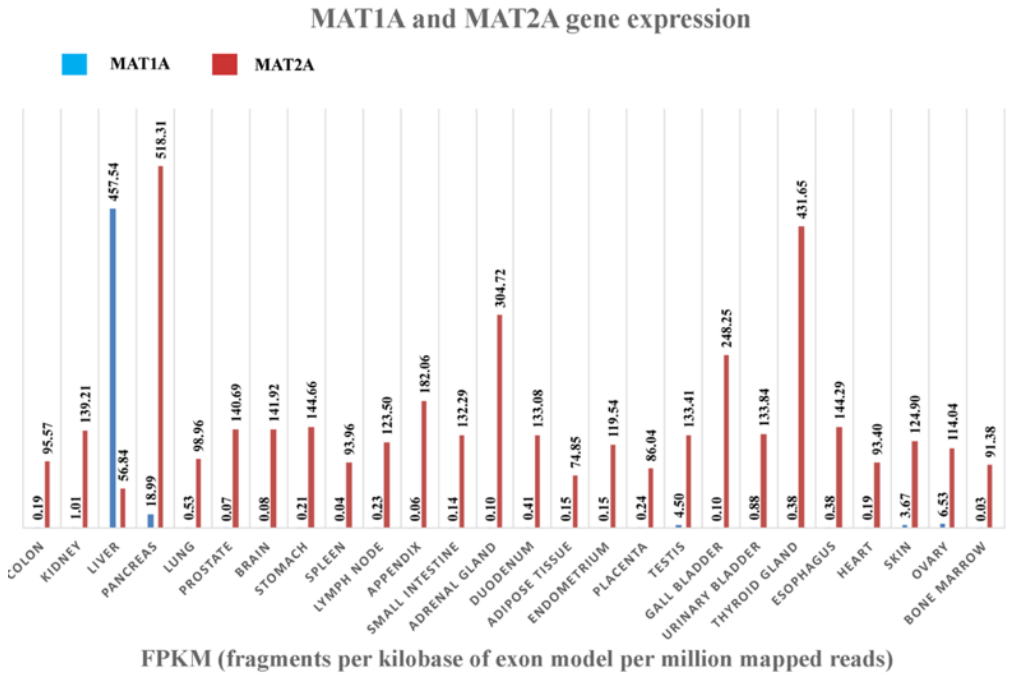

Fig. 1.2 MAT1A and MAT2A gene tissue-specific expressions. MAT1A gene encoding MATα1 protein is highly expressed in an adult liver and a small amount is found in the pancreas. MAT2A gene encoding MATα2 protein is expressed in several tissues and a small amount is found in the liver. The raw data used to reproduce this figure were taken from the supplementary Data Set S1 of reference [25] with permission (License ID: 1010272-1).

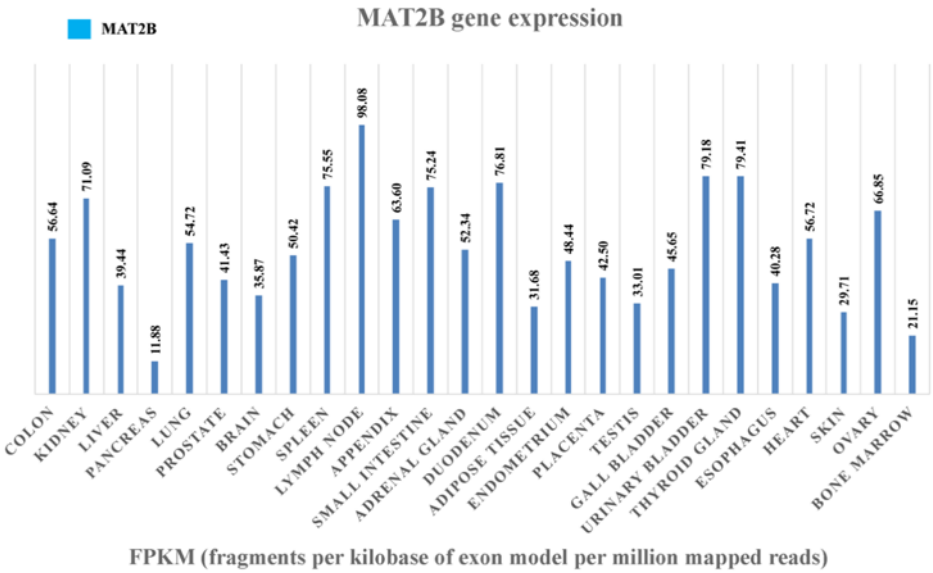

Fig. 1.3 MAT2B gene expressions in different tissues. The high levels of MAT2B gene expression were found in lymph node, thyroid gland, urinary bladder, spleen and kidney. The raw data used to reproduce this figure were taken from the supplementary Data Set S1 of reference [25] with permission (License ID: 1010272-1).

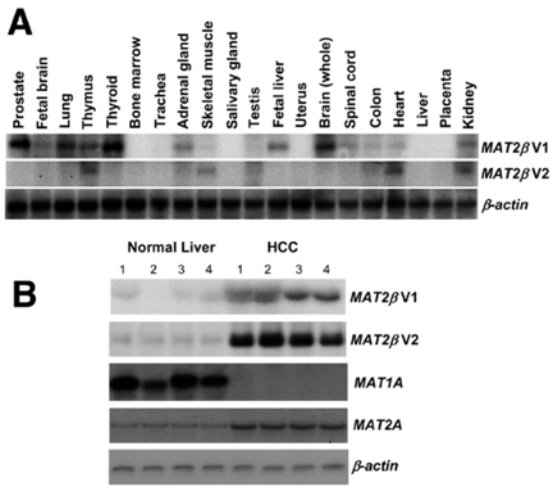

Fig. 1.4 Northern blot analysis of MAT2B gene expressions. (A) Normal tissue expression patterns of MAT2B genes (V1 and V2 variants) **(B)** MAT gene expressions (MAT2B, MAT1A and MAT2A) in normal liver were compared with HCC samples. The figure was taken from reference [10] with permission (License Number: 4734280795189).

1.1.2 SAMe synthesis reaction

MAT catalyses SAMe synthesis from two-step reactions [26].(i) The sulphur atom of Met attacks C-5' atom of ATP, known as the nucleophilic substitution SN2 reaction, to produce SAMe (Fig. 1.5). Tripolyphosphate (PPPi) is an intermediate of ATP cleavage as SAMe is formed [27, 28].; (ii) MAT subsequently hydrolyses the PPPi to pyrophosphate (PPi) and orthophosphate (Pi) by its tripolyphosphatase activity [29]. The PPPi hydrolysis is believed to facilitate the product release from MAT enzymes as PPi and Pi interactions to the active site are less stable in comparison with the PPPi binding. Human MATα2 structure with the PPPi bound in the active site showed an open conformation of the gating loop, indicating that SAMe could be released prior to the hydrolysis of PPPi [30].

Divalent cations are essential for the phosphatase activity of MAT, similar to other reported phosphatases. The phosphatase activity needs Mg^{2+} ions and can be stimulated by K^{+} ions. Two types of cations, the monovalent (K^{+}) and the divalent (Mg^{2+}, Mn^{2+} or Ca^{2+}) ions which bound to the active site of MAT enzymes were confirmed in *E. coli* MAT studies [31-34]. At least three Mg^{2+} ions were present in MAT crystal structures from rat liver [35]. AMP-PNP (non-hydrolysable analogue of ATP) producing non-hydrolysable PPNP as an intermediate during SAMe formation was used in the study of *E. coli* MAT by Komoto J et al., (2004) [36]. The stable ternary complex forms of crystals were obtained and revealed that Mg^{2+} ions interacted with PPNP at its O atoms and these interactions stabilised the negative charges of PPNP [36]. The K^{+} ion was suggested to indirectly relate to the SAMe formation, as it was in the distant position to the catalytic site. For the half maximal activation of MAT, more than 5 mM of K^{+} ions was required [34]. However, the human MATα2 structure in a complex with SAMe+Met+Adenosine+PPNP later showed that PPNP directly interacted with two Mg^{2+} ions and one K^{+} ion via its phosphate oxygen atoms. The conformations of the triple phosphate and

the metal ion binding sites were preserved in AMP-PNP from *E. coli* MAT (PDB: 1P7L) to human MAT structure (PDB: 5A1I) as shown in Fig. 1.6A. The two Mg^{2+} ions and one K^{+} ion coordinating with PPNP, water molecules and four residues in the active site (Asp31, Glu57, Asp258 and Ala259) are illustrated in Fig. 1.6B. The first Mg^{2+} ion interacted with two oxygen atoms (O1G and O2A) of PPNP and four oxygen atoms of water molecules. The second Mg^{2+} ion interacted with four oxygen atoms of Asp31 (OD2), PPNP (O2G, O1A and O1B) and also two oxygen atoms of water molecules. The K^{+} ion interacted with one water and four oxygen atoms of PPNP (O1B), Glu57 (OE2), Asp258 (OD1) and Ala259 (O).

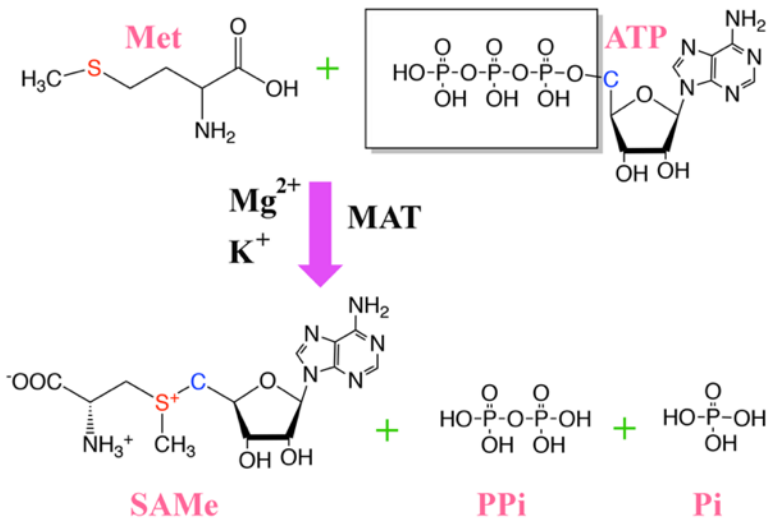

Fig.1.5 MAT catalytic reaction. SAMe is synthesized by the MAT enzyme from ATP and L-methionine in two consecutive reactions. The first step is involved in the synthesis of SAMe and tripolyphosphate (PPPi) from ATP and methionine. Orthophosphate (Pi) and pyrophosphate (PPi) are generated during the second step, PPPi hydrolysis. The figure was modified from [36].

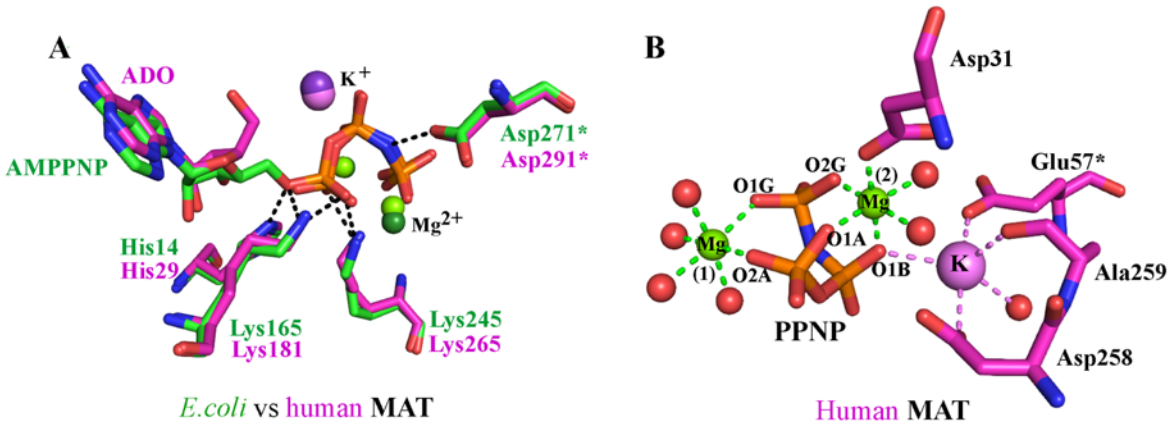

Fig.1.6 AMP-PNP and metal ion binding sites in *E. coli* and human MAT structures. (A) An alignment of the AMP-PNP molecule from an eMAT structure (PDB: 1P7L, green sticks) and the PPNP molecule from a human SAMe+Adenosine+Met+PPNP structure (PDB: 5A1I, pink sticks) is illustrated. Mg^{2+} and K^{+} ions are shown in green and purple spheres of dark and light colour corresponding to *E. coli* and human MAT, respectively. **(B)** Two Mg^{2+} ions and one K^{+} ion interact with PPNP and water molecules in the active site. Water molecules are represented by red spheres. All H-bonds are shown in black dots. Asterisks (*) indicate the residue from the dimeric subunit.

1.2 S-adenosylmethionine (SAMe)

SAMe is the sulfonium compound containing a very reactive methyl group which makes SAMe become the principle methyl donor for methylation reactions. The electrophilic structure of SAMe carbon centre is adjacent to the positively charged sulphur atom that brings SAMe into a contact with the nucleophilic groups in a variety of substrates (Fig. 1.7). SAMe metabolism is involved with many metabolic pathways (Fig.1.8). Once SAMe donates its methyl group, it becomes S-adenosylhomocysteine (SAH), the transmethylation inhibitor. SAH is subsequently hydrolysed to adenosine (ADO) and homocysteine (Hcy). Hcy can be remethylated to methionine or it can participate in the trans-sulfuration pathway. In this pathway, Hcy is the

precursor of several compound biosynthesis including glutathione (a major cellular antioxidant), cysteine, taurine, etc. Alternatively, SAMe can enter a polyamine biosynthesis pathway after it has been decarboxylated and becomes the propylamine donor for spermidine or spermine biosynthesis [37].

SAMe serves as the methyl group donor for a number of biomolecules including nucleotide bases of DNA and RNA, histones, sugars and amino acids [38]. SAMe is important for the methylation reactions which are involved in many cellular processes ranging from fetal development to brain function in all living organisms. Gene expressions are regulated by DNA methylation and the actions of hormones or neurotransmitters are also regulated by methylation. The methylation of phospholipids maintains the fluidity and the mobility of membranes and receptors [39]. SAMe is found to regulate cellular proliferation, differentiation, and death in the liver [2, 40, 41] and is also involved in cellular antioxidant capacity [42]. Strongly electrophilic properties of a SAMe methyl group allow it to react with the nucleophilic groups of a variety of substrates. SAMe participates in a large number of trans-methylation processes compared to other methyl donors (e.g. folate), indicating that it is more favourable for thermodynamic reactions than other compounds [39].

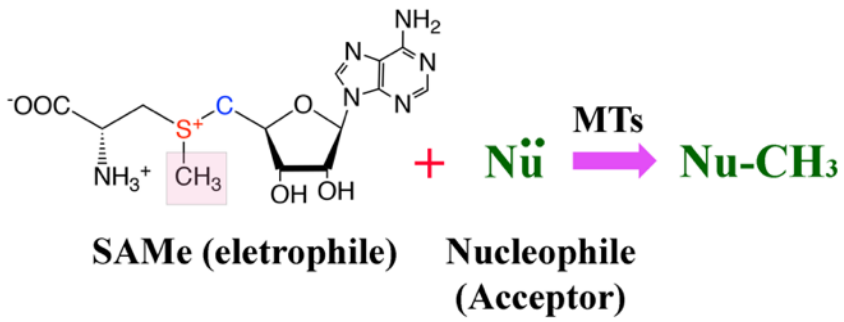

Fig. 1.7 The electrophilic structure of SAMe. Methyltransferases catalyse the transfer of the methyl group of SAMe to nucleophilic substrates. Nu and MTs represent a nucleophilic molecule and methyltransferases, respectively. The figure was modified from reference [39].

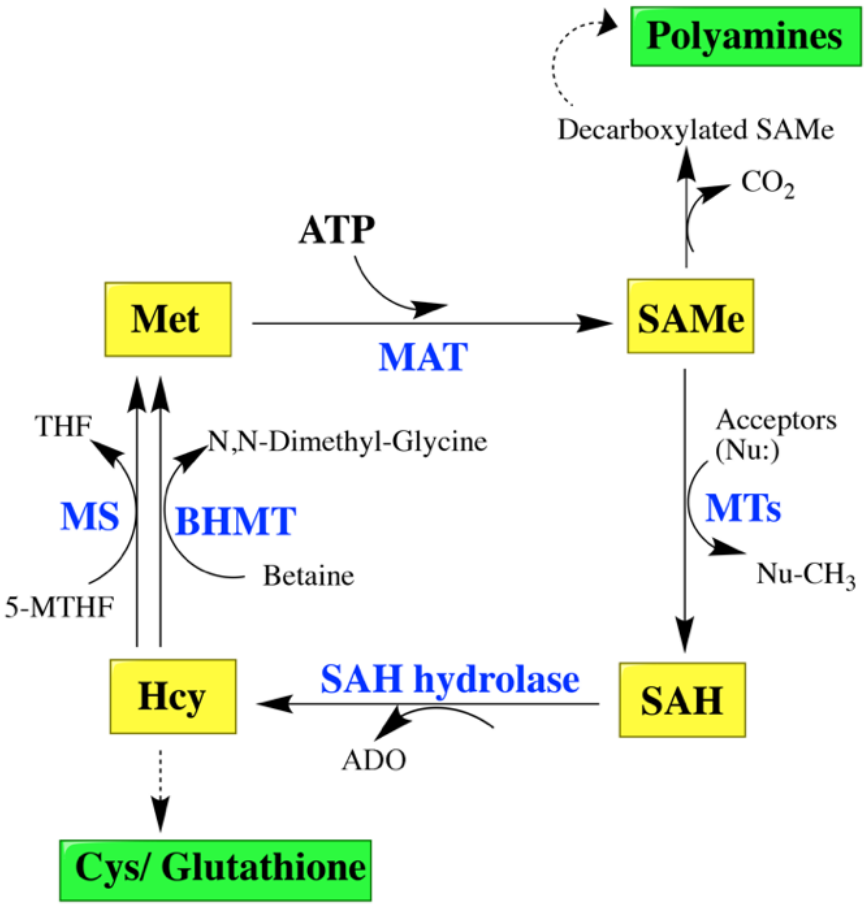

Fig.1.8 SAMe synthesis and related metabolic pathways. SAMe can donate its methyl group to a number of acceptors by the enzyme, methyltransferases (MTs). After decarboxylation by SAMe decarboxylase, SAMe becomes the precursor of polyamines synthesis (e.g. spermine), or it can be converted to SAH after transferring its methyl group to the acceptors. SAH is catalysed by SAH hydrolase to produce Hcy and ADO. Hcy can be remethylated for methionine regeneration by either methionine synthase (MS) or betaine-homocysteine methyltransferase (BHMT) in the reaction that requires 5-MTHF or betaine. In addition, Hcy is the precursor of an amino acid cysteine, the substrate for glutathione synthesis. 5-MTHF and THF stand for 5-methyltetrahydrofolate and tetrahydrofolate, respectively. The figure was modified from reference [4].

1.3 Enzyme structures of catalytic subunit MATα1/2

To date several MAT X-ray crystal structures have been identified from bacteria to mammals in a native state (apo-form) or in a substrate/ product-bound form. The crystal structures of MAT from various species show the conserved secondary structure and the similar order of domain arrangements, in agreement with amino acid sequences that are conserved through evolution. The two functional active sites of MAT assemble between a dimer where both subunits contribute their residues to form the active sites. The α-helices of a monomer distributes along a solvent exposed surface, while each MAT subunit contacts to its partner inversely by hydrophobic interaction using β-sheet domains to form the dimer (e.g. Fig. 1.9A, an archaeal MAT structure).

Several reported MAT structures have a common feature containing a flexible gating loop located at the entrance of the active site. The gating loop contains residues 113-131 in a human MATα1 and a human MATα2 [30], residues 98-108 in an *E. coli* MAT [36] and residues 141-155 in an archaeal MAT [14]. The gating loop is suggested to function as a flexible loop that controls the entry to the active site. The gating loop closes and obstructs the active site entrance when it is occupied by SAMe, but when the active site is empty, the loop orients in the open conformation (disordered and invisible in most reported crystal structures). This allows access to the active site. The ordered gating loops in their closed conformation are reported in numerous MAT structures e.g. archaeal MATs (PDB: 4L7I, 4L2Z and 4K0B), eMATs (PDB: 1P7L and 1RG9), and human MAT structures: MATα1 (PDB: 2OBV) and MATα2 (PDB: 2P02 and 5A1I) [14, 30, 36, 43].

1.3.1 Archaeal MAT structures (*S. solfataricus* and *T. kodakarensis*)

The first archaeal MAT was structurally characterised from *Sulfolobus solfataricus* MAT (SsMAT) [44]. The SsMAT has about 20 % amino acid sequence similarity to *E. coli* and human MATs. *Methanococccus jannaschii* MAT contains 22 % and 23 % sequence identity to *E. coli* and human MATs, respectively, while *E. coli* and human sequences are about 59 % identical. [45, 46]. Wang F et al., 2014 reported the structures of the thermostable SsMAT in three different forms: an apo, a SAMe-bound and a S-adenosylethionine (SAE)-bound form [14]. The gating loop of SsMAT (residues 141-151) showed full electron density representing the α-helix when the active site was occupied by SAMe, Pi and PPi (Fig. 1.9A), while residues 141-155 were mostly invisible when the active site was unbound (Fig. 1.9B, an apo form). In various structures of *E. coli* MAT [36] and human MAT [13, 30, 43, 47], the active site ligand occupation and the ordered gating loop are synchronised, consistent with these observations found in SsMAT structures (Fig. 1.9A-B). Interestingly, Schlesier J et al., 2013 [48] firstly reported the archaeal *Thermococcus kodakarensis* MAT (TkMAT) structure with the complete gating loop organisation in the open conformation (Fig. 1.9C). The observation of the ordered gating loop in the open conformation supports a mechanism proposed in *E. coli* MAT study that upon the substrate binding the interactions of the gating loop and the substrate in the active site facilitate the rearrangement of the flexible gating loop into its closed conformation [36].

The ligand orientations reported in the *E. coli* MAT studies by Komoto J et al., 2004 and human MAT studies by Murray B et al., 2014, 2016 and Shafqat N et al., 2013 are similar to those of the SsMAT structure (Fig.1.9A). However, different ligand orientations with the disordered gating loop had been reported in *E. coli* MAT structures reported by Takusagawa F et al., 1996 [49] and in rat MAT structures proposed by Gonzalez B et al., 2003 [35]. The high temperature factors (B-factors) of ligands in the active site were in excess of 70 $Å^2$ in the rat MAT and more

than 100 $Å^2$ in the *E. coli* MAT structure. This indicated the uncertainty of atomic positions causing by the temperature-dependent atomic movement and the displacement of atomic positions in different unit cells [50]. Moreover, the flexible gating loops were undefined despite the fact that the active sites were occupied. The rat and the *E. coli* MAT share about 59 % of the amino acid sequence similarity and all active site residues are conserved, but they present with the entirely distinct ligand orientations in the active site. In contrast to these rat and *E. coli* MAT structures reported by Gonzalez B et al., 2003 and Takusagawa F et al., 1996, all ligands in the active site of human, *E. coli* (reported by Komoto J et al., 2004) and SsMAT MAT structures showed reasonable B-factors.

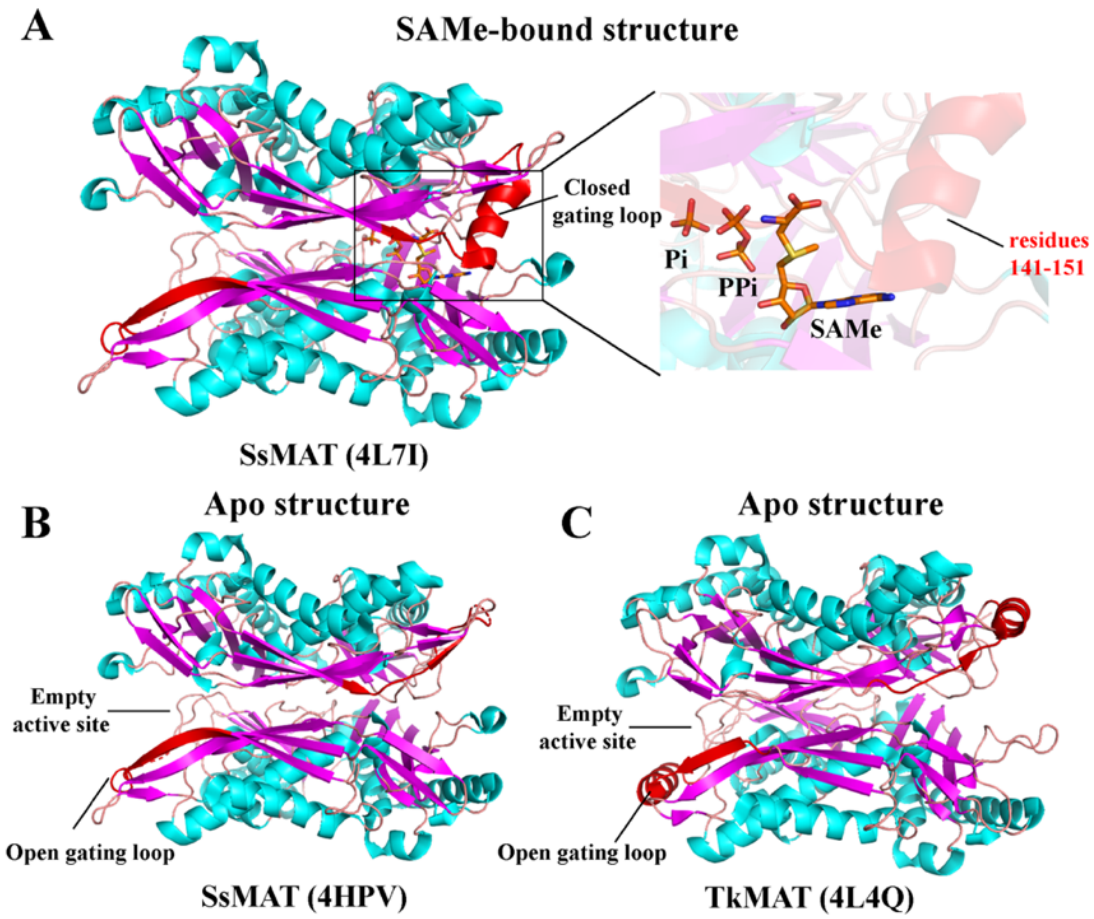

Fig 1.9 Archaeal MAT Structures in the SAMe-bound and the apo form. **(A)** The structure shows asymmetrical binding of SAMe, PPi and Pi in one active site with the ordered, closed conformation of the gating loop (red), while the other half active site is empty with the disordered gating loop (mostly invisible in the model). **(B)** Apo structures of SsMAT and **(C)** TkMAT contain no ligand in the active sites. Apo structures show the open conformation of the gating loop. The SsMAT structure shows mostly disordered (invisible) gating loop, while the TkMAT structure shows the full open conformation of the gating loop (red). α-Helix, β-sheet and connecting loop are shown in blue, pink and wheat colour, respectively.

1.3.2 *E. coli* MAT structure

The first crystal structure of *E. coli* MAT (eMAT) containing two PO_4^{3-} (Pi) molecules and 4 cations (two Mg^{2+} ions and two K^+ ions) was reported by Takusagawa F et al., 1996a at 3 Å (PDB: 1XRA) [51]. This structure showed the open conformation of the flexible loop (gating loop, residues 98-108) [51] (Fig.1.10A). The crystal structure of eMAT obtained by ATP co-crystallisation showed adenosine diphosphate (ADP) and Pi in the active site at 2.8 Å provided by Takusagawa F et al., 1996b (PDB: 1MXB, Fig. 1.10B) [49]. However, the binding position of the ADP (adenosine moiety) was different to adenosine binding site of the eMAT structure that was later proposed by Komoto J et al., 2004 (Fig. 1.10C). The eMAT structures containing AMP-PNP+Met (PDB: 1P7L, 2.5 Å) and SAMe+PPNP in the active sites (PDB: 1RG9, 2.5 Å) showed the closed conformation of the ordered gating loop [36]. AMP-PNP and Met were used as the substrates in Komoto J et al., 2004 studies when the formation of SAMe could occur but the tripolyphosphate hydrolysis was inhibited. This resulted in the formation of a stable crystal form (SAMe+PPNP bound crystals). Fu Z et al., 1996 obtained the apo eMAT structure (1FUG, 3.2 Å) and suggested that the flexible gating loop, which is poorly conserved among species, was involved in the determination of the substrates in the active site [52].

The difference in position of adenosine moiety found in the ADP+Pi bound structure of eMAT also showed the high B factor of ADP (90.21 $Å^2$). In contrast, the AMP-PNP+Met or the SAMe+PPNP bound eMAT structure showed good electron density of SAMe with B-factor of 13.5 $Å^2$ for adenosine moiety and B-factor of 14.2 $Å^2$ for the entire molecule of SAMe. The adenosine ring of SAMe and Met are likely to reside in their correct positions as no empty space was observed in the active site of this structure (Fig. 1.10C). The eMAT structures with different ADP binding sites compared with the human MATα2 structure (PDB 5A1I, 1.1 Å) are shown in Fig. 1.10D-E. The eMAT structure in complex with AMP-PNP+Met or

SAMe+PPNP showing the similar positions of adenine binding sites compared to the human MATα2 structure is shown in Fig. 1.10F.

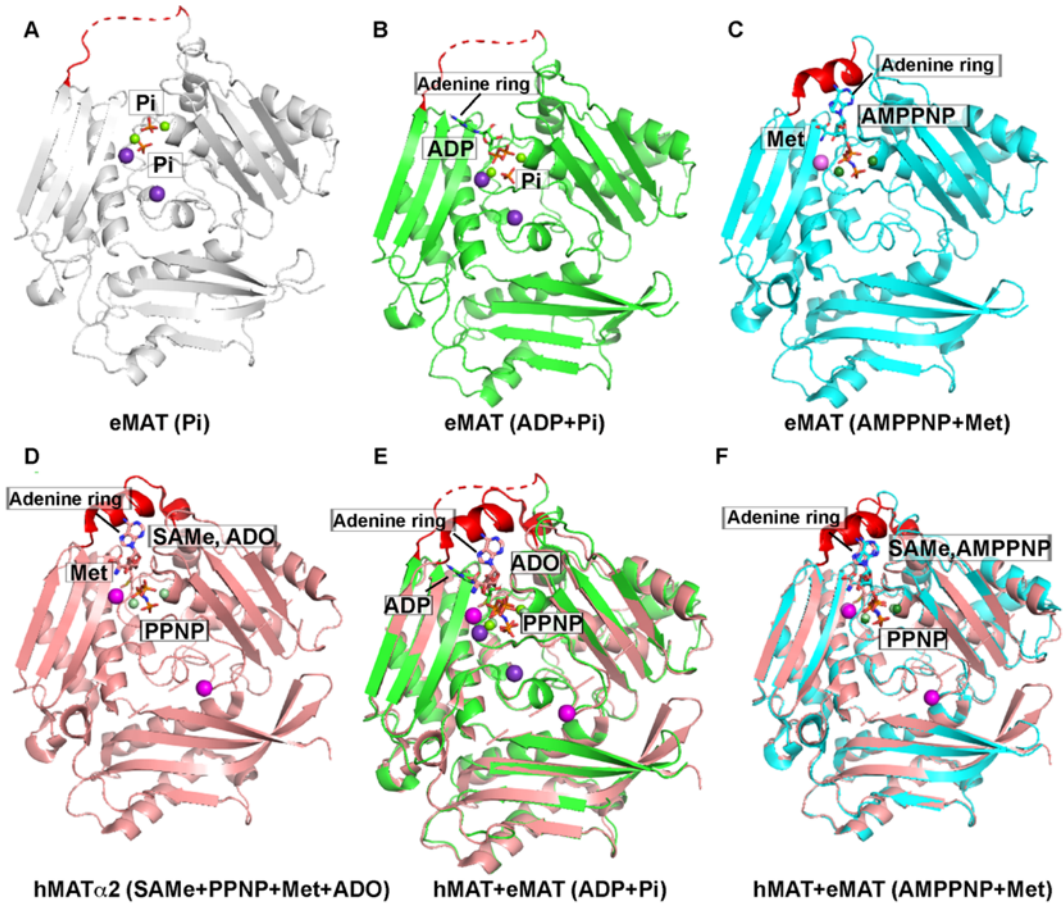

Fig.1.10 Structures of eMAT in comparison with human MATα2 (A) The eMAT structure shows two inorganic phosphates (PDB: 1XRA) **(B)** The eMAT structure shows ADP+Pi in the active site (PDB: 1MXB) **(C)** The eMAT structure contains AMP-PNP+Met in the active site (PDB: 1P7L) **(D)** The human MATα2 structure is bound with SAMe+PPNP+Met+ADO in the active site (PDB: 5A1I) **(E)** The human MAT structure (5A1I, wheat) is aligned with the eMAT structure (1MXB, green) **(F)** The human MAT structure (5A1I, wheat) is compared with the eMAT structure (1P7L, blue) by structural alignment. The gating loop is shown in red. Mg^{2+} and K^{+} ions are represented by green and purple spheres, respectively. Ligands in active sites are shown as sticks.

1.3.3 Eukaryotic MAT structures (*R. norvegicus, H. sapiens*)

1.3.3.1 *R. norvegicus* MAT structure (rMAT)

Several rMAT structures in complex with substrates or their analogues were reported by Gonzalez B et al., 2000, 2003 [35, 53]. Met and its analogue, L-2-amino-4-methoxy-cis-but-3-enoic acid (AMB), were found to bind to the active site of rMAT at the similar position of the ATP (adenine moiety) of eMAT and human MAT which were later reported by Komoto J et al., 2004 and Murray B et al., 2016 (Fig.1.11) [30, 36]. The AMB showed to stack against Phe251 aromatic ring in the AMB bound structure of rMAT (Fig.1.11A). This is in contrast to the usual π-π stacking of ATP adenine ring against Phe251. Also, ATP and ADP positions found in rMAT structures showed the different orientations in both adenine moieties and tripolyphosphate chains (Fig.1.11 B-C and F). The substrate binding positions reported in the eMAT structure (by Komoto J et al., 2004) and the human MAT structure are consistent and almost identical (Fig.1.11D-E). The high-resolution structure of the human MATα2 reported at 1.1 Å (PDB: 5A1I) showed that the adenine moiety of ATP is in the similar conformation after the formation of SAMe (Fig. 1.11E). In addition, the average B-factors of ligands and ions in the active site from these reported rMAT structures were much higher than those of the proteins (Table 1.1), indicating the low occupancy of the substrate or the analogue binding to the active site. There are no X-ray data available in PDB server, therefore the calculation of ligand real space correlation coefficients cannot be performed because of this limitation. Regarding these unavailable data, the unusual features of the ligand binding modes in the active site of rMAT structures should be treated with caution. In addition, this ATP+Met bound structure of rMAT was obtained by soaking ATP into the crystal of Met+2Pi bound structure, while the gating loop remained disordered, suggesting that this structure may not represent the functional states of the enzyme.

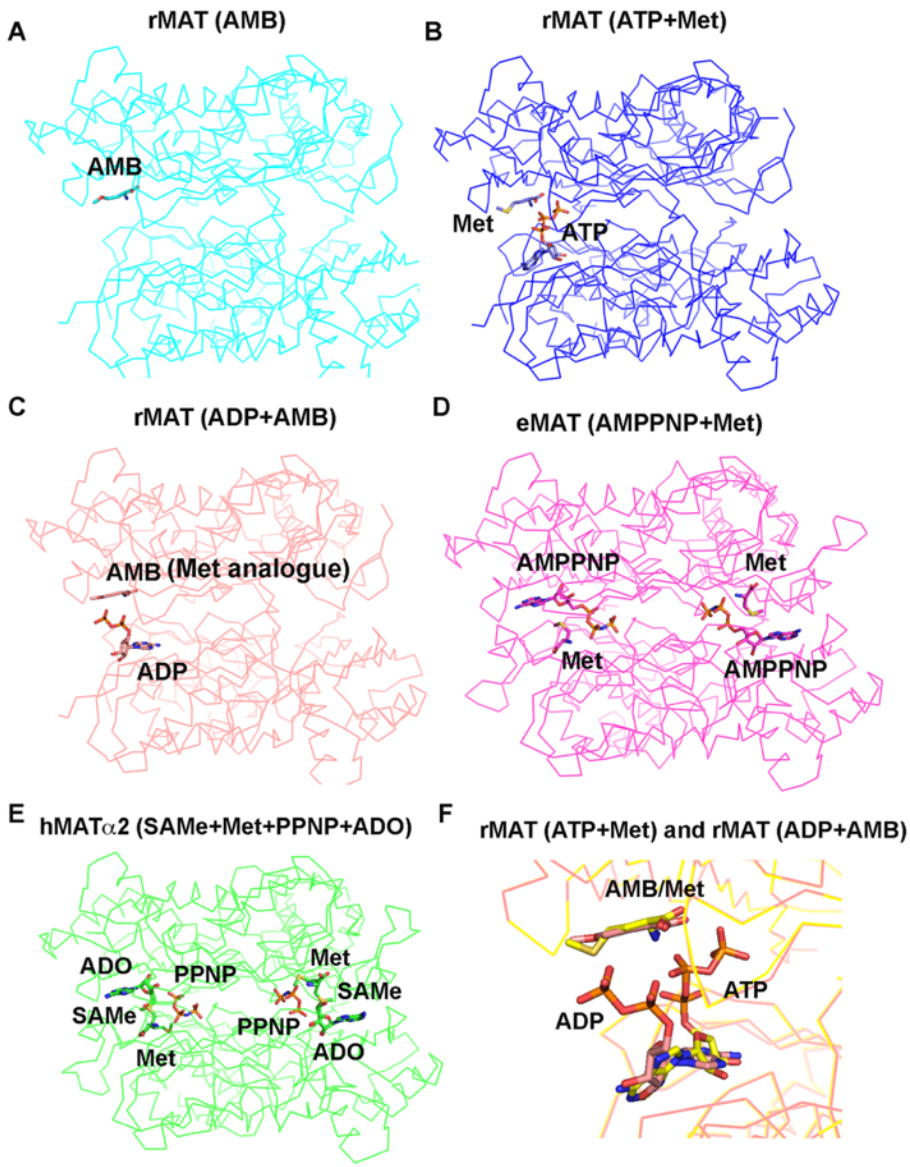

Fig. 1.11 The comparison of substrate binding sites in rMAT, eMAT and human MAT structures. The structure of rMAT was in complex with AMB in the active site (PDB: 1QM4) **(A),** ATP+Met (PDB: 1O9T) **(B),** and ADP+AMP (PDB: 1O92) **(C)**. **(D)** The eMAT structure shows AMP-PNP+Met in the active site (PDB: 1P7L). **(E)** The human MATα2 structure was bound with SAMe+Met+ADO+PPNP (PDB: 5A1I). **(F)** The structural alignment of the ATP+Met bound structure and the ADP+AMB bound structure of rMAT is shown in yellow (PDB: 1O9T) and peach (PDB: 1O92), respectively. MAT substrates or their analogues are shown as sticks.

Table 1.1. The average B-factors of proteins and molecules in the active site. All rMAT structures showed the relative higher B-factors of ligands in the active site compared to those reported in the eMAT structure. The lower B-factors (less than 30 $Å^2$) indicate the higher confidence in the ligand atomic positions.

Complex	PDB	Resolution (Å)	B-factor of protein ($Å^2$)	B-factors of ligands in the active site ($Å^2$)	Ref
eMAT (SAMe+PPNP)	1P7L	2.5	19.6	14.2 (SAMe), 15.1 (PPNP)	[36]
rMAT (ATP+Met)	1O9T	2.9	37.0	82.3 (ATP), 75.2 (Met)	[35]
rMAT (ADP+AMB)	1O92	3.19	24.6	76.0 (AMP), 73.4(ADP)	[35]
rMAT (AMB)	1QM4	2.66	31.4	43.0	[53]

1.3.3.2 *H. sapiens* MAT structure (hMAT)

Numerous structures of hMAT that have been reported to date are summarised in Table 1.2. Structures of hMATα1 and hMATα2 in complex with SAMe in the active site were firstly reported by Shafqat N et al., 2013 [43]. The crystals were obtained by co-crystallisation of proteins with SAMe that showed two molecules of SAMe in the two equivalent active sites (Fig. 1.12A). Structures of hMATα1 and hMATα2 are almost supposable with the root mean square deviation (RMSD) of 0.41 Å and they show the similar SAMe binding site [43]. SAMe directly interacts to Ser247 and Asp258 with its ADO and ribose moieties, while Met mainchain is partly stabilised by Gln113 of the neighbouring gating loop and Glu70 (Fig. 1.12A). A number of hMATα2 structures with different ligands have been studied by Murray B et al., 2016 [30]. The structure of hMATα2 in complex with SAMe+Met+ADO+PPNP

obtained at 1.09 Å showed the atomic details of substrate binding leading to SAMe formation with partial occupancies of ligands in the active site [30]. The structural alignment of hMATα2 (SAMe-bound structure, PDB: 2P02) and hMATα2 (SAMe+Met+ADO+PPNP-bound structure, PDB: 5A1I) reveals RMSD of 0.094 Å and SAMe binding sites of these two structures are identical (Fig. 1.12B). The SAMe-bound crystal of hMATα2 (PDB: 2P02) was obtained by soaking SAMe into the crystal, while the SAMe-bound form of hMATα2 structure (PDB: 5A1I) was produced by co-crystallisation of enzyme substrates (AMP-PNP and methionine), suggesting the functional relevance of enzyme reactions. In the hMATα2 (SAMe+Met+ADO+PPNP) structure, the cleavage of AMP-PNP to ADO and PPNP occurred before SAMe formation, as the reaction is initiated by the nucleophilic attack of the sulphur atom of Met to the C5 atom of ATP. At the transition state of SAMe formation, the enzyme intermediates (ADO and PPNP) including Met were captured in the hMATα2 (SAMe+Met+ADO+PPNP) crystal structure (Fig. 1.13A). Also, Murray B et al., 2016 reported the PPNP-bound structure of hMATα2 (PDB: 5A19) which revealed the open conformation of the gating loop without PPPi hydrolysis taking place (Fig 1.13B-C) [30].

Three crystal structures of MAT$(\alpha 2)_4$MATβ$(V2)_2$ complexes were reported with SAMe+Pi, SAMe+PPNP and ADO+PPi+Pi bound in the active sites [13]. The C-terminal tail of MATβ (residues 316-321) interacted with MATα2 at the dimeric pocket of MATα2 dimers (Fig. 1.14A-B). Forming the complex with MATβV1 and MATβV2 showed an increase in SAMe formation by 4- and 3-fold, respectively, when compared to the activity of MATα2 alone [13]. However, the binding of the regulatory subunit did not alter the positions of residues in the active sites of MATα2, suggesting that MATβ modulated the activity of MATα2 by an allosteric mechanism. The structure of MAT$(\alpha 2)_4$MATβ$(V2)_2$ complex (SAMe+PPNP) have four active sites, two of those showing the closed gating loops with SAMe and PPNP bound to

and the two empty active sites showing the disordered mostly invisible gating loops (Fig. 1.14C-D).

Table 1.2. The structures of hMATα1, hMATα2 and MAT(α2)$_4$MATβ(V2)$_2$ reported to date

Name	PDB	Resolution (Å)	Ligands in the active site	References
MATα1	2OBV	2.05	SAMe	[43]
MATα2	2P02	1.21	SAMe	[43]
MATα2	5A1I	1.09	SAMe+Met+ADO+PPNP	[30]
MATα2	5A19	2.34	PPNP	[30]
MATα2	5A1G	1.83	SAE+PPNP	[30]
MAT(α2)$_4$MATβ(V2)$_2$	4KTT	2.59	SAMe+Pi	[13]
MAT(α2)$_4$MATβ(V2)$_2$	4NDN	2.34	SAMe+PPNP	[13]
MAT(α2)$_4$MATβ(V2)$_2$	4KTV	3.30	ADO+PPi+Pi	[13]

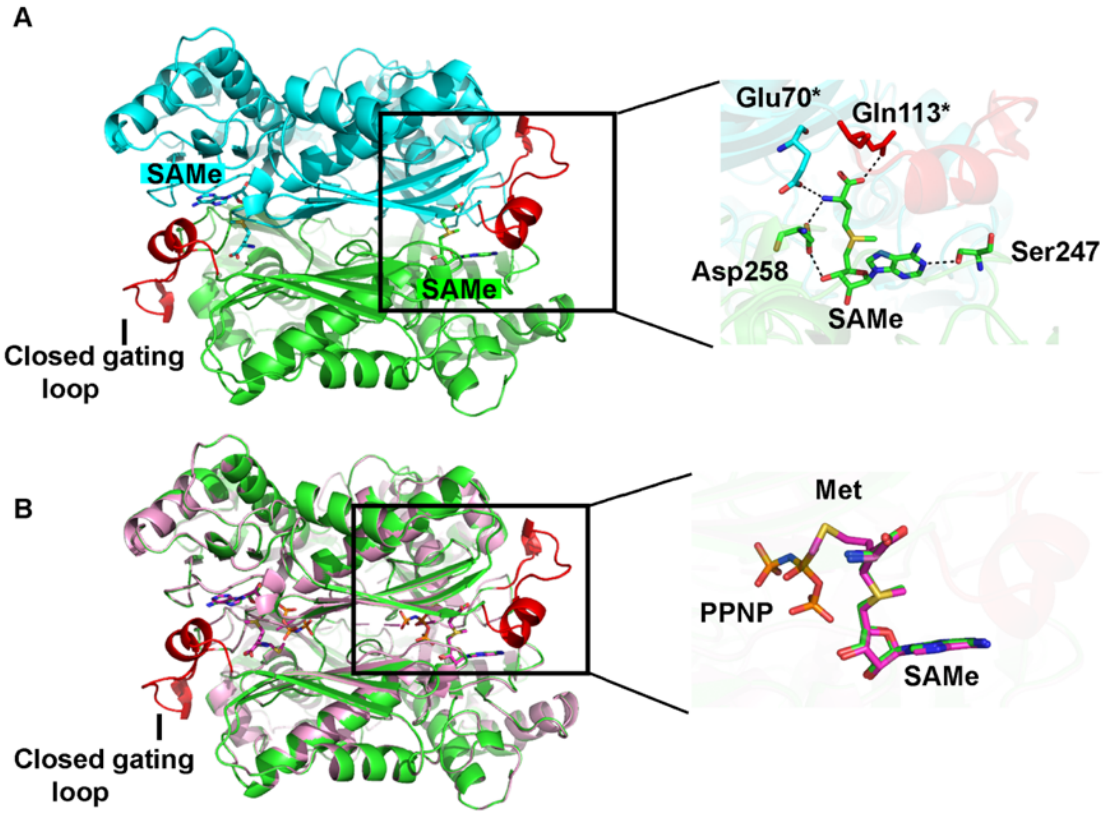

Fig. 1.12 The structure of hMATα2 in complex with SAMe and SAMe+Met+ADO+PPNP in the active site. (A) The SAMe-bound structure of MATα2 (PDB: 2P02) is shown in green and blue ribbons. Carbon atoms of SAMe in each active site are represented by green and blue sticks. The ordered gating loop is shown in red. **(B)** The SAMe-bound structure of MATα2 (PDB: 2P02, green) is aligned with the SAMe+Met+ADO+PPNP-bound structure (PDB: 5A1I, pink). Carbon atoms of SAMe in each active site are represented by green (PDB: 2P02) and pink sticks (PDB: 5A1I). The ordered gating loop is shown in red.

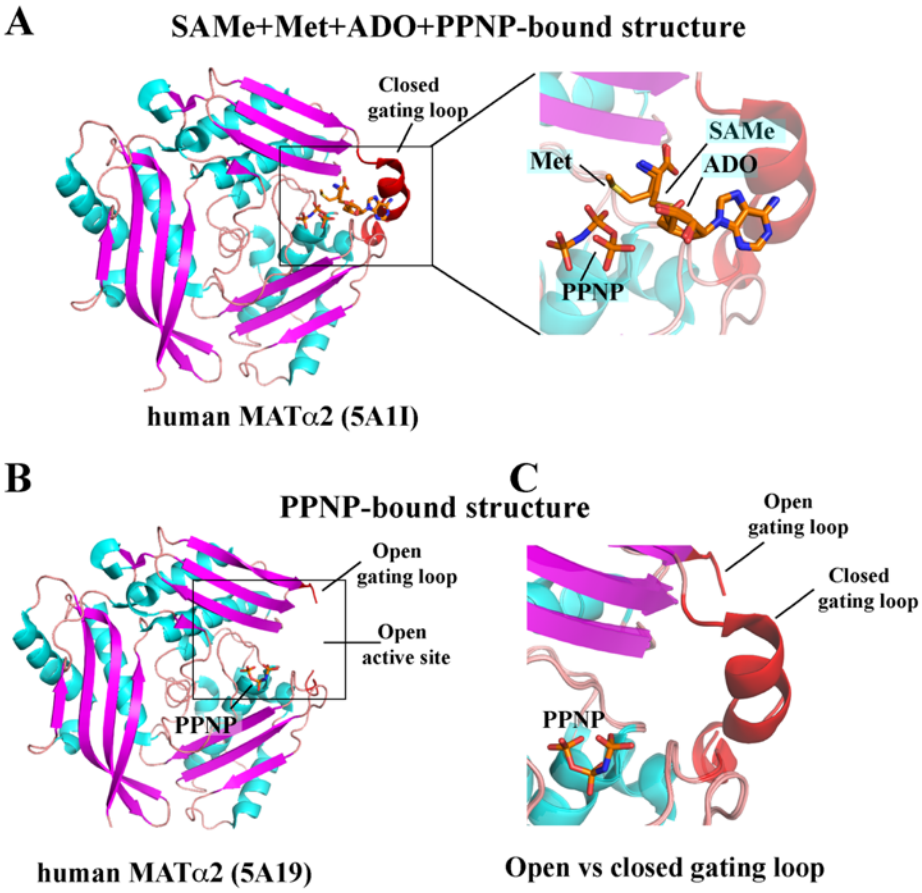

Fig. 1.13 The SAMe+Met+ADO+PPNP structure and PPNP-bound structure of human MATα2 (A) The active site ligands (SAMe, Met, ADO and PPNP) of the human MATα2 structure (PDB: 5A1I) show occupancies of 0.5, 0.3, 0.5 and 0.7, respectively. The gating loop in closed conformation blocks the entrance to the active site. **(B)** The PPNP bound structure (PDB: 5A19) shows the open conformation of the gating loop, the main part of which is not observed in the structure representing its flexibility. **(C)** The alignment of the PPNP bound structure and the SAMe+Met+ADO+PPNP bound structure is shown. The open loop is disordered and invisible in the structure, while the loop in its closed conformation is clearly visible in the structure of the SAMe+Met+ADO+PPNP bound crystal.

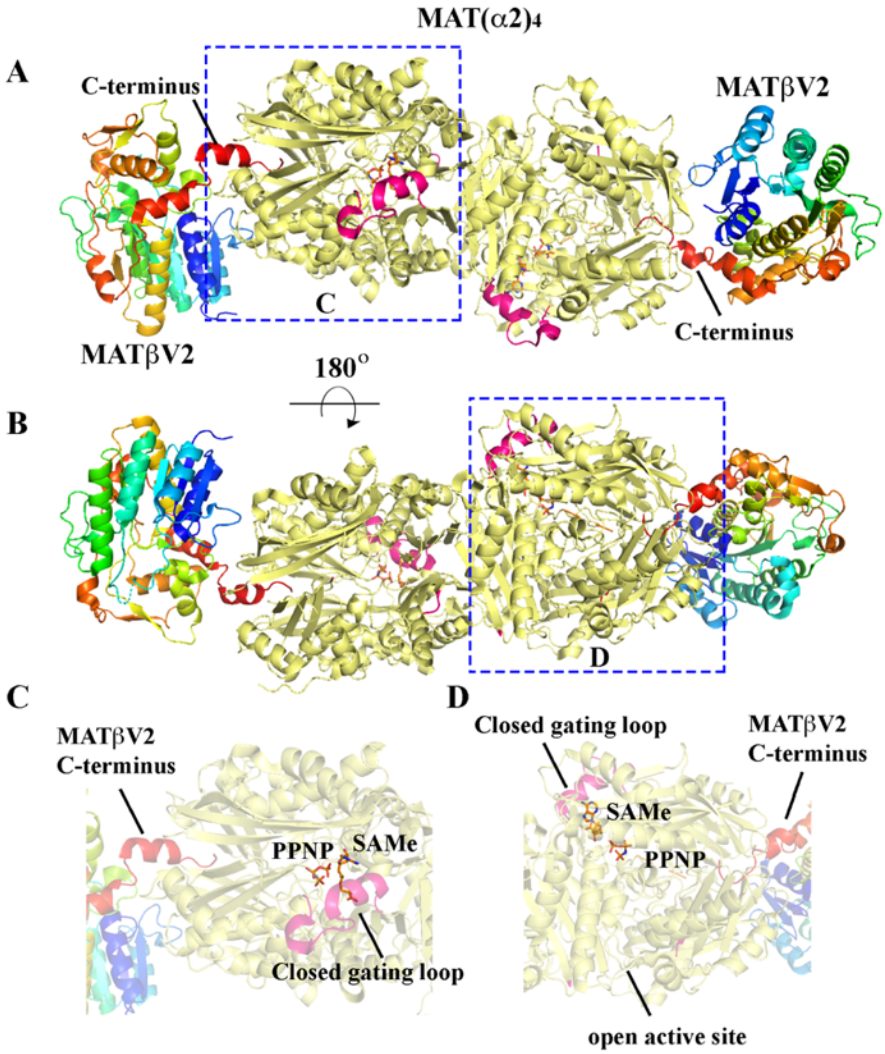

Fig. 1.14 The SAMe+PPNP-bound structure of the human MAT(α2)$_4$MAT(βV2)$_2$ complex (A) The MAT(α2)$_4$MAT(βV2)$_2$ complex (PDB: 4NDN) contains 4 subunits of MATα2 and 2 subunits of MATβV2. The tetramer of MATα2 is shown in pale yellow. One subunit of MATβV2 interacts with a dimer of MATα2 with its C-terminus (red) at the MATα2 dimer interface. The N-terminus of MATβV2 is shown in blue. **(B)** The complex is rotated by 180^o along the x-axis to show the empty active site. **(C)** SAMe and PPNP (orange sticks) were captured in one active site of the MATα2 dimer. **(D)** The dimer of MATα2 contains one occupied and one empty active site which was flanked by the closed and open gating loop (pink), respectively.

1.3.4 SAMe binding sites based on human MATα1 and MATα2 crystal structures

SAMe binding sites are reported in human MATα1 and MATα2 at 2.05 and 1.09 Å resolution, respectively. All residues that interact with SAMe are conserved in both MAT isoforms. The SAMe interacting residues in the active site are described by using MATα2 as the model regarding to its higher resolution. Methionine moieties of SAMe are maintained by Glu70 (OE1 atom), Asp258 (OD1 atom), Gln113 (NE2 atom) and two water molecules (Fig. 1.15A). Adenosine aromatic ring of SAMe forms π-π stacking with Phe250 and three of SAMe's N atoms are coordinated with Ser247 (O atom), Arg249 (O atom) and two water oxygen atoms, while its ribose moiety (O atom) forms the H-bond with Asp179 (OD1 atom), Fig 1.15A.

There are three water molecules interacting with SAMe as observed by the structural comparison of MATα1 and MATα2 (Fig. 1.15B-C). The first water molecule is coordinated by N6 and N7 atoms of SAMe and an OG atom of Ser114 (gating loop). The second water forms H-bond with N3 and O4 atoms of SAMe and an OD1 atom of Asp134. The third water molecule is coordinated with an O atom of SAMe and Ser114 main chain (N atom). For the MATα2 structure, there is one more water molecule which interacts to SAMe at an O atom of methionine moiety. This water molecule (number 4, Fig. 1.15B) is coordinated by the O atom of SAMe and Gly133 main chain (O atom).

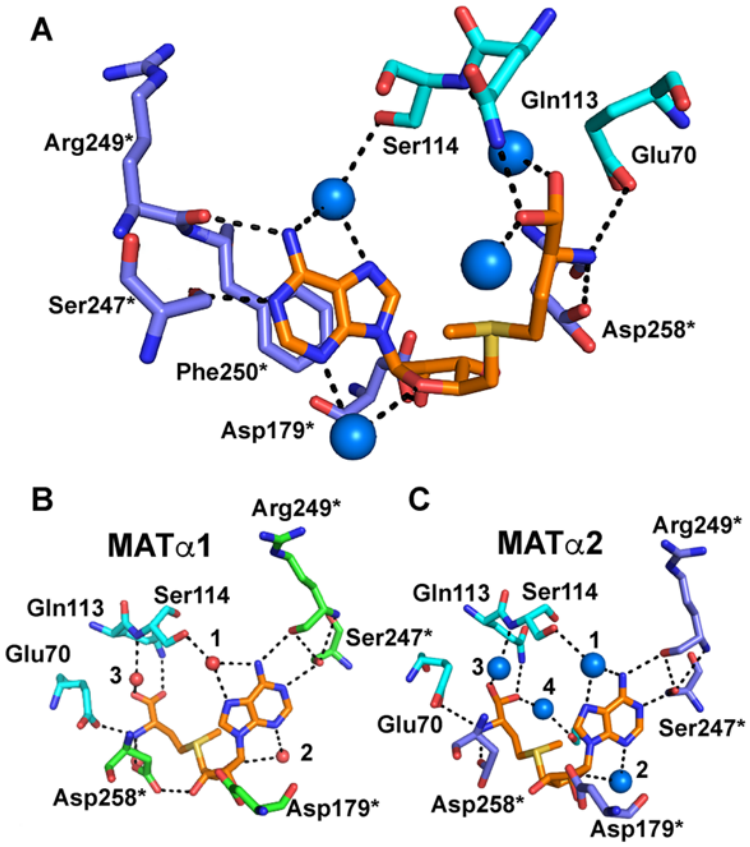

Fig. 1.15 SAMe binding sites from the crystal structures of human MATα1 and MATα2. **(A)** The SAMe binding site is illustrated using the structure of MATα2 as the model (PDB: 5A1I). Carbon atoms of SAMe are shown in orange sticks and waters are shown in blue spheres. **(B)** Waters interacting with SAMe are shown in red spheres of the MATα1 model (PDB: 2OBV). **(C)** Waters interacting with SAMe are shown in blue spheres of the MATα2 model (PDB: 5A1I). Carbon, nitrogen and oxygen atoms of SAMe are represented by orange, blue and red colours, respectively. All residues from the partner subunit are marked with asterisks.

1.4 MAT transcriptional and post-translational regulation

1.4.1 MAT transcriptional and epigenetic regulation

MAT1A and MAT2A gene expressions are mainly regulated by epigenetic controls via DNA methylation and histone (H4) acetylation [54]. The MAT1A gene of the adult liver is unmethylated and actively expresses, while the MAT1A gene of the developing liver and the extrahepatic tissues is suppressed by being hypermethylated at CpG sites on MAT1A gene promoter regions and vice versa for MAT2A expressing tissues. Histone acetylation levels have been found to increase in both MAT1A and MAT2A expressing tissues (2 and 3.5-fold for hepatic MAT1A and kidney MAT2A genes, respectively), suggesting that these epigenetic modifications are crucial for the tissue-specific expression of both MAT1A and MAT2A genes [55]. Moreover, HepG2 cells (human hepatocellular carcinoma cell line) showed an undetectable level of the MAT1A gene expression due to hypermethylation, while treatment of HepG2 cells with the demethylating agent (5-aza-2'-deoxycytidine) or the histone deacetylase inhibitor (trichostatin) could regain the cell's ability to express the MAT1A gene [22, 55].

The promoters of MAT1A [56-58], MAT2A [59, 60] and MAT2B [9] genes have been cloned and sequenced. The consensus binding sites for transcription factors including activator protein 1 (AP-1), cyclic AMP response element binding protein (CREBP), CCAAT enhancer binding protein (C/EBP), Transcription factor family including E2F- and DP-like subunits (E2F), glucocorticoid response elements (GRE), hepatocyte-enriched nuclear factor (HNF), interleukin-6 (IL-6), signal transducers and activators of transcription (STAT), avian myeloblastosis viral oncogene homologue (v-Myb) and myelocytomatosis viral oncogene homologue (c-Myc) were characterised in the MAT1A gene [58] and some of them were studied in detail. The combined actions of HNF and C/EBF as the transcriptional activator are important for liver-specific gene expression. The transcriptional activity of hepatic MAT

promoters is positively regulated by the binding of a nuclear factor 1 (NF1) family, a NF1-like protein or a liver-enriched transcription factor (HNF3 family) [56]. Glucocorticoid (GC) could bind to GRE on the MAT1A promoter, and this elevated MAT1A expression and promoter activity in rat hepatoma H35 cells and primary cultures of hepatocytes in both dose- and time-dependent manners [61]. Healthy hepatocytes and bile duct epithelial cells expressed high levels of the MAT1A gene. These two cell types showed the increased levels of c-Myc and c-Maf (cellular muscular aponeurotic fibrosarcoma) during cholangiocarcinoma (CCA) development. The MAT1A gene expression was found to decrease in developing CCA, while overexpression of MAT1A gene could inhibit c-Myc induction and CCA proliferation [62]. H69 cells (Cholangiocytes: benign bile duct epithelial cells) treated with IL-6 showed the reduction of MAT1A mRNA levels by 20 %, while this elevated c-Myc and c-Maf about 40 % [63]. Also, overexpression of c-Myc was found to lower the MAT1A promoter activity by 75 % in KMCH cells (human cholangiocarcinoma cell lines) [62]. The active rat MAT1A promoter was reported in non-hepatic cell types (e.g. Chinese hamster ovary cells), suggesting that the liver-specific expression maybe not specifically controlled by these transcriptional factors, but it is rather regulated by epigenetic modifications (i.e. methylation of CpG islands as mentioned above or compaction of chromatin). The summary of MAT1A gene regulators is shown in Fig. 1.16.

The promoter of MAT2A contains NF-κB (nuclear factor kappa B) and AP-1 response elements. NF-κB and AP-1 could bind to the MAT2A promoters after they were activated by TNF-α (tumour necrosis factor-α). NF-κB and AP-1 binding to MAT2A promoter was found to increase in hepatocellular carcinoma of HepG2 cells and this promoted MAT2A transcription [64]. Transcription factors including Sp1 (specificity protein 1), c-Myb and E2F also up-regulated the activity of the MAT2A promoter [65, 66]. The MAT2A gene was overexpressed in the CCl_4-induced fibrosis mice, while the administration of the NPLC0393

(the inhibitor of transforming growth factor beta-1 (TGF-β1) signalling pathway) could inhibit the upregulation of the MAT2A gene [67]. This underlying mechanism was studied in hepatic stellate cells. When TGF-β1 activated the phosphorylation of p65 (nuclear factor kappa B p65), the phosphorylated p65 entered the nucleus and promoted MAT2A transcription and protein expression. In addition, the hypoxic environment of hepatoma cells could trigger MAT2A expression via the binding of a HIF-1α (hypoxia-inducible factor-1α) on the MAT2A promoter [68]. Upstream regulatory regions of the MAT2A promoter contains several peroxisome-proliferator activated receptor (PPAR) response elements (PPREs). Nuclear receptors including the PPAR of rat activated hepatic stellate cells were found to bind on PPREs. PPARγ and PPARβ share the similar binding site on the MAT2A promoter [69]. PPARγ was predominant in silent hepatic stellate cells, while PPARβ was activated during the liver fibrogenesis [70, 71]. In quiescent hepatic stellate cells, binding of the PPARγ to PPREs negatively regulated MAT2A transcriptions. During hepatic stellate cell activation, the PPARγ expression and activity significantly decreased and this promoted the binding of the PPARβ to PPREs on the MAT2A promoter, resulting in MAT2A expressions [69]. A summary of MAT2A gene regulators is described in Fig. 1.17.

The switch of MAT1A to MAT2A gene expressions and lower SAMe levels were found to be related with CpG hypermethylation and deacetylation of histone H4 of the MAT1A promoter. CpG hypomethylation and histone H4 acetylation of MAT2A were reported in F344 rats (genetically predispose to HCC) and human liver cancer cells [72]. The methylation of MAT1A genes at +10 and +88 sites (relative to the transcriptional start site) down-regulated MAT1A gene transcriptions [73]. In addition, the MAT1A gene hypermethylation and low levels of mRNA expressions were also reported in patients with the advanced non-alcoholic fatty liver disease [74].

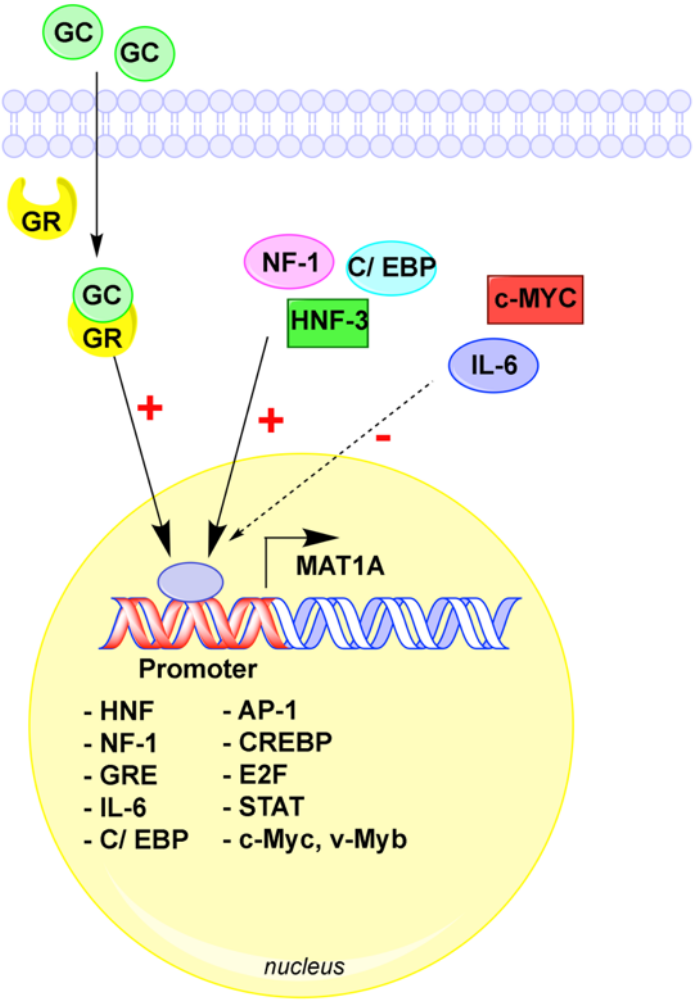

Fig. 1.16 Transcriptional regulations of the MAT1A gene. MAT1A expression can be regulated by several transcriptional factors that contain their response elements on the MAT1A promoter. Positive and negative regulators are represented by plus and minus, respectively. Glucocorticoid (GC); glucocorticoid receptor (GR); hepatocyte-enriched nuclear factor (HNF); nuclear factor 1 (NF1); glucocorticoid response element (GRE); interleukin-6 (IL-6); CCAAT enhancer binding protein (C/EBP); activator protein 1 (AP-1); cyclic AMP response element binding protein (CREBP); transcription factor family including E2F- and DP-like subunits (E2F); signal transducers and activators of transcription (STAT), myelocytomatosis viral oncogene homologue (c-Myc); avian myeloblastosis viral oncogene homologue (v-Myb).

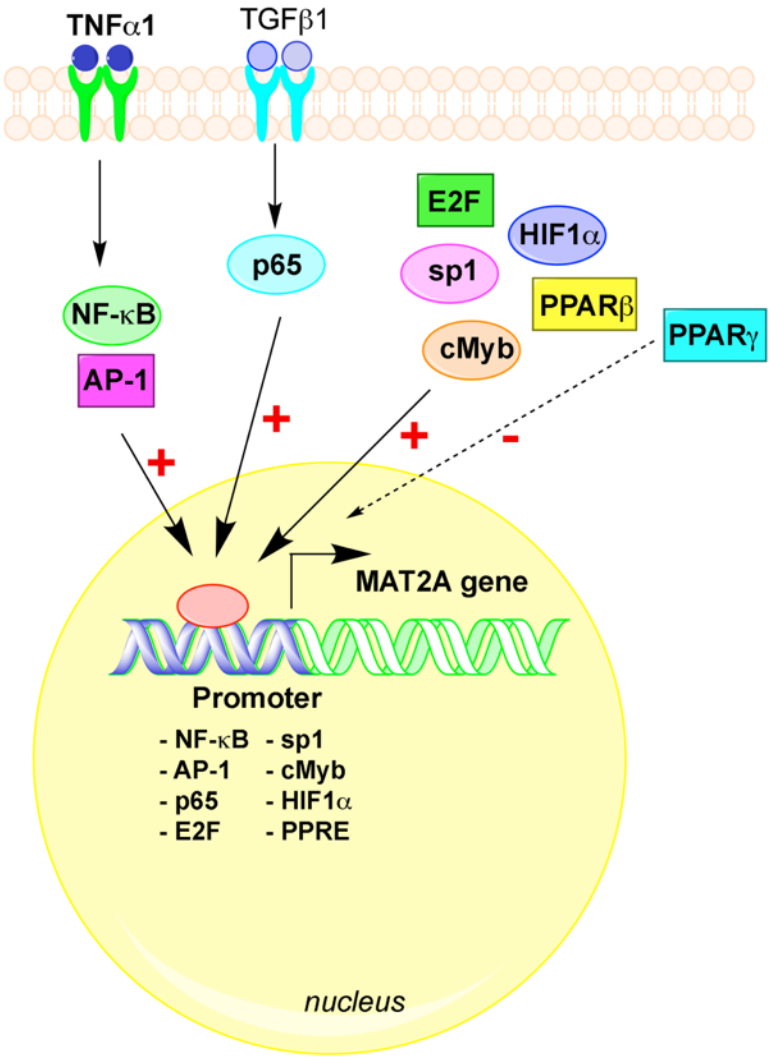

Fig. 1.17 Transcriptional regulation of the MAT2A gene. Positive and negative regulators are represented by plus and minus, respectively. Tumour necrosis factor alpha-1 (TNF-α1); transforming growth factor beta-1 (TGF-β1); nuclear factor kappa B (NF-κB); activator protein 1 (AP-1); transcription factor family including E2F- and DP-like subunits (E2F); specificity protein 1 (sp1), hypoxia-inducible factor-1α (HIF-1α); peroxisome-proliferator activated receptors (PPAR) response elements (PPRE); myeloblastosis viral oncogene homologue (c-Myb); nuclear factor kappa B p65 (p65).

1.4.2 MAT post-translational modification

Post-translational modification (e.g. phosphorylation, nitrosylation, sumoylation, ubiquitylation and acetylation) can regulate MAT enzyme activity and stability (Fig. 1.18). Treatments of the rat liver MAT with nitric oxide (NO) donors (e.g. linsidomine, S-nitroso-N-acetylpenicillamine or S-nitrosoglutathione monoethyl ester) showed the decrease in an enzyme activity in a dose-dependent manner. Removal of the NO donors or the administration of some reducing agents (e.g. β-ME or glutathione) could reverse the effect of these NO releasing agents. The NO binding site was determined in the rat liver MAT showing that Cys121 (equivalent to Cys120 in human MATα1) was involved in the inhibition effect of the NO on MAT enzymes [75]. Cys121 is only found in MATα1 (Gly121 in MATα2) and it is a part of the enzyme gating loop. The serine substitution of acidic or basic amino acids (e.g. Asp335, Arg357 and Arg363) around Cys121 could inhibit the effect of NO on MATα1 activity, suggesting that these Cys121 surrounding residues were involved in the inhibition of MATα1 activity by S-nitrosylation [76].

The regulation of the rat liver MAT by protein kinase C (PKC) phosphorylation was studied and Thr342 was identified as the phosphorylation site. The phosphorylated Thr342 in a hepatic MAT dimer caused enzyme dissociation to a monomeric form [77]. Tyr371/Tyr374 and Thr257/Tyr259 were determined as the phosphorylation sites of MATα2 and MATβ proteins, respectively. They were phosphorylated by mitogen-activated protein kinase (MAPK) family members (Ras/Raf/MEK/ERK cascade reaction) [78]. Only the MATβ subunit showed the decrease in phosphorylation and enzyme stability when B-Raf or ERK1/2 were silenced, while MEK inhibition had effect on both MATβ and MATα2 proteins.

Sumoylation is the SUMOs (small ubiquitin-like modifiers) addition process to the target protein which can affect the protein structure (stability), and subcellular localisation [79]. In

human colon and liver cancer cell lines (e.g. HepG2 and RKO), MATα2 required Ubc9 (Ubiquitin-conjugating enzyme 9) for sumoylation at Lys340, Lys372 and Lys394 to increase their stability. Colon cancer showed greater levels of MATα2 sumoylation, total MATα2 and Ubc9 levels which in turn facilitated tumour cell growth by maintaining Bcl-2 (B-cell lymphoma 2) expression [80].

P300 (E1A binding protein p300) acetylated MATα2 at Lys81 and destabilised MATα2 by the activation of ubiquitylation processes which resulted in proteasomal degradation [81]. In contrast, MATα2 was deacetylated and stabilised by a histone deacetylase-3 by inhibiting the proteasomal degradation process. Acetylation of MATα2 at Lys81 was also found to decrease in human hepatocellular cancer.

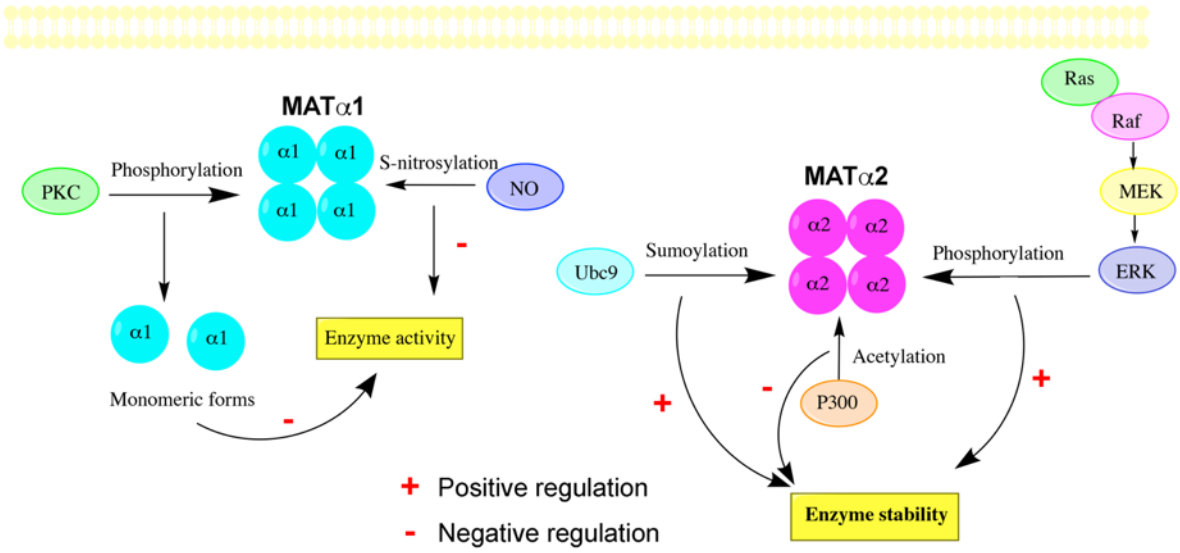

Fig. 1.18 Post-translational modification of MAT enzymes. MATα1 and MATα2 can be regulated by post-translational modification processes e.g. phosphorylation, acetylation, sumoylation, etc. These processes result in enzyme activity and stability alteration. Nitric oxide (NO); protein kinase C (PKC); Ubc9 (Ubiquitin-conjugating enzyme 9); P300 (E1A binding protein p300).

1.5 Introduction to X-ray crystallography

1.5.1 Structural biology through X-ray crystallography

The origin of X-ray diffraction of macromolecule crystals can be traced back to the finding of X-ray in 1895 by Wilhelm Conrad Röntgen whose scattering and polarisation nature was illustrated by Charles Glover Barkla [82-85]. This finding gave rise to the first diffraction experiments by Max von Laue. Those Röntgen rays (X-rays) were generated by the impact of cathode rays on a solid object. The X-rays can penetrate the solid material and cast the shadow on pieces of film. Max von Laue showed X-ray diffraction patterns of a salt crystal in 1912, demonstrating that X-rays are electromagnetic waves that can produce a diffraction pattern when they travel through a crystal [86, 87]. In 1913 William Henry Bragg (father) and William Lawrence Bragg (son), introduced the Bragg's equation (Bragg's Law) to explain the interference pattern of X-rays scattered by crystals [88]. In 1953, the double-helix model of DNA was proposed by James Watson and Francis Crick using X-ray diffraction images obtained from Rosalind Franklin [89]. In 1959, Max Perutz and John Kendrew firstly elucidated the myoglobin structure and just a few months later the haemoglobin structure was successfully obtained (about 64 years after X-rays were discovered) [90, 91]. Since then numerous structures of important biochemical substances have been discovered by X-ray crystallography techniques including vitamin B12 and insulin by Dorothy Hodgkin [92-94], the photosynthetic reaction centre, which is the first membrane protein structure, by Johann Deisenhofer, Robert Huber and Hartmut Michel [95], the ATP synthase structure by John E Walker [96] and the G-protein-coupled receptor (GPCR) structure by Brian Kobilka and Robert Lefkowitz [97].

1.5.2 Protein crystallisation

Protein crystallisation is a trial-and-error experiment in which the presence of impurities, crystallisation nuclei and other unknown factors can affect crystallisation processes either interfering with or promoting crystal growth. Contaminants should be at the least amount and all protein molecules should retain their surface charge distribution, as these factors have an effect on the packing of the molecules in the crystal. Crystallisation depends on many parameters including the purity and homogeneity of proteins. In order to obtain starting crystallisation conditions, many reservoir conditions are tested using commercial screens and robotics. Over the last 50 years, requirements for large crystals have diminished going from mm to micron when synchrotron radiation [98, 99] and cryo-crystallography [100-102] are used for data collection. Cryo-crystallography is a technique used to decrease the effect of radiation damage on protein crystals by soaking the crystals with cryoprotectants and freezing them with liquid nitrogen before being exposed to X-ray beams (the crystals will be in cold stream during data collection).

When the achievable highest purity of protein is obtained, the purified protein is mixed with a suitable buffer combined with a precipitant solution for crystallisation. The initiation of crystallisation nuclei is induced by the supersaturation of the protein solution that promotes the formation of small aggregates (Fig.1.19). The surface tension energy is needed for spontaneous crystal nucleation. Crystal growth can begin once the energy barrier of nucleation is overcome. The successful formation of crystal nuclei usually occurs at high levels of supersaturation (the state that the energy barrier is easy to overcome) [103]. Protein solubility depends upon a number of factors (e.g. protein concentrations, types of salt in the buffer, the pH of the buffer, etc.). Different crystallisation methods can be used to drive the solution into the supersaturated state and the easiest way to adjust protein concentrations is to vary temperatures or precipitant concentrations. The protein solubility should be gradually decreased to the point where

spontaneous precipitation can occur. Addition of precipitants is the most prevalent procedure to lower protein solubility for protein crystallisation. Polyethylene glycols (PEGs) and inorganic salts (e.g. ammonium sulphate, $(NH_4)_2SO_4$), are commonly used as the protein precipitant reagents.

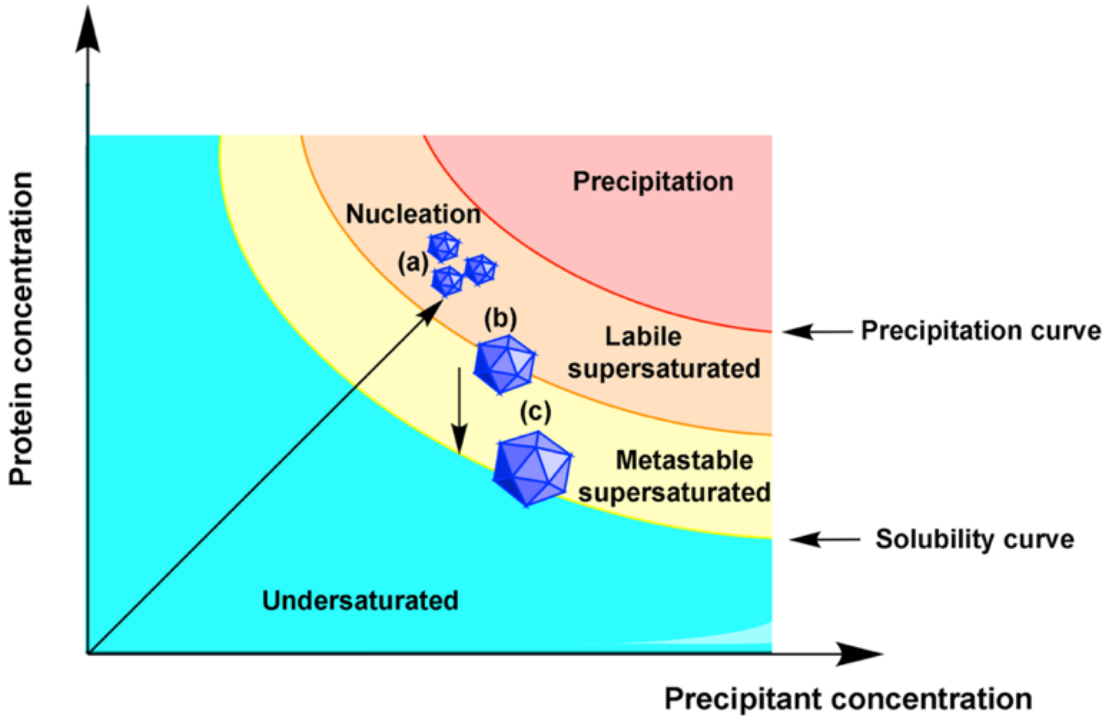

Fig. 1.19 The crystallisation phase diagram of macromolecules. The supersaturation zones contain two phases (metastable and labile regions). Nucleation can be formed in the labile region, while the metastable region is where nuclei develop into crystals (no new nuclei occur in this zone). A precipitation occurs when protein drops are highly supersaturated. Growth of crystals during crystallisation is shown in diagram via a vapour diffusion (a to c) technique. Crystals stop growing once the concentration of proteins is at the equilibrium between the solution and the solid state.

1.5.2.1 Crystallisation solutions

A salt usually acts by salting out proteins from solutions once high salt concentrations increase ionic strengths in the system. Proteins and salt ions will compete for water to keep their solubility at high ionic strength [104]. At this point, when the concentrations of ions become adequately high, the proteins are forced to neutralise their surface charges (to fulfil their electrostatic requirements) by interacting with one another [105, 106]. This interaction may create an ordered arrangement of the proteins in a crystalline lattice [107]. The advantages of using salts as the precipitating agent are their nontoxic and soluble properties.

Some polymers (PEGs are mostly used) [108, 109], create volume exclusion effects that promote the separation of proteins from solutions [108, 110]. PEGs are the effective precipitating agent at low cost and contain different sizes that can be used for crystallisation screening. PEG molecules move randomly in solution and occupy much larger space than their molecular weights due to the flexibility and the water-soluble property. This volume exclusion effect limits free space for proteins and induces protein molecules to segregate and nucleate, transitioning to form a solid state (either amorphous or crystalline). In addition, PEGs are very hydrophilic and can immobilise water molecules (the same property as found in salt solutions) [111]. PEGs compete with proteins to bind to water molecules, and the water will be less available in the solution, mimicking higher protein concentration.

1.5.2.2 Crystallisation methods

To adjust protein solutions to the supersaturated state, several crystallisation techniques can be used [112, 113], while the basic principles of these methods (e.g. micro-batch, vapour-diffusion and micro-dialysis) are different.

The micro-batch method has been developed by Chayen N et al., 1992 [114]. Protein crystals can be grown in 1–2 μL protein drops mixed with the precipitant. The drops are kept in an oil (e.g. paraffin oil) to prevent evaporation (Fig. 1.20A). This technique is not suitable for using organic compounds that can be dissolved in the oil as precipitating agents [115, 116]. The volume of the drop and the concentration of precipitants do not change during the incubation time because of the limited evaporation rate. The protein concentration will instantly change once crystals or amorphous precipitants are formed. If the starting point of protein concentrations is in the under-saturated or supersaturated state (too low or too high concentrations), only a small chance of crystal formation can take place. The protein solution will rapidly precipitate if its starting concentration is in the precipitation zone (Fig. 1.19). Therefore, only protein concentrations that are high enough, but not too high to cause precipitations will favour crystal growth. For this technique, the equilibration develops very rapidly, therefore it influences the crystal growth rate and the crystal quality. The optimal starting concentration of proteins is needed to avoid too rapid growth of crystals which is generally not good for producing high quality crystals.

The vapour-diffusion technique is done by mixing proteins and reservoir solutions (e.g. 1:1 or 1:2 ratio) on a cover slip. The cover slip containing the protein drop will be hung upside down against the reservoir (well) solutions that contain precipitating agents (Fig. 1.20B). Alternatively, the vapour-diffusion technique can be performed by the sitting drop method which protein drops are set on micro-bridges to prevent the protein from falling down the cover

slip (Fig. 1.20C). The ratios of proteins and reservoir solutions can be varied in order to adjust the protein concentrations during screening. Water from reservoir solutions normally evaporates from protein drops (lower precipitating agent concentration) and this will bring the protein solution into the supersaturated state.

Dialysis technique is based on the diffusion rate of the precipitating solution through the dialysis selective membrane that contains protein solutions (Fig. 1.20D). The protein concentration will slowly approach the equilibrium concentration at which it can be crystallised.

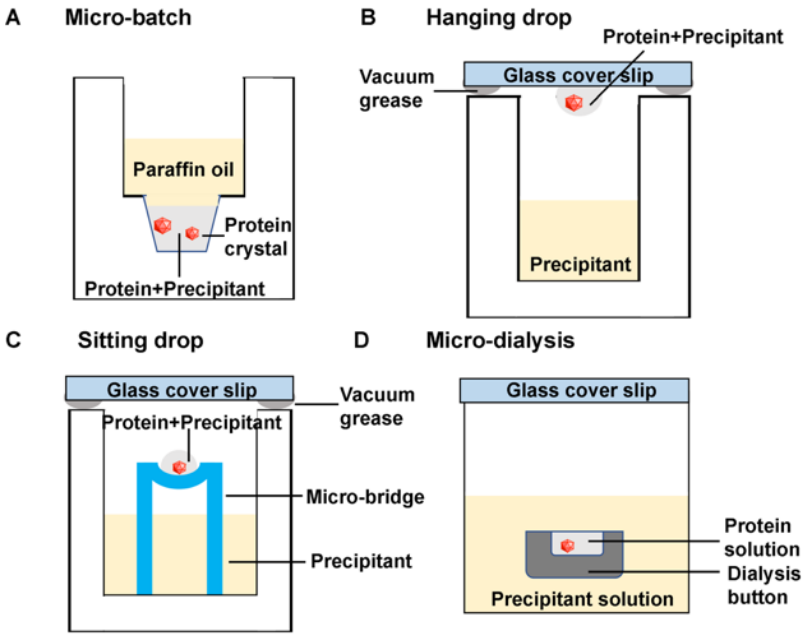

Fig. 1.20 Protein crystallisation techniques. (A) Micro-batch **(B)** Vapor diffusion (hanging drop) and **(C)** Vapour diffusion (sitting drop) and **(D)** Micro-dialysis. Protein crystals are shown in red.

1.5.3 X-ray diffraction

1.5.3.1 Overview

X-rays have very short wavelength (about 1 Å) compared to other electromagnetic waves (e.g. infrared, 100-1 μm and visible light, 720-400 nm) and they can interact with matters differently [117]. There are four principal phenomena when X-rays interact with matters including two scattering (Rayleigh scattering and Compton scattering) and two absorption processes (photoelectric effect and pair production). The energy applied for X-ray crystallographic experiments is usually about 10 keV which can interact with atoms of the crystal by three major ways [118, 119]. Firstly, the X-rays (photons) that collide with atoms and scatter coherently resulting in an observed diffraction pattern are called Thomson or Rayleigh scattering (Fig. 1.21A). Secondly, Compton scattering (Fig.1.21B) may occur if photons inelastically scatter and transfer their energies to electrons in atoms which finally emit the lower energy incoherently. A background on diffraction images is generally generated by the Compton scattering. The third way is photoelectric interaction (Fig.1.21C) that occurs when the incident X-rays are completely absorbed, and photoelectrons are ejected. The entire energy of photons is often deposited into the crystal.

X-ray diffraction is a phenomenon happening when X-rays are scattered by electrons inside the atom of crystalline materials (e.g. salt or protein crystals). The atom hit by X-rays becomes a small secondary X-ray source that emits scattered waves. These waves either coherently or incoherently interfere to each other (Fig. 1.22). If the scattered waves coherently interact with each other (in phase), the phenomenon called a constructive interference will occur (Fig. 1.22A). If the scattered waves cancel out each other (out of phase), a destructive interference will take place (Fig. 1.22B). Only the certain condition that satisfies Bragg's Law will produce constructive interferences and can give diffraction reflections (see below, section 1.5.3.2).

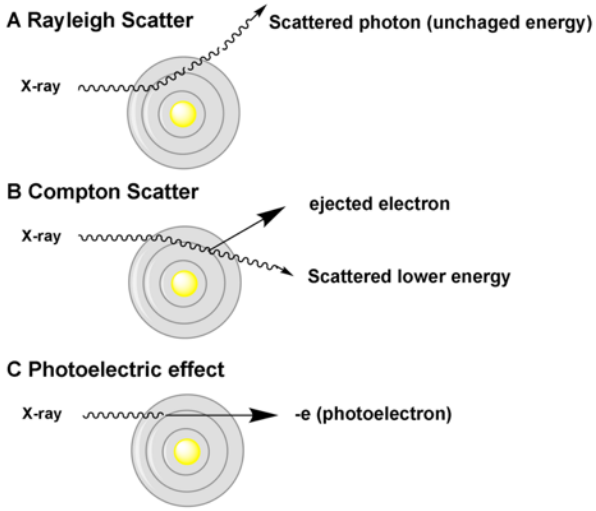

Fig 1.21 Illustration of main phenomena of X-ray interactions with matters. (A) Rayleigh scattering **(B)** Compton scattering **(C)** Photoelectric effect.

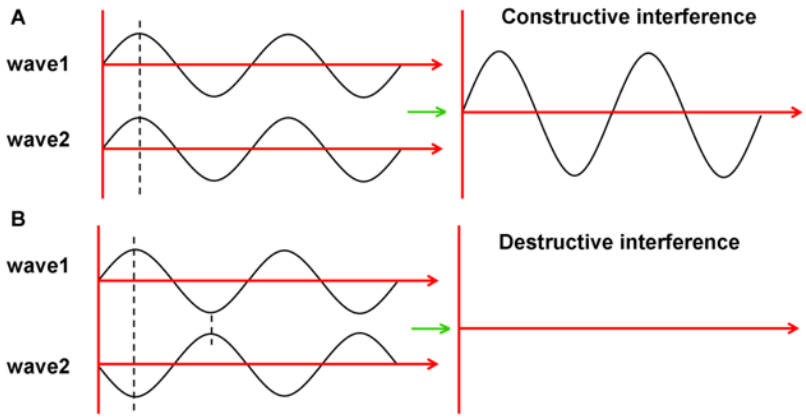

Fig. 1.22 Addition of two waves of the same wavelength. This phenomenon yields a third wave of the same wavelength, while the phase and amplitude of this resulting wave can either be the same or different from those of the two summed waves. In fact, the relative phase of the two summed waves critically affects the appearance of the third wave. **(A)** The two waves to be added are perfectly in phase, and the resulting wave contains an amplitude twice that of the wave1 and wave2, with the same phase. **(B)** The two added waves are 180^{o} out of phase and cancel each other so that the resulting wave has zero amplitude.

1.5.3.2 Single-crystal X-ray diffraction (XRD) and electron density distribution

The interaction of X-rays and crystal lattices giving to diffractions is ruled by Bragg's law which states that the constructive interference is only observed when Bragg's equation [1] is satisfied.

$$n\lambda = 2d\sin\theta \qquad [1]$$

where n is an integer (a whole number of wavelength), λ is the wavelength of X-ray, d is the distance between parallel planes in the crystal lattice, and θ is the angle of incidence between the X-ray beam and the diffracting planes (Fig. 1.23).

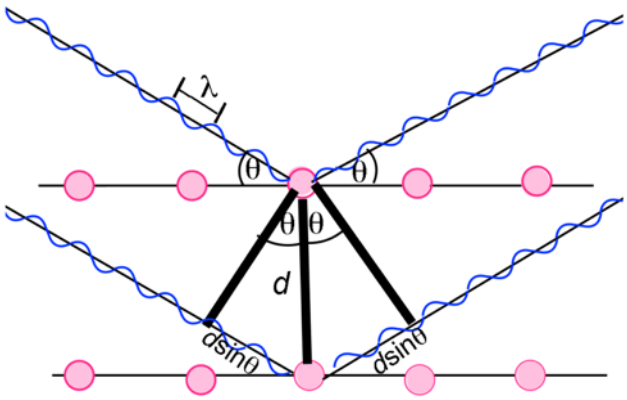

Fig. 1.23 Bragg diffraction in a crystal. The resulting waves will be in phase at the certain angle of the X-ray beam hitting the crystal lattice plane, resulting in diffraction intensities (i.e. Bragg's Law is fulfilled when the total path difference (nλ) is equal to 2$d$sinθ).

The electron density $\rho(xyz)$ is constructed by the equation [2] and the structure factors (F_{hkl}) can be obtained experimentally from the measured reflection *hkl* (*hkl* indices corresponding lattice planes of the reflection *hkl*).

$$\rho(xyz) = \sum \boldsymbol{F}_{hkl} \exp[2\pi i\,(hx_j + ky_j + lz_j)] \qquad [2]$$

where F_{hkl} is the structure factor, $x_j y_j z_j$ is the fractional coordinates (atomic position in the unit cell) of the atom *j* and *i* is the imaginary number $(-1)^{1/2}$.

In the experiment, the Bragg reflection intensities (I_{hkl}) are measured and they represent the amplitudes of the resulting waves (diffraction patterns). I_{hkl} is related to F_{hkl} by the equations listed below.

$$I(hkl) = |F(hkl)|^2 \quad [3]$$

$$F(hkl) = |F(hkl)|\exp(i\phi_{hkl}) \quad [4]$$

$$F(hkl) = \sum f_j \exp[2\pi i\,(hx_j + ky_j + lz_j)] \quad [5]$$

where F_{hkl} is the structure factor of a reflection *hkl*, ϕ_{hkl} is the phase angle, *i* is the imaginary number $(-1)^{1/2}$, f_j is the scattering factor which contains information of the crystal structure and $x_j y_j z_j$ is the fractional coordinates of the atom *j*.

Only an absolute structure factor $|F_{hkl}|$ is obtained from the experiment, but in order to calculate the electron density $\rho(xyz)$, F_{hkl} is necessary (require both phase and amplitude). However, the phase (ϕ_{hkl}) cannot be obtained directly by experiments (known as phase problem), while it needs to be solved for electron density calculation (see section 1.5.5.2).

1.5.4 Data collection

1.5.4.1 X-ray sources (Synchrotron)

An enormous improvement in X-ray generation techniques took place in the mid-1970s, when the application of synchrotron radiation was developed [120, 121]. A synchrotron facility is constructed with a gigantic storage ring, where electrons move at a very high speed (nearly the speed of light) in the straight channel that forces electrons to slow down intermittently when they meet the bending magnet and change their direction to meet the curvature of the ring

(Fig.1.24). At this moment, when electrons change their direction, they emit a high intensity radiation known as the synchrotron radiation covering the whole electromagnetic spectrum from far-infrared to X-rays [122]. X-rays are selected by the use of a combination of X-ray mirrors with monochromators. A single wavelength of X-rays is selected for crystallographic experiments. The storage ring used to generate X-rays at a synchrotron is shown in Fig. 1.24.

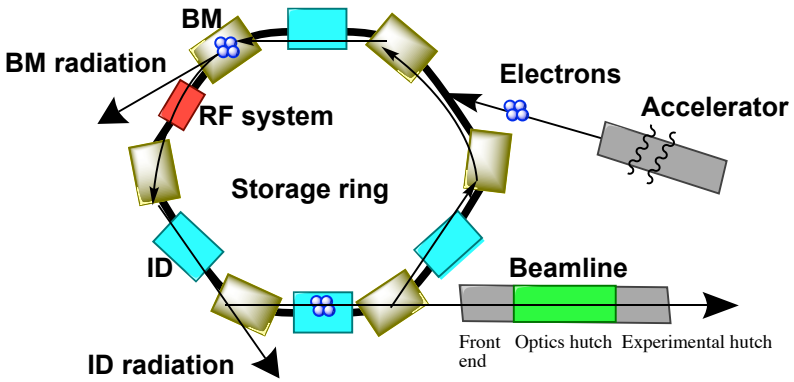

Fig. 1.24 The layout of the synchrotron storage ring. Accelerated electrons are injected into the storage ring which contains several dipole bending magnets (BMs). BMs produce the magnetic field which is perpendicular to the direction of electron movement. Lorentz (electromagnetic) force controls electrons to move around the storage ring. Electrons emit electromagnetic radiation when they reach the curve of the BMs, while RF (radiofrequency) system provides the accelerating field for an electron beam to compensate the energy loss during radiation emission. ID (insertion device) is a linear periodic magnetic array which can enhance the radiation intensity emitted by electrons. The figure was modified from reference [122].

1.5.4.2 Mounting, aligning the crystals and data collection

The protein crystal is picked from crystallisation drops using nylon loops and is soaked with appropriate cryoprotectants (e.g. glycerol, ethylene glycol, PEGs, etc) under a light microscope before being frozen with liquid nitrogen. The crystal is then aligned on the goniometer head

and positioned to the centre of the X-ray beam using the video screen (Fig. 1.25). During data collection, the crystal will be treated with the cold stream at all times to decrease radiation damage when being exposed to X-ray beams. The diffraction quality of the crystal can be tested at a few different angles for optimising some parameters (detector distance, exposure time and beam intensity). When the data collection parameters are optimised, the crystal will be exposed to X-ray beams repeatedly by rotating the crystal about 0.1-0.2° at a time (oscillation). The crystal can diffract and give diffraction spots only when the Bragg's condition is fulfilled. Therefore, the crystal needs to be rotated to increase the set of crystal planes that satisfy Bragg's law, and this will increase the completeness of the data. If the protein crystal used in the experiment has never been determined before, full data collection of 360° is recommended. For most protein crystals, 180° of data collection should be adequate as the low symmetry crystals (i.e. 2-fold symmetry) need 180° collection. The higher symmetry crystals will require less than 180° of data collection. The intensity of diffraction spots will be used for the structure determination following a series of data processing and model building (e.g. indexing, integration, scaling, phasing, model building and refinement).

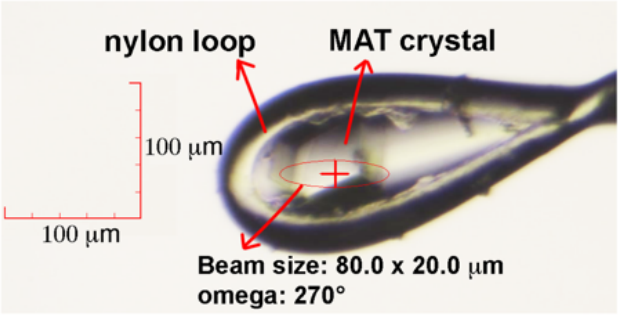

Fig. 1.25 The alignment of the MAT crystal to X-ray beams. The MAT crystal was mounted onto the nylon loop and kept in liquid nitrogen before being exposed to X-ray beams.

1.5.5 Data analysis for structure determination

1.5.5.1 Data processing

Data processing contains four key steps including (i) crystal evaluation and indexing from initial images, (ii) integration of reflection intensities of the full set of oscillation images (iii) scaling/ merging and (iv) truncation. The output file provides information of space group, cell dimension, *hkl* intensity and sigma (background or noise) for all of the unique reflections that were measured.

Indexing is the process to determine the lattice plane indicated by Miller (*hkl*) index that gives each reflection spot. When the specific lattice plane of each spot (*hkl*) is indexed, the unit cell dimension (a, b, c and α, β, γ), lattice type and crystal orientation can be identified. Each *hkl* reflection will be measured its intensity (I) by the process called integration. All detected spots on diffraction images will be determined, and the background around the spots will be calculated and determined as the sigma value (σ). After integration, the reflection data will be subjected to a common scale (scaling) which minimises the inconsistency causing by various factors (e.g. detector, incident X-ray beam, etc.) between the individual data and average data of the equivalent symmetry-related spots. However, the overall intensities of *hkl* reflections may be extracted in several thousands, they usually contain the symmetry-related spots representing the redundancy or multiplicity of the data (redundancy of 3.5 or above is considered acceptable). The unique set of data will be obtained after the data are scaled and merged the symmetry-related spots (merging). Finally, the intensities (I_{hkl} or $|F_{hkl}|^2$) will be truncated to $|F_{hkl}|$ by the truncation process.

1.5.5.2 Phasing by molecular replacement (MR)

To calculation the electron density $\rho(xyz)$, the structure factor $F(hkl)$ is needed as shown in equation [2]. F_{hkl} contains both amplitude and phase (as shown earlier in equation [4]). Only I_{hkl} or $|F_{hkl}|^2$ obtained from experiments by measuring the diffraction intensities is not enough to calculate the structure factor F_{hkl} [123]. The missing information of phases is known as phase problem and it needs to be solved to construct the electron density of the crystal structure.

The Patterson map provides the distribution of the interatomic distance that is directly computable from the data. MR [124] compares the Patterson map of the homology known structure (search model) with the unknown structure [125]. Rotation of the search model in three dimensions will give different calculated structure factor values, $|F\text{calc}|(hkl)$, which will be matched to the $|F\text{obs}|(hkl)$ of the experimental diffraction data. The orientation that gives the best match of $|F\text{calc}|(hkl)$ to $|F\text{obs}|(hkl)$ will be used to define the correct translation of the model in the unit cell of the crystal. When the correct orientation and translation of the search model can be determined, the phases ($\phi_{hkl}\text{calc}$) of the search model can be calculated and applied to the experimental structure factor calculation (equation [4]) by using $|F\text{obs}|(hkl)$ derived from the measured intensity and $\phi_{hkl}\text{calc}$ as shown below.

$$F\text{obs}(hkl) = |F\text{obs}(hkl)|\exp(i\phi_{hkl}\text{calc})$$

Therefore, the electron density which is the Fourier transform of $F\text{obs}(hkl)$ can be calculated as shown earlier in equation [2].

1.5.6 Structure refinement and validation

Once the initial model is obtained, refinements of the model against the data by varying x,y,z coordinates (atomic positions) and B-factors (thermal motions) will be performed to find the best agreement of the experimental |Fobs|(*hkl*) from diffraction intensities and the calculated |Fcalc|(*hkl*) from the initial model (R-factor, equation [6]). This R-value is the measurement of an atomic model quality derived from the crystallographic data. Refinement incorporates restraints on an atomic position relied on the known chemical properties of the protein structure (e.g. bond lengths, angles, side chain rotation) and the R value less than 20 % indicates that the model is in reasonable agreement to the experimental data.

$$R - factor = \frac{\sum_{hkl} ||Fobs(hkl)| - |Fcalc(hkl)||}{\sum_{hkl}|Fobs(hkl)|} \quad [6]$$

The quality of models will be better through the process of structural refinements. The model will fit better to the electron density (experimental data). However, too many cycles of refinement normally introduce bias to the system as the refined model is used to calculate the electron density. The R-free value is the parameter to be used along with the R-factor value to prevent this bias. About 5 % of the experimental data will be excluded from the original data and will not be refined to calculate the R-free value. For a good refined model, R-free and R-factor values should be very similar to each other. Typically, R-free will have about 3-5 % higher than the R-factor value and it is considered acceptable for the model validation [126].

The Ramachandran plot is used to evaluate the Φ (phi) and Ψ (psi) angles of amino acids in peptide bonds. The irregular or inappropriate rotations of amino acid main chains can be identified from this plot. Other molecules (e.g. waters, ions, chemical reagents, cryoprotectants, etc.) which are contained in purification buffers or crystallisation reagents might be existing in the electron density and are needed to be built in the model. Interatomic distances are

investigated for preventing adjacent atomic clashes. Bond lengths, bond angles and other parameters (e.g. clash score, Ramachandran outliers) of the model can be calculated and compared to the expected value using Protein Data Bank (PDB) validation report server (https://www.wwpdb.org/validation/validation-reports) or MolProbity server (http://molprobity.biochem.duke.edu). These online servers allow users to validate the quality of models before performing structural deposition on PDB.

1.6 Research aim of my project

My project can be divided into three main objectives. The first part is to investigate the functional role of a gating loop on MAT activity both SAMe formation and PPPi hydrolysis. The gating loop is located above an active site entrance undergoing structural changes during substrate binding and product release. The direct evidence of the gating loop's functional relevance on SAMe formation is still elusive. The consequences caused by mutations of some key residues of the gating loop that are directly or indirectly involved in substrate (methionine) or product (SAMe) binding will be accomplished by site-directed mutagenesis, activity assay and crystallographic structure with a variety of ligands.

The second objective is to investigate the effect of Arg264 mutations on MAT function and structure. Arg264 is located at the dimer interface where the active sites assemble. Arg264His mutations of MATα1 have been reported to be the most common cause of isolated persistent hypermethioninemia (i.e. high levels of the methionine in blood plasma). Arg264Ala and Arg264His mutants will be generated in MATα1 as well as Arg264Ala mutant in MATα2. The mutants will be characterised for the enzyme activity and the oligomeric form in solution and crystal structures.

The last objective is to investigate the effect of quinolone-based compounds on MAT activity. The compound binding positions on MAT are preliminarily predicted by molecular docking

and are shown to interact with MAT catalytic subunits at the same binding interface where the regulatory subunit, MATβ, has been reported to bind at. The effects of these compounds on MAT activity will be studied in comparison with MATβ subunits. The compound bound crystals will be produced by co-crystallisation method using commercial screens.

Chapter II

Materials and Methods

2.1 Plasmid DNA and bacterial culture

MATα1 and MATα2 (pNIC28-Bsa4 vector, with a kanamycin-resistance gene) constructs were kindly provided by structural genomic consortium (University of Oxford, UK) and MATβV1 and MATβV2 constructs were generously provided from Dr. Shelly Lu (University of California Los Angeles). MATβV1 and MATβV2 genes were sub-cloned into pET-28M-SUMO3 vector, with a kanamycin-resistance gene.

For protein expression of MATα1, MATα2 and MATβ (V1/V2 variants), BL21 (DE3) cells were used, while Stellar^{TM} (Clontech) cells were used for site-directed mutagenesis and DNA amplification. Bacterial cells were cultured in LB (Lysogeny or Luria broth, Miller) containing yeast extract (5.0 g/L), peptone from casein (10.0 g/L) and NaCl (10.0 g/L). 12.5 g of LB Broth was dissolved in 500 mL RO (reverse osmosis) water and was autoclaved for 15 min at 121 °C. Kanamycin or ampicillin was added at a final concentration of 50 μg/mL or 100 μg/mL, respectively.

2.2 Site-directed mutagenesis

Primers for site-directed mutagenesis were designed by using SnapGene software (from GSL Biotech; available at snapgene.com). Primer sequences used in this study are shown in Table 2.1. The desired plasmids of mutants were generated by using a CloneAmp HiFi Polymerase Chain Reaction (PCR) Premix (Clontech). 12.5 μL of the CloneAmp HiFi PCR Premix was mixed with 7.5 pmol of each primer and 100 ng of the wild-type plasmid DNA. Autoclaved water was added at a final volume of 25 μL and the reaction was centrifuged shortly. A thermal cycler was programmed with the following cycling conditions: 10 min 98 °C (1); 10 sec 98 °C

(2); 15 sec 55-60 °C (3); 45 sec 72 °C (4); 10 min 72 °C (5). Steps 2 to 4 were repeated for 34 times. DpnI (NEB) was added at a final concentration of 800 units/mL to remove DNA templates, and the PCR product was incubated at 37 °C for 2 h. The plasmids were then transformed to Stellar™ competent cells. Transformed cells were plated on selective agar plates and incubated at 37 °C overnight. A single colony was picked and inoculated to 5 mL of selective media and incubated at 250 rpm, 37 °C overnight. Plasmid DNA was purified and sent for DNA sequencing at GATC biotech or DNA Sequencing and Services (University of Dundee, UK). The desired mutated plasmids were collected and stored at -20 °C until use.

Table 2.1 Primers used for site-directed mutagenesis

Primers	Primer Sequences (5'-3')
Q113A MAT2A F	CTGGTAGCCTTGGAGCAAGCGTCACCAGATATTGCTCAA
Q113A MAT2A R	TTGAGCAATATCTGGTGACGCTTGCTCCAAGGCTACCAG
S114A MAT2A F	GTAGCCTTGGAGCAACAGGCACCAGATATTGCTCAAGGT
S114A MAT2A R	ACCTTGAGCAATATCTGGTGCCTGTTGCTCCAAGGCTAC
P115G MAT2A F	GTAGCCTTGGAGCAACAGGGACCAGATATTGCTCAAGGT
P115G MAT2A R	ACCTTGAGCAATATCTGGTCCCTGTTGCTCCAAGGCTAC
R264A MAT2A F	GATGCTGGTTTGACTGGAGCGAAAATCATTGTGGACACT
R264A MAT2A R	AGTGTCCACAATGATTTTCGCTCCAGTCAAACCAGCATC
R264H MAT1A F	GATGCGGGTGTCACTGGCCATAAGATTATTGTGGACACC
R264H MAT1A R	GGTGTCCACAATAATCTTATGGCCAGTGACACCCGCATC
R264A MAT1A F	GATGCGGGTGTCACTGGCGCTAAGATTATTGTGGACACC
R264A MAT1A R	GGTGTCCACAATAATCTTAGCGCCAGTGACACCCGCATC
R299H MAT1A F	TCAGCCGCTTATGCTGCCCACTGGGTGGCCAAGTCTCTG
R299H MAT1A R	CAGAGACTTGGCCACCCAGTGGGCAGCATAAGCGGCTGA
R356W MAT1A F	CATAAGAACTTCGACCTCTGGCCGGGCGTCATTGTCAGG
R356W MAT1A R	CCTGACAATGACGCCCGGCCAGAGGTCGAAGTTCTTATG

2.3 Plasmid transformation

BL21 (DE3) or Stellar^{TM} cells were thawed on ice. Each tube containing 50 µL of cells was mixed with 1 µL of a plasmid DNA (50-100 ng/µL) in 1.5 mL tubes. All tubes were rested on ice for 30 min in cold room (4 ^{o}C). The cells were incubated at 42 ^{o}C using water bath for 45 sec and placed on ice for 10 min. 200 µL of LB broth or S.O.C medium (Thermo Fisher Scientific) without the antibiotics was added to the cells and followed by incubation for 1 h at 250 rpm, 37 ^{o}C. 150 µL of transformed cells were plated on LB agar supplemented with appropriate antibiotics and incubated overnight at 37 ^{o}C. All plates were kept at 4 ^{o}C until use.

2.4 Plasmid purification

The transformed bacterial cells were grown overnight (16-18 h) at 250 rpm, 37 °C. An overnight culture was then centrifuged at 5000 g to collect cell pellets. DNA purification was performed using Wizard Plus SV Minipreps DNA Purification System (Promega)'s centrifugation protocol. Briefly, cell pellets were resuspended with 250 µL of Cell Resuspension Solution and 250 µL of Cell Lysis Solution was added to each sample. 350 µL of Neutralisation Solution was added and all tubes were centrifuged at 13000 rpm at room temperature by using a bench top centrifuge (Eppendorf). The clear lysate was transferred to a Spin Column (provided by the kit) and centrifuged at 13000 rpm for 1 min. The collected flow-through was discarded and 750 µL of Wash Solution was added. All tubes were centrifuged at 13000 rpm for 1 min. The flow-through was discarded and the centrifugation with 250 µL of Wash Buffer was repeated for 5 min. The Spin Column was transfer to a 1.5 mL microcentrifuge tube and 100 µL of warm nuclease-free water was added. All tubes were centrifuged at 13000 rpm for 1 min and DNA concentrations were measured (concentration ranges: 40-60 ng/µL) before being stored at -20 ^{o}C.

2.5 Bacterial glycerol stock

For long term storage of plasmid-transformed bacterial cells, an overnight culture was mixed with sterile glycerol at a final concentration of 25 %. The cells' glycerol stocks were then flash frozen by liquid nitrogen and being stored at -80 ^{o}C until use. The cells could be regrown by streaking onto LB agar plates and incubated at 37 ^{o}C overnight.

2.6 Protein expression

A single colony of transformed cells was taken from the LB plate using a sterile pipette tip. The tip was dropped into a 5 mL starter culture tube. All tubes were incubated at 250 rpm, 37 ^{o}C for 12-18 h. The growth of bacteria was inspected by a cloudy haze in the media. 5 mL of a freshly grown starter culture was added to a flask containing 500 mL of LB media supplemented with appropriate antibiotics. All flasks were shaken at 250 rpm, 37 ^{o}C for 3-4 h until OD_{600} reached 0.6-0.8 (optimum number of bacterial cells for induction). Protein expression was induced by the addition of 1 mM isopropyl β-D-1-thiogalactopyranoside (IPTG). Then, the culture was incubated overnight at 250 rpm, 20 ^{o}C (for all proteins used in this work). The culture was then centrifuged at 6000 x g for 20 min at 4 ^{o}C. Pellets were harvested and flash frozen in liquid nitrogen before being stored at -80 ^{o}C until use.

2.7 Purification of MATα1 and MATα2 (pNIC vector)

All buffers used in protein purification are indicated in Table 2.2. Cell pellets were resuspended with ice-cold Lysis Buffer in 1:4 ratio (pellet, g: buffer, mL). All tubes were placed on ice and PMSF (phenylmethylsulfonyl fluoride) was added at a final concentration of 1 mM. Cell suspensions were sonicated for 15 cycles at 8 Amp for 30 sec (on/ off). Sonication was carried out on ice to avoid an increasing temperature from the sonication. Cell suspensions were centrifuged at 20,000 x g for 40 min to remove cell debris. Clear supernatant was collected and

loaded into a His-trap HP column (GE Healthcare) pre-equilibrated with 10 times (10X) column volumes (CV) of Lysis Buffer. The column was washed with Lysis Buffer (10X) followed by Wash Buffer (5X). Proteins were eluted with the Elution Buffer and fractions containing proteins were confirmed by sodium dodecyl sulphate polyacrylamide gel electrophoresis (SDS-PAGE). To cleave the His-tag from MATα2, eluted proteins were incubated with tobacco etch virus (TEV) protease in 100: 1 (protein, mg: TEV, mg) ratio by dialysis against Dialysis Buffer (2L) overnight at 4 ºC, using a 10k cut off dialysis membrane (SnakeSkin™ Dialysis Tubing, Thermo Fisher Scientific). The cleavage of His tag was checked by Western Blot analysis (Fig. 2.1).

Proteins were then centrifuged at 4000 x g for 30 min and clear supernatants were loaded into an anion-exchange chromatography column (HiTrap Q HP, GE Healthcare) pre-equilibrated with Buffer A (5X). Proteins were eluted by using isocratic gradient from 0.05 M to 1 M NaCl containing Buffer A. Selected fractions of proteins were then concentrated using a 30K cut-off centrifugal concentrator and loaded into a HiLoad 16/600 or a 10/300 Superdex 200 gel filtration column (GE healthcare) pre-equilibrated with 25 mM HEPES pH 7.5 (2X). Fractions containing proteins were pooled and stored in 500 mM NaCl, 0.5 mM TCEP (Tris(2-carboxyethyl)phosphine) and 5 % glycerol. Proteins were flash frozen using liquid nitrogen and kept at -80 ºC. MAT activity was measured in comparison of fresh, 1-day and 30-day frozen samples which were stored at -80 ºC to confirm the activity intact after storage (Fig. 2.2).

Table 2.2 The buffers used in the purification of MATα1, MATα2, MATβV1 and MATβV2

Buffer	Compositions
Lysis Buffer	500 mM NaCl, 5 % (v/v) glycerol, 5 mM Imidazole and 10 mM β-ME (β-mercaptoethanol)
Wash Buffer	500 mM NaCl, 5 % (v/v) glycerol, 30 mM Imidazole and 10 mM β-ME
Elution Buffer	500 mM NaCl, 250 mM Imidazol and 10 mM β-ME
Dialysis Buffer	25 mM HEPES pH 7.5, 50 mM NaCl and 10 mM β-ME
Buffer A	25 mM HEPES pH 7.5, 25 mM NaCl and 5 mM β-ME

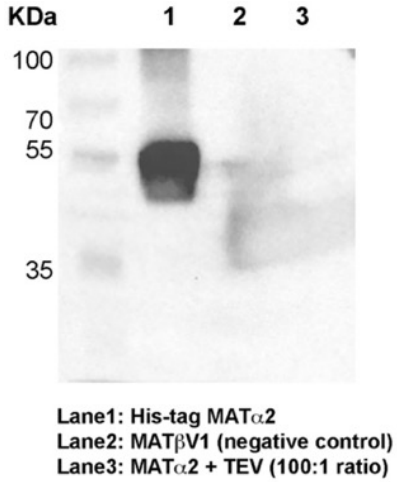

Fig. 2.1 Western blot analysis of His-tag removal in MATα2. Anti His-tag antibody was used to detect His-tag removal of MATα2 after incubation with TEV protease overnight at 4 ^{o}C.

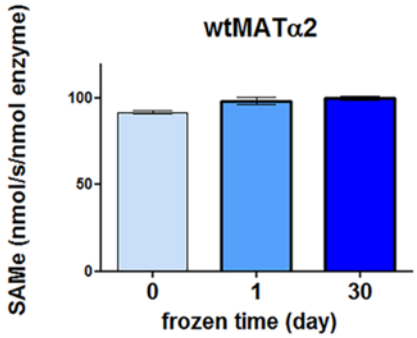

Fig. 2.2 A measurement of the MATα2 activity from the fresh and frozen enzyme. MAT activity was measured in comparison of fresh, 1-day and 30-day frozen enzymes at -80 ºC.

2.8 Purification of MATβV1 and MATβV2 (pET_SUMO vector)

The buffers used in the purification were shown in Table 2.2. Cell pellets were resuspended with ice-cold Lysis Buffer in 1:4 ratio. All tubes were placed on ice and PMSF was added at a final concentration of 1 mM. Cell suspensions were sonicated for 15 cycles at 8 Amp for 30 sec and stopped 30 sec and cell suspensions were centrifuged at 20,000 x g for 40 min to remove cell debris. The clear supernatant was collected and loaded into a pre-equilibrated His-trap HP column in Lysis Buffer (10X). The column was washed with Lysis Buffer (10X) followed by Wash Buffer (5X). Then, proteins were eluted with Elution Buffer and fractions containing proteins were pooled. To cleave a SUMO (small ubiquitin-like modifier) tag from MATβV1 and MATβV2, the proteins were incubated with Sentrin-specific protease 2 (SENP2) in 1500 (protein, mg):1 (SENP2, mg) ratio. The proteins were incubated at room temperature for 1 hour on an orbital shaker and then dialysed against 2L Dialysis Buffer at 4 ºC overnight. The cleavage of the SUMO tag could be analysed by SDS-PAGE as the target protein had about 12 kDa lower molecular weight. The cleaved SUMO tag bands could be detected at about 10 kDa of the standard marker (Fig 2.3).

Proteins were then centrifuged at 4000 x g for 30 min and loaded into an anion-exchange chromatography column pre-equilibrated with Buffer A (5X). Proteins were eluted by using isocratic gradient from 0.05 M to 1 M NaCl (the buffer containing Buffer A and NaCl). The selected fractions of proteins were then concentrated and loaded into a HiLoad 16/600 or a 10/300 Superdex 75 gel filtration column (GE healthcare) pre-equilibrated with 25 mM HEPES pH 7.5 (2X). The fractions containing proteins were pooled and stored in 500 mM NaCl, 0.5 mM TCEP and 5 % glycerol. Proteins were flash frozen by liquid nitrogen and stored at -80 ^{o}C.

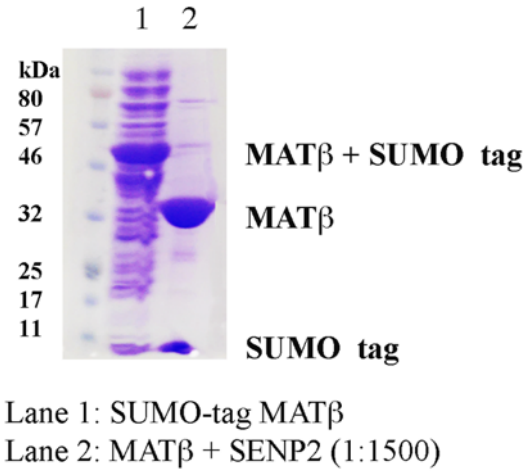

Fig. 2.3 SDS-PAGE gel showing a removed SUMO-tag of MATβ proteins. MATβ proteins before and after SUMO-tag cleavage by SENP2 were analysed by SDS-PAGE. SUMO (small ubiquitin-like modifier); SENP2 (Sentrin-specific protease 2).

2.9 Production of TEV protease

Cell pellets were resuspended and sonicated in the same manner as described in MAT protein purification (section 2.7). Cell suspensions were centrifuged at 20,000 x g for 40 min to get rid of cell debris. The clear supernatant was loaded into a His-trap HP column pre-equilibrated with Lysis Buffer (10X). The column was washed with Wash Buffer (5X). Then, proteins were eluted with Elution Buffer. The eluted proteins were dialysed against Dialysis Buffer (2L)

overnight at 4 ºC. Proteins were then centrifuged at 4000 x g for 30 min and the collected supernatant was loaded into an anion-exchange chromatography column pre-equilibrated with Dialysis Buffer (5X). TEV protease was eluted in the flow-through and concentrated using a 10K cut-off centrifugal concentrator. The samples were dialysed against Storage Buffer (1L) overnight. The proteins were flash frozen in liquid nitrogen and stored at -80 ºC until use. The buffers used in the purification were modified from Alsarraf HM et al., 2011 [127] and shown in Table 2.3.

Table 2.3. The buffers used for the purification of TEV protease

Buffer	Compositions
Lysis Buffer	50 mM Tris–HCl pH 8, 400 mM NaCl, 20 mM imidazole, 5 mM β-ME and 1 mM PMSF
Wash Buffer	50 mM Tris–HCl pH 8, 1 M NaCl, 50 mM imidazole, 5 mM β-ME and 1 mM PMSF
Elution Buffer	50 mM Tris–HCl pH 8, 400 mM NaCl, 500 mM imidazole and 5 mM β-ME
Dialysis Buffer	50 mM Tris–HCl pH 8 and 5 mM β-ME
Storage Buffer	50 mM Tris–HCl pH 8, 5 mM β-ME and 50 % glycerol

2.10 Production of SENP2 protease

Cell pellets were resuspended and sonicated in the same manner as described in MAT protein purification (section 2.7). Cell suspension was centrifuged at 20,000 x g for 40 min and cell debris was discarded. Clear supernatant was collected and loaded into the His-trap HP column pre-equilibrated with Lysis Buffer (10X). The column was washed with Wash Buffer (5X). Then, proteins were eluted with Elution Buffer and fractions containing proteins were pooled. The eluted proteins were dialysed against Dialysis Buffer (2L) overnight at 4 ^{o}C. The proteins were then centrifuged at 4000 x g for 30 min and the collected supernatant was loaded into the anion-exchange chromatography column pre-equilibrated with Buffer A (5X). Proteins were eluted by using isocratic gradient from 0.05 M to 1 M NaCl (buffer containing Buffer A and NaCl). Eluted proteins were concentrated and stored in 10 % glycerol. SENP2 protease was flash frozen in liquid nitrogen and stored at -80 ^{o}C. The buffers used for the purification were indicated in Table 2.4.

Table 2.4. The buffers used in the purification of SENP2 protease

Buffer	Compositions
Lysis Buffer	20 mM Tris-HCl pH 8.0, 1 mM β-ME, 350 mM NaCl and 10 mM imidazole
Wash Buffer	20 mM Tris-HCl pH 8.0, 350 mM NaCl, 1 mM β-ME and 20 mM imidazole
Elution Buffer	20 mM Tris-HCl pH 8.0, 350 mM NaCl, 1 mM β-ME and 400 mM imidazole
Dialysis Buffer	20 mM Tris-HCl pH 8.0, 100 mM NaCl and 1 mM β-ME
Buffer A	20 mM Tris-HCl pH 8.0, 50 mM NaCl and 1 mM β-ME

2.11 Activity assay

The enzyme activity assay was performed by following the procedure described in Murray B et al., 2014 [13]. SAMe synthetic activity was measured using methionine and ATP at final concentrations of 200 µM and 1 mM, respectively. The phosphatase activity of MAT enzymes was measured under various concentrations of ATP (0.1-4.0 mM) by detecting inorganic phosphate (Pi) production. Briefly, the reaction was prepared in a final volume of 100 µL. All enzymes (50 nM) were preincubated with 200 µM methionine in the reaction buffer (50 mM HEPES pH 7.5, 25 mM $MgCl_2$ and 25 mM KCl) for 15 min. ATP was added to initiate the reactions and all mixtures were agitated at 1400 rpm using Titramax 100 (Heidolph Instruments) for 10 min at 37 °C. All enzymes and substrates were diluted in the dilution buffer containing 10 mM HEPES pH 7.5, 500 mM NaCl, 5 % glycerol and 0.5 mM TCEP. The reactions were stopped by adding 50 µL of 100 mM EDTA pH 8.0 before measuring SAMe and Pi production.

2.12 SAMe formation detection

SAMe formation was analysed by S-adenosylmethionine enzyme-linked immunosorbent assay (ELISA) kit (Cell biolabs) following the manufacturer's protocol. Data are the mean of three independent experiments ± Standard Error of Mean (SEM). All experiments were performed using protein samples from the same batch of protein purification (different aliquots). Significance was assessed using a one-way analysis of variance (ANOVA), followed by Tukey–Kramer tests using GraphPad Prism version 5. P-values less than 0.05 were considered significant.

2.13 Phosphatase activity

The detection of inorganic phosphates was modified from the protocol described by Baginski ES et al., 1967 [128]. 50 µL of samples were mixed with 150 µL of 2 % Ascorbic acid in 10 % trichloroacetic acid (A-TCA). 50 µL of ultrapure water (Milli-Q® Type 1 Ultrapure Water Systems) was added in each sample followed by addition of 75 µL of 2 % ammonium molybdate, and 150 µL of 2 % (w/v) Arsenite-citrate in 10 % TCA. All samples were mixed thoroughly (vortex) and incubated at room temperature for 20 min. Phosphate ions react with ammonium molybdate to produce a phospho-molybdenum blue complex, which can be measured by the absorbance at 750 nm using SpectraMax® Plus 384 Microplate Reader (Molecular Devices). Pi quantification was obtained by using the calibration curve of various standard KH_2PO_4 solutions (0.125-2.0 µg/ mL). Pi standard curve is shown in Fig. 2.4.

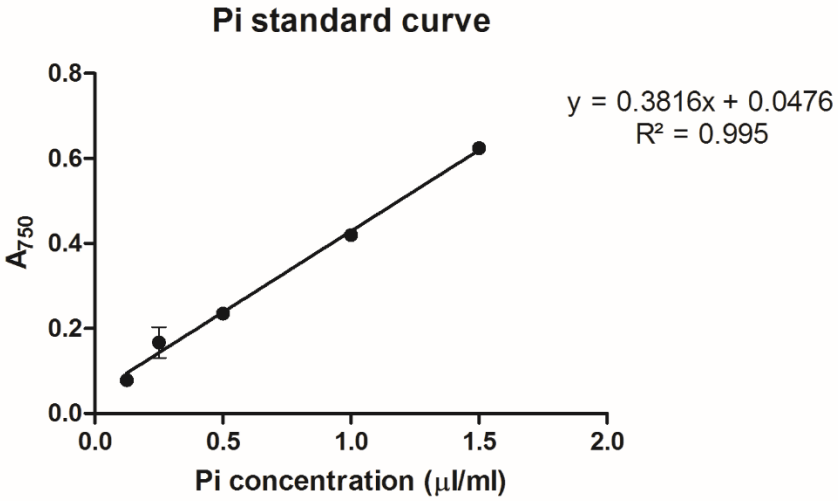

Fig. 2.4 Standard curve of Pi measurement. All reactions of enzyme assays were measured by the absorbance at 750 nm. The Pi quantification of an unknown sample was obtained by using the calibration curve of various standard KH_2PO_4 solutions (0.125-2.0 µL/ mL).

2.14 Quinolone-based compounds

All quinolone-based compounds were kindly provided by Prof. Paul M. O'Neill (Department of Chemistry, School of Physical Sciences, University of Liverpool, UK). The synthesis of quinolone-based compounds has been described by Charoensutthivarakul S et al., 2015 [129]. Structures of the compounds are shown in Fig. 2.5. Stock solutions were made in DMSO (Dimethyl sulfoxide) before being diluted to a final concentration using dilution buffer containing 10 mM HEPES pH 7.5, 500 mM NaCl, 5 % glycerol and 0.5 mM TCEP.

2.15 Differential scanning fluorimetry (DSF)

All samples were prepared in a Fast Optical 96-well reaction plate (Life Technologies) using a StepOnePlus™ Real-Time PCR instrument (Applied Biosystems). Each well (20 µL) contained 10 µL of 0.5 mg/mL proteins and 10 µL of SYPRO™ Orange protein gel stain (Life Technologies) at a final concentration of 10X. For the quinolone-based compound study, the protein was incubated with or without the compound. All enzyme and compounds were diluted in 10 mM HEPES pH 7.5 buffer containing 500 mM NaCl, 5 glycerol and 0.5 mM TCEP and the final concentration of DMSO in the protein sample was less than 1 %. Fluorescence intensities were measured from 25 °C to 99 °C with a ramp rate of 1° C/min. Data were analysed using MATLAB® executable TmTool™ following TmTool™ Quick Set-Up Guide (Life technologies). Data are represented as the mean of Tm (melting temperature) of three independent experiments using protein samples from the same batch of protein purification ± SEM.

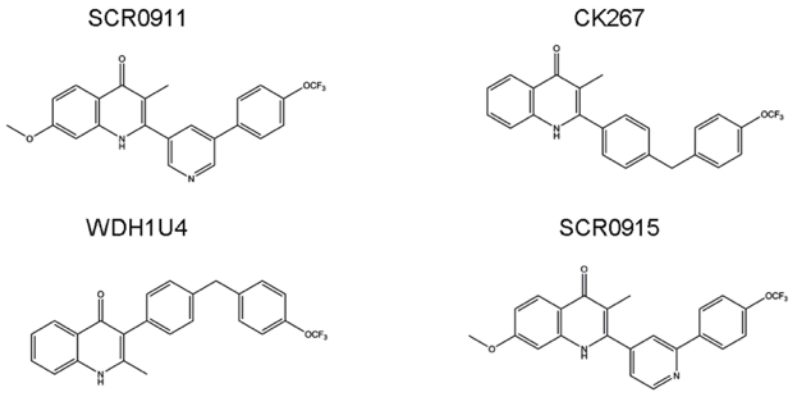

Fig. 2.5 Quinolone-based compounds used in this study. The synthesis of quinolone-based compounds has been described in reference [129].

2.16 Complex formation of MATα1/α2 and MATβ

The complex formation was performed using the protocol described by Murray B et al., 2014 [13]. Briefly, MATα1/2 was incubated with MATβV1 or MATβV2 at 1:2 ratio for 1 h, at 4 °C in the buffer containing 50 mM HEPES pH 7.5, 10 mM $MgCl_2$ and 50 mM KCl. The complex was then loaded into a Superdex 200 10/300 column and eluted with 25 mM HEPES pH 7.5 buffer containing 200 mM NaCl, 1 mM $MgCl_2$, 5 mM KCl and 1 mM TCEP. The complex formation was confirmed by SDS and Native-PAGE analysis.

2.17 SDS-PAGE analysis

SDS-PAGE analysis for protein purity determination was performed using 12 % (w/v) acrylamide gels. Samples were mixed with loading buffer (4X) containing 100 mM Tris-Cl pH 6.8, 4 % (w/v) SDS, 0.2 % (w/v) bromophenol blue, 20 % (v/v) glycerol and 200 mM DTT (Dithiothreitol) in 1:4 ratio. All samples were heated in an aluminium heating block at 90 °C for 5 min. PageRuler™ Plus Prestained Protein Ladder (Thermo Fisher Scientific) was used as the molecular weight markers (10 to 250 kDa). Electrophoresis was carried out using fixed

voltage (200 Volt) in running buffer (0.025 M Tris, 0.192 M glycine and 0.1 % (w/v) SDS, pH 8.5) for 50 min using a Mini Gel Tank (Thermo Fisher Scientific) and a power supply apparatus from Biorad. The gel was stained in Coomassie brilliant blue solution (see section 2.19).

2.18 Native-PAGE analysis

Native-PAGE analysis for complex assessment was carried out using 8 % (w/v) acrylamide gels. The gels and electrophoresis solutions were prepared without SDS and a reducing agent (DTT). Samples were mixed with loading buffer (4X, 100 mM Tris-Cl pH 6.8, 0.2 % (w/v) bromophenol blue and 20 % (v/v) glycerol). All samples were prepared on ice and loaded immediately onto acrylamide gel. NativeMark™ Unstained Protein Standard (Thermo Fisher Scientific) was used as the molecular weight markers (20 to 1200 kDa). Electrophoresis was carried out at 200 Volt in running buffer (0.025 M Tris and 0.192 M glycine pH 8.5) for 45 min using a Mini Gel Tank and a power supply apparatus from Biorad. The gel was stained in Coomassie brilliant blue solution (see section 2.19).

2.19 Protein gel staining

Gels were stained for 30 min in staining solution containing 0.1 % (w/v) Coomassie Brilliant Blue R-250, 40 % (v/v) methanol and 10 % (v/v) glacial acetic acid. De-staining solution (40 % (v/v) methanol and 10 % (v/v) glacial acid) was used to visualise protein bands. Stained gels were incubated with de-staining solution until the background colour faded out and protein bands were clearly visible.

2.20 Size exclusion chromatography-small-angle X-ray scattering (SEC-SAXS)

SEC-SAXS experiments were carried out at beam-line SWING at Synchrotron SOLEIL using a1.79 sample detector distance and 12 keV incident beam energy. An Agilent BioSEC Advance 300Å, 4.6 x 300 mm column equilibrated with 25 mM HEPES pH 7.5 and used for size exclusion chromatography instantly prior to exposure to X-rays. 20 µL of protein at 10 mg/mL was loaded into an Agilent 1200 High Performance Liquid Chromatography (HPLC) system at a flow rate of 0.3 mL/min and column temperature of 15 °C. Exposures were collected prior to the column void volume, for the purposes of buffer scattering subtraction, and over the course of protein elution. Exposures were 1 sec interspersed with 0.5 sec dead-time. Frames were inspected and averaged in Foxtrot [130] and analysed in with Primus [131].

The scattering data obtained by SEC-SAXS were analysed using FoXS Server [132] in which the scattering profile of the input crystallographic structure could be calculated and fitted onto the experimental data.

2.21 Crystallisation and data collection

All purified MAT proteins were stored at -80 °C in storage buffer containing 500 mM NaCl, 5 % glycerol and 0.5 mM TCEP. Prior to crystallisation, aliquots containing stored proteins were quickly thawed using cold tap water and were immediately kept on ice. MATα2 proteins and their variants were then concentrated to 5.8 mg/mL and pre-equilibrated with substrates (10 mM Met and 150 µM AMP-PNP) in 50 mM HEPES buffer pH 7.5 containing 10 mM $MgCl_2$, 50 mM KCl and 10 mM DTT before crystallisation. Crystal drops containing 1 µL of the protein and 1 µL of the precipitation agent (100 mM HEPES pH 6.5 and 30 % PEG 600) were equilibrated against a reservoir solution (100 mM HEPES pH 6.5 and 30 % PEG 600). Crystals appeared at 25 °C within 1-2 days. Prior to data collection, crystals were soaked in reservoir solution with additional 20 % ethylene glycol and were flash frozen in liquid nitrogen. Different

crystallographic datasets were collected at the I24, I03 and I04-1 beamlines at Diamond Light Source (Oxford, England) and the PROXIMA-1 beamline at SOLEIL synchrotron (Saint-Aubin, France).

The MATα1 (R264H) mutant protein was concentrated to 5 mg/mL and pre-equilibrated with substrates (10 mM Met and 150 µM AMP-PNP) in 50 mM HEPES buffer pH 7.5 containing 10 mM $MgCl_2$, 50 mM KCl and 10 mM DTT before crystallisation. Wild-type protein (MATα1) was concentrated to 5 mg/mL in 50 mM HEPES buffer pH 7.5 containing 10 mM $MgCl_2$, 50 mM KCl and 10 mM DTT before crystallisation to produce crystals of apo forms. Crystal drops containing 1 µL of the protein and 1 µL of the precipitation agent (200 mM NaF, 20 % PEG 3350 and 15 % ethylene glycol) were equilibrated against a reservoir solution (200 mM NaF, 20 % PEG 3350 and 15 % ethylene glycol). Crystals appeared at room temperature within 3-7 days. Prior to data collection, crystals were soaked and frozen in the same manner to MATα2 proteins. Different datasets were collected at the I03 (R264H crystals) and I04 (wild-type crystals) beamlines at Diamond Light Source (Oxford, England).

Data were integrated by iMosflm [133] and scaled using Aimless [134]. The crystal structures were solved by MOLREP [135] using human MATα1 (PDB: 2OBV) and MATα2 (PDB: 5A1I) as search models. The model building and restrained refinement were carried out using Coot [136] and REFMAC [137]. Crystallographic data collection and refinement statistics are given in Table 3.4.3a, 3.4.3b (Chapter III, section 3.4.2) and Table 4.4 (Chapter IV, section 4.4.2).

2.22 Molecular docking

Autodock Vina [138] and SwissDock [139] were used to perform a local and blind docking, respectively. Ligand binding modes by the local docking were determined in the defined box, while the binding modes generated by the blind docking were performed in the vicinity of all target cavities. SCR0911 and SCR0915 molecules in Tripos Mol2 File Format (.mol2) were created using a Marvinsketch tool (https://chemaxon.com/products/marvin). The ligand-free crystal structures of wtMATα2 (PDB: 5A1I) and MATα2 (R264A) mutant (PDB: 6FCD) were generated by the UCSF Chimera suite [140]and used as the target protein models.

For Autodock Vina docking, the docking box was defined (box centre: x,y,z = -2.43, 11.29, -29.28 Å: box size: x,y,z = 29.08, 67.52, 59.57 Å) and used for both wtMATα2 and MATα2 (R264A) mutant docking. Ligand binding modes were predicted in the determined box with a number of all possible clusters. The most favourable energy binding site was selected based on its binding energy ($\Delta G_{binding}$: kcal/mol).

For Swissdock docking, the target model in a PDB file format and a compound in .mol2 format were uploaded on web browser interface (http://www.swissdock.ch/docking). A number of ligands binding modes were predicted in the vicinity of all target cavities. After docking process termination, all predicted binding clusters were available to download on the server. The results could be visualised by the Viewdock tool in UCSF Chimera. The best binding pose was chosen by the lowest Gibbs free energy (ΔG) and FullFitness scores.

The best binding poses of SCR0911 or SCR0915 were selected and combined with the protein model. A protein-ligand complex structure in PDB file format was written by using the UCSF Chimera tool. The protein-ligand interaction profiles were determined and visualised by DS visualiser (Dassault Systèmes BIOVIA, Discovery Studio Modelling Environment, Release 2017, San Diego: Dassault Systèmes, 2016).

2.23 Western blot

Samples were loaded onto a 12 % polyacrylamide gel and electrophoretically transferred to a polyvinylidene difluoride (PVDF) membrane. The membrane was blocked with 5 % non-fat dry milk in Tris-buffered saline containing 0.1 % Tween-20 for 1 h and then incubated overnight at 4 °C with mouse anti-His-tag (ab18184, Abcam) in 1:5,000 dilution. The membrane was then incubated with a horseradish-conjugated anti-mouse IgG (1:10,000) for 2 h at room temperature and was visualised by enhanced chemiluminescence using ECL reagents (GE Healthcare). The protein bands were assessed by automated gel imaging system (Biorad).

2.24 MAT sequence analysis

A multiple sequence alignment analysis of the human MATα1 protein was performed by using 2,963 sequences of MAT protein family by GREMLIN Co-evolution Analysis [141]. A sequence conservation analysis was generated by using WebLogo 3 [142].

Chapter III

A structural and functional analysis of the gating loop in human MAT enzymes

The results of this chapter were largely derived from the published paper which I mainly wrote the manuscript, performed experiments, analysed data and deposited all reported structures to the PDB server.

The apo wtMATα2 crystal was crystallised by J. Bradley-Clarke and this structure was processed and refined by me (PDB: 6FAJ). Prof. J.M. Mato reviewed the manuscript. Prof. P.M. O'Neill provided the quinolone compounds. Dr. S.V. Antonyuk and Prof. S.S. Hasnain conceptualised the study and supervised the project for J. Bradley-Clarke and me.

Paper detail:

"Panmanee, J., J. Bradley-Clarke, J. M. Mato, P. M. O'Neill, S. V. Antonyuk and S. S. Hasnain (2019). "Control and regulation of S-Adenosylmethionine biosynthesis by the regulatory beta subunit and quinolone-based compounds." FEBS J 286(11): 2135-2154"

3.1 Background and objective

The crystallographic structures of MAT enzymes suggest that the gating loop (residue 113-131) is required for substrate entry and product release [13, 30, 36]. It is a flexible polypeptide loop located near the active site. When the active sites of MATα1 and MATα2 are occupied by SAMe, the gating loop is shut (well-ordered) [30, 43]. A recent study has found that the gating loop is opened (disordered) when PPNP is bound in the active site, indicating that the opening of the gating loop is not driven by the breakdown of the tripolyphosphate (PPNP). In addition, only few interactions between residues of the gating loop (Gln113 and Ser114) and SAMe were reported. The mechanism that opens up the gating loop and releases SAMe remains unclear despite a number of high-resolution structures of the enzyme in different ligated forms.

Mutation of the *E. coli* gating loop showed the decrease in SAMe formation more than two hundred-fold compared with the wild type, while these mutations had only little effect on the hydrolysis rate of the tripolyphosphate [143].

Previously, the study of the wild-type MATα2 was found that Gln113 is the only residue of the gating loop that interacts with SAMe directly through its NE2 atom by forming a hydrogen bond with the O atom of SAMe, while Ser114 indirectly interacts with SAMe via a water molecule (Fig. 3.1.1). MAT gating loop sequences are quite variable among species, whereas these two amino acids are conserved in all species from bacteria to mammals (Fig. 3.1.2). Therefore, both of these residues (Gln113 and Ser114) as well as their neighbouring residue (Pro115) were further investigated by site-directed mutagenesis, activity assay and crystallographic study with a variety of ligands.

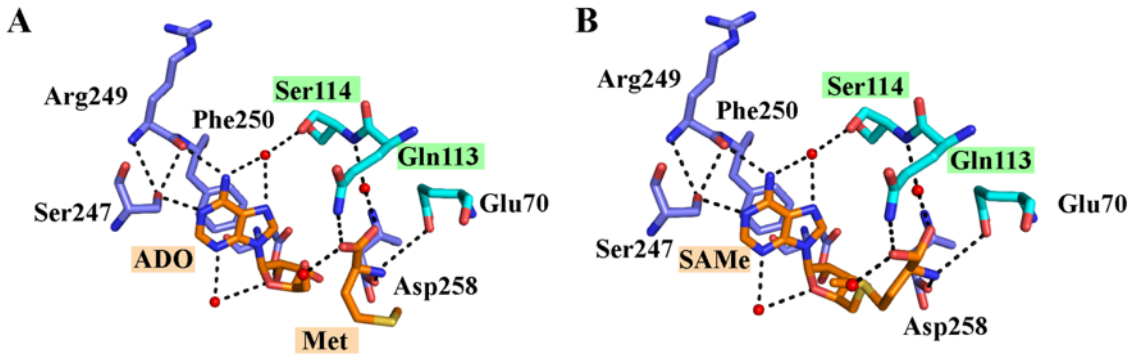

Fig. 3.1.1 Interactions between the gating loop and the substrate (Met+ADO)/ product (SAMe). Gln113 and Ser114 are highlighted in green boxes. Two MATα2 subunits forming a dimer represented by different colours (blue and slate). Carbon, nitrogen and oxygen atoms of substrates are coloured in orange, blue and red, respectively. H-bonds are shown in black dots and water oxygens are shown in red spheres. The figure was depicted from the reported MATα2 structure at 1.09 Å (PDB: 5A1I) [30].

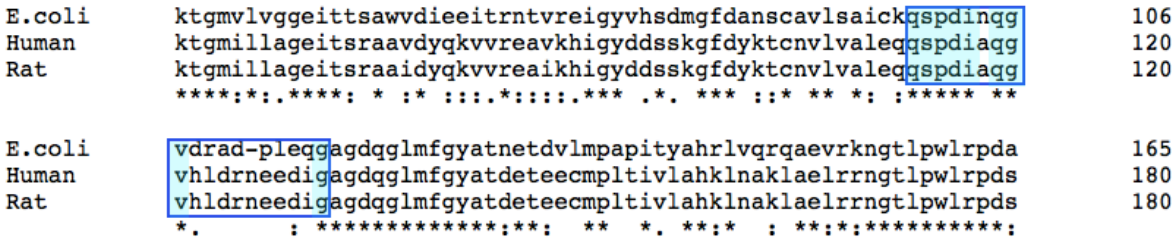

Fig. 3.1.2 Sequence alignment of *E. coli*, human MATα2 and rat MATα1 enzyme. An amino acid residue is numbered according to the human MAT. The gating loop amino acid sequences are indicated in blue boxes (residues 113-131). The first five residues are conserved from *E. coli* to mammal (rat and human). The conserved residues of the gating loop are highlighted in blue colour. An asterisk (*) indicates fully conserved residues. A colon (:) shows residues that are conserved between groups and share similar properties. A period (.) period shows amino acid conservation between groups of weakly similar properties.

3.2 Production of MATα2 and its mutants: Gln113Ala, Ser114Ala and Pro115Gly

The mutants produced by site-directed mutagenesis were confirmed by DNA sequencing (Fig. 3.2.1) and full DNA sequence results obtained from DNA sequencing for each mutant are shown in Table 3.2. The suitable annealing temperature for mutant generation was at 55-60 ^{o}C. All mutant plasmids were transformed into *E. coli* cells, BL21 (DE3), for protein expression and purification. The wild-type and mutant proteins were purified in the same manner using three different chromatography columns (section 2.7, chapter 2), including immobilised metal affinity chromatography (IMAC), anion exchange chromatography and size-exclusion chromatography. As all proteins were histidine-tagged, purification by IMAC was the obvious choice for crude purification. For the second step the anion exchange chromatography, a Q-column was used. Due to the negative charges of MATα2 (pI 6.0) in the buffer solution of pH 7.5, NaCl gradient (0.05-1.0 M) was applied for the second purification step. MATα2 was

eluted with 0.05-0.4 M NaCl. The last step of purification, size-exclusion chromatography was used for separating protein oligomeric forms.

Each step of purification was checked by SDS-PAGE and estimated molecular weight of MATα2 subunit is about 45 kDa. Protein purity of all mutants was assessed by SDS-PAGE gel staining (Fig. 3.2.2-3.2.5). The high purity was observed after proteins had been purified by anion-exchange chromatography. The major problem of mutant production was the protein precipitation during the dialysis and the concentrating procedure which caused a reduction in protein yield. Any aggregated protein was removed by centrifugation and soluble aggregates were separated in the final step of purification, gel filtration chromatography. The soluble aggregated protein was eluted firstly at the void volume of the gel filtration column and was discarded. Protein yields of MATα2 and its mutants ranged from 2-5 mg/L. This amount was sufficient to grow protein crystals and for other related experiments. The purity of the proteins was high enough to produce good quality protein crystals.

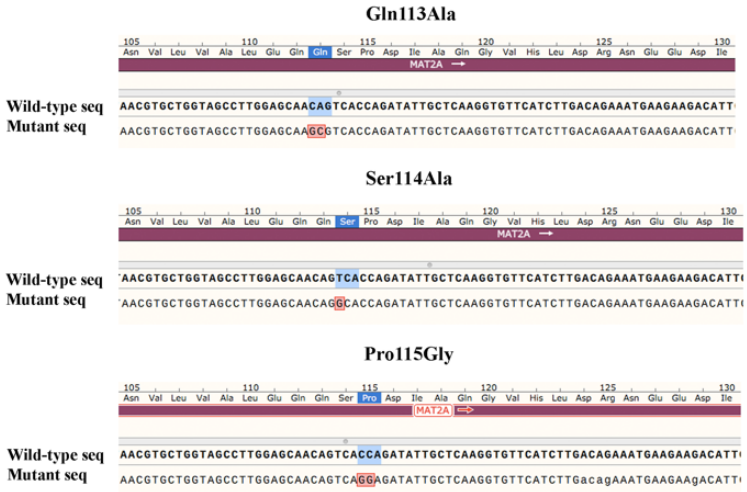

Fig. 3.2.1 The alignment of wild-type and mutant DNA sequences. DNA sequences of MATα2 mutants (Gln113Ala, Ser114Ala and Pro115Gly) were aligned to the wild-type DNA using SnapGene. Gln (CAG) and Ser (TCA) were mutated to Ala (GCG and GCA, respectively). Pro (CCA) was mutated to Gly (GGA).

Table 3.2 DNA sequencing results for Gln113Ala, Ser114Ala and Pro115Gly mutants

Mutant	Sequences
Gln113Ala (MAT2A)	CATGAACGGACAGCTCAACGGCTTCCATGAGGCGTTCATCGAGG AGGGCACATTCCTTTTCACCTCAGAGTCGGTCGGGGAAGGCCACC CAGATAAGATTTGTGACCAAATCAGTGATGCTGTCCTTGATGCCC ACCTTCAGCAGGATCCTGATGCCAAAGTAGCTTGTGAAACTGTTG CTAAAACTGGAATGATCCTTCTTGCTGGGGAAATTACATCCAGAG CTGCTGTTGACTACCAGAAAGTGGTTCGTGAAGCTGTTAAACACA TTGGATATGATGATTCTTCCAAAGGTTTTGACTACAAGACTTGTA ACGTGCTGGTAGCCTTGGAGCAAGCGTCACCAGATATTGCTCACT GGTAGCCTTGGAGCAAGCGTCACCAGATATTGCTCACTGGTAGCC TTGGAGCAAGCGTCACCAGATATTGCTCCTGGTAGCCTTGGAGCA AGCGCCACCAGATATTGCTCAAGGTGTTCATCTTGACAGAAATGA AGAAGACATTGGTGCTGGAGACCAGGGCTTAATGTTTGGCTATGC CACTGATGAAACTGAGGAGTGTATGCCTTTAACCATTGTCTTGGC ACACAAGCTAAATGCCAAACTGGCAGAACTACGCCGTAATGGCA CTTTGCCTTGGTTACGCCCTGATTCTAAAACTCAAGTTACTGTGCA GTATATGCAGGATCGAGGTGCTGTGCTTCCCATCAGAGTCCACAC AATTGTTATATCTGTTCAGCATGATGAAGAGGTTTGTCTTGATgAA ATGAGGGATGCCCTAAnGGAGAAnGTCATCAAAGCAGTTGTGCCT GCgAAaTAccTTGATGAGGATaCAATctaCCACCTACAGCCAAGTGG CAGATttgttaTTGgtGGgCCTCAaGgTGATGCTggtttgActg
Ser114Ala (MAT2A)	CATGAACGGACAGCTCAACGGCTTCCATGAGGCGTTCATCGAGG AGGGCACATTCCTTTTCACCTCAGAGTCGGTCGGGGAAGGCCACC CAGATAAGATTTGTGACCAAATCAGTGATGCTGTCCTTGATGCCC ACCTTCAGCAGGATCCTGATGCCAAAGTAGCTTGTGAAACTGTTG CTAAAACTGGAATGATCCTTCTTGCTGGGGAAATTACATCCAGAG CTGCTGTTGACTACCAGAAAGTGGTTCGTGAAGCTGTTAAACACA TTGGATATGATGATTCTTCCAAAGGTTTTGACTACAAGACTTGTA ACGTGCTGGTAGCCTTGGAGCAACAGGCACCAGATATTGCTCAA GGTGTTCATCTTGACAGAAATGAAGAAGACATTGGTGCTGGAGA CCAGGGCTTAATGTTTGGCTATGCCACTGATGAAACTGAGGAGTG TATGCCTTTAACCATTGTCTTGGCACACAAGCTAAATGCCAAACT GGCAGAACTACGCCGTAATGGCACTTTGCCTTGGTTACGCCCTGA TTCTAAAACTCAAGTTACTGTGCAGTATATGCAGGATCGAGGTGC TGTGCTTCCCATCAGAGTCCACACAATTGTTATATCTGTTCAGCAT GATGAAGAGGTTTGTCTTGATGAAATGAGGGATGCCCTAAnGGA GAAAGTCATCAAAGCAGTTGTGCCTGCGAAATACCTTGATGAGG ATACAATCTACCACCTACAGCCAAGTGGCAGATTTGTTATTGGTG GGCCTCAGGGTGATGCTGGTTTGACTGGACGCAAAATCATTGTGG ACACTTATGGCGGTTGGGgTGCTCATGGaggAGGTGCCTTTTCAGG AAAGGATTATACCAAGGTCGACCGTTCAGCTGCTTATGCTGCTCG TTGGGTGGCAAAATCCCTTGTTAAaGGaggTCTGTGCCGGaaGgTTC TTgttCAGGTCtCTTATGctATTGgaaTtnctcATCCATTATCTATcnCcATT TtCCATTnngnnnCctcTCanaaga

Mutants	Sequences
Pro115Gly (MAT2A)	CATGAACGGACAGCTCAACGGCTTCCATGAGGCGTTCATCGAG GAGGGCACATTCCTTTTCACCTCagagTCGGTCGGGGAAGGCCAC CCAGATAAGATTTGTGACCAAATCAGTGATGCTGTCCTTGATGC CCACCTTCAGCAGGATCCTGATGCCAAAGTAGCTTGTGAAACTG TTGCTAAAACTGGAATGATCCTTCTTGCTGGGGAAATTACATCC AGAGCTGCTGTTGACTACCAGAAAGTGGTTCGTGAAGCTGTTAA ACACATTGGATATGATGATTCTTCCAAAGGTTTTGACTACAAGA CTTGTAACGTGCTGGTAGCCTTGGAGCAACAGTCAGGAGATATT GCTCAAGGTGTTCATCTTGACAGAAATGAAGAAGACATTGGTGC TGGAGACCAGGGCTTAATGTTTGGCTATGCCACTGATGAAACTG AGGAGTGTATGCCTTTAACCATTGTCTTGGCACACAAGCTAAAT GCCAAACTGGCAGAACTACGCCGTAATGGCACTTTGCCTTGGTT ACGCCCTGATTCTAAAACTCAAGTTACTGTGCAGTATATGCAGG ATCGAGGTGCTGTGCTTCCcATCAGAGTCCACACAATTGTTATAT CTGTTCAGCATGATGAAGAGGTTTGTCTTGATGAAnTGAGGGAT GCCCTAAAGGAnAanGTCATCAAAGCAGTTGTGCCTGcgAanTACC TTGATGAGGATACAATCTACCACCTACAGCcAAGTGGCAGaTTtG TTATTGGTGGGCCTCagntnGATGC

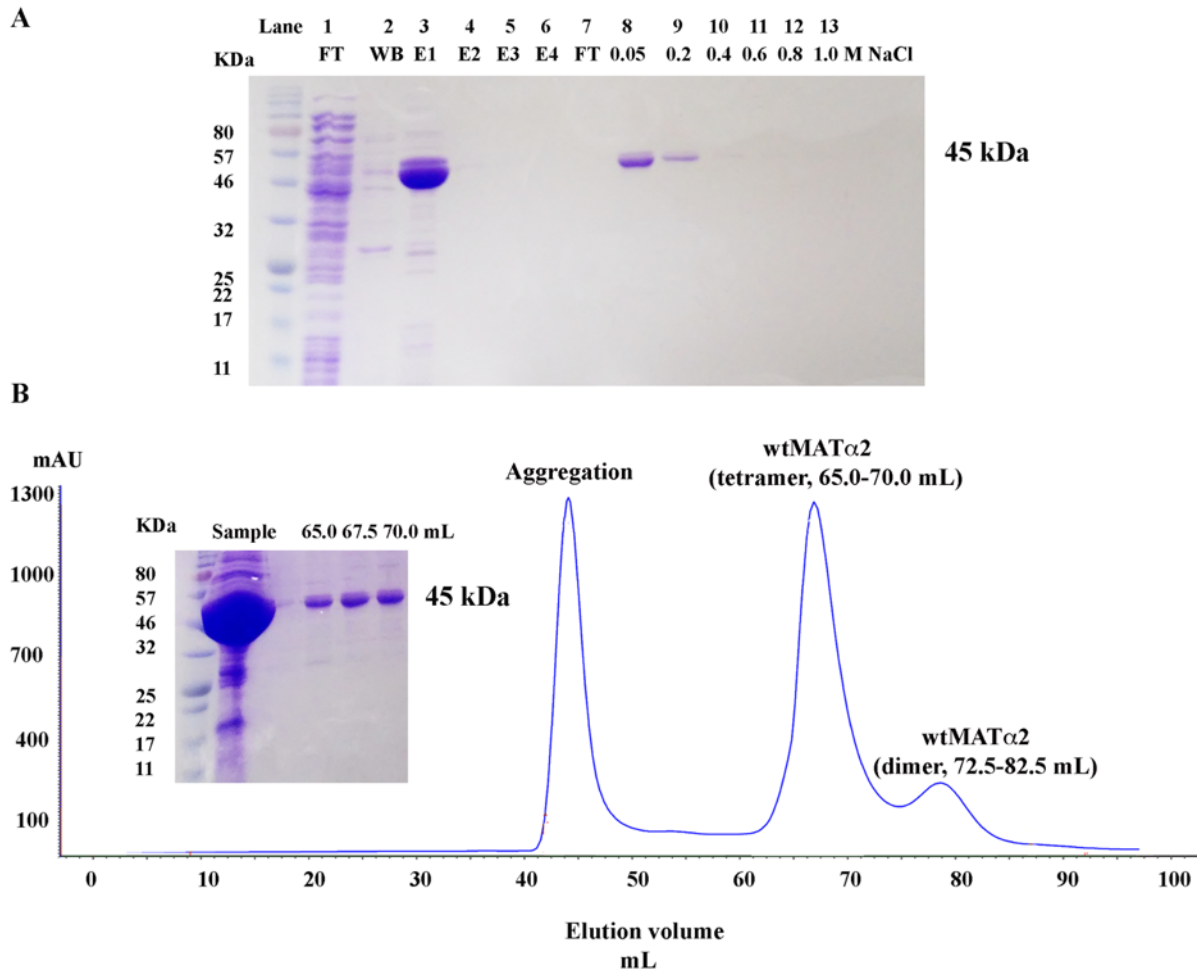

Fig. 3.2.2 wtMATα2 purification. **(A)** SDS-PAGE of the wtMATα2 protein from the Ni-affinity purification is shown (lane 1 = flow-through; lane 2 = Wash buffer; lane 3-6 = Elution fractions from the Ni-affinity column). The eluted fraction containing proteins was collected and loaded into the Q column (lane 7 = flow-through; 8 = Elution of 0.05 M NaCl; 9 = Elution of 0.2 M NaCl; 10 = Elution of 0.4 M NaCl; 11 = Elution of 0.6 M NaCl; 12 = Elution of 0.8 M NaCl; 13 = Elution of 1.0 M NaCl). The fractions containing proteins were pooled and followed by size-exclusion chromatography. **(B)** The size-exclusion chromatography profile is shown by the absorbance at 280 nm (indicating a protein peak). The first peak is protein aggregation, and the second peak is the protein in a tetrameric state (65.0-70.0 mL). The third peak is a dimeric form of wtMATα2 (72.5-82.8 mL). The SDS-PAGE of the fractions containing the tetrameric wtMATα2 eluted at 65.0- 70.0 mL is shown.

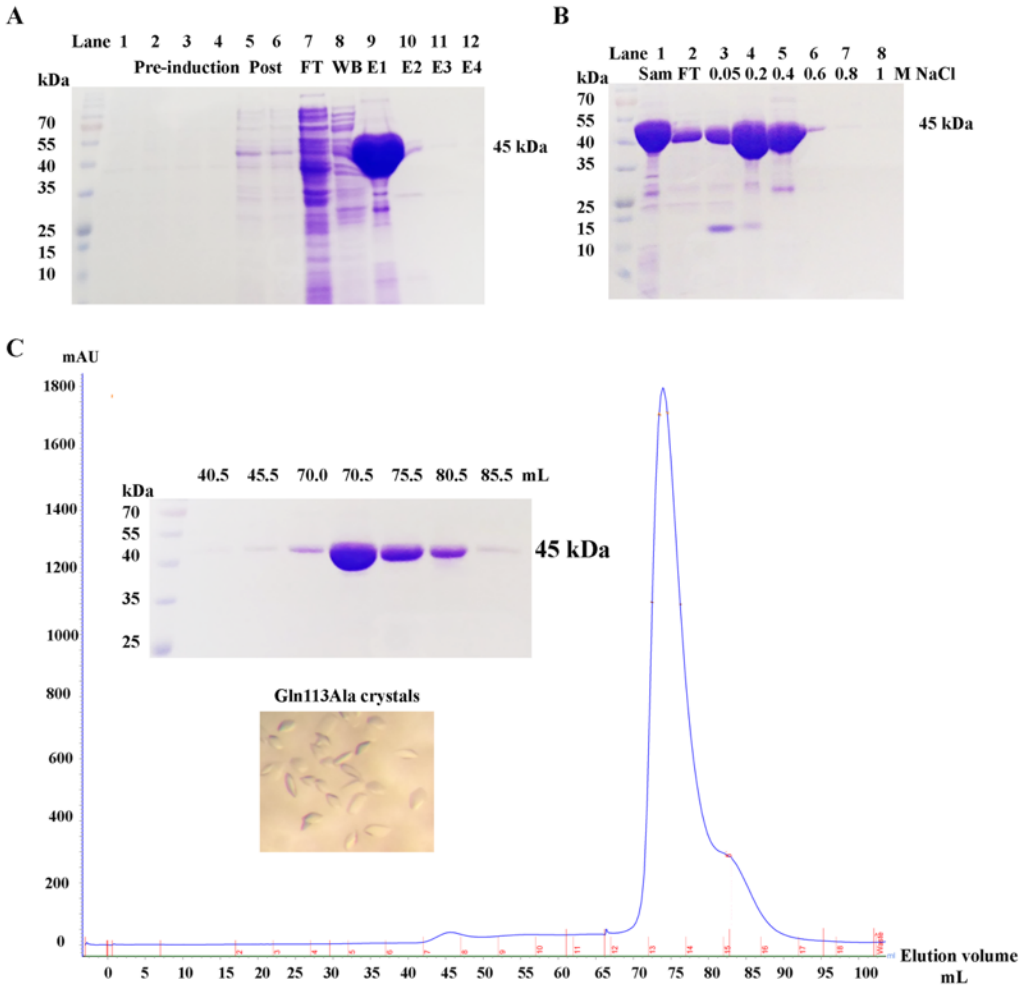

Fig. 3.2.3 MATα2 Gln113Ala mutant purification. **(A)** SDS-PAGE of the Gln113Ala protein from the Ni-affinity purification is shown (lane 1-4 = Pre-induction; 5-6 = Post-induction; 7 = flow-through; 8 = Wash buffer; 9-12 = Elution fraction 1-4). **(B)** SDS-PAGE of the proteins from the anion-exchange purification is exhibited (lane 1 = protein sample; 2 = flow-through; 3 = Elution of 0.05 M NaCl; 4 = Elution of 0.2 M NaCl; 5 = Elution of 0.4 M NaCl; 6 = Elution of 0.6 M NaCl; 7 = Elution of 0.8 M NaCl; 8 = Elution of 1.0 M NaCl). **(C)** The size-exclusion chromatography profile is shown by the absorbance at 280 nm. The main peak indicated that the majority of protein was eluted at 70.0-80.5 mL. The SDS-PAGE of the fractions eluted at 40.5-80.5 mL is shown. The mutant crystals were obtained from the pooled fractions of 70.5-80.5 mL fractions.

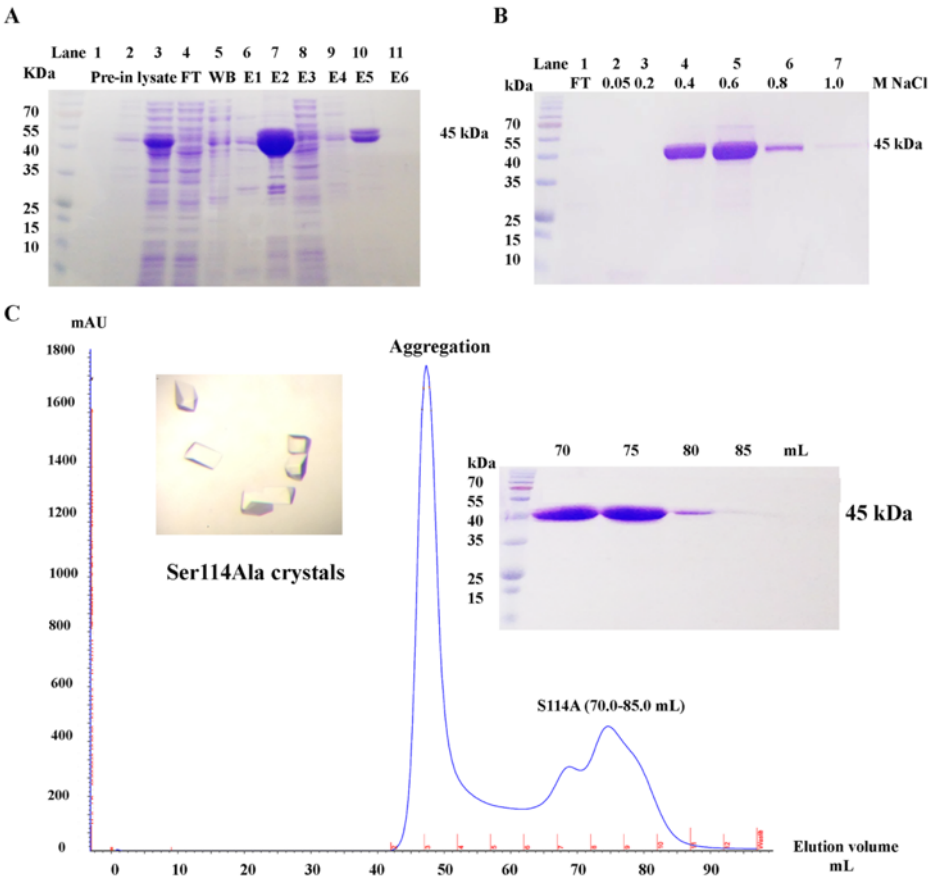

Fig. 3.2.4 MATα2 Ser114Ala mutant purification. **(A)** SDS-PAGE of the Ser114Ala protein from the Ni-affinity purification is shown (lane 1, 2 = Pre-induction; 3 = lysate of protein sample; 4 = flow-through; 5 = Wash buffer; 6-11 = Elution fraction 1-6). **(B)** SDS-PAGE of the protein from the anion-exchange purification is exhibited (lane 1 = flow-through; 2 = Elution of 0.05 M NaCl; 3 = Elution of 0.2 M NaCl; 4 = Elution of 0.4 M NaCl; 5 = Elution of 0.6 M NaCl; 6 = Elution of 0.8 M NaCl; 7 = Elution of 1.0 M NaCl). **(C)** The size-exclusion chromatography profile is shown by the absorbance at 280 nm. The first peak indicated the protein aggregation and the second peak was eluted at 70.0-80.5 mL fractions. The SDS-PAGE of fractions containing Ser114Ala is shown. The mutant crystals were obtained from the pooled fractions of 70.0-85.0 mL fractions.

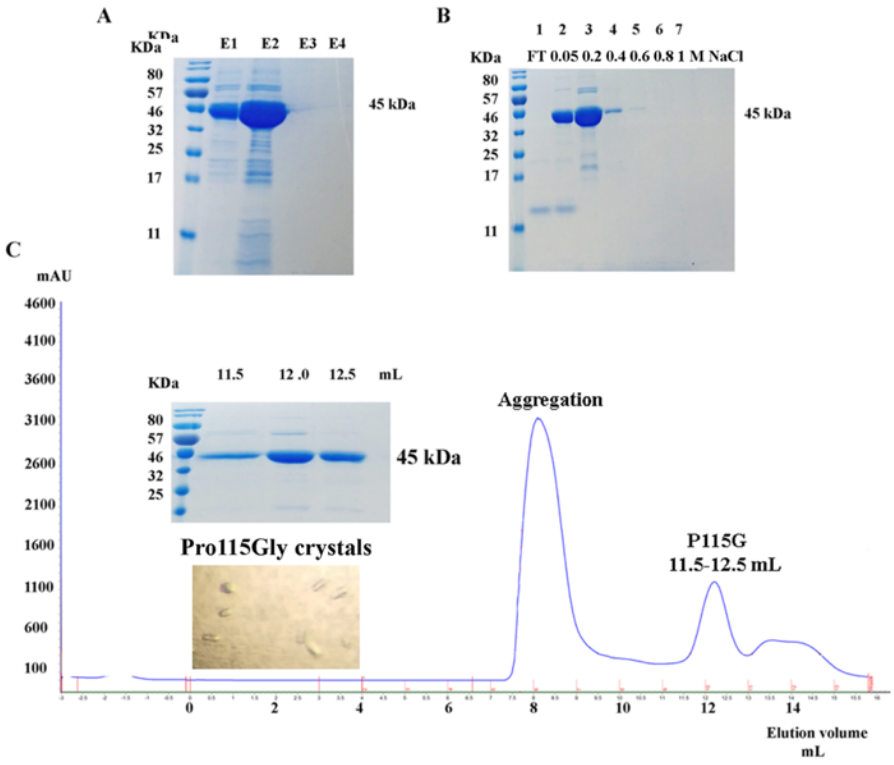

Fig. 3.2.5 MATα2 Pro115Gly mutant purification. SDS-PAGE of the Pro115Gly protein from Ni-affinity purification is shown (lane 1-4 = Elution fraction 1-4). **(B)** SDS-PAGE of the protein from the anion-exchange purification is shown (lane 1 = flow-through; 2 = Elution of 0.05 M NaCl; 3 = Elution of 0.2 M NaCl; 4 = Elution of 0.4 M NaCl; 5 = Elution of 0.6 M NaCl; 6 = Elution of 0.8 M NaCl; 7 = Elution of 1.0 M NaCl). **(C)** The size-exclusion chromatography profile is shown by the absorbance at 280 nm. The first peak indicated the protein aggregation and the second peak was eluted at 11.5-12.5 mL. The SDS-PAGE of fractions containing Pro115Gly is displayed. The crystals were obtained from the pooled fractions containing proteins (11.5-12.5 mL).

3.3 Production of MATβV1 and MATβV2

MATβV1 and MATβV2 variants were purified using Ni-affinity, anion exchange and gel filtration chromatography (section 2.8, chapter 2). MATβ has an estimated isoelectric point (pI) around 6.9, while the pH of the buffer solution is 7.5. At pH 7.5, MATβ proteins containing negative charges bound to a positively charged anion exchange resin and could be eluted by 0.05-0.4 M NaCl gradient. At lower ionic strength, proteins with pI values closer to 7.5 are eluted before proteins with lower pI. Size-exclusion chromatography using a gel filtration column was used as a polishing step in purification. The SUMO tag was cleaved from MATβ proteins using SENP2 protease and the tag could be removed from the protein sample by size-exclusion chromatography. SDS-PAGE analysis was performed for each step of purification to check protein purity (Fig. 3.3.1-3.3.2). No protein aggregation was observed in MATβ purification as shown by the gel filtration profiles. Protein yield was about 3-5 mg/L for each batch of purification.

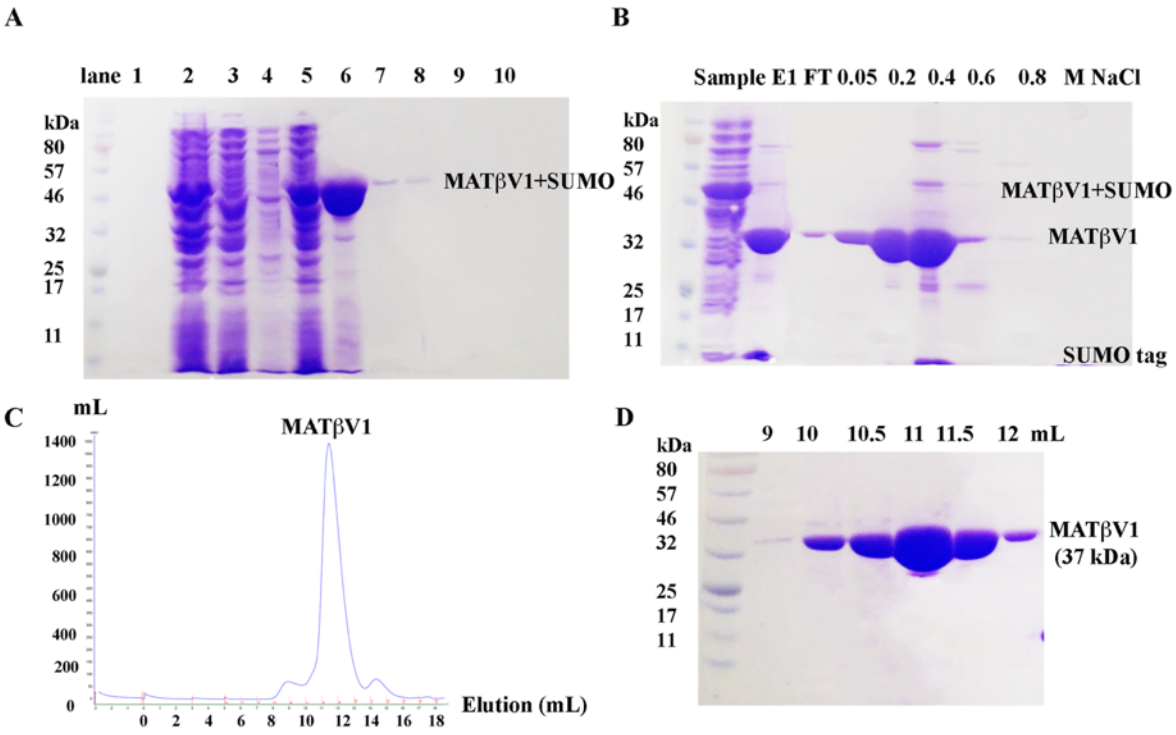

Fig. 3.3.1 MATβV1 purification. (A) SDS-PAGE of MATβV1 proteins from Ni-affinity purification is displayed (1 = Pre-induction; 2= Sample; 3 = Flow-through; 4 = lysis buffer, 5 = wash buffer, 6-10 = Elution 1-6). **(B)** SDS-PAGE of the protein from anion-exchange purification with 0.05-0.8 M NaCl gradient is shown. **(C)** The gel filtration profile is shown by the absorbance at 280 nm. The main peak indicated that the majority of protein was eluted at 11.0-12.0 mL. **(D)** SDS-PAGE of fractions containing MATβV1 is exhibited.

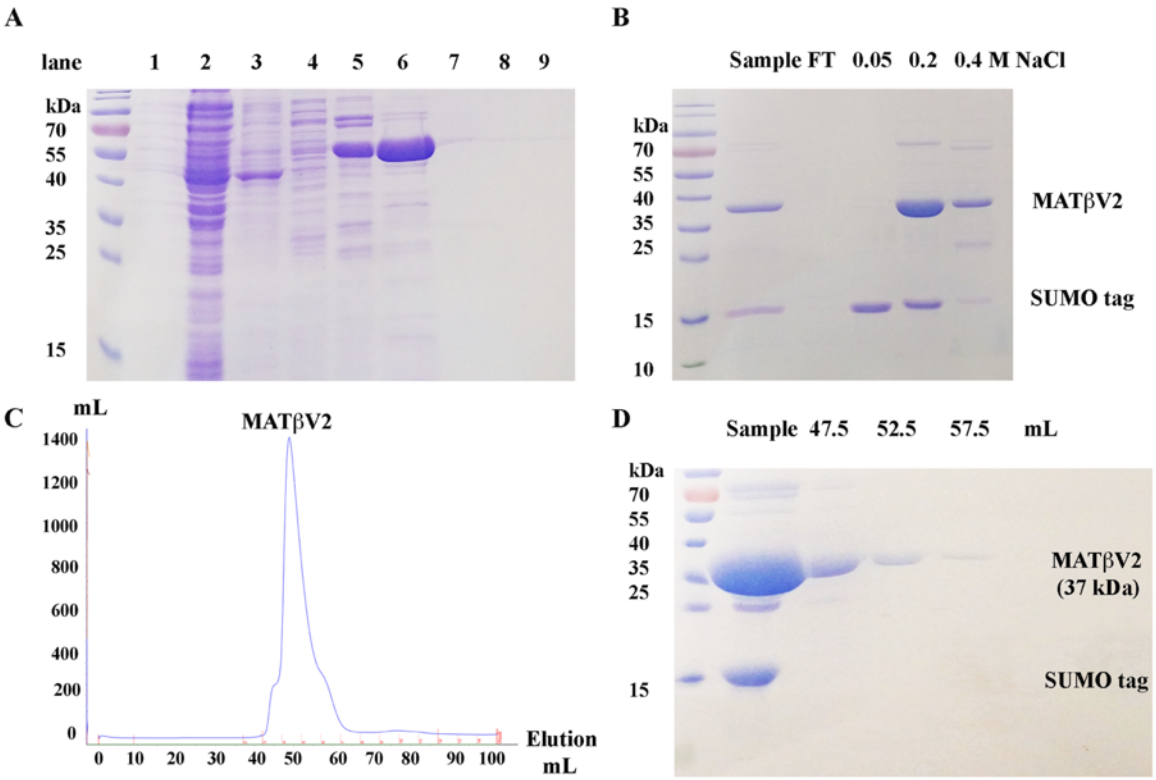

Fig. 3.3.2 MATβV2 purification. (A) SDS-PAGE of MATβV2 proteins from Ni-affinity purification is shown (1 = Pre-induction; 2 = Flow-through; 3 = lysis buffer, 4 = wash buffer, 5-9 = Elution 1-5). **(B)** SDS-PAGE of the protein from anion-exchange purification with 0.05-0.8 M NaCl gradient is displayed. **(C)** The gel filtration profile is shown by the absorbance at 280 nm. The main peak was eluted at 47.5-57.5 mL. **(D)** SDS-PAGE of fractions containing MATβV2 is shown at 47.5-57.5 mL.

3.4 A structural and functional analysis of the gating loop's role in human MAT enzymes

3.4.1 The enzymatic and phosphatase activity of MATα2

The functional significance of the active site gating loop was explored using various mutants of the human MATα2. The mutants were designed based on the well-characterised residues of the gating loop that showed to interact with SAMe. The conserved residues (Gln113, Ser114 and Pro115) of the gating loop were mutated to Gln113Ala, Ser114Ala and Pro115Gly by site directed mutagenesis. Proline (Pro115) is the only amino acid that connects its side chain to backbone, therefore it is mutated to Gly which has no side chain at all. Glutamine (Gln113) and serine (Ser114) contain polar side chains (amide group ($-NH_2$) of Gln and hydroxyl group (-OH) of Ser) that were reported to interact with Met and SAMe [30]. Thus, these two amino acids (Gln and Ser) are mutated to alanine (Ala) that contains only the nonpolar $-CH_3$ group to investigate the functional role of their side chains.

A recent study has shown that Gln113 and Ser114 residues interact with both Met and SAMe in the active site of the enzyme on its own and when it complexes with MATβ subunits [13, 30]. Gln113Ala mutation results in a decrease in SAMe production to 75.6 ± 4.5 %, while Ser114Ala mutation shows only 2.5 ± 0.8 % ($p < 0.05$) of SAMe formation when compared to wtMATα2 (Fig. 3.4.1A). In contrast, Pro115Gly mutation has no effect on enzymatic activity (Fig. 3.4.1A). Remarkably, the SAMe production is recovered in Gln113Ala and Ser114Ala mutants when they complex with either MATβV1 or MATβV2 to the extent that the production of SAMe by Gln113Ala/Ser114Ala MATα2:MATβ complexes is the same as for the wtMATα2:MATβ complex (Fig. 3.4.1A). The concentrations of substrates used for measuring SAMe formation (200 μM Met and 1 mM ATP) were likely to be insufficient to allow Ser114Ala mutant's activity reaching its Vmax without forming complexes with the regulatory

subunits (MATβV1/V2). This indicates a reduction in enzyme-substrate affinity leading to the decrease in SAMe formation of the mutant.

Surprisingly, none of the mutants show any change in the phosphatase activity compared to the wtMATα2 (Fig. 3.4.1B), suggesting that structural elements which involve in SAMe formation are different from those responsible for PPPi hydrolysis. ATPase activity of MAT enzymes was suggested to be independent from SAMe synthesis [49, 53]. The ADP-bound MATα1 crystal structure was derived from the co-crystallisation of ATP and methionine analogue (LcisAMB) confirming that the hydrolysis of ATP could take place without SAMe formation [35]. Complexation with MATβV1 generally results in higher activity than when wtMATα2 or its mutants complex with MATβV2. These observations suggest that MATβ binding has a profound effect on MAT enzymes where the length of the MATβ protein has a significant impact on MATα2 activity (Fig. 3.4.1A) [13].

There is limited published work concerning the phosphatase activity of MAT enzymes. The findings in the current study are consistent with the two reported studies which had shown that MAT activity decreased in the mutants associated with the gating loop or the active site mutations, while the phosphatase activity was unaffected. The first study in *E. coli* MAT showed that k_{cat} of SAMe formation decreased by more than two hundred fold caused by mutations at the enzyme's gating loop without effecting the PPPi hydrolysis rate [143]. This study suggested that the mutations caused the unorganised active site and decreased the enzymes' ability to catalyse SAMe formation, while the hydrolysis of the tripolyphosphate took place in different parts of the protein and is less affected by these mutations. A study of MATα1 variants (18 mutations) identified in patients with persistent hypermethioninemia [144] found that seven of these variants (Arg249Trp, Ile252Thr, Gly257Arg, Asp258Gly, Ala259Val, Lys289Asn, and Gly381Arg) showed a reduction in MAT activity (SAMe formation), while their phosphatase activity was unaffected. The structural study of MATα2

by Murray B et al., 2016 [30] provided structural elements to explain a loss of activity for these reported mutants based on their residues' roles. Arg249 is found to stabilise the binding of adenosine to the active site prior to SAMe formation, while Asp258 and Ala259 are observed to coordinate with the K^+ ion. In addition, Asp258 also interacts with substrate methionine and is involved in SAMe formation. Taken together, it is likely that the phosphatase activity is independent to SAMe formation and the gating loop has an important role in SAMe production which does not affect the PPPi hydrolysis rate upon its mutations.

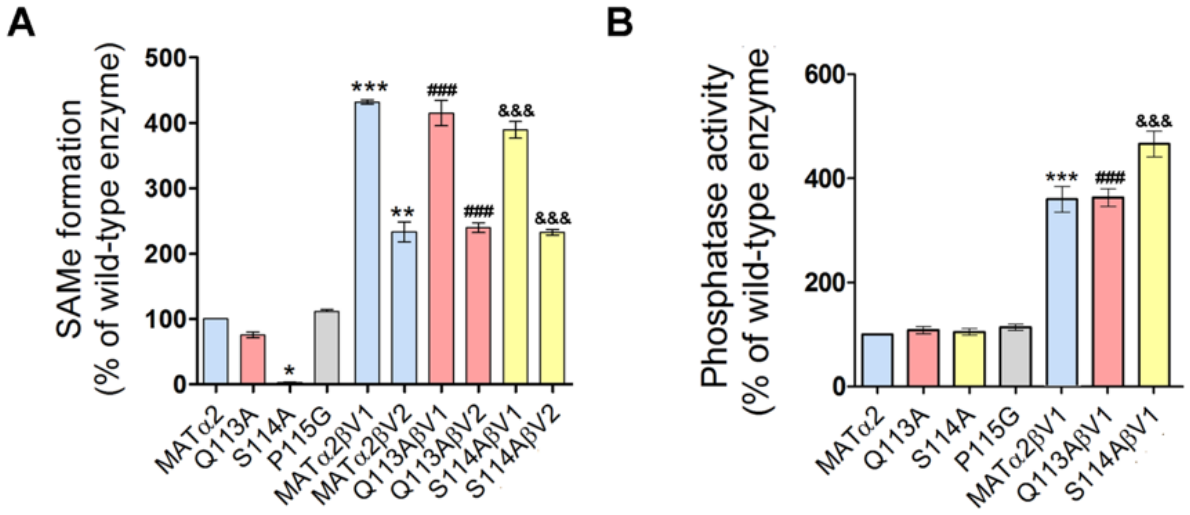

Fig. 3.4.1 The enzymatic activity of wild-type and mutant MATα2 (A) SAMe formation of wtMATα2 and complexes compared to its mutants. **(B)** Phosphatase activity of the wild-type enzyme and the complexes compared to the mutants. '*' '**' and '***' denote statistical significance at $p < 0.05$, $p < 0.1$ and $p < 0.001$ compared with wtMATα2, respectively. '###' and '&&&' indicate statistical significance at $p < 0.001$ compared to Q113A and S114A mutants, respectively. Data are the mean of three independent experiments ± SEM (n =3). All experiments were performed using protein samples from the same batch of protein purification (different tubes).

MATβ subunits interact with the active site residues that recognise the PPPi of the catalytic subunits [13] via the helical loop (Fig. 3.4.2A). The complex structure of MATαβ shows that His323 (NE2 atom) of MATβV2 interacts with Gly273 (O atom) which constitutes the tripolyphosphate recognition loop (Arg264-Gly273) of MATα2, where the NE atom of Arg264 (MATα2) interacts with the O1G and O3G atom of PPNP (Fig. 3.4.2A). The current study has found that the phosphatase activity of MAT complexes is significantly higher than that of the catalytic subunit alone (Fig. 3.4.2B). The V_{max} and K_m values of MATα2, MATα2βV1and MATα2βV2 are reported in Table 3.4.1.

Triphosphate is an intermediate generated during ATP cleavage when SAMe is formed. It needs to be hydrolysed to PPi and Pi before being released from the active site. The PPPi hydrolysis allows enzymes for proceeding to the next reaction cycle. The activity of the mutants which are recovered by complex formation may be in part facilitated by an increase in the phosphatase activity of enzyme complexes. This observation is in agreement with the protein dynamics study showing that the ATP binding region of MATα2 undergoes allosteric modifications upon binding of MATβ [145]. The structural alignment of the wtMATα2 and the MATα2β complex revealed that the conformation of residues in the active site of wtMATα2 were similar compared to those with or without MATβ binding, however several movements of the solvent-exposed α-helices are observed in MATα2β complexes. The increase in the solvent exposed area along the $MAT(\alpha2)_4$ surface is found in MATα2β complexes when compared to the homo-oligomer of the wild type (Fig. 3.4.2C). Additionally, the complex thermal stability of both MATα2βV1 (Tm = 55.2 ± 0.1 °C, $p < 0.001$) and MATα2βV2 (Tm = 48.4 ± 0.1 °C, $p < 0.001$) are higher than that of the catalytic subunit alone (Tm = 47.2 ± 0.2 °C). The normalised fluorescence curves of MATα2, MATα2βV1 and MATα2βV2 are shown in Fig. 3.4.2D.

Table 3.4.1. The effect of regulatory subunits on kinetic properties of MATα2 phosphatase activity.

Protein	Vmax (x10^3 Pi, pmol/s/nmol of protein)	Km (ATP, mM)
MATα2	5.2 ± 0.4	0.3 ± 0.1
MATα2βV1	27.2 ± 2.4	0.5 ± 0.2
MATα2βV2	17.8 ± 1.3	0.6 ± 0.1

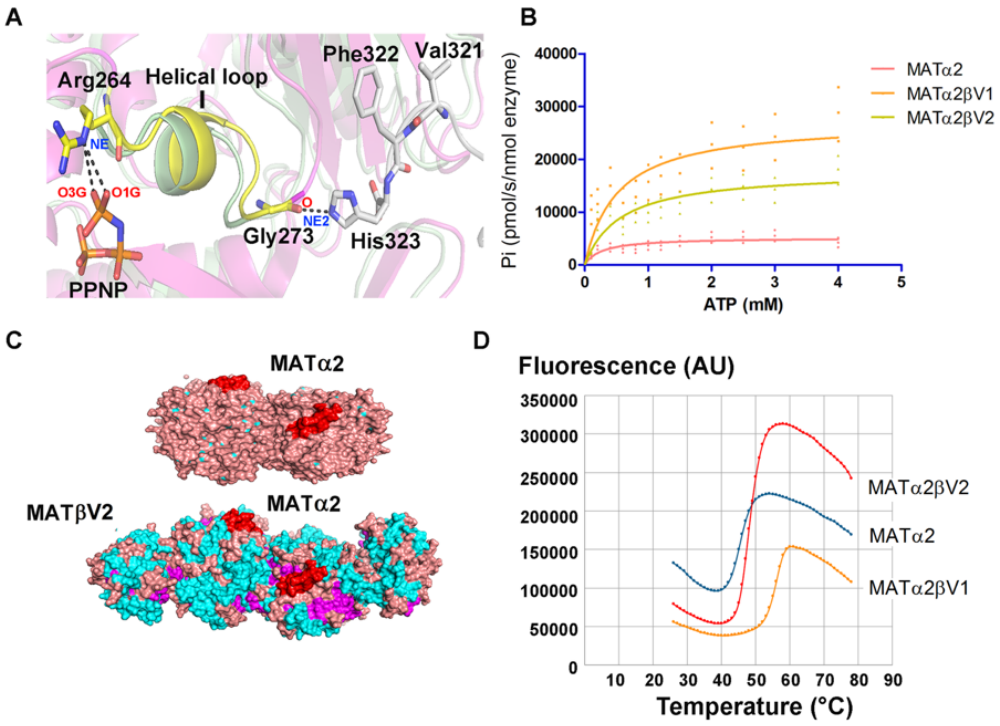

Fig. 3.4.2 Structural comparison and phosphatase activity of MATαβ complexes and homo-oligomeric wtMATα2 (A) The structural alignment of MATα2 (pale green) with MATαβ complex (pink) shows the helical PPPi recognition loop (yellow, residues 264-273) that interacts with the MATβ subunit. **(B)** Michaelis-Menten plots of phosphatase activity of the wild-type enzyme and complexes using various ATP concentrations. Curve fitting by nonlinear regression was performed using GraphPad Prism 5 software. **(C)** An overview of MATα2 (upper) and MATα2βV2 complex (lower, PDB ID: 4NDN) shows the overall enzyme surface. The gating loop is displayed in red. The α-helices, β-sheets and connecting loops are

shown in cyan, purple and pink, respectively. **(D)** Thermal shift assay was used to determine the wtMATα2 stability with or without MATβV1 and MATβV2 complex formation.

3.4.2 Crystallographic structures of the gating loop mutants

Ser114Ala (S114A) mutant structures have been obtained in two different crystallographic space groups (I222 and $P22_12_1$), while the structure of Pro115Gly (P115G) has only been obtained in the I222 symmetry. The Gln113Ala (Q113A) mutant also crystallised in the space group $P22_12_1$. All mutants were incubated with the same ligands (Met and AMP-PNP) prior to crystallisation. SAMe is observed in wtMATα2, Q113A and P115G, all of which show similar enzymatic activity (75-110 % of wtMATα2). However, SAMe is absent in the structure of S114A mutant which has less than 4 % enzymatic activity, consistent with the inability of this mutant to convert methionine into SAMe. Only enzyme intermediates (PPNP and ADO) are found in S114A active sites and it is consistent in both crystallographic forms (I222 and $P22_12_1$). The enzyme product and intermediate found in the active site of each mutant are summarised in Table 3.4.2. Data collection and refinement statistics of the gating loop mutants (Q113A, S114A and P115G) are shown in Tables 3.4.3a and 3.4.3b.

Table 3.4.2 Summary of the enzymatic activity and ligands found in the active site of MATα2 mutants and wtMATα2.

Mutant*	Resolution (Å)	Space group	Active site ligands	SAMe synthesis (%)
Q113A	2.70	$P22_12_1$	PPNP, SAMe	75.6 ± 4.5
S114A	1.65	$P22_12_1$	PPNP, ADO	2.5 ± 0.7
S114A	1.80	I222	PPNP, ADO	2.5 ± 0.7
P115G	2.70	I222	PPNP, SAMe	111.4 ± 2.8
wtMATα2	1.35	I222	PPNP, SAMe	100.0

The crystal structure of S114A in the I222 space group contains one monomer in the asymmetric unit in which full occupancies of PPNP and ADO are clearly observed in the active site (Fig. 3.4.3A). The crystal structure of S114A in the $P22_12_1$ space group shows two monomers in the asymmetric unit with the gating loop in different conformations. One monomer shows the active site occupied by PPNP (occupancy 0.5) and ADO (occupancy 0.75) neighbouring with the well-ordered, closed gating loop, while the other active site is empty showing the ordered, visible gating loop in the open conformation (Fig. 3.4.3B). This is the first time that the main part of the gating loop (residues 113-125) is clearly visible in its open conformation of the human MAT enzyme family (Fig. 3.4.3B and D). Additionally, the similar behaviour was found in the archaeal MAT that showed structural rearrangement of its gating (flexible) loop (residues 139-156) in apo- and holo-states. The open conformation of the gating loop found in *Thermococcus kodakarensis* MAT (apo-state) showed the movement of the gating loop domain (residues 144-155) from its closed conformation (residues 142-142), which was reported in another thermophilic archaeal MAT, *Sulfolobus solfataricus* [14, 48] (Fig. 3.4.3E, 3.4.3F).

The presence of enzyme intermediates (PPNP and ADO) observed in the S114A structure (Fig. 3.4.3C) indicates that the early step of the reaction (ATP cleavage: ADO and PPNP) has taken place, but the S114A mutant fails to provide the nucleophilic attack of methionine's sulphur atom against C'5 atom of AMP-PNP, thus unable to produce SAMe. These observations are consistent with the suggestion that C-O bond breaking occurs prior to C-S bond formation at the catalytic transition state of human wtMATα2 [146]. The previous high-resolution structure of SAMe+ADO+MET+PPNP bound wtMATα2 (PDB: 5A1I) showed that Ser114 is the only residue in the gating loop that interacted with AMP-PNP via a water molecule. The functional group (-OH) of Ser114 side chain cooperates with the water molecule in positioning AMP-PNP or ATP via its adenine ring and facilitates SAMe production. Ser114 also interacts with

the neighbouring gating loop residues (Asp116, Ile117 and Ala118) and stabilises the helix conformation of the ordered gating loop.

The S114A structure shows that the gating loop becomes more ordered in the closed conformation as observed by comparing helical initiation and termination residues of the closed (Pro115-His122) to the open (Ile117-Val121) conformation (Fig. 3.4.3B). In the wtMATα2 (PDB: 5A1I), two active sites are identical, occupied by substrates or products with the gating loop in the closed conformation blocking reactive intermediates from escaping into solution. In contrast, in both S114A and Q113A mutants (see below), only one active site is occupied by substrate or product indicating that the gating loop is unable to rearrange itself properly to the closed conformation during the substrate binding step, therefore the reactive intermediates might be able to leave the enzyme. Two loop conformations showing in the S114A structure suggest that the loop has ability to adopt different conformations when SAMe formation does not occur.

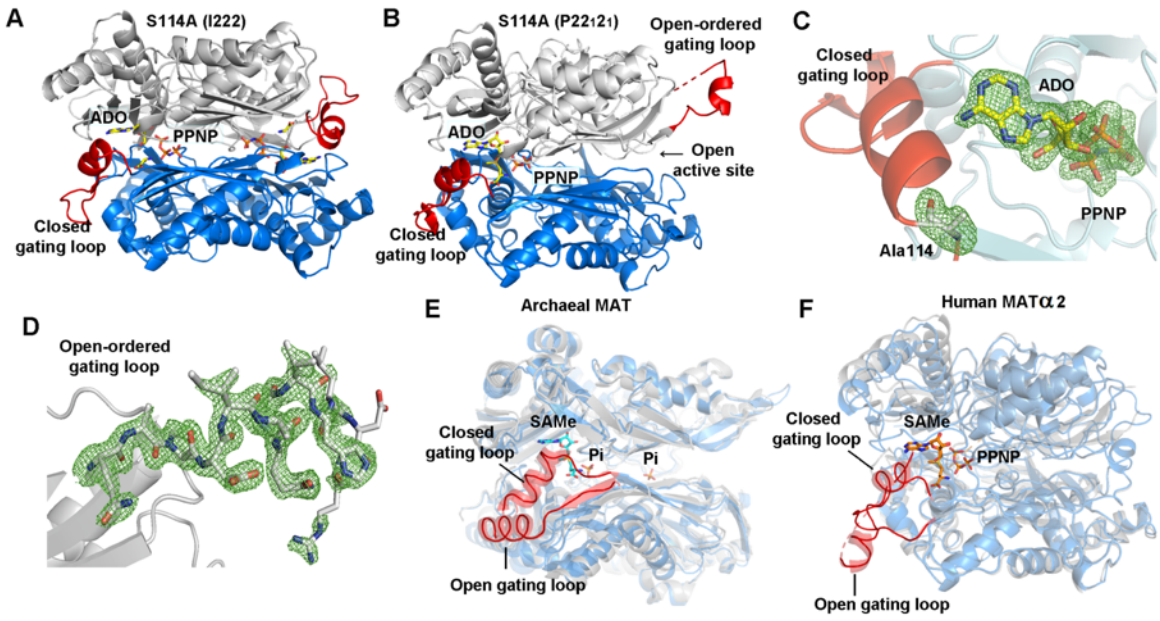

Fig. 3.4.3 The structure of S114A MATα2 mutant. **(A)** The S114A mutant structure (I222 space group) contains PPNP and ADO in the active site showing the closed gating loop (red). **(B)** The S114A mutant structure ($P22_12_1$ space group) contains PPNP and ADO in the active site of one subunit showing a closed gating loop (red), while the other subunit is empty having an ordered, visible gating loop in the open conformation. **(C)** The mutation site and intermediates (PPNP and ADO) are shown with omit maps. **(D)** The ordered, open gating loop (residues 113-125) is shown with omit maps. **(C, D)** Fo-Fc omit maps (green) are contoured at the 3 σ level (sigma or noise level) allowing only electron density regions above the noise value to be calculated. **(E)** The structures of archaeal MAT in an apo-state with the gating loop in the open conformation (PDB: 4L4Q, grey) and a holo-state with the closed gating loop (PDB: 4L7I, cyan) are aligned to compare the movement of gating loops in the different conformations. The gating loops are represented in red ribbons and all active site ligands (SAMe and Pi) are shown as sticks. **(F)** Structural alignment of the apo human MATα2 (PDB: 6FAJ, grey) and the holo form with the closed gating loop (PDB: 5A1I, cyan) is shown. SAMe and PPNP are shown as sticks.

The Q113A crystal structure was obtained in the $P22_12_1$ space group showing two MATα2 monomers in the asymmetric unit (Fig. 3.4.4A). One subunit shows the closed, well-ordered gating loop with SAMe and PPNP (full occupancy) binding in the active site (Fig. 3.4.4B). The active site of the second subunit is empty with the open conformation of gating loop. Most of residues of the open gating loop (residues 117-131) are disordered, and electron density is not observed in the structure (Fig. 3.4.4A). In the wtMATα2, Met (N and O atom) forms H-bonds with MAT enzyme at Glu70 (OE1 atom) and Gln113 (NE2 atom) of one subunit. Met (N atom) also interacts with Asp258 (OD1 atom) that belongs to the partner subunit. Gln113 to Ala113 mutation shows no effect on the binding of Met or SAMe to the active site. SAMe can bind to MAT enzymes by various interactions. It (N atom) forms H-bonds with OE1 atom of Glu70 (2.6 Å) and OD1 atom of Asp258 (2.5 Å), while its oxygen atom (O3 atom) interacts with OD2 atom of Asp258 (3.0 Å). These interactions maintain the position of SAMe in the active site (Fig. 3.4.4C). A loss of the interaction of Met's main chain with Gln113 arising from the mutation to Ala113 is likely to be responsible for the less efficiency of SAMe production (75 % compared to wtMATα2). In addition, the possible role of Gln113 is to sense the substrate entry and stabilises the closed gating loop through its interaction with Met, while the entire orientation of Met or SAMe position is maintained by other residues in the active site as observed from the crystal structure.

The different conformations of the gating loop observed in the mutant structures (Q113A and S114A) clearly show the importance of these two residues in regulating the gating loop rearrangement to different conformations. These residues sense the presence of substrate Met and ATP in the active site via the interaction of Gln113 with Met and Ser114 with an adenine ring of ADO or ATP (Fig. 3.4.4D). These important interactions of the gating loop with the substrates drive the rearrangement of the gating loop to its closed conformation.

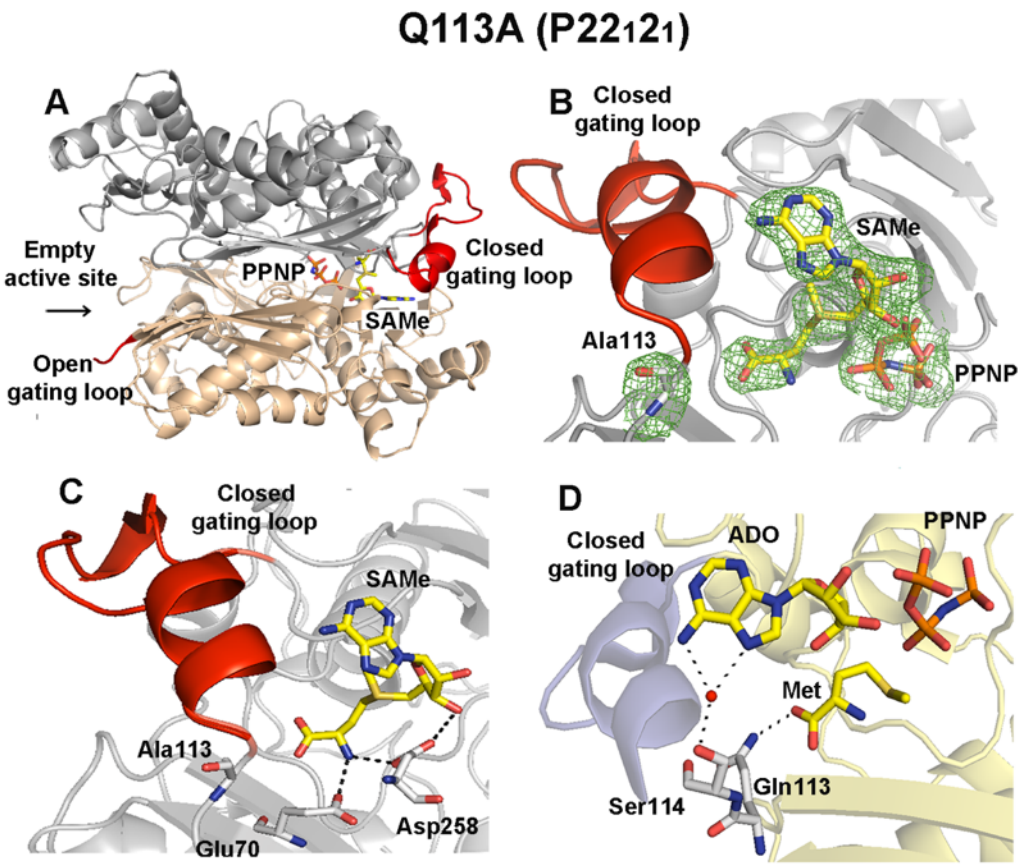

Fig. 3.4.4 Q113A mutant and wild-type structure. **(A)** The closed and the open conformation of the gating loop are shown in red. One subunit contains product SAMe and PPNP in the active site neighbouring with the closed gating loop. The other subunit has no ligand in the active site showing the disordered, open gating loop. **(B)** Close view of the Q113A structure showing the omit map contoured around Ala113 is illustrated. An intermediate PPNP or a product SAMeare shown as sticks. Fo-Fc omit maps are contoured at the 3 σ level (noise value) and coloured in green. Only electron density regions above the noise value are drawn. **(C)** Close view of SAMe in the active site of Q113A mutant is displayed. **(D)** The interactions of Gln113 and Ser114 with Met and ADO found in the structure of wtMATα2 (PDB: 5A1I) is demonstrated. Water is shown as a red sphere.

The crystal structure of the P115G mutant shows a full occupancy of SAMe and PPNP in the active site (Fig. 3.4.5A-B) with the closed, well-ordered gating loop. Pro115 is not associated with the substrate or the product interaction as observed in the wild-type structure (Fig. 3.4.5C). This mutation has no effect on the overall arrangement of the gating loop. The identical subunits with the gating loops in their closed conformation are found in this mutant structure, the same as observed in the wild-type structure.

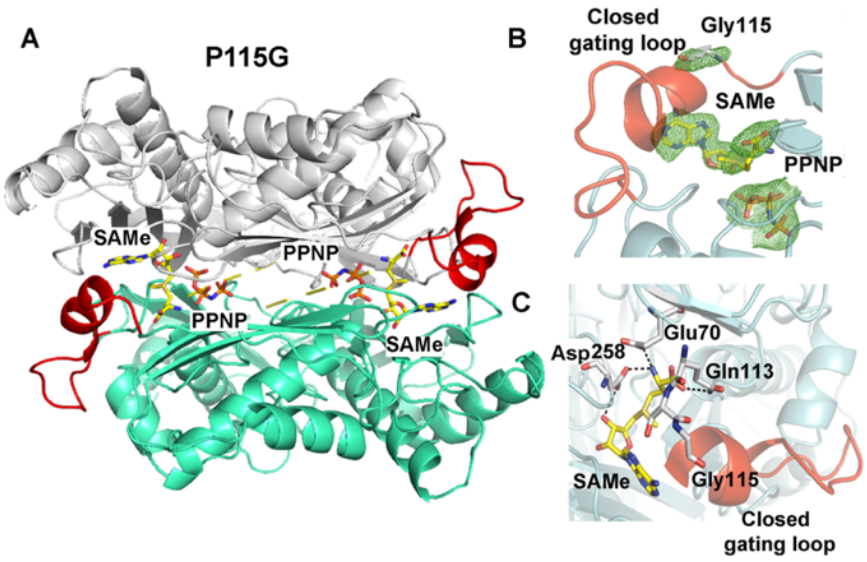

Figure 3.4.5 P115G MATα2 mutant structure (**A**) The I222 crystal form displays the closed conformation of the well-ordered gating loop (red) with SAMe and PPNP in the active site. (**B**) The omit maps of P115G mutation site and products (SAMe, PPNP) are exhibited with the closed gating loop. Fo-Fc omit maps are coloured in green and contoured at the 3 σ level (noise level). Only electron density regions above the noise value are shown. (**C**) Close view of SAMe in the active site of the P115G mutant structure and its interacting residues is displayed.

The wtMATα2 structure in an apo state (PDB: 6FAJ) was crystallised in the $P22_12_1$ crystal form. The active sites of both subunits are empty anchoring with the gating loop in the open conformation. Interestingly, one subunit has the ordered, visible gating loop with the clear

electron density as found in the S114A ($P22_12_1$) structure (Fig. 3.4.6A). The dilation along with the dimer interface is found in one active site because of the gating loop, adjacent loop (residues 245-264) and residues 320-328 being oriented outwardly to the substrate binding cleft, while the other subunit active site shows a disordered open gating loop with less dilated binding cleft (Fig. 3.4.6B). Structural alignment of the wtMATα2 (apo form) with the ligand-bound (holo form) wtMATα2 or the MATα2 (S114A) mutant reveals that apart from the movement in the gating loop region itself, the adjacent loop and residues 320-328 that contribute to substrate/ product binding pocket (Fig 3.4.6A, B) of wtMATα2 (holo form) line inward to the active site pocket. In contrast, the substrate binding clefts of wtMATα2 (apo form) are oriented outwardly from the active site which also found in the S114A structure. This finding suggests the importance of Ser114 interaction to the substrate binding during the rearrangement of the gating loop into its closed conformation. The interaction of the gating loop and the substrates prevent the substrate binding pocket residues from moving apart from the active site, which fails in the S114A mutant. Most residues that are involved in SAMe formation including Ser247, Arg249 have a similar conformation in apo- and holo-wtMATα2, except for Phe250 and Asp258. These two residues move from their original positions in the apo-wtMATα2 as shown in Fig. 3.4.6C. In holo-state of wtMATα2, Ser247 (OG atom), Arg249 (O atom) and Asp258 (OD1 and OD2 atom) interact with the N1 (2.81 Å), N6 (2.90 Å), N (2.76 Å), and O3 atom (2.70 Å) of SAMe, respectively, while Phe250 forms the π-π stacking with the SAMe adenine ring (Fig. 3.4.6C). The position of other residues (His29, Lys181, Lys265, Lys285, Lys289 and Asp291) that were previously reported to be involved in SAMe formation are preserved in both the apo and the holo-wtMATα2 structure. The dilation of the substrate binding pocket found in the $MAT(\alpha2)_4(\beta V2)_2$ complex is identical to the dilated active site found in the present apo-wtMATα2 structure, suggesting that this dilation is not the unique property of the MATαβ complex.

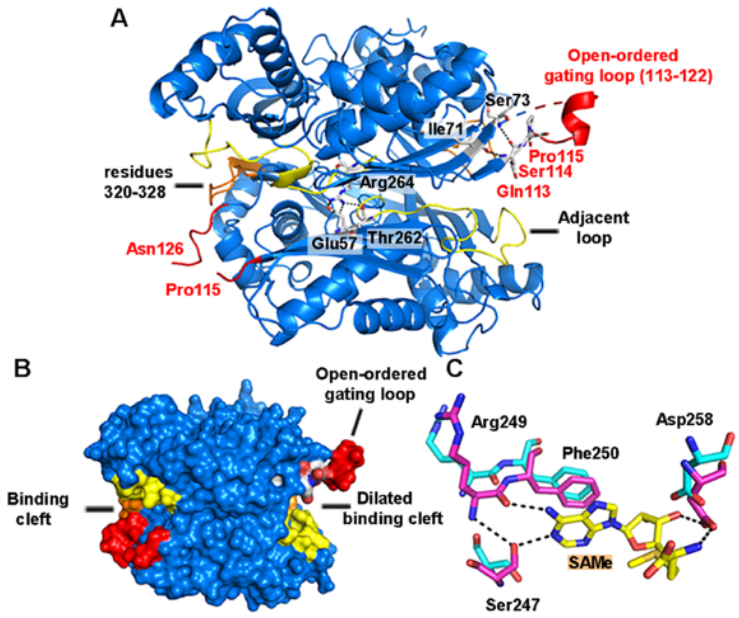

Fig. 3.4.6 The structure of apo wtMATα2 and its conformational changes upon substrate binding (A) The crystal structure of wtMATα2 (blue) shows two subunits with the different gating loop conformations (red ribbons). The substrate/ product binding pocket are shown in yellow (an adjacent loop, residues 245-264) and orange (residues 320-328) loops. The interactions of the key residues Gln113, Ser114, Pro115 and Arg264 are shown with the local surrounding. **(B)** The surface view of substrate binding clefts is shown with the gating loop (red), adjacent loop (245-264, yellow) and residues 320-328 (orange). **(C)** Structural comparison of the holo (pink sticks) and the apo (blue sticks) of the wtMATα2 structure reveals SAMe interacting residues including Ser247, Arg249, Phe250 and Asp258 of their positions in the apo state.

The overall active site conformation of the S114A mutant are similar to the wild type with 0.2 Å differences of residues 250-286 being oriented away from the dimer interface. The apo S114A mutant structure is similar to the apo-wtMATα2 structure which shows the wider open active cleft than that found in the holo-wtMATα2 structure, while in the MATα2β complex this cleft takes intermediate position (between apo and holo state). The less dilated substrate binding pocket of MATα2β is a result of MATβ interaction. The local changes in the complex

suggest that MATβ insertion modulates the tightness of the dimer interface (residues 250-286) that comprising substrate binding pocket for the S114A mutant which could result in different degrees of the activity recovery.

3.5 Conclusion.

The gating loop features different conformations during substrate binding, SAMe formation and product release, suggesting that it facilitates the enzyme reaction. Functional analysis and crystallographic structures are used to investigate the role of the gating loop where the single residue, Ser114, is found to involve with SAMe formation and structural movement of the gating loop. Ser114 coordinates the adenine ring of the substrate ATP via a water molecule and it also stabilises a rigid helix conformation of the closed gating loop. The finding of the visible, ordered gating loop in the open conformation for the first time in human MATs provides an understanding of how this loop undergoes structural changes upon substrate binding and product release as evidenced by the different conformations found in the mutant structures (Q113A and S114A). The gating loop interacts with substrates and drives the rearrangement to its closed conformation. SAMe formation and phosphatase activity are indeed regulated by a different part of the enzyme as no alteration of the PPPi hydrolysis is observed in the mutant that exhibits the loss of SAMe formation. In addition, the ligated structure of human MATα2 reported in this study shows that ADO and PPNP tightly bind to MAT enzyme at the transition state of the enzyme reaction, indicating that these intermediates could be a potential model for designing enzyme inhibitor which competitively binds to the active site. The catalytic reaction of SAMe formation combined with structural movements (e.g. gating loop) at each step is proposed in Fig. 3.4.7.

Table 3.4.3a Crystallographic data collection and refinement statistics for wtMATα2 and its mutants

	Q113A	**P115A**	**wtMATα2 (Apo)**	**wtMATα2 (Holo)**
Data collection				
Space group	$P22_12_1$	I222	$P22_12_1$	I222
Cell dimensions				
a, b, c (Å)	63.63, 103.93, 109.79	66.33, 94.87, 117.37	62.18, 103.23, 108.36	67.63, 94.00, 116.69
α, β, ϒ (Å)	90, 90, 90	90, 90, 90	90, 90, 90	90, 90, 90
Resolution (Å)	103.93-2.70	54.36-2.70	74.74-1.95	73.20-1.35
(last shell) (Å)	(2.83-2.70)	(2.83-2.70)	(2.00-1.95)	1.37-1.35
No. of reflections	20580	8945	51446	80461
Rmerge (%)	14.3 (77.6)	16.2 (56.4)	18.1 (38.7)	8.6 (57.5)
I/ϭI	10.6 (2.1)	5.2 (2.0)	4.7 (2.1)	8.5 (2.1)
Completeness (%)	99.5 (100)	85.0 (89.6)	99.6 (99.8)	98.7 (97.1)
Redundancy	5.6 (5.9)	4.4 (4.3)	3.5 (3.6)	5.0 (4.2)
Wilson B factor ($Å^2$)	44.90	51.10	9.94	11.10
Refinement				
R_{work}/R_{free}**	17.89/ 19.02	19.19/ 23.41	18.96/ 22.39	13.73/ 16.19
No. of atoms				
Protein	5711	2977	5711	3089
Ligand	77	50	31	74
Waters	87	3	302	430
Average B-factors ($Å^2$)				
Protein	47.05	49.89	14.66	12.93
Ligand	54.28	54.83	31.43	24.14
Water	33.85	41.80	20.66	28.16
R.m.s. deviations				
Bond lengths (Å)	0.012	0.012	0.013	0.012
Bond angles (°)	1.552	1.587	1.666	1.690
PDB Code	6FBN	6FCB	6FAJ	6G6R

Table 3.4.3b Crystallographic data collection and refinement statistics for wtMATα2 and its mutants

Mutants	**S114A**	**S114A**
Data collection		
Space group	$P22_12_1$	I222
Cell dimensions		
a, b, c (Å)	62.09, 102.87, 108.17	66.62, 94.68, 116.55
α, β, ϒ (Å)	90, 90, 90	90, 90, 90
Resolution (Å)	54.08-1.65	58.28-1.80
(last shell) (Å)	(1.68-1.65)	(1.84-1.80)
No. of reflections	81704	34507
Rmerge (%)	10.8 (56.6)	17.0 (76.6)
I/σI	8.0 (1.9)	5.80 (2.0)
Completeness (%)	97.2 (98.4)	99.8 (100.0)
Redundancy	5.3 (5.3)	5.3 (5.4)
Wilson B factor ($Å^2$)	14.90	17.10
Refinement		
R_{work}/R_{free}**	16.32/ 19.46	15.10/ 17.44
No. of atoms		
Protein	5902	3005
Ligand	78	79
Waters	499	224
Average B-factors ($Å^2$)		
Protein	21.72	15.30
Ligand	27.77	32.78
Water	27.77	24.81
R.m.s. deviations		
Bond lengths (Å)	0.015	0.014
Bond angles (°)	1.760	1.670
PDB Code	6FBP	6FBO

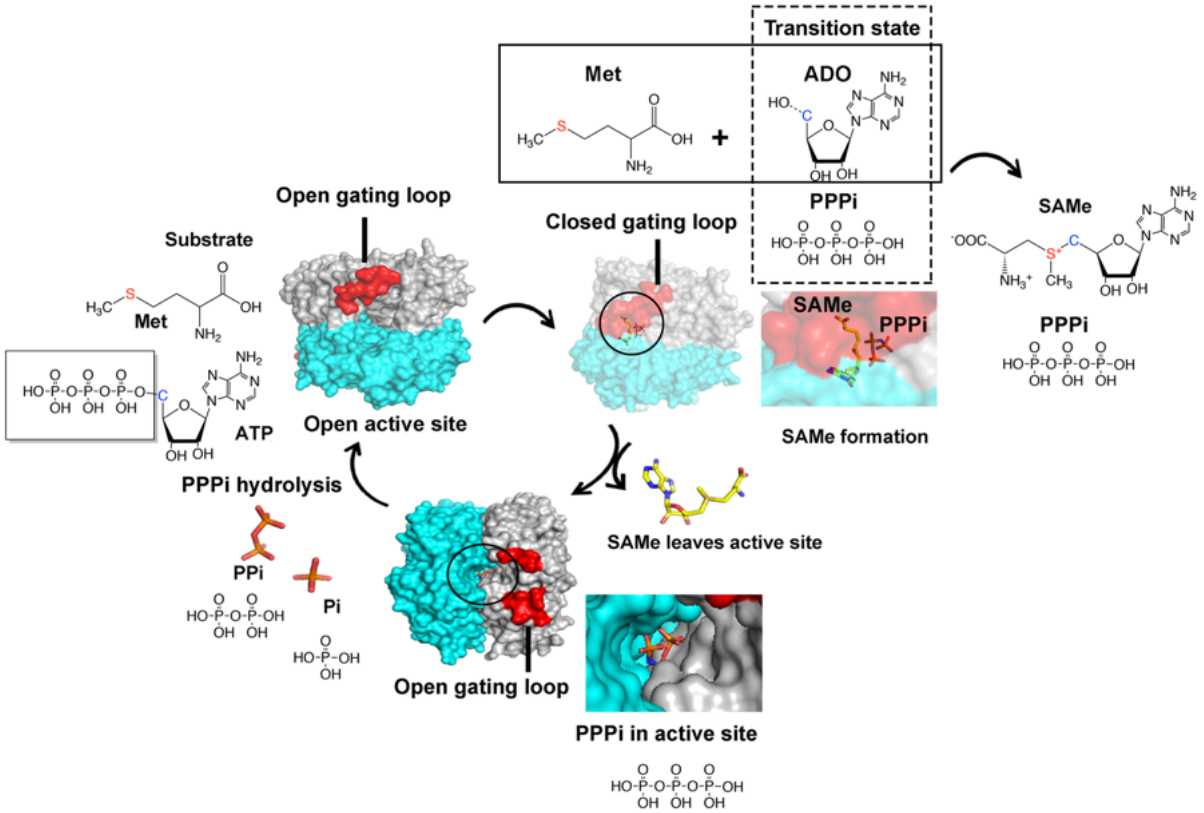

Fig. 3.4.7 The proposed MAT catalytic cycle. The functional active site is formed between the monomer interface (cyan and grey), and the gating loop (red) is located beside the active site of MAT enzymes. The entrance of the active site is accessible when the gating loop is in the open conformation which substrates and products can bind or release from the active site. The first step Met and ATP binds to the active site following by the cleavage of the C-O bond of the ATP and C-S bond formation of ATP and Met to produce SAMe. During enzyme reaction the gating loop is in the closed conformation. At the transition state ADO and tripolyphosphate (PPPi or PPNP) are formed. After the production of SAMe, it exits from the active site before the hydrolysis of tripolyphosphate. The enzyme is ready for the next reaction cycle after Pi and PPi are released from the active site.

Chapter IV

The functional and structural study of a disease related residue Arg264 in hypermethioninemia

4.1 Background and objective

MAT deficiency (OMIM 250850) is characterized by *isolated persistent hypermethioninemia* (IPH). This condition is associated with mutations in the MAT1A gene encoding MATαl (the major hepatic MAT). IPH is detected as an inborn error of methionine metabolism. MAT enzymes are found in almost all living organisms [1]. SAMe formation and its level in cellular tissues is crucial for normal cell functions which are derived from its versatile roles (Fig. 4.1.1) [3-5, 23], while its level is found to be relatively low when Met level is high in patients with IPH [147].

Case reports with MATα1 deficiency were identified through new born screening programmes when the activity of MATα2 in erythrocytes, fibroblasts and lymphocytes was normal [148, 149]. Hepatic MAT deficiency is mostly transmitted by an autosomal recessive inheritance [15, 150-152] or the exceptional Arg264His (R264H) autosomal dominant mutations [152-156]. Neurological problems including demyelination, abnormal mental development and cognitive impairment have been reported in severe cases of autosomal recessive IPH patients, while the majority of patients with mild to moderate condition present no clinical manifestations [15, 150, 157-160]. R264H is the most prevalent mutation associated with IPH observed in new born screening programmes, as previously reported in USA (3 of 13), Spain (15 of 18), Japan (14 of 24), Portugal (all 12 cases) and Taiwan (3 of 16) [153, 155, 156, 161, 162]. Patients with IPH related with R264H mutation is usually clinically benign at the early stage of life [155,

161], however a report of the 3-year-old girl developing demyelination and severe vascular diseases found in some cases associated with R264H mutation suggest that clinical monitoring should be taken [156].

In the central region of the MATα1 and MATα2 dimer, the dimeric subunit interacts through a few polar interactions involving a salt bridge between Arg264 of one subunit and Glu57 of the other (Fig. 4.1.2). These two residues, Arg264 and Glu57, are conserved in both MATα1 and MATα2. Their interactions were reported to be essential for subunit dimerization, facilitating the active site formation [17, 163].

To understand the structure and function relationship of the dominant effect of the R264H mutation in the hepatic MAT enzyme (MATα1), Arg264 was mutated to His264 in MATα1. The oligomeric forms of R264H mutant were characterised in solution and crystal structures. In addition, to investigate the role of Arg264 side chain, Arg264 was mutated to Ala264 in both MATα1 and MATα2. All mutants were generated by site-directed mutagenesis and were confirmed by DNA sequencing (Fig. 4.1.3). Full DNA sequencing results are shown in Table 4.1.

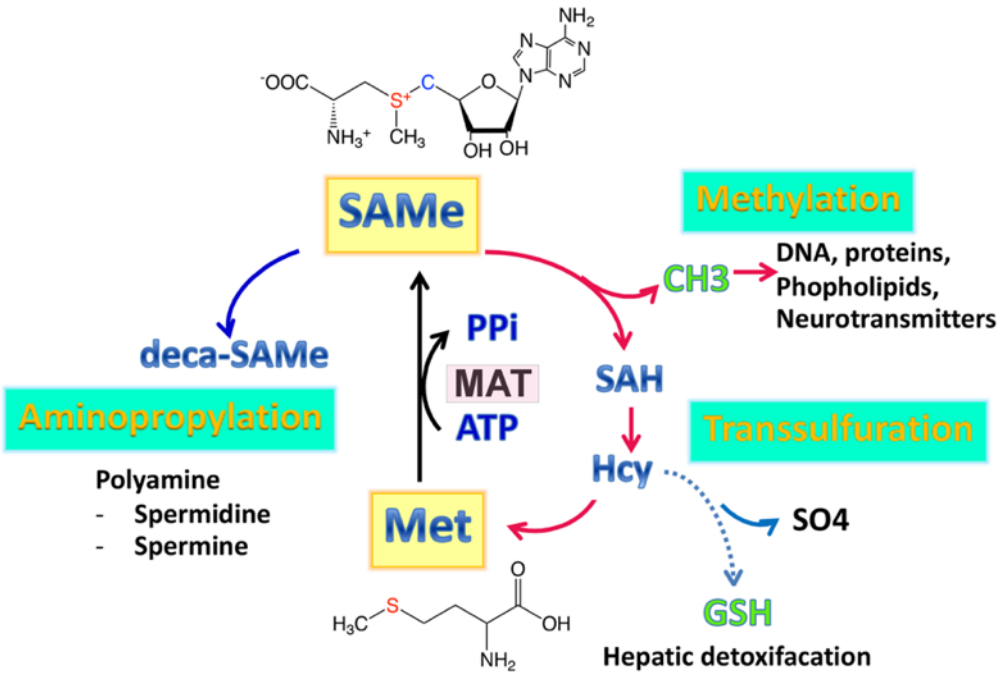

Fig. 4.1.1 Simplified synthesis and metabolic pathways of SAMe. SAMe is synthesized from methionine and ATP by MAT enzymes and can participate three pathways; (i) methylation; (ii) transsulfuration; (iii) aminopropylation. (i) The methyl group of SAMe is transferred to methyl acceptors and SAMe is converted to SAH. SAH is then hydrolysed by SAH hydrolase to adenosine and Hcy. (ii) Hcy has two alternative pathways; Hcy can be methylated to methionine which can re-enter the trans-methylation cycle or it can undergo the trans-sulfuration process for the biological compound synthesis e.g. Cys or GSH (glutathione, a major cellular antioxidant). (iii) SAMe is able to participate the decarboxylation pathway and acts as the propylamine donor for the polyamine biosynthesis. Polyamines are important for many cellular functions including cell growth and differentiation. In this pathway SAMe is catalysed by SAMe decarboxylase for the removal of its carboxyl group. The figure was modified from [164].

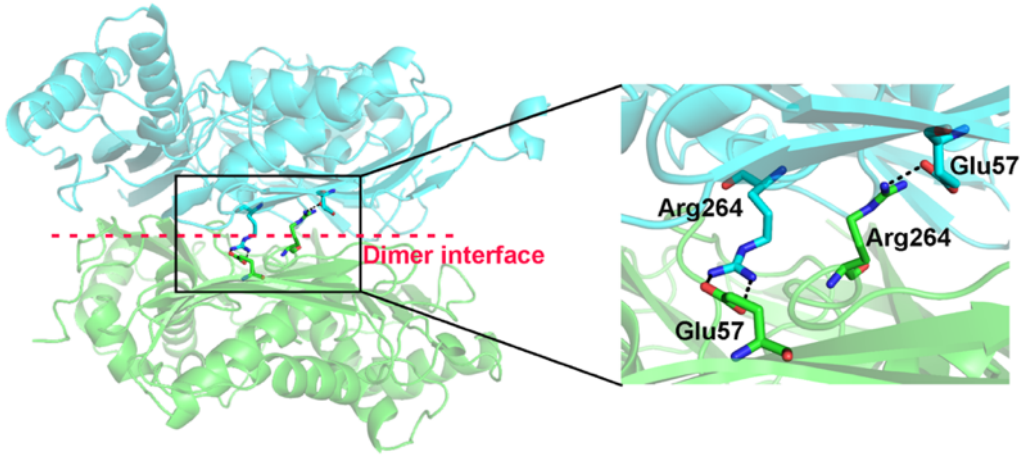

Fig. 4.1.2 Salt bridge interaction of Arg264 and Glu57 at the dimer interface. Arg264 of one subunit interacts with Glu57 of its partner subunit through the H-bonds and electrostatic interactions (ionic boding) aiding the dimer formation. The model was derived from the native state (apo form) of the wild-type MATα2 structure (PDB: 6FAJ).

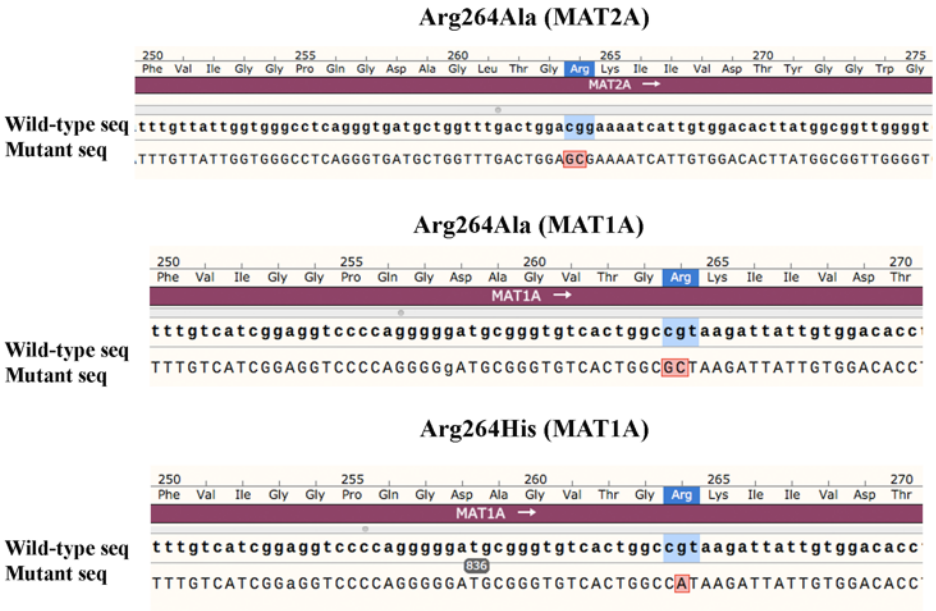

Fig. 4.1.3 DNA sequencing results for Arg264 mutation variants. DNA sequences of MATα2 (Arg264Ala) and MATα1 (Arg264Ala and Arg264His) mutants were aligned to the wild-type DNA using SnapGene. The mutation sites are highlighted in red boxes.

Table 4.1 DNA sequences of Arg264His (MAT1A), Arg264Ala (MAT1A) and Arg264Ala (MAT2A) mutants

Mutants	DNA sequences
Arg264His (MAT1A)	GGAGTCTTCATGTTCACATCGGAGTCTGTGGGAGAGGGACAC CCGGATAAGATCTGTGACCAGATCAGTGATGCAGTGCTGGAT GCCCATCTCAAGCAAGACCCCAATGCCAAGGTGGCCTGTGAG ACAGTGTGCAAGACCGGCATGGTGCTGCTGTGTGGTGAGATC ACCTCAATGGCCATGGTGGACTACCAGCGGGTGGTGAGGGAC ACCATCAAGCACATCGGCTACGATGACTCAGCCAAGGGCTTT GACTTCAAGACTTGCAACGTGCTGGTGGCTTTGGAGCAGCAA TCCCCAGATATTGCCCAGTGCGTCCATCTGGACAGAAATGAG GAGGATGTGGGGGCAGGAGATCAGGGTTTGATGTTCGGCTAT GCCACCGACGAGACAGAGGAGTGCATGCCCCTCACCATCATC CTTGCTCACAAGCTCAACGCCCGGATGGCAGACCTCAGGCGC TCCGGCCTCCTCCCCTGGCTGCGGCCTGACTCTAAGACTCAG GTGACAGTTCAGTACATGCAGGACAATGGCGCAGTCATCCCT GTGCGCATCCACACCATCGTCATCTCTGTGCAGCACAACGAA GACATCACGCTGGAGGAGATGCGCAGGGCCCTGAAGGagCAA GTCATCAGGGCCGTGGTGCCGGCCAAGTACCTGGACGAAGAC ACCGTCTACCACCTGCAGCCCAGTGGGCGGTTTGTCATCGGA GGTCCCCAGGGGGATGCGGGTGTCACTGGCCATAagATTATTG TGGACACCTATGGCGGCTGGGGGgCTCATGgTGGTGGGGCCTT CTCTGggAAGGACTACACCAAGGTGGACCGCTCAGCCGCTTAT GCTGCCCGCTGGGTGGCCAAGTCTCTGGTGAAAGCAgggnTCT GCCggaanGTGCTTGTCcaGgTTTCCTATGCCATTggtgtggccnnanCc GCTGtccATTtCCATCttcaccTacGgaac
Arg264Ala (MAT1A)	GGAGTCTTCATGTTCACATCGgAGTCTGTGGGAGAGGGACAC CCGGATAAGATCTGTGACCAGATCAGTGATGCAGTGCTGGAT GCCCATCTCAAGCAAGACCCCAATGCCAAGGTGGCCTGTGAG ACAGTGTGCAAGACCGGCATGGTGCTGCTGTGTGGTGAGATC ACCTCAATGGCCATGGTGGACTACCAGCGGGTGGTGAGGGAC ACCATCAAGCACATCGGCTACGATGACTCAGCCAAGGGCTTT GACTTCAAGACTTGCAACGTGCTGGTGGCTTTGGAGCAGCAA TCCCCAGATATTGCCCAGTGCGTCCATCTGGACAGAAATGAG GAGGATGTGGGGGCAGGAGATCAGGGTTTGATGTTCGGCTAT GCCACCGACGAGACAGAGGAGTGCATGCCCCTCACCATCATC CTTGCTCACAAGCTCAACGCCCGGATGGCAGACCTCAGGCGC TCCGGCCTCCTCCCCTGGCTGCGGCCTGACTCTAAGACTCAG GTGACAGTTCAGTACATGCAGGACAATGGCGCAGTCATCCCT GTGCGCATCCACACCATCGTCATCTCTGTGCAGCACAACGAA GACATCACGCTGGAGGAgaTGCGCAGGGCCCTGAAGGAGCAA GTCATCAGGGCCGTGGTGCCGGCCAAGTACCTGGACGAAGAC ACCGTCTACCACCTGCAGCCCAGTGGGCGGTTTGTCATCGGA GGTCCCCAGGGGgATGCGGGTGTCACTGGCGCTAAGATTATT GTGGACACCTATGGCGGCTGGGGGGCTCATGGTGGTGGggCC TTCTCTGGGAAGGACTACACCAAGGTGGACCGCTCagCcGCTT ATGCTGCCCGCTGGgTGGCCAAGTCTCTGGTgAanGCAGGGCT CTGCCggaangTGCTTGTCCAGGTTTCCTATGCCATtggnggnGgCC GanccnGCTGtccAtTtnCCATCTtcacctnACGGAanc

Mutants	DNA sequences
Arg264Ala (MAT2A)	CATGAACGGACAGCTCAACGGCTTCCATGAGGCGTTCATCGA GGAGGGCACATTCCTTTTCACCTCAGAGTCGGTCGGGGAAGG CCACCCAGATAAGATTTGTGACCAAATCAGTGATGCTGTCCT TGATGCCCACCTTCAGCAGGATCCTGATGCCAAAGTAGCTTG TGAAACTGTTGCTAAAACTGGAATGATCCTTCTTGCTGGGGA AATTACATCCAGAGCTGCTGTTGACTACCAGAAAGTGGTTCG TGAAGCTGTTAAACACATTGGATATGATGATTCTTCCAAAGG TTTTGACTACAAGACTTGTAACGTGCTGGTAGCCTTGGAGCA ACAGTCACCAGATATTGCTCAAGGTGTTCATCTTGACAGAAA TGAAGAAGACATTGGTGCTGGAGACCAGGGCTTAATGTTTGG CTATGCCACTGATGAAACTGAGGAGTGTATGCCTTTAACCAT TGTCTTGGCACACAAGCTAAATGCCAAACTGGCAGAACTACG CCGTAATGGCACTTTGCCTTGGTTACGCCCTGATTCTAAAACT CAAGTTACTGTGCAGTATATGCAGGATCGAGGTGCTGTGCTT CCCATCAGAGTCCACACAATTGTTATATCTGTTCAGCATGATG AAGAGGTTTGTCTTGATGAAATGAGGGATGCCCTAAAGGAGA AAGTCATCAAAGCAGTTGTGCCTGCGAAATACCTTGATGAGG ATACAATCTACCACCTACAGCCAAGTGGCAGATTTGTTATTG GTGGGCCTCAGGGTGATGCTGGTTTGACTGGAGCGAAAATCA TTGTGGACACTTATGGCG

4.2 Production of MATα2 (R264A) mutant

The mutant was purified by three different columns (nickel affinity, anion-exchange and gel filtration chromatography). Protein purity of the MATα2 (R264A) mutant was assessed by SDS-PAGE (Fig. 4.2.1). The high purity was observed after proteins had been purified by the last step (size-exclusion chromatography). The estimated molecular weight of the MATα2 subunit is about 45 kDa. The precipitation of the protein during a dialysis and a concentrating procedure was removed by centrifugation. The remaining soluble protein aggregates were separated by the gel filtration column and were discarded. Protein yield of the MATα2 (R264A) mutant was about 5 mg/L. This amount was sufficient to produce protein crystals and to perform functional experiments. The purity of the mutant was also enough for producing good quality diffracting crystals.

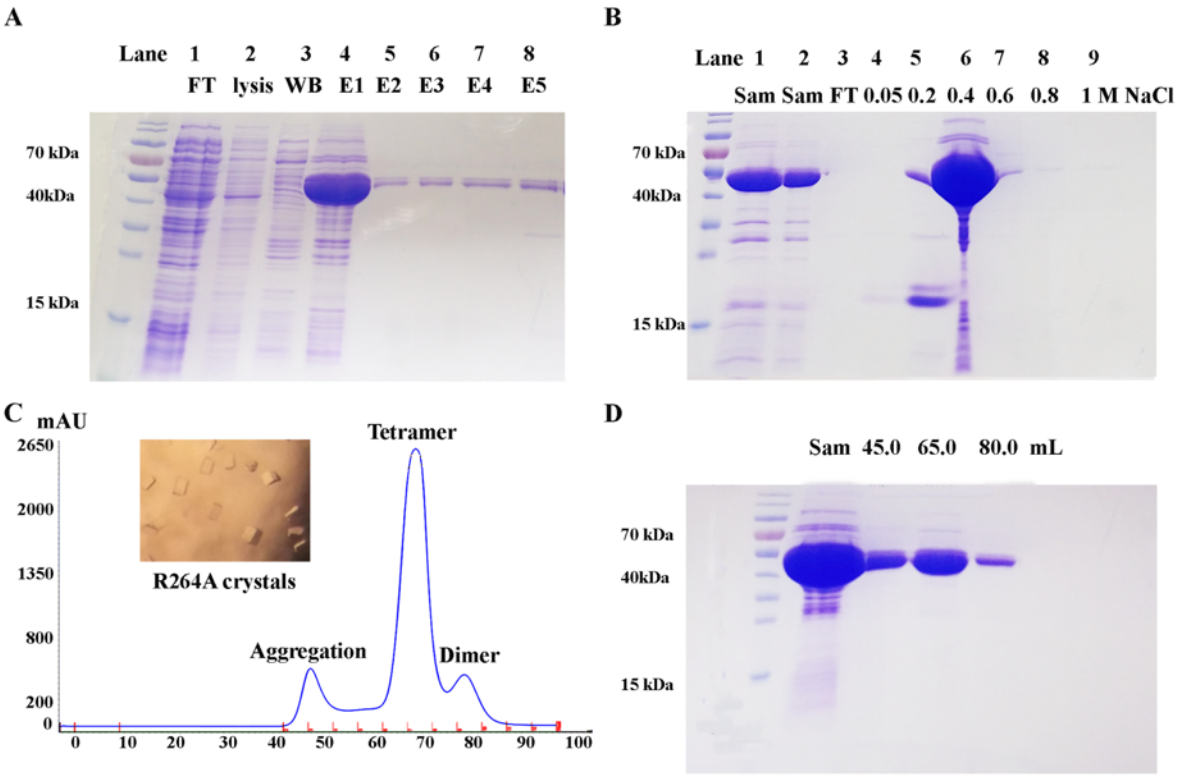

Fig. 4.2.1 MATα2 (R264A) mutant purification. **(A)** SDS-PAGE of the mutant from Ni-affinity purification is shown. **(B)** SDS-PAGE of the protein from anion-exchange purification with 0.05-1 M NaCl gradient is displayed. **(C)** The gel filtration profile is shown by the absorbance at 280 nm. The main peak indicated that the majority of protein was eluted at 62.5-72.5 mL. The crystals were produced from the eluted peak at 62.5-72.5 mL. **(D)** SDS-PAGE of fractions containing MATα2 (R264A) proteins is shown. The eluted fractions containing proteins at 45.0, 65.0 and 80.0 mL were an aggregation, a tetramer and a dimer, respectively. Sam, FT, lysis, WB and E indicate protein sample, flow through, flow through of lysis buffer, wash buffer and elution fraction, respectively.

4.3 Production of MATα1 (wild type, R264A and R264H mutants)

MATα1 was purified in the same manner as MATα2 (section 2.7, chapter 2). SDS-PAGE analysis was performed in each step of purification to check protein purity and production (Fig. 4.3.1-4.3.3). Protein precipitation occurred during the dialysis and the concentrating procedure was removed by centrifugation before proceeding to the next step of purification. The remaining soluble aggregated protein could be separated from the protein samples by size-exclusion chromatography and it was firstly eluted at the void volume of the column. Protein yield of MATα1 and its mutants ranged from 2-4 mg/L. This amount was sufficient for producing protein crystals and performing activity measurements. The purity of all purified proteins was high enough to produce protein crystals. However, MATα1 protein crystals generally gave lower resolution crystals compared to those of the MATα2. The wild-type MATα1 crystal structure was obtained at 2.35 Å, and its mutants (R264H and R264A) were diffracted at 2.85 and 3.1 Å, respectively. In contrast, the MATα2 (R264A) mutant crystal structure was obtained at 1.6 Å.

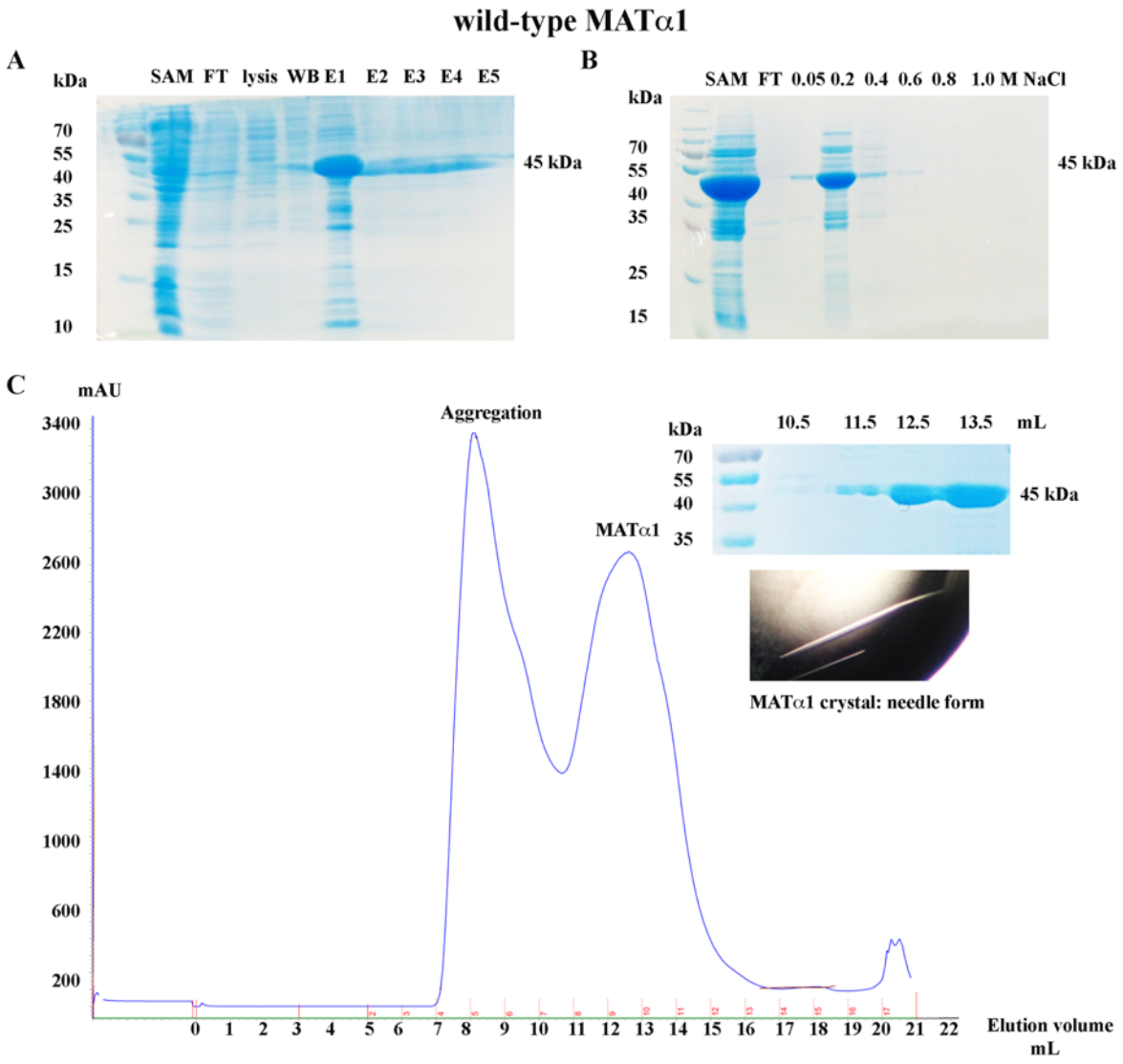

Fig. 4.3.1 wtMATα1 purification (A) SDS-PAGE of the protein from Ni-affinity purification is shown. **(B)** SDS-PAGE of the protein from anion-exchange purification with 0.05-1.0 M NaCl gradient is exhibited. **(C)** The gel filtration profile is shown by the absorbance at 280 nm. The first peak indicated that the majority of protein was aggregated in a soluble form (7.0-10.0 mL). SDS-PAGE of the fractions containing wtMATα1 (no aggregation) was shown at 11.5-13.5 mL. SAM, FT, lysis, WB and E represent protein sample, flow through, flow through of lysis buffer, wash buffer and elution fraction, respectively. The protein crystals of wtMATα1 (needle form) are shown.

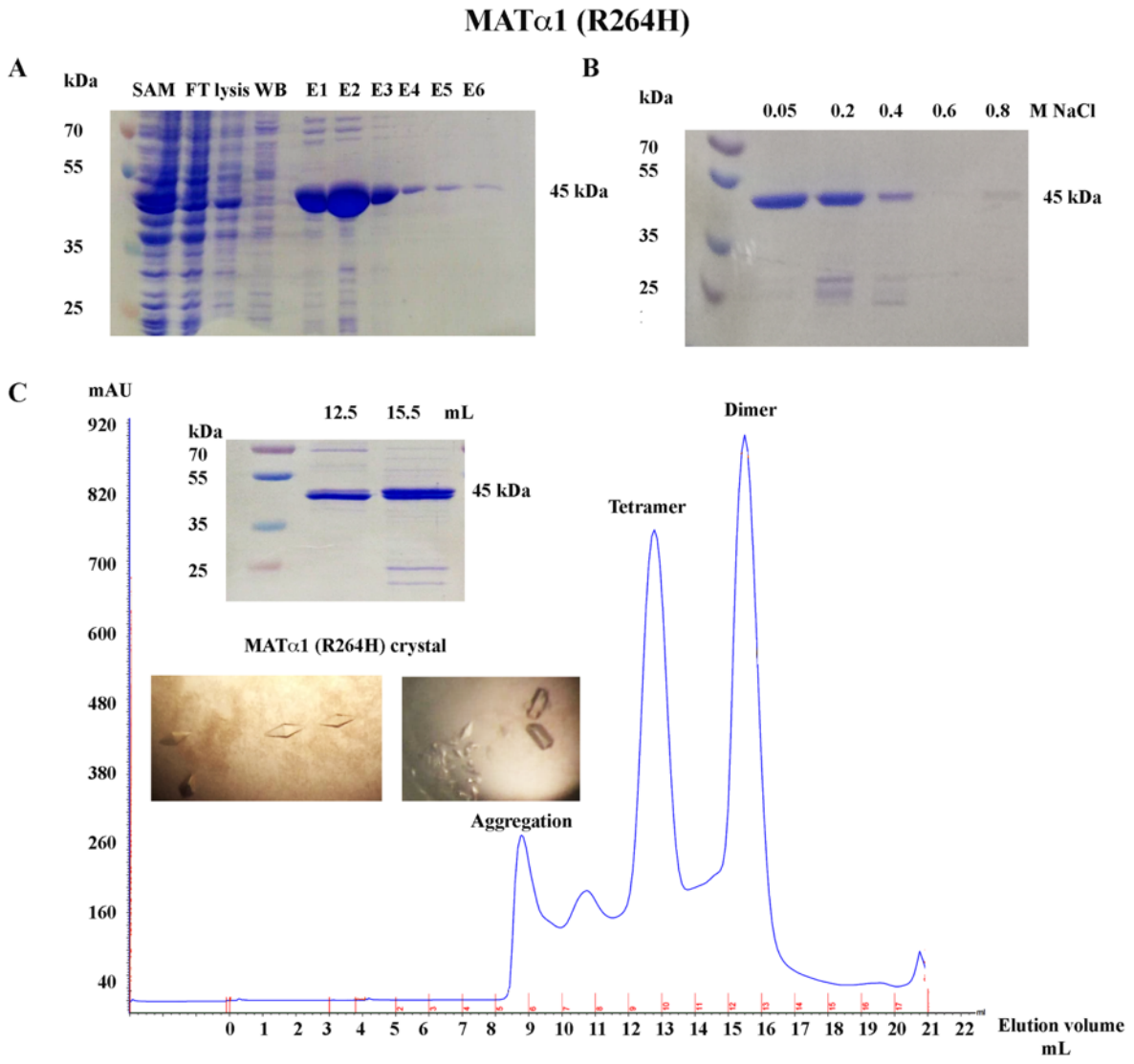

Fig. 4.3.2 MATα1 (R264H) mutant purification. (A) SDS-PAGE shows the proteins from Ni-affinity purification. **(B)** SDS-PAGE of proteins from anion-exchange purification is shown. **(C)** The gel filtration profile (the absorbance at 280 nm) showed that proteins were largely eluted at 12.5 mL and 15.5 mL corresponding to a tetramer and a dimer, respectively. SDS-PAGE of the proteins from the fractions eluted at 12.5 mL and 15.5 mL is shown. Crystals obtained from the tetrameric and the dimeric fractions were displayed. SAM, FT, lysis, WB and E stand for protein sample, flow through, flow through of lysis buffer, wash buffer and elution fraction, respectively.

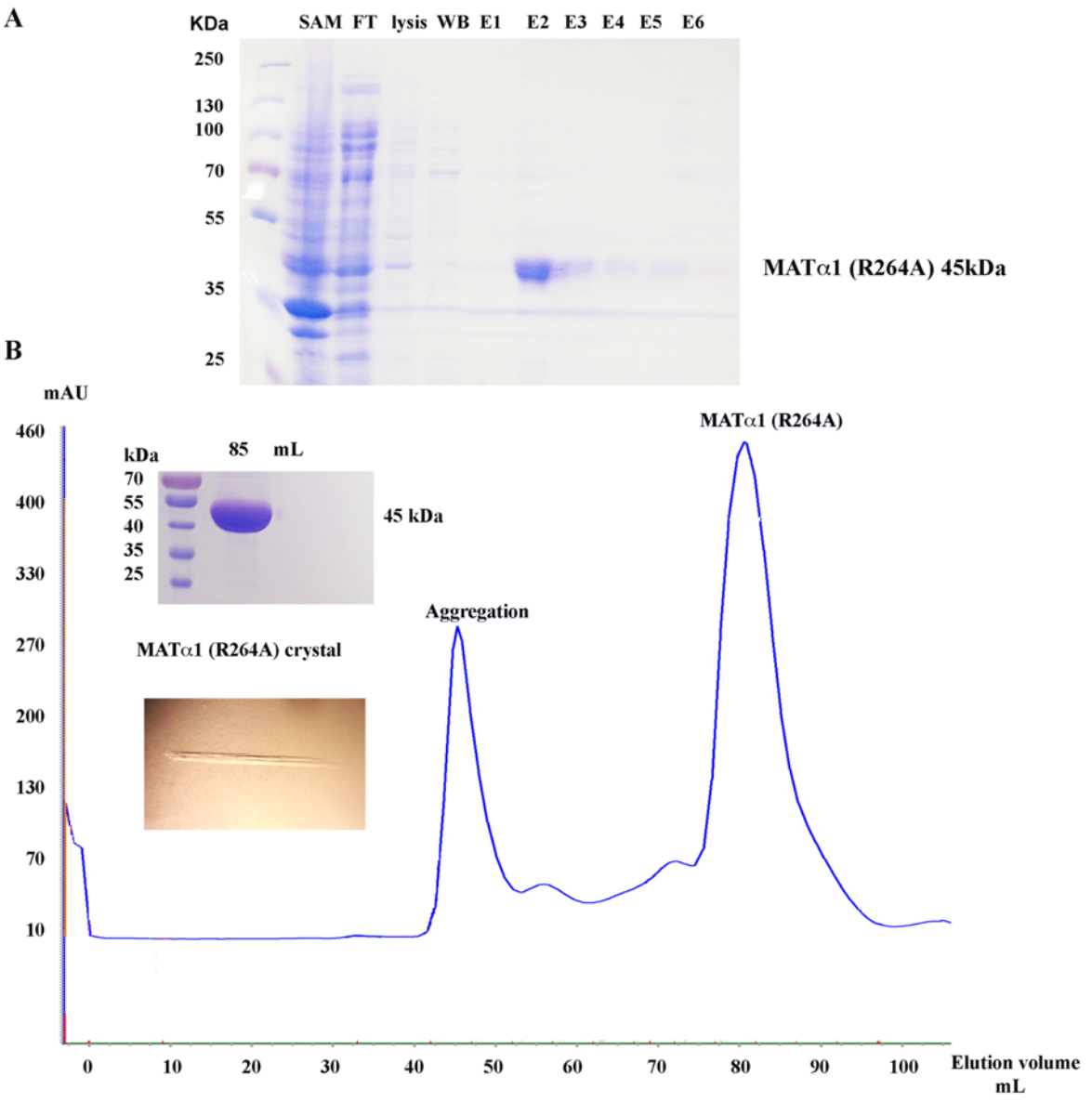

Fig. 4.3.3 MATα1 (R264A) mutant purification. (A) SDS-PAGE of proteins from Ni-affinity purification is shown. **(B)** The gel filtration profile is shown by the absorbance at 280 nm. SDS-PAGE showed the protein bands corresponding to a fraction of 85.0 mL. Crystals were obtained in needle forms. SAM, FT, lysis, WB and E are protein sample, flow through, flow through of lysis buffer, wash buffer and elution fraction, respectively.

4.4 The structural and functional analysis of Arg264 mutation in human MAT enzyme

4.4.1 The SAMe synthetic and phosphatase activity of Arg264 mutants: Arg264Ala (MATα2) and Arg264His (MATα1)

A number of mutations causing IPH were identified in human MATα1 which resulted in lower enzymatic activity and decreased SAMe production, while Met is accumulated in blood plasma. In some cases, patients show developmental delay or neurological problems [165]. Some mutations causing IPH were reported at the dimer interface (e.g. Arg249Trp, Ala259Val and Arg264Cys/His) and these residues are conserved in both catalytic isoforms of MAT enzymes (MATα1 and MATα2). In particular, Arg264 is involved in the salt-bridge formation with the dimeric partner, Glu57. Arg264 mutation to Cys264 or His264 caused a loss of SAMe synthetic activity. The activity reduction was hypothesized to be the result of the inability to form a dimer [163, 166]. The study in the hepatic rMAT showed that the substitution of the homologous Arg265 by His265 (Arg265His) only produced a monomeric species with 0.4 % of SAMe production [166].

The present study of human MAT mutants found that both MATα1 (R264H) and MATα2 (R264A) mutants can form the oligomeric states in solution. Using size-exclusion chromatography (SEC), the MATα1 (R264H) mutant showed two peaks, corresponding to a tetramer and a dimer, respectively, while the wtMATα1 and the MATα2 (R264A) mutant eluted primarily as a tetramer (Fig. 4.4.1A). The equivalent mutants (Arg244Leu and Arg244His) of eMAT were reported to form a tetramer in solution [167]. In addition, both MATα1 (R264H) and MATα2 (R264A) mutants can form the hetero-oligomeric complex with the MATβ subunit as shown by the analytical SEC for MATα2 (R264A): MATβ (Fig 4.4.1B) and the native/ SDS-PAGE analysis (Fig. 4.4.1C). To confirm the oligomeric state of the MATα2 (R264A) mutant in solution, the SEC-SAXS experiment of the purified MATα2

(R264A) was performed. The data exhibit that the dominant species of the MATα2 (R264A) mutant forms a tetramer in solution (Fig. 4.4.1D). The native-PAGE/SDS-PAGE analysis of a dimer and a tetramer of the MATα1 (R264H) mutant is provided in Fig. 4.4.2.

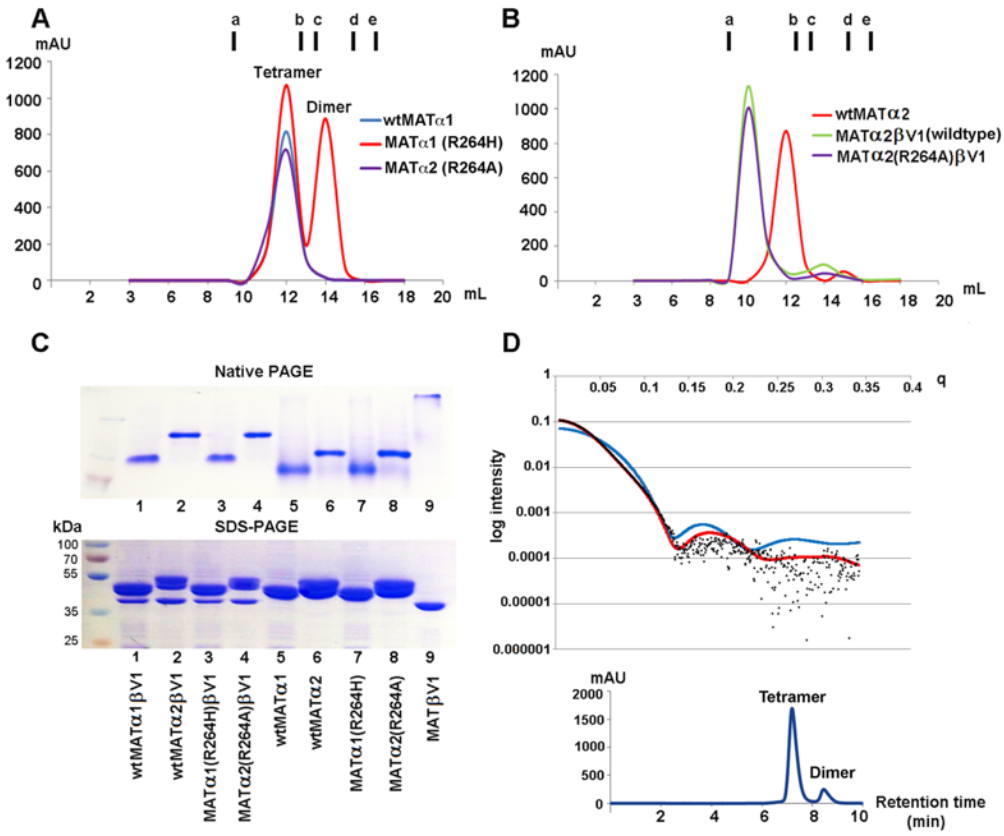

Fig. 4.4.1 The oligomeric state analysis of MATα2 (R264A) and MATα1 (R264H) mutant **(A)** Gel filtration profiles of wtMATα1 compared to MATα1 (R264H) and MATα2 (R264A) mutants. **(B)** Gel filtration profiles of MATα2:MATβV1 (wild type) and MATα2 (R264A):MATβV1 complexes compared to wtMATα2 alone. **(A, B)** a, ferritin (440 kDa); b, aldolase (158 kDa); c, conalbumin (75 kDa); d, ovalbumin (43 kDa); e, ribonuclease (13.7 kDa). **(C)** Native and SDS-PAGE analysis of the complexes (MATα1/2 variants:MATβV1) compared to each protein on its own are shown. **(D)** The SAXS profile (upper panel) was calculated from the crystal structure (model) and was fitted to the obtained scattering data of the MATα2 (R264A) mutant (black dots). The calculated SAXS profile of the tetrameric crystal

model (PDB: 5UGH) is shown by a red line; χ = 1.65, C1 = 1.01, C2 = 3.65, Rg = 36.55, while the dimeric crystal model (PDB: 1QM4) is shown by a blue line; χ = 27.38, C1 = 1.05, C2 = 4.00, Rg = 24.73. The experimental scattering data of the mutant better fit to the tetrameric crystal model. The Chi (χ) value of 1.65 suggests a tetrameric state compared to the χ value of 27.38 of a dimeric form. Retention time of the tetrameric MATα2 (R264A) elution peak that used for the oligomeric state analysis was 7.24 min (lower panel).

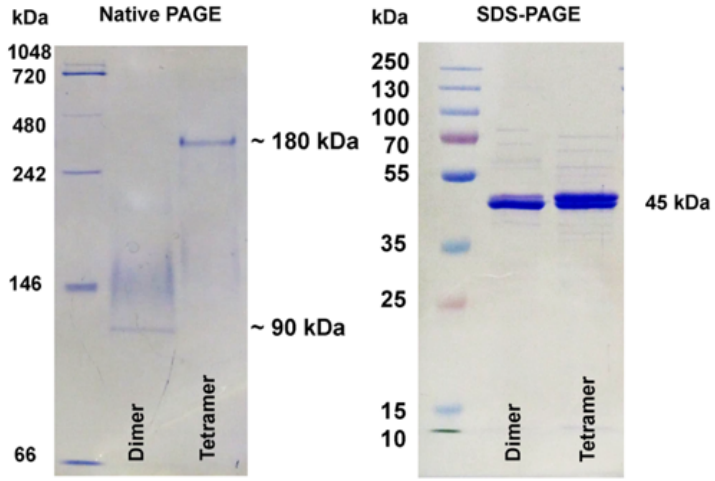

Fig. 4.4.2 Native and SDS-PAGE analysis of the MATα1 (R264H) mutant. The dimer and the tetramer of R264H are shown with the estimated molecular weight. One monomer contains 395 amino acids and the estimated molecular weight is 45 kDa.

MATα1 is the liver specific enzyme and it is found to work as a homotetramer or homodimer, while MATα2 functions as a hetero-oligomer forming complexes with its regulatory subunit MATβV1 or MATβV2 [13]. MATβV1 contains 20 N-terminal amino acids longer than those found in MATβV2, while the remaining amino acids are identical [10]. An *in vitro* study has suggested that MATα1 can also form the hetero-complex with MATβV1, but to a lesser extent with MATβV2 [13]. In the present study, both MATβV1 and MATβV2 are incubated with the MATα1 (R264H) mutant, only MATβV1 was found to form the heterocomplex with R264H mutant (Fig. 4.4.1C).

Although these MATα1 and MATα2 mutants are multimeric in solution, a substantial decrease in SAMe production is found without MATβV1 or MATβV2 subunits. The activity loss caused by Arg264 mutation can be recovered to the wtMATα1/2 levels when the mutants form the hetero oligomer with MATβV1/V2 (Fig. 4.4.3A). However, the regulatory subunits are normally not co-expressed with MATα1 in the healthy adult liver. Additionally, PPPi hydrolysis rates of these mutants are relatively similar to the wild-type enzyme (Fig. 4.4.3B). Arg264 was suggested to be involved with the PPPi C-O bond cleavage of ATP during SAMe formation and also associated with stabilising PPPi orientation in the active site. Arg264 is less related to the subsequent PPPi hydrolysis [167]. Perez Mato I, et al., 2001 also found that the monomer of the Arg265His mutant (rMAT) showed the normal activity of PPPi hydrolysis. The results of the equivalent Arg264 mutation studies carried out in eMAT and rMAT are consistent with the present study showing that the PPPi hydrolytic reaction is less affected by this Arg mutation compared to the SAMe synthetic activity [166, 167].

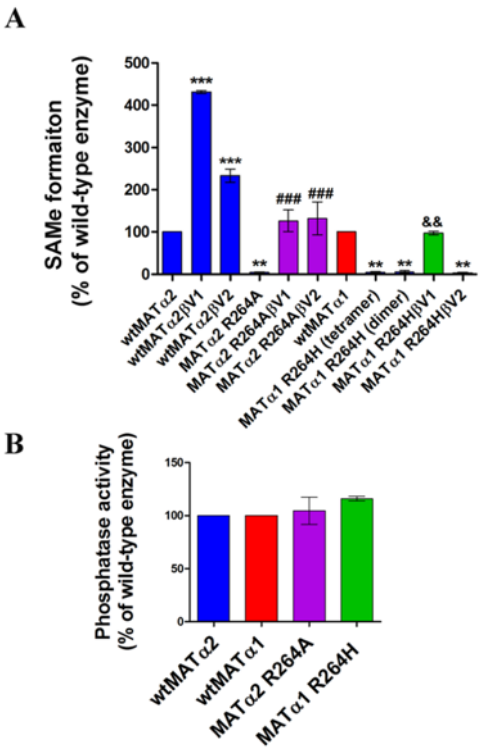

Fig. 4.4.3 SAMe synthetic and phosphatase activity of wild-type and mutant enzymes. (A) SAMe formation of wtMATα1 and MATα2 compared to their mutant enzymes. **(B)** Phosphatase activity of wild-type enzymes and complexes compared to the mutants. '**' and '***' indicate statistical significance at $p < 0.01$ and $p < 0.001$, respectively, when compared with the wild type (MATα1 or MATα2). '###' corresponds to statistical difference at $p < 0.001$ compared to the MATα2 (R264A) mutant. '&&' corresponds to statistical difference at $p < 0.01$ compared to the MATα1 (R264H) mutant. Data are mean of three independent experiments ± SEM (n=3). All experiments were performed using protein samples from the same batch of protein purification (different aliquots).

4.4.2 The structural study of disease related residue Arg264 in hypermethioninemia

Data collection and refinement statistics of wtMATα1 and Arg264 mutants (Arg264His MATα1, Arg264Ala MATα1 and Arg264Ala MATα2: R264H MATα1, R264A MATα1 and R264A MATα2, respectively) are shown in Table 4.4.

4.4.2.1 The crystal structure of the tetrameric wild-type MATα1: an apo form

Numerous MAT structures are available in the protein data bank ranging from archaeal bacteria, *E. coli* to human MAT structures with the ligand or un-liganded form. However, the native form of human MATα1 (apo form) is not yet available. The crystal structure of the tetrameric form of human MATα1 was obtained at 2.3 Å. The crystal was crystallised in the C2 space group containing the cell solvent content of 45.29 %. The asymmetric unit contains two dimers of four subunits (Fig. 4.4.4A). A dimer constitutes two equivalent active sites forming at the dimer interface. Each MATα1 subunit has 395 residues mostly visible in the structure. However, there are two main regions that are typically invisible in electron density maps of MAT enzymes. The first region is the N-terminal Met1-Glu15 which is found to be missing in most reported MAT structures due to its flexibility. The second region is the gating loop region, Asp116-Glu127, which was also found to be flexible in an *E. coli* MAT, a rat liver MAT and a human MATα1/ MATα2 structure. This loop regulates the access to active site by undergoing conformational changes in the open or closed conformation. The previous reported structure of SAMe bound MATα1 showed the closed formation of the gating loop and SAMe binding was partially stabilised by this loop. The gating loop is disordered and invisible in unliganded structure (apo form), and this open conformation allows the active site to be solvent-accessible [43]. These two regions (Met1-Glu15 and Asp116-Glu127) are missing in all subunits (Chain A-D) of the present MATα1 structure. The last absent region is Phe250-Ala259 which contains the methionine binding site and is located at the dimer interface in which active sites reside. This region has been reported to show high flexibility in the rMAT structure [53], while it was clearly seen in the apo structure of the human MATα2 despite the similarity of their sequences to MATα1 [47]. Once a substrate binding to the active site, the gating loop adopts the reorientation to its closed conformation and SAMe binding stabilises Phe250-Ala259 making it visible in the SAMe-bound structures [13, 30, 36, 43]. In addition,

the Asp94-Phe99 region that is usually found in MAT structures is absent in Chain A and Chain D of the current apo MATα1 structure. This region is located at the surface where the two domains of the α-helix (Tyr79-Ile90) and the β-sheet (Lys53-Thr72 and Asn105-Gln112) are connected.

Each subunit of the dimer largely interacts via β-sheets in an inverse contact generating two active sites per dimer at the dimer interface (Fig. 4.4.4B). Only few polar interactions are found at the dimer interface and Arg264 is the most studied residue at the dimer interface of MAT enzymes [17, 150, 152, 163, 167]. Arg264 forms salt bridges with Glu57 of the partner subunit at the dimeric centre (Fig. 4.4.4C). Beyond its role in dimer stabilisation, mutation of this residue to histidine can cause IPH for which less than 30 % of the activity was observed in this mutant [163]. However, the structural study of this mutant has not been available, while prediction of IPH clinical manifestations caused by this mutation are usually variable from genotype to phenotype. In order to address these questions, the crystal structure of R264H mutant of the human hepatic MAT is solved and provides structural understanding of this disease's causing residue (section 4.4.2.2).

Structural comparison of the SAMe-bound structure (PDB: 2OBV) and the present apo structure of MATα1 at the active site residues reveals that an aromatic ring of Phe250 in the apo structure is located in the SAMe binding site, while it forms the π-π stacking with adenine moiety of SAMe in the SAMe-bound structure (Fig 4.4.4D) [43]. In addition, O atom of Ser247, OE1 atom of Glu70 and OD1 atom of Asp258 in the apo structure show to move by 3.9, 6.5 and 3.9 Å, respectively, from their positions in the SAMe-bound structure (Fig 4.4.4D-E). According to the conformational change of the gating loop upon substrate binding and SAMe production, Gln113 which directly bind to SAMe and is also a part of the gating loop shows 8.1 Å movement of its position in the apo structure (Fig 4.4.4E).

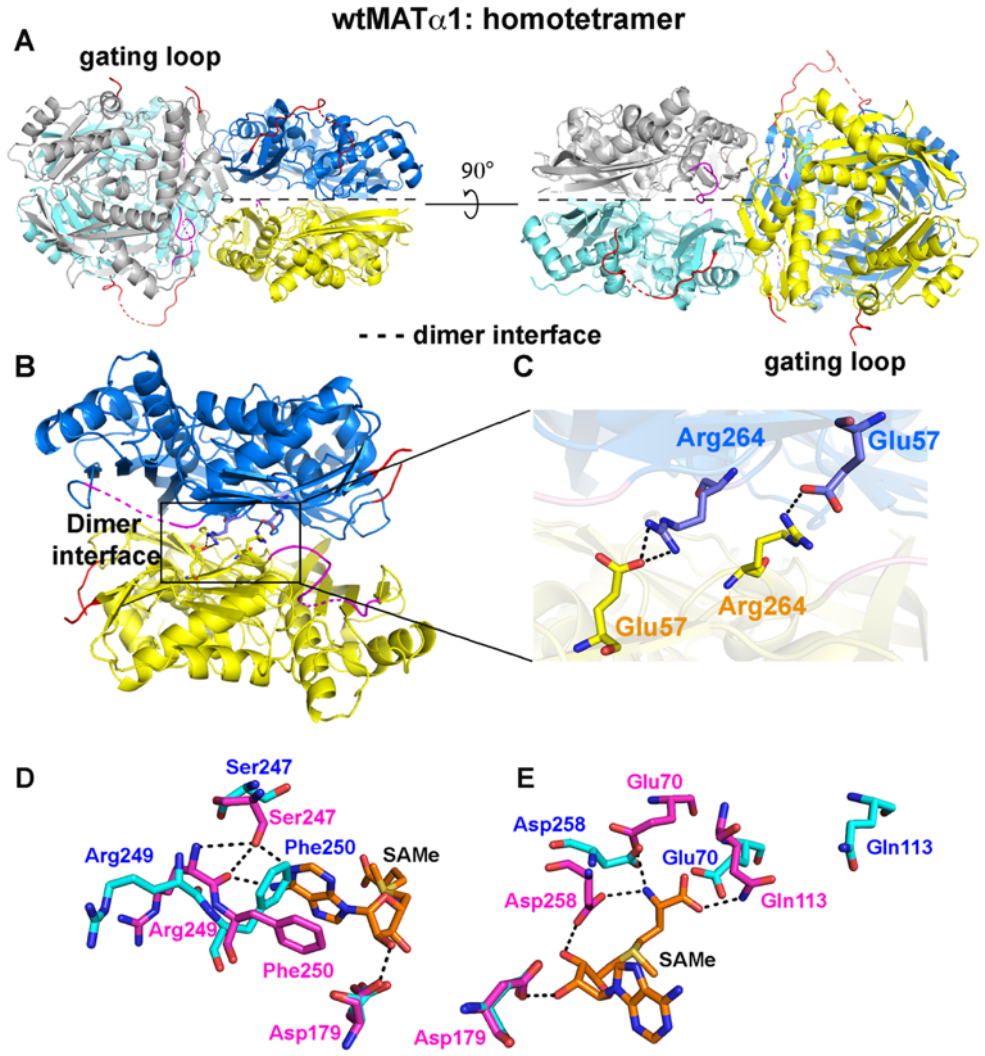

Fig. 4.4.4 The structure of apo wtMATα1. (A) Each subunit of a tetrameric wtMATα1 tetramer is shown in grey, cyan, yellow and blue. The tetramer is composed by the self-assembly of two dimers (4 subunits of wtMATα1). **(B)** One dimer is shown in blue and yellow. The gating loop and residues 250-259 are shown in red and pink, respectively. A central part of the dimer interface is shown in a black square. **(C)** Arg264 and Glu57 of each partner subunit forms a salt bridge and stabilise the dimer formation. **(D, E)** The active site residues that interact with SAMe of the apo structure (current study) and the SAMe-bound structure (PDB: 2OBV) are shown in blue and pink sticks, respectively. H-bonds are represented by black dots.

Table 4.4 Data collection and refinement statistics for wtMATα1, R264H MATα1, R264A MATα1 and R264A MATα2 structure

Data collection	wtMATα1	R264H MATα1	R264A MATα1	R264A MATα2
Wavelength (Å)	0.9795	0.97624	0.9785	0.9785
Space group	C2	C2	C2	I222
a, *b*, *c* (Å)	218.68, 61, 119.76	108.56, 83.62, 87.56	217.82, 61.38, 119.51	67.14, 94.23, 116.82
α, β, γ (Å)	90.00, 90.55, 90.00	90.00, 107.99, 90.00	90.00, 90.47, 90.00	90.00, 90.00, 90.00
Resolution (Å)	58.76-2.35 (2.41-2.35)	51.62-2.85 (3.00-2.85)	46.87-3.10 (3.29-3.10)	58.41-1.70 (1.73-1.70)
No. of reflections	66266	17484	27923	40576
R_{merge} (%)	10.8 (50.2)	17.7 (85.8)	16.1 (71.9)	12.4 (51.3)
$I/\sigma(I)$	6.4 (1.9)	5.1 (1.5)	5.6 (1.5)	5.9 (1.9)
CC (1/2)	0.991(0.762)	0.974 (0.755)	0.977 (0.618)	0.985 (0.619)
Completeness (%)	100.0 (99.9)	99.3 (97.9)	97.2 (96.1)	98.7 (99.8)
Redundancy	3.4 (3.4)	5.1 (5.2)	2.8 (2.6)	4.3 (4.1)
Wilson B factor (Å)^2	29.3	55.5	53.8	12.4
Refinement				
R_{work} / R_{free}	18.38/ 23.73	24.10/ 29.38	21.64/ 25.89	16.00/ 18.42
No. atoms				
Protein	11211	5683	11242	2963
Ligand/ion	62	-	-	66
Water	408	3	5	284
Average B-factor (Å)^2				
Protein	36.88	58.95	60.97	15.3
Ligand	46.76	-	-	21.77
Water	31.92	50.34	19.78	29.36
Ramachandran statistics				
Residues in preferred regions	1395	709	1375	372
Residues in allowed regions	29	21	56	6
Outlier	11	5	12	0
R.m.s deviations				
Bond lengths (Å)	0.014	0.010	0.011	0.015
Bond angles (°)	1.638	1.363	1.638	1.695
PDB Code	6SW5	6SW6		6FCD

4.4.2.2 The crystal structure of the dimeric R264H: an apo form

The crystal structure of MATα1 (R264H) mutant was solved at 2.85 Å. The crystal belongs to the C2 space group containing the cell solvent content of 42.2 %. The asymmetric unit containing a dimer of 2 subunits (Chain A-B). R264H mutation sites are shown in the Fo-Fc omit map (Fig. 4.4.5A). Three regions are invisible in this mutant structure including an N-terminus (Met1-Glu15), gating loop (Asp116-Glu127) and Phe250-Gly257 region. Only Chain B that contains all of these three invisible regions, while Chain A shows electron density maps of the gating loop and the Phe250-Gly257 region.

The R265H mutant (corresponding to Arg264 in human) of rMAT and human MATα1 (R264H) were reported to fail in dimerization [163, 166], whereas the analogous eMAT R244H mutant remained as a tetramer [167]. The crystal structure of MATα1 (R264H) mutant shows a huge difference of the dimeric interface orientation due to Arg264 substitution by His264. His264 forms stronger H-bonds with Glu57 (2.7 and 2.9 Å) than those found in the wild type (Arg264) due to the shorter side chain of histidine rendering the displacement of the residues that are located at the dimer interface (Fig. 4.4.5B). At the mutation site, the distance between His264 of each subunit is 7.38 Å, about 2.06 Å difference to the wild type (Fig. 4.4.6A). Residues that line the dimer interface are found to be displaced along this mutation site causing difference in the dimerization forces (Fig. 4.4.6A-B). The upper part of the interface (Thr262-Gly263) that neighbours the mutation site (Arg264His) becomes generally tighter along the dimer interface, while the mutation site itself loosens up. Distance displacement caused by R264H mutation compared to wtMATα1 is shown in Table 4.5.

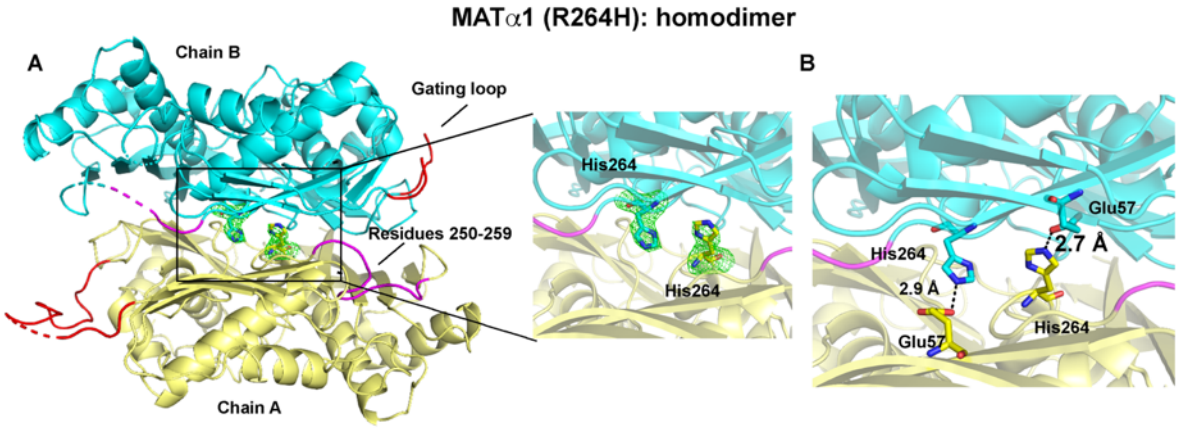

Fig. 4.4.5 The structure of apo MATα1 (R264H) mutant. (A) Each subunit of the mutant's dimer is shown in yellow and blue ribbons. The dimer is composed by self-assembly of the MATα1 (R264H) monomer (chain A and chain B). The Arg264His mutation site is shown in the Fo-Fc omit map contoured at the 3 σ level (green). The gating loop and residues 250-259 are shown in red and pink, respectively. **(B)** His264 and Glu57 of each subunit forms H-bonds at 2.7 and 2.9 Å stabilising dimer formation.

Table 4.5 Cα to Cα measurements of the residues (Val262-Ile267) along the mutation site of each subunit in comparison to wild type.

Residue	Cα-Cα (Wild Type, Å)	Cα-Cα (R264H, Å)
Thr262	12.01	10.23
Gly263	10.14	7.75
Arg264/ His264	5.47	7.53
Lys265	11.37	12.73
Ile266	9.22	9.63
Ile267	10.58	10.88

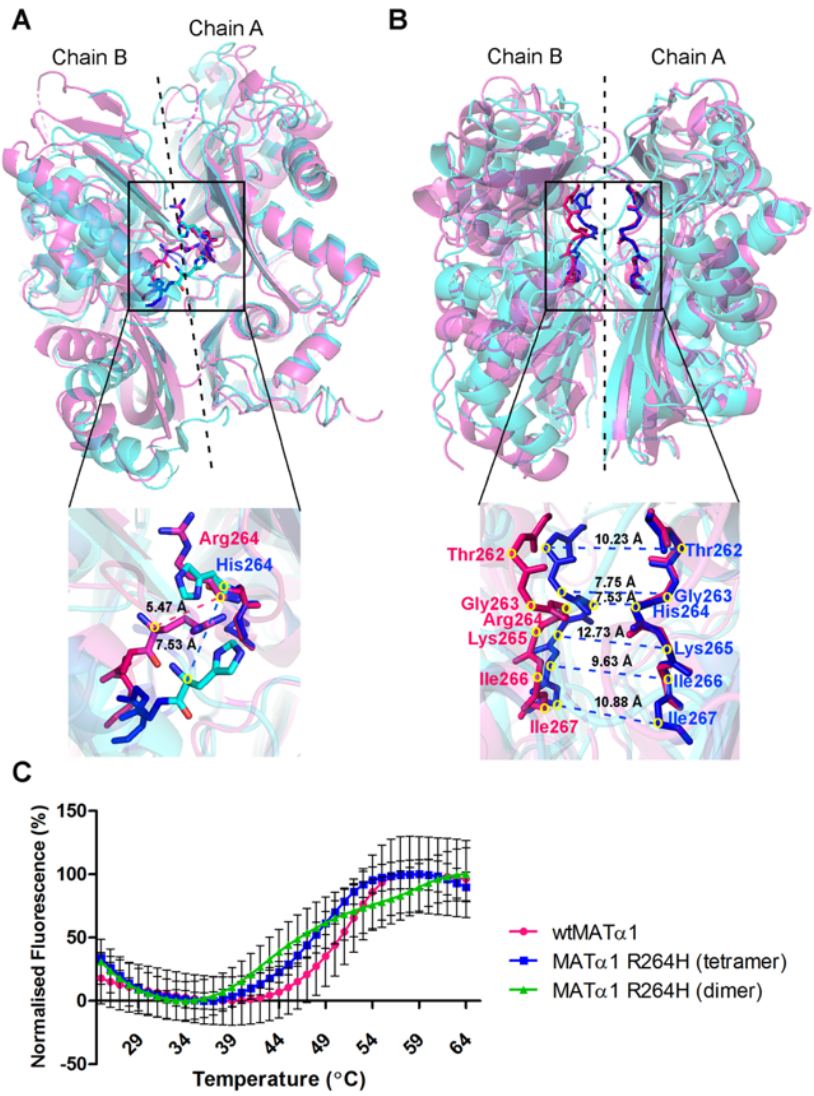

Fig. 4.4.6 The structural comparison of the wtMATα1 and MATα1 (R264H) mutant. The wtMATα1 and the MATα1 (R264H) mutant are shown in pink and blue ribbons, respectively with alignment of chain A to chain A of each protein. **(A)** The dimer interface is represented by dash line and a Cα to Cα distance at Arg264 and the mutation site (His264) are illustrated. Cα atoms are marked by yellow circles. **(B)** The distance displacement causing by R264H mutation is shown by Cα to Cα measurements of these residues (Val261-Ile267) of each subunit compared to the wild type. Thr262-Ile266 main chains are shown in dark pink (wild type) and blue (R264H) sticks. Cα atoms are marked by yellow circles. **(C)** Normalised fluorescence curves used for Tm determination of the wild type and the mutant are shown.

The MATα1 (R264H) mutant is statistically less stable than the wild-type enzyme, its Tm being 47.50 ± 0.15 ($p < 0.001$), 47.27 ± 0.37 °C ($p < 0.001$) of a tetramer and a dimer, respectively, compared to 50.30 ± 0.10 °C of the wild type (Fig. 4.4.6C). The crystal structure of R264H mutant in an apo form was obtained, although R264H proteins were mixed with their substrates (Met and AMP-PNP) before crystallisation. The loss of enzymatic activity caused by this mutation may thus originate from its inability to bind the substrates in the first place which may arise from the change in position of residues at dimer interface. This results in the lower affinity for a tetrameric assembly and greater propensity of a dimeric assembly.

4.4.2.3 Dimer-dimer interface: the structural comparison of the apo form of the wtMATα1 (tetramer) and the R264H mutant (dimer)

The subunit interactions in the dimer may play a crucial role in contribution of forming the tetramer as described in Fig. 4.4.7A-C. The tetrameric form of wtMATα1 structure reveals a dimer to a dimer contact surface which consists of only few polar interactions including Thr62 (chain A, B) to Asn105 (Chain C, D) and Arg84 (chain A, B) to Glu111 (Chain C, D) (Fig. 4.4.7B). Also, no disulphide bond is observed in both dimer and tetramer subunit interactions. The R264H mutation causes residues at the dimer interface to be displaced from their original position in the wild type. Accordingly, overall protein architectures are changed, despite that the secondary structures are preserved. As a consequence of mutation effect, Thr62 and Arg84 which participate in dimer to dimer contact are relocated 8.6 and 9.8 Å compared to the wild-type structure (Fig. 4.4.7C), resulting in the instability of forming the tetramer.

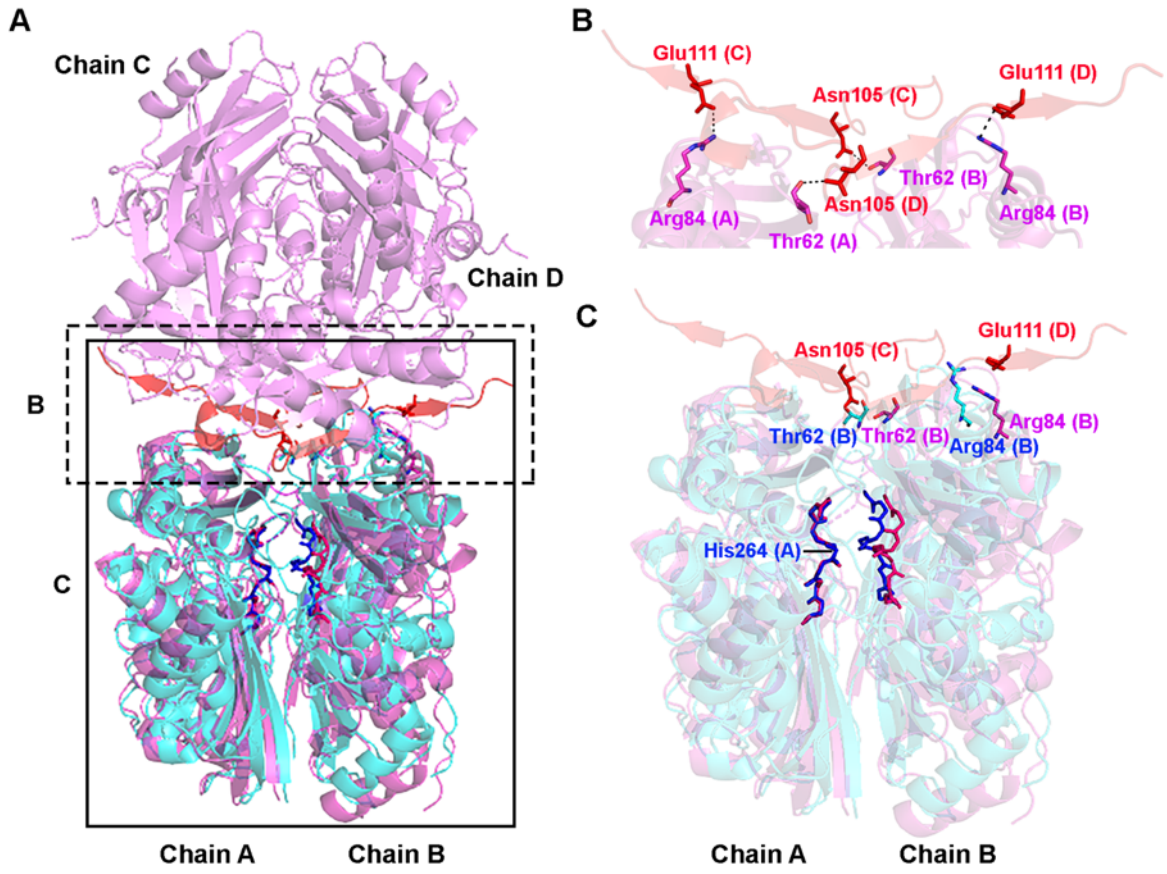

Fig. 4.4.7 The structural comparison of wtMATα1 and MATα1 (R264H) mutant. (A) The wtMATα1 and MATα1 (R264H) mutant are shown in pink and blue ribbons, respectively with alignment of chain A to chain A of each protein. The dimer to dimer interface of wtMATα1 is shown in red color (chain C and chain D). **(B)** The polar interactions at dimer to dimer interfaces found in the wild type are illustrated at chain A to chain C and chain B to chain D. The residues of chain A and B are shown in pink sticks, while the residues of chain C and D are shown in red sticks. **(C)** The wtMATα1 and MATα1 (R264H) mutant are shown in pink and blue, respectively with alignment of chain A to chain A of each protein. The distance displacement of Thr62 and Arg84 caused by the R264H mutation is shown compared to the wild type. Thr62 and Arg84 are presented by pink and red sticks for the wild type and blue sticks for the R264H mutant. Thr262-Ile266 main chains are shown in dark pink (wild type) and blue sticks (R264H) to mark the mutation regions.

4.4.2.4 The crystal structure of the tetrameric MATα1 (R264A) mutant: an apo form

The crystal structure of the MATα1 (R264A) mutant was solved at 3.1 Å. The crystal was crystallised in the C2 space group containing the cell solvent content of 45.29 %. The asymmetric unit shows two dimers (Chain A-D), the same as found in the wild-type structure (Fig. 4.4.8A). R264A mutation sites are shown in Fo-Fc omit maps confirming positive peaks for alanine in the model (Fig. 4.4.8B). Three regions are invisible in this mutant structure including the N-terminus (Met1-Glu15), gating loop (Asp116-Glu127) and substrate binding region (Phe250-Asp258) indicating their flexibility. At the mutation site, the distance between Ala264 of each subunit is 6.80 Å (Fig. 4.4.8B), while R264H mutant showed 7.53 Å compared to wtMATα1 (5.47 Å). In contrast to R264H MATα1, there is no prominent displacement in positions of the residues that line the dimeric interface along this mutation site when compared to the wild-type structure (Fig. 4.4.8C). Only a small difference is observed by structural alignment of the wtMATα1 and the R264A mutant, RMSD of 0.340 Å.

As relatively lower resolution was usually obtained from the MATα1 mutant crystal, the R264H and R264A mutant structures were solved at 2.85 Å and 3.1 Å, respectively. In addition, the mutation of Arg264 to His264 in MATα1 caused a substantial change at the dimeric interface which could lead to an inability to bind the substrates of the mutant. MATα2 has sequence similarity of 84 % to MATα1 and Arg264 is conserved among these two proteins. The equivalent mutation in MATα2 (Arg264Ala: R264A) was designed in order to produce the substrate-bound crystal form, allowing to understand the functional role of Arg264's side chain in the active site. Therefore, the MATα2 (R264A) mutant was generated and characterised both structurally and functionally (see below, section 4.4.2.5).

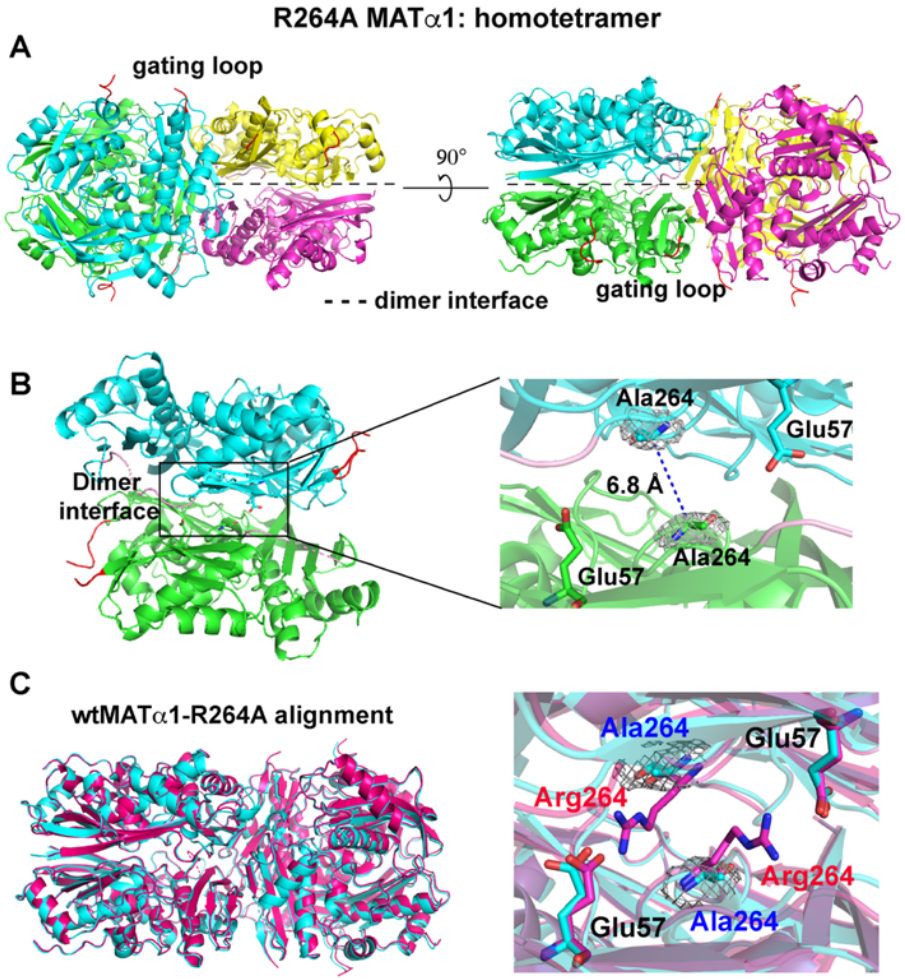

Fig. 4.4.8 The structure of apo R264A MATα1 mutant. (A) Each subunit (chain A-D) of R264A MATα1 tetramer is shown in blue, green, yellow and pink ribbons. The tetramer is composed by self-assembly of two dimers. **(B)** A dimer is shown in blue and green robbons. The gating loop and residues 250-259 are shown in red and pink, respectively. The Arg264Ala mutation site is shown in the Fo-Fc omit map contoured at the 3 σ level (grey colour). The substitution of Arg264 to Ala264 changes the Cα to Cα distance between this residue of each subunit to 6.80 Å (wild type: 5.47 Å). **(C)** The wtMATα1 and the MATα1 (R264A) mutant are shown in pink and blue, respectively, with the structural alignment of chain A to chain A of each protein (left panel). The structural comparison of the wtMATα1 and the MATα1 (R264A) mutant is shown at the dimer interface (right panel).

4.4.2.5 The crystal structure of the MATα2 (R264A) mutant: a holo form

The R264A MATα1 and R264H MATα1 crystals diffracted at the resolution of 3.1 Å and 2.85 Å, respectively. Only apo form is obtained when the R264H MATα1 protein was co-crystallised with methionine and ATP analogue. It is likely that substitution of Arg to His causes a huge change to the orientation of the enzyme's dimeric interface that also affects diffraction-quality, therefore Arg264Ala (R264A) mutant in MATα2 was used as the model to study the functional role of Arg264 in MAT active sites. The crystal structure of MATα2 (R264A) mutant was obtained at 1.7 Å and it was in complex with an enzyme intermediate. Arg264 side chain is involved in tripolyphosphate interaction during enzyme reaction, while the dimer interface of the R264A mutant and the wild-type MATα2 is in similar orientation and no significant movement has been observed. In contrast, the R264H crystal structure of MATα1 shows a huge difference of the dimeric interface orientation at the central part where His264 was substituted to Arg264 (Fig. 4.4.5B), resulting in the disordered active site.

R264A MATα2 protein was co-crystallised with Met and AMP-PNP and its structure contains enzyme intermediates that are well-defined in the active sites. The crystal structure of R264A MATα2 does not contain SAMe in the active site, but the full occupancy of ADO and Pyrophosphate (PPi) is observed (Fig. 4.4.9A-B). In the wild type, Arg264 stabilises the Pγ of the tripolyphosphate (PPPi or PPNP) via its NH2 and NE atoms (Fig. 4.4.9C). Therefore, the Pγ of PPNP is invisible in the R264A mutant structure, suggesting the important role of Arg264 in stabilising the PPPi conformation for ATP cleavage. The loss of the Arg264-Glu57 salt bridges of the mutant results in a decrease of thermal stability of the enzyme. The Tm of the R264A mutant is significantly decreased to 42.50 ± 0.06 ºC ($p<0.001$), compared to 47.10 ± 0.10 ºC of the wtMATα2. The normalised fluorescence curves used to determine the Tm of each protein are shown in Fig. 4.4.9D.

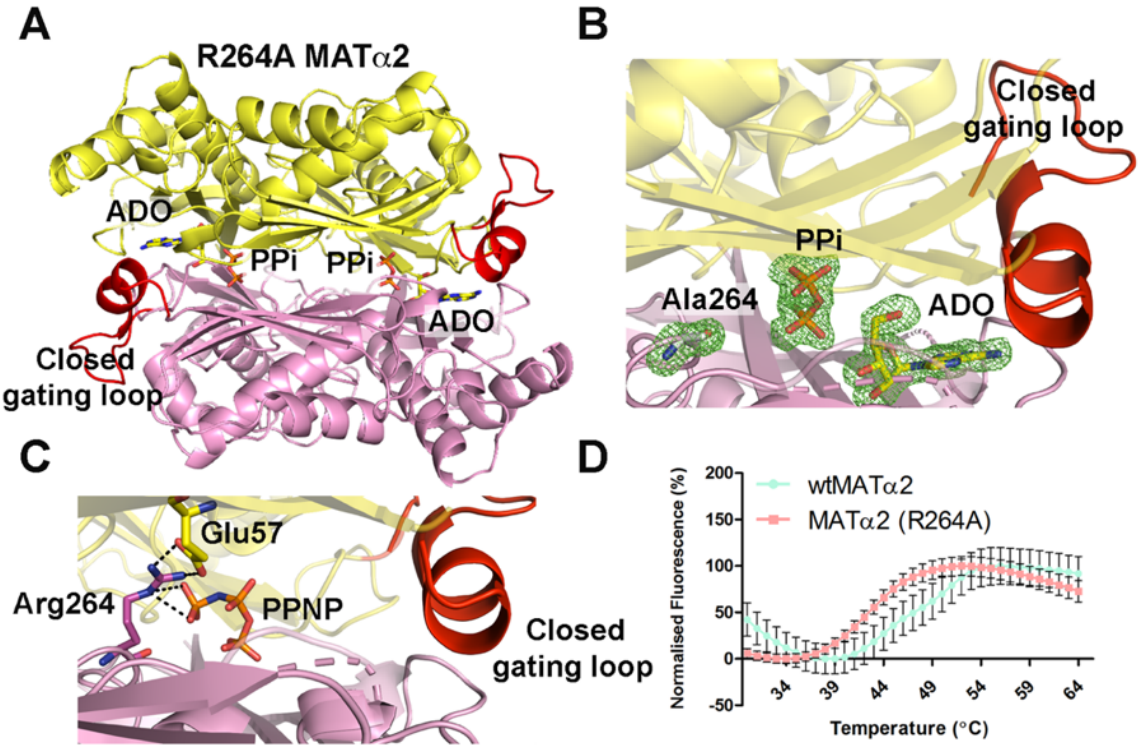

Fig. 4.4.9 The structural comparison of the R264A MATα2 mutant and the wild-type structure. **(A)** The crystal structure of R264A MATα2 is shown with fully symmetrical crystallographic dimer (yellow and pink) with the closed gating loop (red). **(B)** The active site of the R264A mutant is shown with the omit map contoured around Ala264 and enzyme intermediates (ADO and PPi). The Fo-Fc omit map is contoured at the 3 σ level (green). **(C)** Arg264 forms a salt bridge with its dimeric Glu57. Arg264 interacts with PPNP at O2G and O3G atoms via its NE and NH2 atom. The figure is derived from the wtMATα2 structure (PDB: 5A1I). H-bonds are represented by black dots. **(D)** Normalised fluorescence curves used for Tm determination of each protein are shown.

4.5 The conservation sequence analysis and insight from structural analysis of MAT enzymes

The multiple sequence alignment of MAT homologous proteins in all living organisms have been performed using 2,963 amino acid sequences (Fig. 4.5.1). The residues involve in SAMe formation including 5 acidic (Asp31, Glu57, Glu70, Asp258 and Asp291), 6 basic (His29, Lys181, Arg264, Lys265, Lys285 and Lys289) and 1 neutral amino acid (Gln113) (Fig. 4.5.2A). These catalytic residues are highly conserved through organisms (Fig. 4.5.1). Three of these catalytic residues including Asp258, Arg264 and Lys289 play direct roles in the substrate binding and have been reported to cause IPH when the MAT1A gene has genetic mutations at these residues: Asp258Gly, Arg264His/Cys and Lys289Asn [144, 150, 153, 168]. All mutation points of MAT1A gene causing IPH reported to date are illustrated in Fig. 4.5.1 and 4.5.2B. MAT1A gene sequences where the missense mutations mostly take place are the fully conserved amino acid residues: Ser22Leu, Ser38Asn, Ala55Asp, Gly69Ser, Tyr92His, Pro255Ser, Tyr271Cys, Gly280Val, Arg292Cys, **Arg299His**/Cys, Ile322Val/Met, Val361Phe, Gly378Ser and Gly381Arg [15, 144, 150, 152, 153, 159, 160, 169] (Fig. 4.5.1).

In addition to Arg264His, the functional role of Arg299 was aimed to investigate using the Arg299His mutant which causes IPH in patients. Though it was successful in producing Arg299His mutant, the majority of this mutant protein formed aggregate in solution, so the functional oligomeric form could not be obtained. Arg299 is located at the middle of the solvent inaccessible α-helix domain. The Arg299's side chain forms H-bond with Tyr141 of the underlining β-sheet domain and also Glu148, Cys149 and Glu388 of the connecting loop (Fig. 4.5.2C), suggesting its importance in protein folding and overall structural stability. Some of the IPH causing mutants arise from highly conserved amino acid residues: Leu42Pro, Arg177Trp, Arg199Cys, Arg249Trp, Ile252Thr, Gly257Arg, Ala259Val, Ala297Asp,

Gly336Arg, **Arg356Trp**/Pro/Gln, and Pro357Leu [15, 144, 150, 152, 153, 160, 169, 170] (Fig. 4.5.1). The Arg356Trp mutant was generated, but its purification exhibited the problem similar to that observed in the Arg299His mutant. The protein was highly aggregated in solution and eluted at the void volume of a gel filtration column. Arg356 is located at the surface of the solvent accessible α-helix domain and it forms several H-bonds with Glu128, Asp129 of the gating loop and Asp354 of the neighbouring connecting loop (Fig. 4.5.2D), suggesting its important role in overall protein architecture. Only few mutations causing IPH have been found with poorly conserved amino acids (Leu305Pro and Glu344Ala and Val361Phe) (Fig. 4.5.1) [150, 152, 170]. In addition, Arg356His and Glu344Ala were reported to cause the increase of susceptibility to a thoracic aortic aneurysms when mutations occur in the MAT2A gene, suggesting their importance in enzyme stability and function [171].

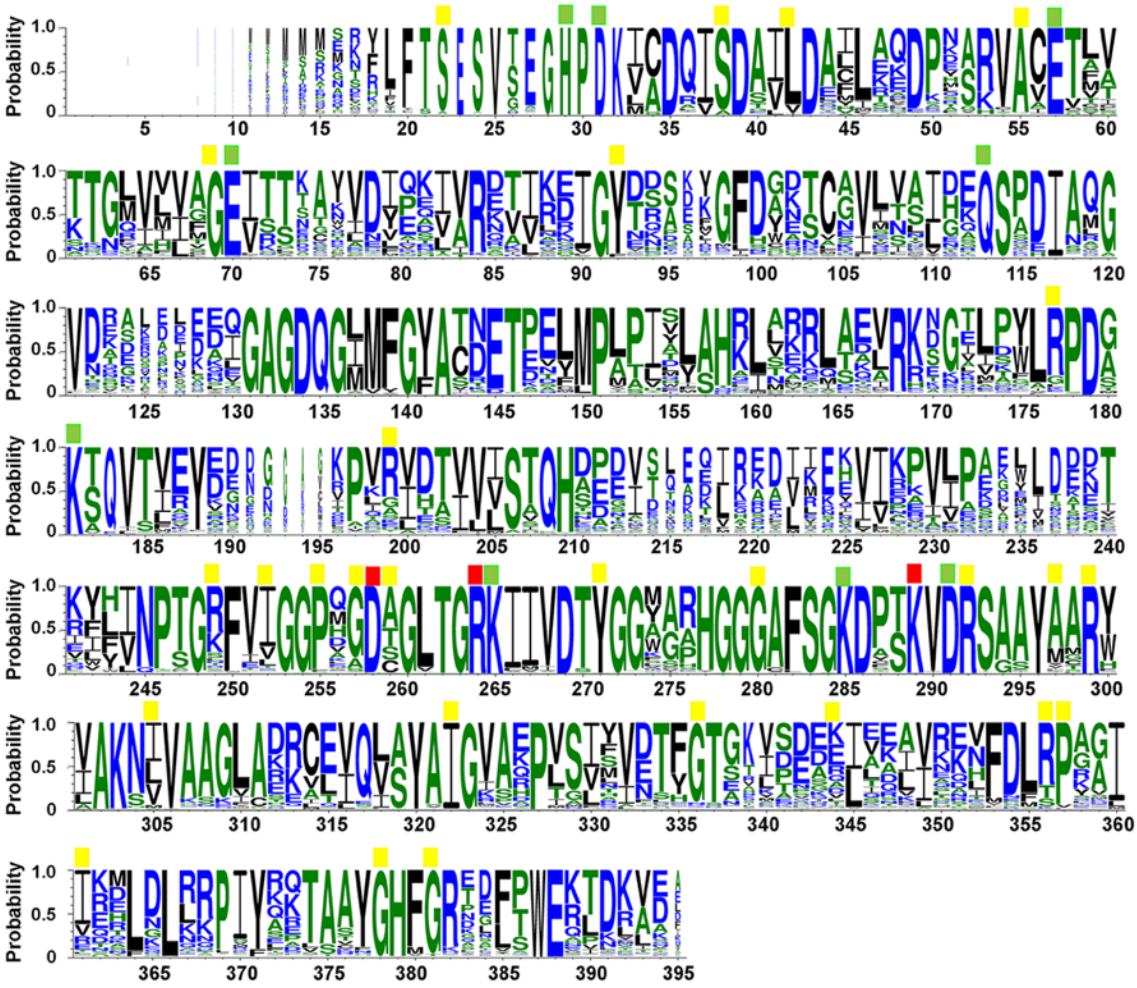

Fig. 4.5.1 Amino acid conservation of MATα1 with catalytic residues and mutation sites causing hypermethioninemia. Different colour is used to show amino acid hydrophobicity (blue: hydrophilic, green: neutral and black: hydrophobic). Catalytic residues are marked by green squares. Residues reported to have mutations which cause hypermethioninemia are marked with yellow squares. Red marks represent residues involved in both SAMe formation and missense mutations causing IPH.

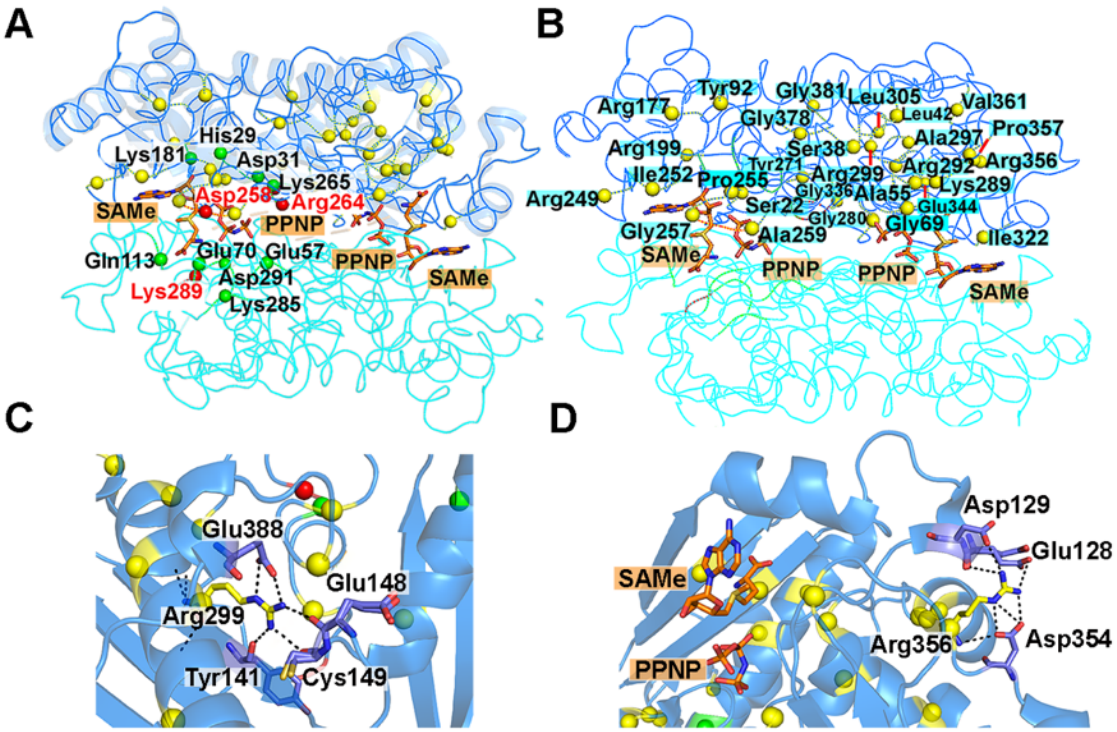

Fig. 4.5.2 Catalytic residues and mutation sites causing IPH of MATα1 (A) Two active sites of MATα2 are shown with SAMe and PPNP highlighted with orange colour. Residues involved in SAMe formation are shown in green spheres. Missense mutations causing hypermethioninemia are shown with yellow spheres. Red spheres are represented residues that involved in both catalysis and mutations causing hypermethioninemia. **(B)** The mutations causing hypermethioninemia are shown with yellow spheres. The two subunits are shown by dark and light blue using the MATα2 structure as a model (PDB: 5A1I). **(C)** Arg299 interaction sites are illustrated. Black dots indicate H-bonds and the interacting residues are shown as sticks. **(D)** Arg356 interaction sites are presented. H-bonds are shown in black dots and the interacting residues are shown as sticks.

4.6 Conclusion

This study provides the structural basis of the R264H mutation at the MATα1 dimer interface. This mutation changes the position of residues that constitute the dimer interface where the active sites are located. This results in an inability to bind the substrate which causes a loss in activity. The changes at the dimeric interface also give rise to the lower affinity for a tetrameric assembly and greater propensity of a dimeric assembly. Arg264 is also involved in providing enzyme stability by forming a salt bridge with Glu57, so mutation to histidine causes the lower thermal stability of the enzyme as observed by the decreased melting temperatures of the mutants.

The data show that the MATα1 (R264H) mutant is able to assemble as a dimer or a tetramer in solution and exists as a dimeric form in the crystal structure. However, the R264H mutation causes a substantial loss in activity, suggesting that Arg264 may be overrated for subunit dimerization but it is indeed crucial for the optimal enzyme reaction. The crystal structure of the MATα1 (R264H) mutant is obtained in apo form with no Met or SAMe bound, although the mutant protein was co-crystallised with the substrate Met and AMP-PNP, consistent with a reduction in enzyme activity. The functional impairment is also related to the residue's role in the interaction with the tripolyphosphate as shown in the R264A MATα2 mutant structure. Also, the R264H mutation causes a disordered active site which results from a disorganised dimer interface. This change of the dimer interface attenuates the ability of the mutant enzyme to bind with substrates. In addition, the incubation of the R264A MATα2 mutant and the R264H MATα1 mutant with the regulatory subunits, MATβV1/V2, shows activity restoration of these mutants. This observation opens up an opportunity of modifying enzyme defect in the disease-causing mutants by small molecules to mimic the effect of the binding of the regulatory subunits.

Chapter V

The regulation of human MAT enzymes by quinolone-based compounds

5.1 Background and objective

A decrease in SAMe formation is varying from a partial loss in the Q113A mutant to a substantial loss in the S114A mutant or the R264A/R264H mutant. Forming complexes with MATβV1 or MATβV2 can restore the activity of MATα2 mutants. Only the regulatory subunit, MATβV1, can form the complex with the MATα1 (R264H) mutant and has the recovery effect on the mutant activity, while this mutant is unable to form the complex with MATβV2. This observation suggests that modifying enzyme defect that cause a disease by using the protein-protein interacting surface (e.g. MATαβ binding interface) by small molecules either designed for restoring or inhibiting enzyme function could be a promising approach for therapeutic treatment. The idea is not limited to the restoring of disease's causing enzyme, but it could be extended to other aspects including designing the inhibitor for MATα2, e.g. anticancer therapeutics. Structural data on MAT enzymes bound with Met, ADO and PPNP are in agreement with the hypothesis that MAT catalyses SAMe via the asymmetrical reaction of S_N2 nucleophilic substitution mechanism [146]. The C-O bond of ATP is broken to the intermediates (ADO and PPNP) and is suggested to occur prior to the formation of the C-S bond between C atom of ADO and S atom of Met at the transition state [146]. The chemical form in the transition state differs to those found in the substrate or product [172] and the reactive intermediate is formed in this state (i.e. C-S bond formation between ADO and Met, which will be further converted to SAMe). Although, the transition state cannot be directly studied by X-ray crystallography using crystal structures, a number of the reported ligand-bound structures of human MATα2 can shed some light on what is happening at the transition

state and are also useful for structural-based drug design (Table 5.1). For instance, ADO and PPNP tightly bind to the active site (prior to SAMe formation), indicating that these intermediates could be a potential model for designing enzyme inhibitors which competitively bind to the active site.

The PF-9366 (1-[2-(dimethylamino) ethyl] quinoline benzodiazepine derivative) was found to regulate MATα2 by binding at the same interacting interface reported to form MATα2β complexes (Fig. 5.1.1A). [145]. The PF-9366 bound structure of MATα2 showed that two molecules of PF-9366 interacted with one MAT dimer (Fig. 5.1.1B) and inhibited MATα2 activity. PF-9366 is a 1,2,4-triazolo[4,3-a]-class inhibitor and its main scaffold is similar to the 4(1H) quinolone. Coincidentally, a number of quinolone-based compounds (SCR0911, SCR0915, CK267 and WDH1U4) are available for testing their effect on MAT activity. The possible binding sites of the compounds on MAT enzymes were preliminary predicted by molecular docking using SwissDock (Table 5.2). The binding energies of these quinolone-based compounds are shown in comparison with the PF-9366 compound using the wtMATα2 as the target model. The results show that PF-9366 is the most favourable compound to bind with the wtMATα2 as indicated by its lowest binding energies (Gibbs free energy (ΔG) of -8.53 kcal/mol and FullFitness of -3146.97 kcal/mol). The most energetically favourable ligand binding site of these quinolone-based compounds is predicted to be the compound, SCR0915, which show comparable binding energies to PF-9366 (ΔG of -8.40 kcal/mol and FullFitness of -3055.58 kcal/mol). The potential binding energies of other compounds used in this study (WDH1U4, CK267 and SCR0911) are shown in Table 5.2. The compound, SCR0911, is the most energetically unfavourable ligand showing highest energies for binding to the wtMATα2 (ΔG of -7.62 kcal/mol and FullFitness of -3045.93 kcal/mol), when compared to other compounds reported here (Table 5.2). Interestingly, the predicted binding sites of all quinolone-based compounds on MATα2 are similar to the protein-protein interacting surface where PF-

9366 and MATβ have been reported to bind at. Therefore, the effect of these compounds on MAT activity has been further investigated. An attempt to obtain the compound-bound structure of MAT enzymes by co-crystallisation technique has been done using a variety of available commercial screens. The quinolone-based compound structures used in this study are shown in Fig. 5.1.2.

Table 5.1 Human MATα2 structures with ligands in the active site

hMATα2	Resolution (Å)	PDB	Active site ligands	Reference
Wild type	1.09	5A1I	SAMe+ADO+MET+PPNP	[30]
Wild type	2.34	5A19	PPNP	[30]
Q113A	2.70	6FBN	SAMe+PPNP	[47]
S114A ($P22_12_1$)	1.65	6FBP	PPNP+ADO	[47]
S114A (I222)	1.80	6FBO	PPNP+ADO	[47]
P115G	2.70	6FCB	SAMe+PPNP	[47]
R264A	1.70	6FCD	PPi+ADO	[47]
MATα2β	2.34	4NDN	SAMe+PPNP	[13]
MATα2β	2.59	4KTT	SAMe+Pi	[13]

Table 5.2. The binding energy of compounds predicted by SwissDock. wtMATα2 (PDB: 5A1I) was used as the model.

Compounds	Delta Gibbs free energy (kcal/mol)	FullFitness score (kcal/mol)
PF-9366	-8.53	-3146.97
SCR0911	-7.62	-3045.93
SCR0915	-8.40	-3055.58
CK267	-8.08	-3054.34
WDH1U4	-8.26	-3043.29

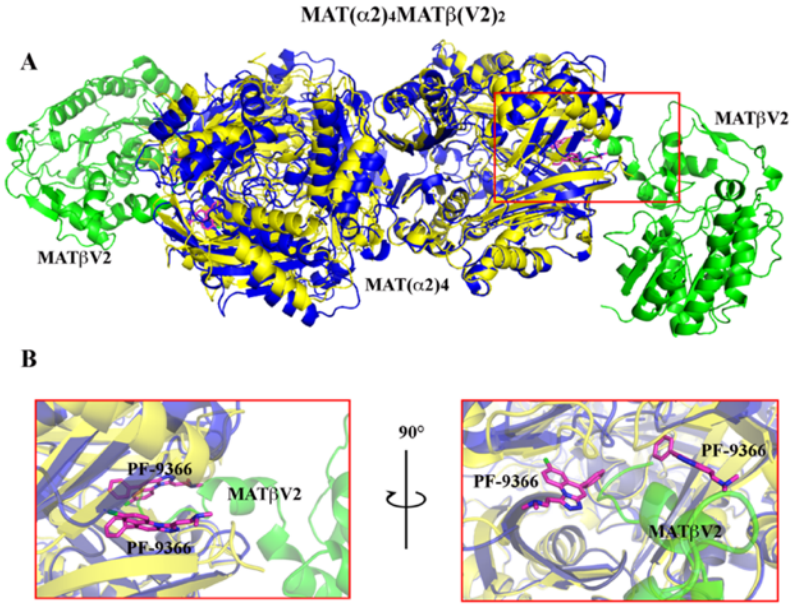

Fig. 5.1.1 The structural comparison of MAT(α2)$_4$(MAT(βV2)$_2$ complex and the PF-9366 bound MATα2 structure. (A) MAT(α2)$_4$MAT(βV2)$_2$ complex (PDB: 4NDN, blue and green) and the PF-9366 bound MATα2 structure (PDB: 5UGH, yellow) are aligned. PF-9366 compounds are shown in pink sticks. **(B)** Two molecules of PF-9366 bind to MATα2 showing the same binding site of MATβV2.

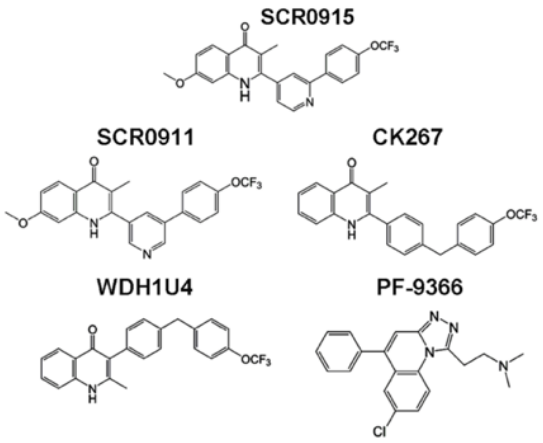

Fig. 5.1.2 Quinolone-based compound structures. The PF-9366 structure is shown in comparison with the quinolone-based compounds used in this study.

5.2 The regulation of human MAT enzymes by quinolone-based compounds

The effect of quinolone-based compounds on MAT activity has been tested for wtMATα1, R264H MATα1, wtMATα2, S114A MATα2 and R264A MATα2. The final concentration of DMSO in protein samples was less than 1 %. The effect of DMSO on enzyme activity and melting temperature has been examined at 2 % which shows no effect on both SAMe formation and thermal stability of enzymes. The mutants of MATα2 that their mutations cause a reduction of enzyme activity show the recovery of SAMe formation by these quinolone-based compounds, whereas the wtMATα2 activity is inhibited by these compounds (Fig. 5.2.1A). Each mutant responds differently to the tested compounds. SCR0911 and WDH1U4 compounds can recover the MATα2 (S114A) mutant, while they have no effect on the MATα2 (R264A) mutant. The R264A MATα2 can produce SAMe of about 50 % compared to the wild-type activity when it is incubated with CK267 or SCR0915 compounds (Fig. 5.2.1A). Additionally, the compounds have no effect on the phosphatase activity of the enzyme and its mutants (Fig. 5.2.1B).

The compound, SCR0915, is selected as the model to study the effect of these quinolone-based compounds on MATα2 activity. This compound inhibits the wild-type activity (Fig. 5.2.2A), while it recovers SAMe formation of the MATα2 (R264A) mutant (Fig.5.2.2B). The determination of SCR0915 IC_{50} using an inhibition curve of wtMATα2 is shown in Fig. 5.2.2C. SCR0915 also slightly increases the thermal stability of wtMATα2 to 48.17 ± 0.23 ºC ($p < 0.01$) when compared to the Tm of an untreated wtMATα2 (47.20 ± 0.15 ºC). The thermal stability of the MATα2 (R264A) mutant significantly increases to 41.48 ± 0.06 ºC ($p < 0.001$) when compared to the Tm of an untreated R264A mutant (39.2 ± 0.07 ºC). The fluorescence curves used to determine the Tm of each protein are shown in Fig. 5.2.2D. The compound treatments show the different effect on wtMATα2 and its mutant. It is likely that the compound

can render the MATα2 to be more sensitive to SAMe inhibition. Therefore, this results in a reduction of SAMe formation found in the wild type, while the compound can increase SAMe formation in the MATα2 (R264A) mutant just only to 41.2 ± 1.4 % relative to the wild type (Fig. 5.2.1A).

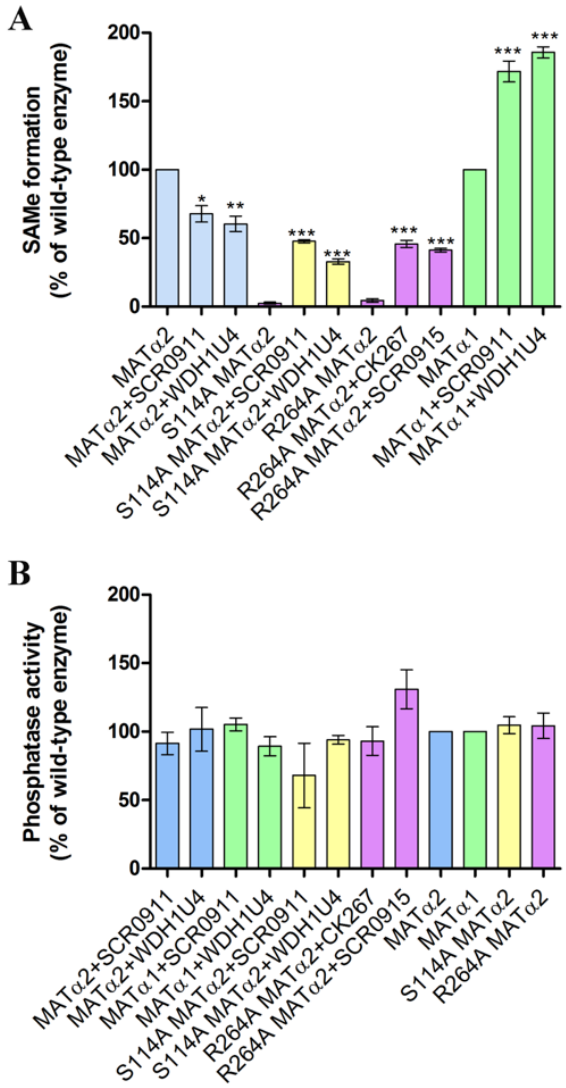

Fig. 5.2.1 Effect of quinolone-based compounds on wild-type and mutant MAT enzymes **(A)** 10 μM of the compound was incubated with Met and ATP before SAMe formation was measured by ELISA kit (Cell biolabs). **(B)** The compounds show no effect on the PPPi hydrolysis. ('*', '**' and '***' indicates statistical significance at $p < 0.05$, $p < 0.01$ and $p < 0.001$, respectively, compared to the untreated enzymes). Data are mean of three independent

experiments ± SEM (n=3). All experiments were performed using protein samples from the same batch of protein purification (different aliquots).

In contrast to wtMATα2, the incubation of wtMATα1 with the compound SCR0911 or WDH1U4 shows the increase in SAMe production as shown in Fig. 5.2.1A. Therefore, SCR0911 has been selected to investigate its effect on the activity of the MATα1 (R264H) mutant. The results show that the R264H mutant treated with SCR0911 is able to restore its function to the similar level compared to the wild type (Fig. 5.2.2E). However, pre-incubation with the compound SCR0911 does not prevent the hetero-complex (R264H-MATβV1) formation (Fig. 5.2.2F). The addition of SCR0911 to R264H-MATβV1 complex does not give the synergistic effect, suggesting that SCR0911 competes with MATβV1 for binding at the same dimeric interface and MATβV1 binding prevent SCR0911 to interact with the mutant protein (Fig. 5.2.2E-F). These compounds show different effects on MATα1 and MATα2 activity which may be related to the different kinetic properties of these two isoforms. MATα1 has higher Km for Met (23 μM-1 mM) compared to MATα2 (4-10 μM) and MATα1 is not very sensitive to SAMe inhibition compared to MATα2 [41, 72]. The compounds may lower Km for Met of MATα1 which results in the observed higher SAMe formation. The kinetic study of the compounds on MAT enzymes needs further investigation to understand how these compounds indeed regulate MAT activity.

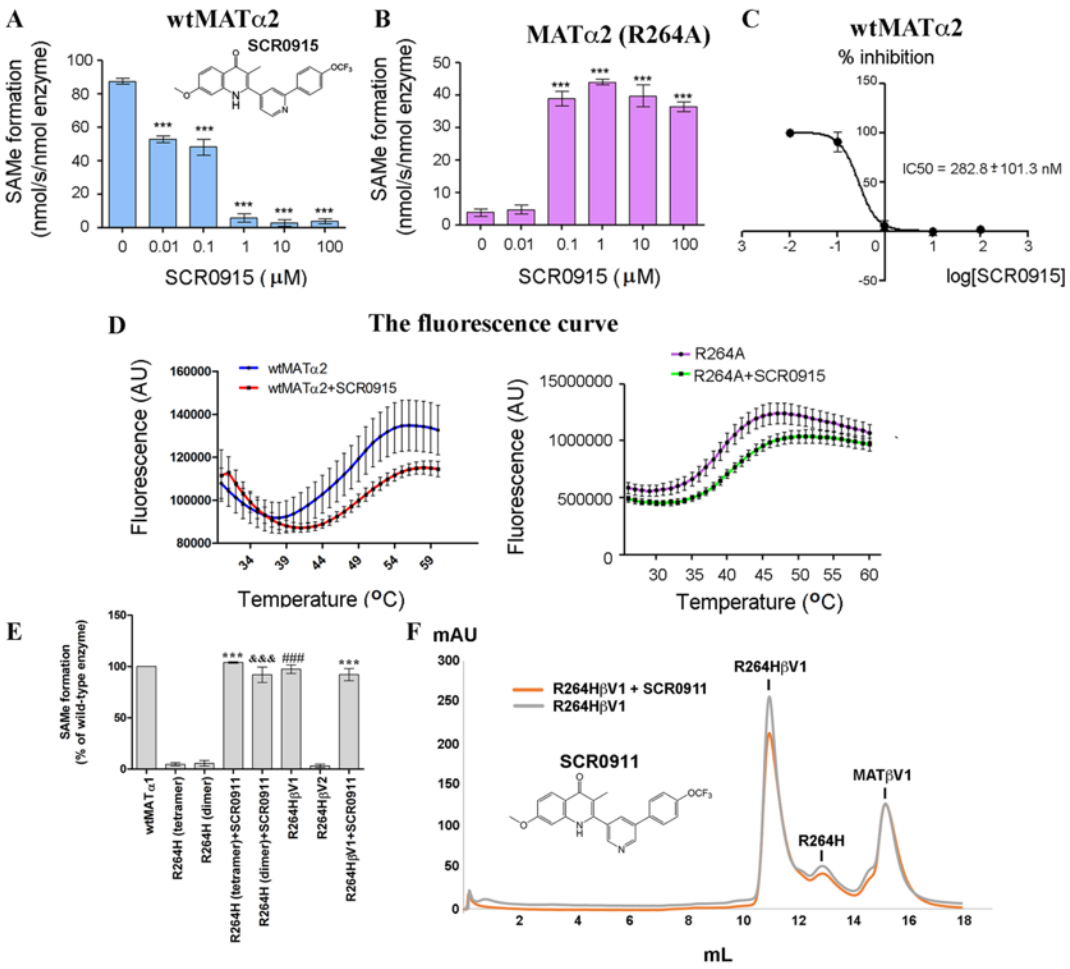

Fig. 5.2.2 The effect of SCR0915 and SCR0911 compound on MAT activity (A) The effect of SCR0915 on the wild-type MATα2 is exhibited. **(B)** The effect of SCR0915 on the MATα2 (R264A) mutant is shown. '***' corresponds to the statistical difference at $p < 0.001$ when compared to the untreated enzyme (0 μM). **(C)** The SCR0915 IC_{50} (half-maximal inhibitory concentration) are shown with the inhibition curve. The IC_{50} was calculated from a log([SCR0915]) versus normalised response curve fit using GraphPad Prism version 5.00. **(D)** The fluorescence curves used to determine the thermal stability of each protein are shown. **(E)** The effect of regulatory subunits (MATβ) and SCR0911 on the MATα1 (R264H) activity are shown by measuring SAMe formation. '***', '&&&' and '###' denote statistical significance at $p < 0.001$ compared with R264H (tetramer), R264H (dimer) and both oligomeric forms of R264H, respectively. **(F)** Gel filtration profiles of R264HβV1 with or without SCR0911 pre-incubation are shown by the absorbance at A280. (A-B, E) Data are mean of three independent experiments ± SEM (n=3). All experiments were performed using protein samples from the same batch of protein purification (different aliquots).

5.3 Compound screening: co-crystallisation of R264A MATα2 and SCR0915

In order to obtain the crystallisation conditions for producing SCR0915-bound crystals, fifteen commercial screens (96 conditions each) were tested by co-crystallisation of the R264A MATα2 with the SCR0915. All screening trays were kept at room temperature (18 °C) and for each condition 200 nL of protein was mixed with 200 nL of precipitant (200:200 nL) (protein: precipitant). Crystals appeared in some of the commercial screens (JCSG plus, SALTRx and PACT premier screens). The screening conditions that promote crystal growth are provided in Table 5.3.1-5.3.3. Some screening solutions showed protein precipitation which was scored from 1 to 5 depending on the levels of observed precipitations (5 indicated a highly aggregated state). Blank cells in the table correspond to the clear drop, while good hit is shown with H (i.e. crystal is growing). If the reservoir condition was suitable for growing protein crystals, the crystal would normally appear in 3-4 days.

The crystals from these three screens were tested with X-ray beam but diffracted to only 8-10 Å. Despite the low-resolution, the diffraction patterns were originated from protein crystals (Fig. 5.3). Therefore, further optimisation is necessary (section 6.2.2, chapter 6).

Table 5.3.1 JCSG plus screening of the R264A MATα2 co-crystallised with SCR0915

	1	2	3	4	5	6	7	8	9	10	11	12
A	+2	+2	+2	+2	+2	+3	+2	+2	+2	+1	+1	+1
B	+3	+1	+1	+1	+1	+1	+1	+3			+1	
C	+3	+3	+3	+3	+3	+3	+1				+1	+1
D				+4		+2						+1
E	+1	+1									H	
F	H											
G			+5		+4			+3	+1			
H	+1		+2		+1	+1	+1	+1	+1	+2	+1	

Screening conditions:

Protein: R264A MATα2 (5mg/ml) + SCR0915 200:200 nL

E11 0.16 M Calcium acetate hydrate, 0.08 M Sodium cacodylate pH 6.5, 14.4 % w/v PEG 8000 and 20 % v/v glycerol: **F1** 0.05M Cesium chloride, 0.1 M MES pH 6.5 and 30 % v/v Jeffamine® M-600.

Table 5.3.2 SALTRx screening of the R264A MATα2 co-crystallised with SCR0915

	1	2	3	4	5	6	7	8	9	10	11	12
A												
B												
C												
D												
E	+2	+1		+1	+1			+2	H			H
F	+1			+1			+1			+1		
G	+1											
H												

Screening conditions:

Protein: R264A MATα2 (5mg/ ml) + SCR0915 200:200 nL

E9 1.8 M Sodium phosphate monobasic monohydrate and Potassium phosphate dibasic pH 6.9: **E12** 1.0 M Succinic acid pH 7.0 and 0.1 M BIS-TRIS propane pH 7.0.

Table 5.3.3 PACT premier screening of the R264A MATα2 co-crystallised with SCR0915

	1	2	3	4	5	6	7	8	9	10	11	12
A	+2	+2					+3	+3	+3	+2	+2	+2
B	+3	+3	H	+2	+1	+2	+2	+2	+2	+2	+2	+2
C	+3	+3	+3	+3	+3	+2	H		H	+2	+2	+2
D	+1	+1	H									
E												
F										H		
G												
H												

Screening conditions:

Protein: R264A MATα2 (5mg/ml) + SCR0911 200:200 nL

B3 0.1M MIB (Malonic acid, Imidazole and Boric acid) pH 6.0 and 25 % w/v PEG 1500: **C7** 0.2 M Sodium chloride, 0.1 M HEPES pH 7.0 and 20 % w/v PEG 6000: **C7** 0.2 M Sodium chloride, 0.1 M HEPES pH 7.0 and 20 % w/v PEG 6000: **C9** 0.2 M Lithium chloride, 0.1 M HEPES pH 7.0 and 20 % w/v PEG 6000**: D3** 0.1 M MMT (Malic acid, MES and Tris) pH 6.0 and 25 % w/v PEG 1500: **F10** 0.02 M Sodium/potassium phosphate, 0.1M Bis-Tris propane pH 6.5 and 20 % w/v PEG 3350.

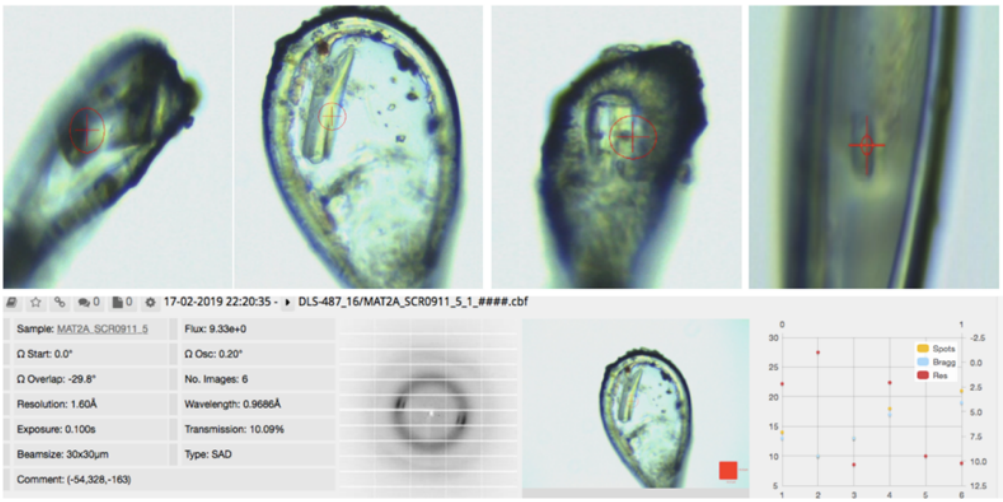

Fig. 5.3 Crystal diffraction test at Diamond Light Source (DLS). Numerous crystals from the screens were sent to test at DLS (I24 beamtime). All tested crystals were protein crystals and diffracted at only 8-10 Å resolution.

5.4 The molecular modelling of SCR0915 and SCR0911 binding site on MAT enzymes

The prediction of SCR0915 binding sites was performed using SwissDock (blind docking) and Autodock Vina (local docking). The wild type and MATα2 (R264A) mutant were used as the target proteins. The best binding position are selected based on the Gibbs free energy (ΔG) and FullFitness score. Both SwissDock and Autodock Vina predicted the most favourable binding position at the same binding interface where PF-9366 and MATβ were reported to bind to MATα2 [13, 145]. The SCR0915 binding position predicted by Autodock vina using the wild-type structure as the model (PDB: 5A1I) shows ΔG of -11.4 kcal/mol, while ΔG of -7.8 kcal/mol and FullFitness of -3486.08 kcal/mol are predicted by SwissDock (Fig. 5.4.1 A-C).

The SCR0915 binding position predicted by Autodock Vina using the MATα2 (R264A) structure as the model (PDB: 6FCD) exhibits ΔG of -10.2 kcal/mol, whereas ΔG of -8.1 kcal/mol and FullFitness of - 3111.79 kcal/mol are predicted by SwissDock (Fig. 5.4.1D-F).

The predicted SCR0915 binding site of both the wild type and R264A MATα2 is found to be at the same binding interface as the reported PF-9366 compound (Fig. 5.4.1G). Pre-incubation of the compound SCR0915 with MATα2 partially prevents MATβV1 to form the complex with MATα2 (Fig. 5.4.1I), confirming the similar binding interface. In contrast to SCR0915, SCR0911 cannot prevent the binding of MATβV1 on the MATα1 (R264H) mutant (Fig. 5.2.2F).

MATβ could alter MATα2 activity, while the residues in the catalytic site of MATα2 was preserved in the presence of MATβ [13, 146], indicating that the increase in activity might be modulated by an allosteric regulation rather than the direct binding in the active site. The activity restoration of the MATα1 (R264H) mutant by MATβV1 or SCR0911 suggests a similar binding interface. The best binding position of SCR0911 on MATα1 (R264H) mutant is predicted by blind docking using SwissDock (FullFitness = -3475.04 kcal/mol, and ΔG = -7.76 kcal/mol) and the interaction profiles are shown in Fig 5.4.2A-B. The predicted site is at the same dimeric-interface pocket of MATα2 where SCR0915, MATβ and PF-9366 compound are shown to bind to [13, 145]. Efforts to obtain crystallographic structure with the compounds have not been successful suggesting some flexibility, heterogeneity and/or weaker binding compared to MATβ, consistent with the inability of SCR0911 to compete with MATβ in restoring SAMe activity of the MATα1 (R264H) mutant.

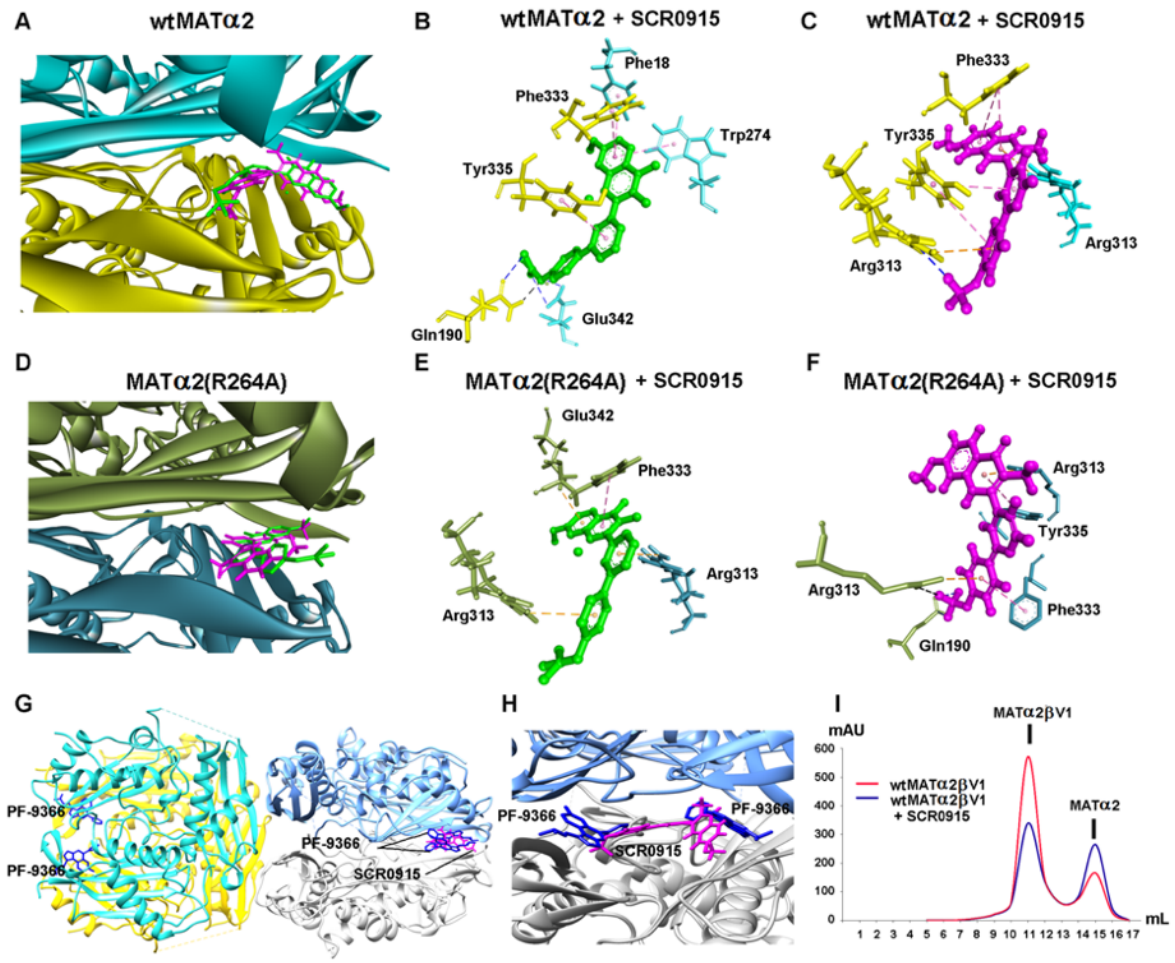

Fig. 5.4.1 The molecular modelling of ligand binding sites using Autodock Vina and SwissDock (A) The best binding positions of SCR0915 were predicted by Autodock Vina and SwissDock. SCR0915 is shown in a green stick (Autodock Vina) and a magenta stick (SwissDock) **(B, C)** The SCR0915 binding interaction profiles on wtMATα2 were predicted by Autodock Vina and SwissDock, respectively. **(D)** The SCR0915 best binding poses on R264A MATα2 were shown. **(E, F)** The interaction profiles of SCR0915 and MATα2 (R264A) mutant were obtained from Autodock Vina and SwissDock, respectively. H-bonds are shown in black dashed lines. Halogen bonds and electrostatic interaction are shown in blue and orange dashed lines. The π-π stacking is shown in pink dashed lines. **(G)** The MATα2 structure in complex with PF-9366 (PDB: 5UGH) is shown. The binding site of SCR0915 is similar to the PF-9366 binding interface. **(H)** Close view of PF-9366 and SCR0915 binding site is exhibited.

(I) The MATαβV1 formation (with or without SCR0915 (10 μM)) are shown by the absorbance at A280.

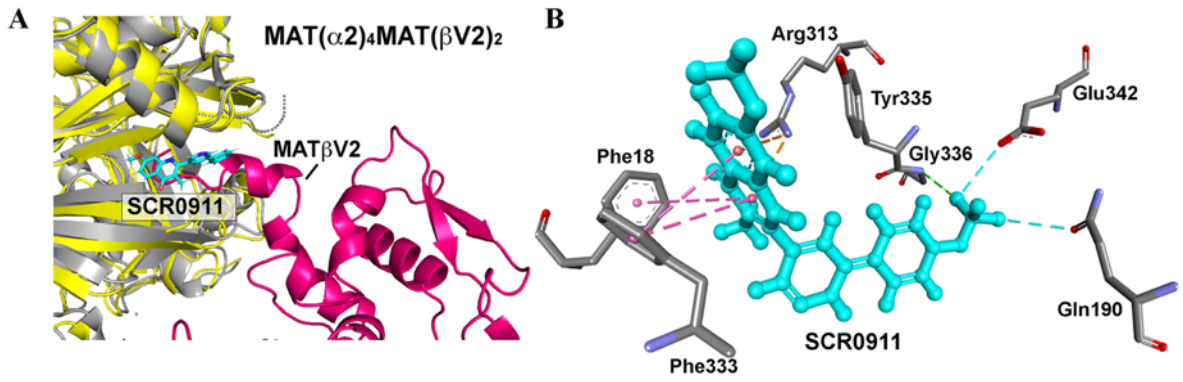

Fig. 5.4.2 The molecular docking of SCR0911 binding site on the MATα1 (R264H) mutant

(A) The SCR0911 binding site of the MATα1 (R264H) mutant (grey) is aligned with MATαβ complex. MATα2 and MATβV2 are shown with yellow and pink, respectively. SCR0911 is shown in the blue stick. **(B)** SCR0911 and R264H interaction profiles obtained from SwissDock are illustrated using DS visualiser. Protein ligand interactions are shown in blue, pink and orange dashed lines corresponding to halogen bonds, π-π stacking, electrostatic interactions, respectively.

Chapter VI

Conclusion and future direction of the project

6.1 Conclusion

The functional and structural role of the gating loop have been studied by site-directed mutagenesis at the conserved residues Gln113, Ser114 and Pro115. The results show that Ser114 (OG atom) coordinates the adenine ring of the substrate ATP (N6 and N7 atom) via a water molecule. This coordination of Ser114, water and adenine moiety of ATP or SAMe is preserved in the structures of both MATα1 and MATα2, while mutation of this residue results in the loss of SAMe formation. Ser114 also stabilises a rigid helix conformation of the closed gating loop with the neighbouring gating residues (Asp116, Ile117 and Ala118). The ordered open conformation of the gating loop is firstly observed in the crystal structure of human MAT providing evidence that the gating loop rearranges to different conformations in each step of enzyme reaction. The conformational changes of the gating loop are driven by the substrate/ product interaction. Gln113Ala mutation results in about 25 % decrease in SAMe production compared to the wild type, while SAMe formation of Pro115Gly is normal. Although Gln113 directly interacts with the oxygen atom of Met or SAMe via its side chain nitrogen atom, mutation of this residue does not completely prevent Met to bind at the active site. In addition, the Gln113Ala and the Ser114Ala mutant structures show asymmetrical active sites; one is empty, while the other is bound with substrates/products. In contrast to Pro115Gly mutant, its structure shows symmetrical active sites which both are fully occupied by substrates or products as found in the wild-type structure.

The loss in activity of Arg264 mutant found in hypermethioninemia patients is not due to an inability to form a dimer or a tetramer in solution. The data show that the Arg264His MATα1 mutant is able to assemble as a dimer or a tetramer, and Arg264Ala MATα2 is also tetrameric

in solution. These Arg264 mutants also exist as the dimeric form in crystal structures. The loss in activity is more likely to be related to the residue's role in interacting with the tripolyphosphate as shown in the Arg264Ala (MATα2) structure. In addition, the Arg264His (MATα1) mutant structure shows the disordered active site due to the changes at the dimer interface caused by Arg264His mutation. Therefore, the ability of the enzyme to bind to substrates may be attenuated, resulting in the loss in activity.

The current results suggest that the phosphatase activity and SAMe production are catalysed in distinct parts of the active site as PPPi hydrolysis is not affected by mutations which cause a decrease in SAMe production. Forming complexes with the regulatory subunit MATβ show the restoration of the mutant activity. This observation has been exploited for using small molecules that may interact with this protein interacting interface and can regulate MAT enzyme activity (Fig. 6.1).

The effects of quinolone-based compounds on MAT activity have been tested and compared to the regulatory subunit MATβ. The compound binding sites are predicted to be at the same interacting interface of MATβ. However, it is likely that MATβ can bind with the catalytic subunits tightly than these quinolone compounds. Pre-incubation of the compound with MATα1/2 prior to MATβ cannot or partially prevent the MATαβ complex formation. The crystals produced by the compound co-crystallisation are obtained but do not diffract at the high resolution, thus the ligand-protein interaction profiles are obtained by using molecular docking tools (SwissDock and AutoDock Vina). The aromatic ring of Phe333 plays an important role in π-π stacking with the compound heterocyclic rings as predicted by both docking programs. Two molecules of PF-9366 compounds also interact with Phe333 and Phe18 of each MAT subunit via its triazoloquinoline core.

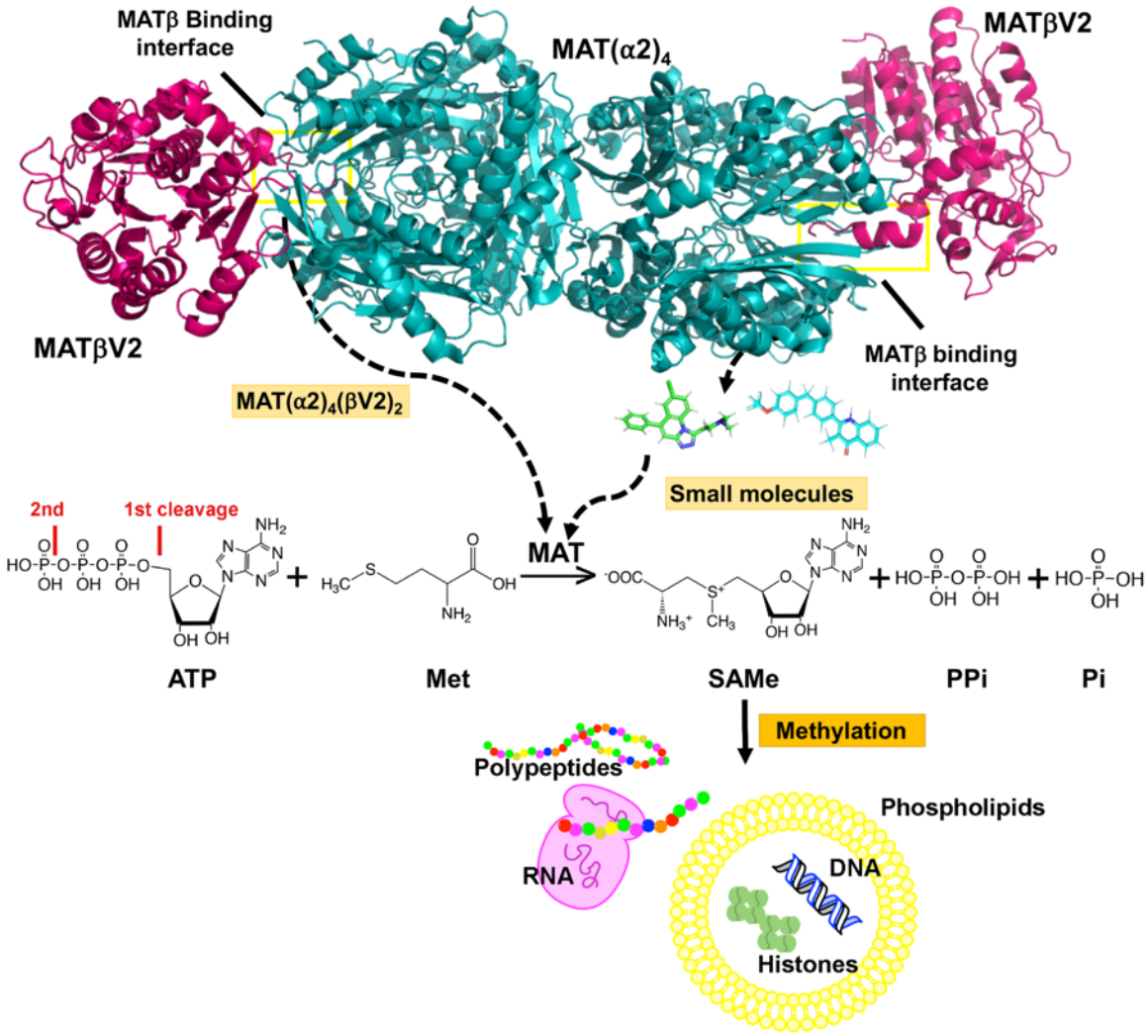

Fig. 6.1 The effect of regulatory subunits and small compounds on MAT activity. MATα2βV2 complex structure is illustrated (PDB: 4NDN) showing protein-protein interacting interface (yellow boxes). Small molecules designed to interact with MATα2 at the similar MATβ binding site can regulate MAT activity responding to Met or SAMe concentrations. SAMe levels control biological function of an organism mainly via methylation processes of numerous biomolecules (DNA, histones, polypeptide, etc.).

6.2 Future direction of the project

6.2.1 Mutant MATα2-MATβ complex formation

The crystal of mutant MATα2β complexes could not be reproduced following the published wild-type condition [13]. To get the complex structure, extensive re-screening of crystallisation conditions might be a way to get a suitable condition by using a crystallisation robot system. This system allows the experiment to be performed in an array of crystallisation's conditions and needs only small amount of proteins. Seeding techniques may be used to facilitate crystallisation by using any existent MATα2 crystals as a nucleation point. There are several ways of seeding that can be performed (e.g. macro-seeding, micro-seeding, streak-seeding, cross-seeding, etc).

6.2.2 Compound-bound crystal optimisation

Although Arg264Ala crystals co-crystallised with SCR0915 compound were obtained, the crystals did not diffract at the high resolution. Further optimisation may be able to improve the quality of crystals. There are a number of factors that can affect crystal quality which can be varied during crystallisation (e.g. pH, additives, temperature, precipitant concentrations, etc). Using the condition obtained from the robot screening can be used as a starting point for a larger batch of crystal production. Varying different kinds of cryoprotectants and also concentration or duration of soaking when freezing crystals can promote crystals to diffract at a higher resolution.

6.2.3 A structural study of MATβV1/V2 and GIT1 interaction

MATα2 and MATβV1/V2 have been reported to be involved in several cellular pathways that trigger cancer cell growth. Besides their role as the regulatory subunits of MATα2, MATβV1/V2 can interact with several proteins related to a cellular survival pathway e.g. ERK and PI3-K pathway [41, 173-175]. The two isoforms of MATβV1/V2 were related to cancer development which involved in their interaction with GIT1 (G-protein-coupled receptor kinase interacting protein 1). GIT1 and MATβ formed a scaffold to recruit and activate MEK1/2 and ERK1/2 (Fig. 6.2.1A) [173]. GIT1 and MATβ were found to be overexpressed in human HCC and colon cancer. This promoted cell growth and tumorigenesis, while cellular apoptosis occurred when GIT1 and MATβ were knocked down [174]. In addition, both variants (V1 and V2) of MATβ are necessary for forming complex with MEK1/2 and GIT1 [173]. The full-length GIT protein contains 5 domains including an N-terminal ARF-GAP (ARF-GTPase activating) domain, three ANK (ankyrin) repeats, a SHD (Spa2-homology) domain, a CC (coiled-coil) domain necessary for dimerization, and a PBS (paxillin-binding site) domain (Fig. 6.2.1B). The truncated GIT1 protein containing 3 domains (lacking the CC domain and C-terminal paxillin binding domain) was reported to lose their ability to interact with both variants of the MATβ proteins, therefore full-length GIT1 would be necessary for forming complex with MATβ [176]. Structural studies of this complex can be performed by forming full-length GIT1 and MATβ complex using SEC analysis or ITC (isothermal titration calorimetry) to identify the complex formation, prior to crystallisation screening or grid preparation for cryoEM (cryogenic electron microscopy) experiments.

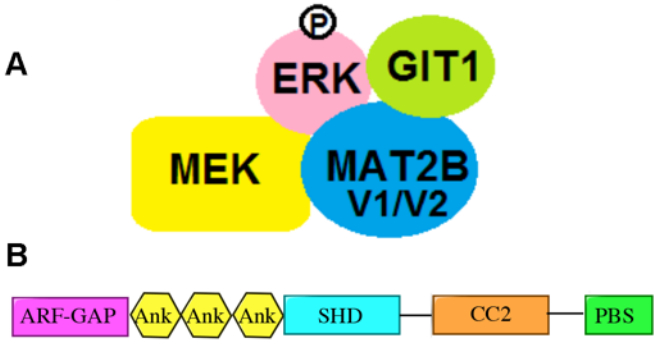

Fig. 6.2.1 The illustration of the GIT1-MATβ scaffold and the GIT1 encoding genes (A) Overexpression of GIT1 and MATβV1/V2 during human HCC and colon cancer promotes the recruitment of GIT1, MEK and ERK which results in the increased ERK phosphorylation. **(B)** The full-length GIT1 protein contains 5 domains including an N-terminal ARF-GTPase activating domain, three ankyrin repeats, a Spa2-homology domain, a coiled-coil domain, and a paxillin-binding site domain. The figure (B) was modified from [177].

6.2.4 Phosphatase activity study of MAT enzymes based on the structural study

The tripolyphosphate binding site is conserved from eMATs to human MATs as seen by the AMP-PNP, Met+PPNP+SAMe+ADO and PPNP-bound structure (Fig. 6.2.2A). There are six residues that involve in PPPi interaction including the three of lysine (Lys181, Lys265 and Lys285), His29, Arg264 and Asp291. Once the conformation of tripolyphosphate changes, as observed in the Met+PPNP+ADO+SAMe and the PPNP-bound structure of MATα2 (Fig. 6.2.2A-B), the positions of these six residues are preserved. Comparison of the PPNP-bound structure to the apo-structure (Fig. 6.2.2C) shows that only Lys181 is in different conformation to the apo state.

From the present study, the phosphatase activity is not affected by the mutations in Ser114 and Arg264, whereas the SAMe production is enormously decreased. In order to investigate the key residues that separately participate in SAMe formation and PPPi hydrolysis-specific site,

mutational analysis of a single amino acid involved in PPPi interaction can be designed using the rational structural basis. Once the purified proteins of mutants are obtained, they can be studied in both functional and structural relevance. Crystallisation can be done with a variety of substrates (e.g. AMP-PNP, ATP, PO_4^{3-}, etc.) in comparison with the apo-state of its own and the wild type. PPPi hydrolysis rate and SAMe production can be tested to investigate whether these residues are either solely involved in phosphatase activity or SAMe formation or in both of them. It will be explained which step depend on each other, since some mutants in the current study show a reduction in SAMe formation, while the PPPi hydrolysis rate is unchanged.

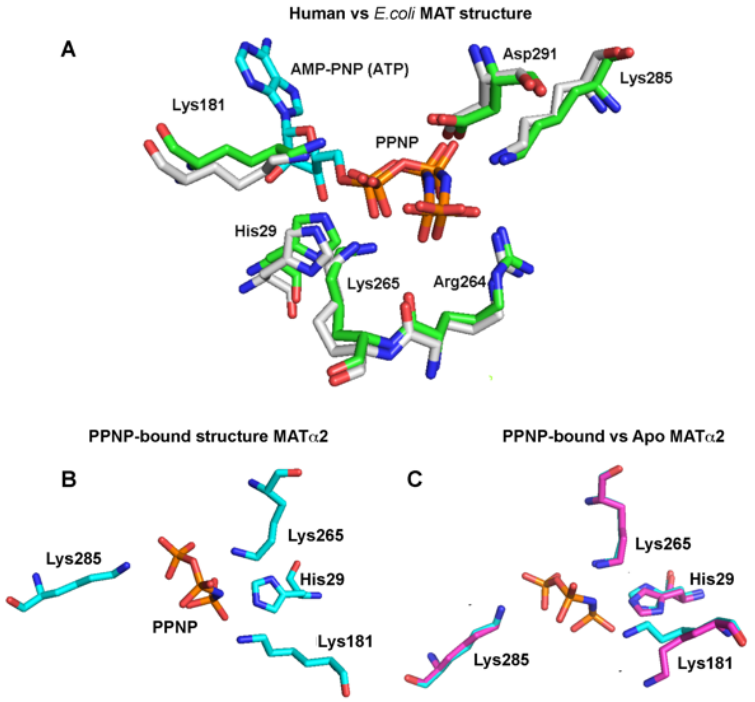

Fig. 6.2.2 The illustration of the tripolyphosphate interacting residues. (A) The human Met+PPNP+SAMe+ADO bound MAT structure (PDB: 5A1I, green sticks) and the *E. coli* AMP-PNP bound MAT structure (PDB: 1P7L, white sticks) are aligned. **(B)** PPNP-bound structure (blue sticks) of MATα2 is shown with the different PPNP conformation in comparison with the Met+PPNP+SAMe+ADO bound structure. **(C)** The PPNP-bound (blue sticks) and apo-structure (pink sticks) are aligned.

References

1. Sanchez-Perez, G. F., Bautista, J. M. & Pajares, M. A. (2004) Methionine adenosyltransferase as a useful molecular systematics tool revealed by phylogenetic and structural analyses, *Journal of molecular biology.* **335**, 693-706.

2. Frau, M., Feo, F. & Pascale, R. M. (2013) Pleiotropic effects of methionine adenosyltransferases deregulation as determinants of liver cancer progression and prognosis, *Journal of hepatology.* **59**, 830-41.

3. Friedel, H. A., Goa, K. L. & Benfield, P. (1989) S-adenosyl-L-methionine. A review of its pharmacological properties and therapeutic potential in liver dysfunction and affective disorders in relation to its physiological role in cell metabolism, *Drugs.* **38**, 389-416.

4. Lu, S. C. (2000) S-adenosylmethionine, *The international journal of biochemistry & cell biology.* **32**, 391-5.

5. Mato, J. M., Alvarez, L., Ortiz, P. & Pajares, M. A. (1997) S-adenosylmethionine synthesis: molecular mechanisms and clinical implications, *Pharmacology & therapeutics.* **73**, 265-80.

6. Kotb, M., Mudd, S. H., Mato, J. M., Geller, A. M., Kredich, N. M., Chou, J. Y. & Cantoni, G. L. (1997) Consensus nomenclature for the mammalian methionine adenosyltransferase genes and gene products, *Trends in genetics : TIG.* **13**, 51-2.

7. Halim, A. B., LeGros, L., Geller, A. & Kotb, M. (1999) Expression and functional interaction of the catalytic and regulatory subunits of human methionine adenosyltransferase in mammalian cells, *The Journal of biological chemistry.* **274**, 29720-5.

8. LeGros, H. L., Jr., Halim, A. B., Geller, A. M. & Kotb, M. (2000) Cloning, expression, and functional characterization of the beta regulatory subunit of human methionine adenosyltransferase (MAT II), *The Journal of biological chemistry.* **275**, 2359-66.

9. LeGros, L., Halim, A. B., Chamberlin, M. E., Geller, A. & Kotb, M. (2001) Regulation of the human MAT2B gene encoding the regulatory beta subunit of methionine adenosyltransferase, MAT II, *The Journal of biological chemistry.* **276**, 24918-24.

10. Yang, H., Ara, A. I., Magilnick, N., Xia, M., Ramani, K., Chen, H., Lee, T. D., Mato, J. M. & Lu, S. C. (2008) Expression pattern, regulation, and functions of methionine adenosyltransferase 2beta splicing variants in hepatoma cells, *Gastroenterology.* **134**, 281-91.

11. Alvarez, L., Mingorance, J., Pajares, M. A. & Mato, J. M. (1994) Expression of rat liver S-adenosylmethionine synthetase in Escherichia coli results in two active oligomeric forms, *The Biochemical journal.* **301 (Pt 2)**, 557-561.

12. Mingorance, J., Alvarez, L., Pajares, M. A. & Mato, J. (1997) Recombinant rat liver S-adenosyl-l-methionine synthetase tetramers and dimers are in equilibrium, *The international journal of biochemistry & cell biology.* **29**, 485-491.

13. Murray, B., Antonyuk, S. V., Marina, A., Van Liempd, S. M., Lu, S. C., Mato, J. M., Hasnain, S. S. & Rojas, A. L. (2014) Structure and function study of the complex that synthesizes S-adenosylmethionine, *IUCrJ.* **1**, 240-9.

14. Wang, F., Singh, S., Zhang, J., Huber, T. D., Helmich, K. E., Sunkara, M., Hurley, K. A., Goff, R. D., Bingman, C. A., Morris, A. J., Thorson, J. S. & Phillips, G. N., Jr. (2014) Understanding molecular recognition of promiscuity of thermophilic methionine adenosyltransferase sMAT from Sulfolobus solfataricus, *The FEBS journal.* **281**, 4224-39.

15. Chamberlin, M. E., Ubagai, T., Mudd, S. H., Wilson, W. G., Leonard, J. V. & Chou, J. Y. (1996) Demyelination of the brain is associated with methionine adenosyltransferase I/III deficiency, *The Journal of clinical investigation.* **98**, 1021-7.

16. De La Rosa, J., Ostrowski, J., Hryniewicz, M. M., Kredich, N. M., Kotb, M., LeGros, H. L., Jr., Valentine, M. & Geller, A. M. (1995) Chromosomal localization and catalytic properties of the recombinant alpha subunit of human lymphocyte methionine adenosyltransferase, *The Journal of biological chemistry.* **270**, 21860-8.

17. Mato JM, A. M., Corrales FJ. (2001) Biosynthesis of S-Adenosylmethionine in *Homocysteine in Health and Disease* pp. 47-61, Cambridge University Press, Cambridge, UK.

18. Gil, B., Casado, M., Pajares, M. A., Bosca, L., Mato, J. M., Martin-Sanz, P. & Alvarez, L. (1996) Differential expression pattern of S-adenosylmethionine synthetase isoenzymes during rat liver development, *Hepatology (Baltimore, Md).* **24**, 876-81.

19. Lu, S. C., Alvarez, L., Huang, Z. Z., Chen, L., An, W., Corrales, F. J., Avila, M. A., Kanel, G. & Mato, J. M. (2001) Methionine adenosyltransferase 1A knockout mice are predisposed to liver injury and exhibit increased expression of genes involved in proliferation, *Proceedings of the National Academy of Sciences of the United States of America.* **98**, 5560-5.

20. Chen, H., Xia, M., Lin, M., Yang, H., Kuhlenkamp, J., Li, T., Sodir, N. M., Chen, Y. H., Josef-Lenz, H., Laird, P. W., Clarke, S., Mato, J. M. & Lu, S. C. (2007) Role of methionine adenosyltransferase 2A and S-adenosylmethionine in mitogen-induced growth of human colon cancer cells, *Gastroenterology.* **133**, 207-18.

21. Rodríguez, J. L., Boukaba, A., Sandoval, J., Georgieva, E. I., Latasa, M. U., García-Trevijano, E. R., Serviddio, G., Nakamura, T., Ávila, M. A., Sastre, J., Torres, L., Mato, J. M. & López-Rodas, G. (2007) Transcription of the MAT2A gene, coding for methionine adenosyltransferase, is up-regulated by E2F and Sp1 at a chromatin level during proliferation of liver cells, *The International Journal of Biochemistry & Cell Biology.* **39**, 842-850.

22. Cai, J., Sun, W. M., Hwang, J. J., Stain, S. C. & Lu, S. C. (1996) Changes in S-adenosylmethionine synthetase in human liver cancer: molecular characterization and significance, *Hepatology (Baltimore, Md).* **24**, 1090-7.

23. Finkelstein, J. D. (1990) Methionine metabolism in mammals, *The Journal of nutritional biochemistry.* **1**, 228-37.

24. Mudd, S. H. & Poole, J. R. (1975) Labile methyl balances for normal humans on various dietary regimens, *Metabolism: clinical and experimental.* **24**, 721-35.

25. Fagerberg, L., Hallstrom, B. M., Oksvold, P., Kampf, C., Djureinovic, D., Odeberg, J., Habuka, M., Tahmasebpoor, S., Danielsson, A., Edlund, K., Asplund, A., Sjostedt, E., Lundberg, E., Szigyarto, C. A., Skogs, M., Takanen, J. O., Berling, H., Tegel, H., Mulder, J.,

Nilsson, P., Schwenk, J. M., Lindskog, C., Danielsson, F., Mardinoglu, A., Sivertsson, A., von Feilitzen, K., Forsberg, M., Zwahlen, M., Olsson, I., Navani, S., Huss, M., Nielsen, J., Ponten, F. & Uhlen, M. (2014) Analysis of the human tissue-specific expression by genome-wide integration of transcriptomics and antibody-based proteomics, *Molecular & cellular proteomics : MCP.* **13**, 397-406.

26. Catoni, G. L. (1953) S-Adenosylmethionine; a new intermediate formed enzymatically from L-methionine and adenosinetriphosphate, *The Journal of biological chemistry.* **204**, 403-16.

27. Markham, G. D., Parkin, D. W., Mentch, F. & Schramm, V. L. (1987) A kinetic isotope effect study and transition state analysis of the S-adenosylmethionine synthetase reaction, *The Journal of biological chemistry.* **262**, 5609-15.

28. Parry, R. J. & Minta, A. (1982) Studies of enzyme stereochemistry. Elucidation of the stereochemistry of S-adenosylmethionine formation by yeast methionine adenosyltransferase, *Journal of the American Chemical Society.* **104**, 871-872.

29. Cantoni, G. L. & Durell, J. (1957) Activation of methionine for transmethylation. II. The methionine-activating enzyme; studies on the mechanism of the reaction, *The Journal of biological chemistry.* **225**, 1033-48.

30. Murray, B., Antonyuk, S. V., Marina, A., Lu, S. C., Mato, J. M., Hasnain, S. S. & Rojas, A. L. (2016) Crystallography captures catalytic steps in human methionine adenosyltransferase enzymes, *Proceedings of the National Academy of Sciences of the United States of America.* **113**, 2104-9.

31. Markham, G. D. (1981) Spatial proximity of two divalent metal ions at the active site of S-adenosylmethionine synthetase, *The Journal of biological chemistry.* **256**, 1903-9.

32. Markham, G. D. (1986) Characterization of the monovalent cation activator binding site of S-adenosylmethionine synthetase by 205Tl NMR of enzyme-bound Tl+, *The Journal of biological chemistry.* **261**, 1507-9.

33. Markham, G. D. & Leyh, T. S. (1987) Superhyperfine coupling between metal ions at the active site of S-adenosylmethionine synthetase, *Journal of the American Chemical Society.* **109**, 599-600.

34. Markham, G. D., Hafner, E. W., Tabor, C. W. & Tabor, H. (1980) S-adenosylmethionine synthetase from Escherichia coli, *The Journal of biological chemistry.* **255**, 9082-92.

35. Gonzalez, B., Pajares, M. A., Hermoso, J. A., Guillerm, D., Guillerm, G. & Sanz-Aparicio, J. (2003) Crystal structures of methionine adenosyltransferase complexed with substrates and products reveal the methionine-ATP recognition and give insights into the catalytic mechanism, *Journal of molecular biology.* **331**, 407-16.

36. Komoto, J., Yamada, T., Takata, Y., Markham, G. D. & Takusagawa, F. (2004) Crystal structure of the S-adenosylmethionine synthetase ternary complex: a novel catalytic mechanism of S-adenosylmethionine synthesis from ATP and Met, *Biochemistry.* **43**, 1821-31.

37. Tabor, C. W. & Tabor, H. (1984) Methionine adenosyltransferase (S-adenosylmethionine synthetase) and S-adenosylmethionine decarboxylase, *Advances in enzymology and related areas of molecular biology.* **56**, 251-82.

38. Chiang, P. K., Gordon, R. K., Tal, J., Zeng, G. C., Doctor, B. P., Pardhasaradhi, K. & McCann, P. P. (1996) S-Adenosylmethionine and methylation, *FASEB journal : official publication of the Federation of American Societies for Experimental Biology.* **10**, 471-80.

39. Fontecave, M., Atta, M. & Mulliez, E. (2004) S-adenosylmethionine: nothing goes to waste, *Trends in biochemical sciences.* **29**, 243-9.

40. GARCÍA-TREVIJANO, E. R., LATASA, M. U., CARRETERO, M. V., BERASAIN, C., MATO, J. M. & AVILA, M. A. (2000) S-Adenosylmethionine regulates MAT1A and MAT2A gene expression in cultured rat hepatocytes: a new role for S-adenosylmethionine in the maintenance of the differentiated status of the liver. **14**, 2511-2518.

41. Lu, S. C. & Mato, J. M. (2012) S-adenosylmethionine in liver health, injury, and cancer, *Physiological reviews.* **92**, 1515-42.

42. Prudova, A., Bauman, Z., Braun, A., Vitvitsky, V., Lu, S. C. & Banerjee, R. (2006) S-adenosylmethionine stabilizes cystathionine beta-synthase and modulates redox capacity, *Proceedings of the National Academy of Sciences of the United States of America.* **103**, 6489-94.

43. Shafqat, N., Muniz, J. R. C., Pilka, E. S., Papagrigoriou, E., von Delft, F., Oppermann, U. & Yue, W. W. (2013) Insight into S-adenosylmethionine biosynthesis from the crystal structures of the human methionine adenosyltransferase catalytic and regulatory subunits, *The Biochemical journal.* **452**, 27-36.

44. Porcelli, M., Cacciapuoti, G., Carteni-Farina, M. & Gambacorta, A. (1988) S-adenosylmethionine synthetase in the thermophilic archaebacterium Sulfolobus solfataricus. Purification and characterization of two isoforms, *European journal of biochemistry.* **177**, 273-80.

45. Graham, D. E., Bock, C. L., Schalk-Hihi, C., Lu, Z. J. & Markham, G. D. (2000) Identification of a highly diverged class of S-adenosylmethionine synthetases in the archaea, *The Journal of biological chemistry.* **275**, 4055-9.

46. Lu, Z. J. & Markham, G. D. (2002) Enzymatic properties of S-adenosylmethionine synthetase from the archaeon Methanococcus jannaschii, *The Journal of biological chemistry.* **277**, 16624-31.

47. Panmanee, J., Bradley-Clarke, J., Mato, J. M., O'Neill, P. M., Antonyuk, S. V. & Hasnain, S. S. (2019) Control and regulation of S-adenosylmethionine biosynthesis by the regulatory beta subunit and quinolone-based compounds, *The FEBS journal.* **286**, 2135-2154.

48. Schlesier, J., Siegrist, J., Gerhardt, S., Erb, A., Blaesi, S., Richter, M., Einsle, O. & Andexer, J. N. (2013) Structural and functional characterisation of the methionine adenosyltransferase from Thermococcus kodakarensis, *BMC Structural Biology.* **13**, 22.

49. Takusagawa, F., Kamitori, S. & Markham, G. D. (1996) Structure and function of S-adenosylmethionine synthetase: crystal structures of S-adenosylmethionine synthetase with ADP, BrADP, and PPi at 28 angstroms resolution, *Biochemistry.* **35**, 2586-96.

50. Kuzmanic, A., Pannu, N. S. & Zagrovic, B. J. N. c. (2014) X-ray refinement significantly underestimates the level of microscopic heterogeneity in biomolecular crystals. **5**, 3220.

51. Takusagawa, F., Kamitori, S., Misaki, S. & Markham, G. D. (1996) Crystal structure of S-adenosylmethionine synthetase, *The Journal of biological chemistry.* **271**, 136-47.

52. Fu, Z., Hu, Y., Markham, G. D. & Takusagawa, F. (1996) Flexible loop in the structure of S-adenosylmethionine synthetase crystallized in the tetragonal modification, *Journal of biomolecular structure & dynamics.* **13**, 727-39.

53. Gonzalez, B., Pajares, M. A., Hermoso, J. A., Alvarez, L., Garrido, F., Sufrin, J. R. & Sanz-Aparicio, J. (2000) The crystal structure of tetrameric methionine adenosyltransferase from rat liver reveals the methionine-binding site, *Journal of molecular biology.* **300**, 363-75.

54. Torres, L., López-Rodas, G., Latasa, M. U., Carretero, M. V., Boukaba, A., Rodríguez, J. L., Franco, L., Mato, J. M. & Avila, M. a. A. (2000) DNA methylation and histone acetylation of rat methionine adenosyltransferase 1A and 2A genes is tissue-specific, *The international journal of biochemistry & cell biology.* **32**, 397-404.

55. Torres, L., Avila, M. A., Carretero, M. V., Latasa, M. U., Caballeria, J., Lopez-Rodas, G., Boukaba, A., Lu, S. C., Franco, L. & Mato, J. M. (2000) Liver-specific methionine adenosyltransferase MAT1A gene expression is associated with a specific pattern of promoter methylation and histone acetylation: implications for MAT1A silencing during transformation, *FASEB journal : official publication of the Federation of American Societies for Experimental Biology.* **14**, 95-102.

56. Alvarez, L., Sanchez-Gongora, E., Mingorance, J., Pajares, M. A. & Mato, J. M. (1997) Characterization of rat liver-specific methionine adenosyltransferase gene promoter. Role of distal upstream cis-acting elements in the regulation of the transcriptional activity, *The Journal of biological chemistry.* **272**, 22875-83.

57. Ikeda, R., Nishida, T., Watanabe, F., Shimizu-Saito, K., Asahina, K., Horikawa, S. & Teraoka, H. (2008) Involvement of CCAAT/enhancer binding protein-beta (C/EBPbeta) in epigenetic regulation of mouse methionine adenosyltransferase 1A gene expression, *The international journal of biochemistry & cell biology.* **40**, 1956-69.

58. Zeng, Z., Huang, Z. Z., Chen, C., Yang, H., Mao, Z. & Lu, S. C. (2000) Cloning and functional characterization of the 5'-flanking region of human methionine adenosyltransferase 1A gene, *The Biochemical journal.* **346 Pt 2**, 475-82.

59. Hiroki, T., Horikawa, S. & Tsukada, K. (1997) Structure of the rat methionine adenosyltransferase 2A gene and its promoter, *European journal of biochemistry.* **250**, 653-60.

60. Mao, Z., Liu, S., Cai, J., Huang, Z.-Z. & Lu, S. C. (1998) Cloning and functional characterization of the 5′-flanking region of human methionine adenosyltransferase 2A gene, *Biochemical and biophysical research communications.* **248**, 479-484.

61. Gil, B., Pajares, M. A., Mato, J. M. & Alvarez, L. (1997) Glucocorticoid regulation of hepatic S-adenosylmethionine synthetase gene expression, *Endocrinology.* **138**, 1251-8.

62. Yang, H., Liu, T., Wang, J., Li, T. W., Fan, W., Peng, H., Krishnan, A., Gores, G. J., Mato, J. M. & Lu, S. C. (2016) Deregulated methionine adenosyltransferase alpha1, c-Myc, and Maf proteins together promote cholangiocarcinoma growth in mice and humans(double dagger), *Hepatology (Baltimore, Md).* **64**, 439-55.

63. Fan, W., Yang, H., Liu, T., Wang, J., Li, T. W., Mavila, N., Tang, Y., Yang, J., Peng, H., Tu, J., Annamalai, A., Noureddin, M., Krishnan, A., Gores, G. J., Martinez-Chantar, M. L., Mato, J. M. & Lu, S. C. (2017) Prohibitin 1 suppresses liver cancer tumorigenesis in mice and human hepatocellular and cholangiocarcinoma cells, *Hepatology (Baltimore, Md).* **65**, 1249-1266.

64. Yang, H., Sadda, M. R., Yu, V., Zeng, Y., Lee, T. D., Ou, X., Chen, L. & Lu, S. C. (2003) Induction of human methionine adenosyltransferase 2A expression by tumor necrosis factor alpha. Role of NF-kappa B and AP-1, *The Journal of biological chemistry.* **278**, 50887-96.

65. Rodriguez, J. L., Boukaba, A., Sandoval, J., Georgieva, E. I., Latasa, M. U., Garcia-Trevijano, E. R., Serviddio, G., Nakamura, T., Avila, M. A., Sastre, J., Torres, L., Mato, J. M. & Lopez-Rodas, G. (2007) Transcription of the MAT2A gene, coding for methionine adenosyltransferase, is up-regulated by E2F and Sp1 at a chromatin level during proliferation of liver cells, *The international journal of biochemistry & cell biology.* **39**, 842-50.

66. Yang, H., Huang, Z. Z., Wang, J. & Lu, S. C. (2001) The role of c-Myb and Sp1 in the up-regulation of methionine adenosyltransferase 2A gene expression in human hepatocellular carcinoma, *FASEB journal : official publication of the Federation of American Societies for Experimental Biology.* **15**, 1507-16.

67. Wang, K., Fang, S., Liu, Q., Gao, J., Wang, X., Zhu, H., Zhu, Z., Ji, F., Wu, J., Ma, Y., Hu, L., Shen, X., Gao, D., Zhu, J., Liu, P. & Zhou, H. (2019) TGF-beta1/p65/MAT2A pathway regulates liver fibrogenesis via intracellular SAM, *EBioMedicine.* **42**, 458-469.

68. Liu, Q., Liu, L., Zhao, Y., Zhang, J., Wang, D., Chen, J., He, Y., Wu, J., Zhang, Z. & Liu, Z. (2011) Hypoxia induces genomic DNA demethylation through the activation of HIF-1alpha and transcriptional upregulation of MAT2A in hepatoma cells, *Molecular cancer therapeutics.* **10**, 1113-23.

69. Ramani, K. & Tomasi, M. L. (2012) Transcriptional regulation of methionine adenosyltransferase 2A by peroxisome proliferator-activated receptors in rat hepatic stellate cells, *Hepatology (Baltimore, Md).* **55**, 1942-53.

70. Guo, Y. T., Leng, X. S., Li, T., Peng, J. R., Song, S. H., Xiong, L. F. & Qin, Z. Z. (2005) Effect of ligand of peroxisome proliferator-activated receptor gamma on the biological characters of hepatic stellate cells, *World journal of gastroenterology.* **11**, 4735-9.

71. Hellemans, K., Michalik, L., Dittie, A., Knorr, A., Rombouts, K., De Jong, J., Heirman, C., Quartier, E., Schuit, F., Wahli, W. & Geerts, A. (2003) Peroxisome proliferator-activated receptor-beta signaling contributes to enhanced proliferation of hepatic stellate cells, *Gastroenterology.* **124**, 184-201.

72. Frau, M., Tomasi, M. L., Simile, M. M., Demartis, M. I., Salis, F., Latte, G., Calvisi, D. F., Seddaiu, M. A., Daino, L., Feo, C. F., Brozzetti, S., Solinas, G., Yamashita, S., Ushijima, T., Feo, F. & Pascale, R. M. (2012) Role of transcriptional and posttranscriptional regulation of methionine adenosyltransferases in liver cancer progression, *Hepatology (Baltimore, Md).* **56**, 165-75.

73. Tomasi, M. L., Li, T. W., Li, M., Mato, J. M. & Lu, S. C. (2012) Inhibition of human methionine adenosyltransferase 1A transcription by coding region methylation, *Journal of cellular physiology.* **227**, 1583-91.

74. Murphy, S. K., Yang, H., Moylan, C. A., Pang, H., Dellinger, A., Abdelmalek, M. F., Garrett, M. E., Ashley-Koch, A., Suzuki, A., Tillmann, H. L., Hauser, M. A. & Diehl, A. M. (2013) Relationship between methylome and transcriptome in patients with nonalcoholic fatty liver disease, *Gastroenterology.* **145**, 1076-87.

75. Avila, M. A., Mingorance, J., Martinez-Chantar, M. L., Casado, M., Martin-Sanz, P., Bosca, L. & Mato, J. M. (1997) Regulation of rat liver S-adenosylmethionine synthetase during septic shock: role of nitric oxide, *Hepatology (Baltimore, Md).* **25**, 391-6.

76. Perez-Mato, I., Castro, C., Ruiz, F. A., Corrales, F. J. & Mato, J. M. (1999) Methionine adenosyltransferase S-nitrosylation is regulated by the basic and acidic amino acids surrounding the target thiol, *The Journal of biological chemistry.* **274**, 17075-9.

77. Pajares, M. A., Duran, C., Corrales, F. & Mato, J. M. (1994) Protein kinase C phosphorylation of rat liver S-adenosylmethionine synthetase: dissociation and production of an active monomer, *The Biochemical journal.* **303 (Pt 3)**, 949-55.

78. Ramani, K., Donoyan, S., Tomasi, M. L. & Park, S. (2015) Role of methionine adenosyltransferase alpha2 and beta phosphorylation and stabilization in human hepatic stellate cell trans-differentiation, *Journal of cellular physiology.* **230**, 1075-85.

79. Ghioni, P., D'Alessandra, Y., Mansueto, G., Jaffray, E., Hay, R. T., La Mantia, G. & Guerrini, L. (2005) The protein stability and transcriptional activity of p63alpha are regulated by SUMO-1 conjugation, *Cell cycle (Georgetown, Tex).* **4**, 183-90.

80. Tomasi, M. L., Ryoo, M., Ramani, K., Tomasi, I., Giordano, P., Mato, J. M. & Lu, S. C. (2015) Methionine adenosyltransferase alpha2 sumoylation positively regulate Bcl-2 expression in human colon and liver cancer cells, *Oncotarget.* **6**, 37706-23.

81. Yang, H. B., Xu, Y. Y., Zhao, X. N., Zou, S. W., Zhang, Y., Zhang, M., Li, J. T., Ren, F., Wang, L. Y. & Lei, Q. Y. (2015) Acetylation of MAT IIalpha represses tumour cell growth and is decreased in human hepatocellular cancer, *Nature communications.* **6**, 6973.

82. Barkla, C. G. (1904) Polarisation in Röntgen rays, *Nature.* **69**, 463-463.

83. Barkla, C. G. (1906) Polarisation in secondary Röntgen radiation, *Proceedings of the Royal Society of London Series A, Containing Papers of a Mathematical and Physical Character.* **77**, 247-255.

84. Barkla, C. G. (1908) The nature of X-rays, *Nature.* **78**, 665-665.

85. Barkla, C. G. (1908) XXVI. Note on X-rays and scattered X-rays, *The London, Edinburgh, and Dublin Philosophical Magazine and Journal of Science.* **15**, 288-296.

86. Bragg, W. H. & Bragg, W. L. (1913) The reflection of X-rays by crystals. **88**, 428-438.

87. Bragg, W. L. & Bragg, W. H. (1913) The structure of some crystals as indicated by their diffraction of X-rays. **89**, 248-277.

88. Bragg, W. L. (1929) The diffraction of short electromagnetic waves by a crystal. **23**, 153.

89. Watson, J. D. & Crick, F. H. C. (1953) Molecular structure of nucleic acids: a structure for deoxyribose nucleic acid, *Nature.* **171**, 737-738.

90. Kendrew, J. C., Bodo, G., Dintzis, H. M., Parrish, R. G., Wyckoff, H. & Phillips, D. C. (1958) A three-dimensional model of the myoglobin molecule obtained by X-ray analysis, *Nature.* **181**, 662-666.

91. Perutz, M. F., Rossmann, M. G., Cullis, A. F., Muirhead, H., Will, G. & North, A. C. T. (1960) Structure of haemoglobin: a three-dimensional Fourier synthesis at 5.5-Å. Resolution, obtained by X-ray analysis, *Nature.* **185**, 416-422.

92. Brink, C., Hodgkin, D. C., Lindsey, J., Pickworth, J., Robertson, J. R. & White, J. G. (1954) X-ray crystallographic evidence on the structure of vitamin B12, *Nature.* **174**, 1169-71.

93. Hodgkin, D. C. (1949) The X-ray analysis of the structure of penicillin, *Advancement of science.* **6**, 85-9.

94. Hodgkin, D. G., Pickworth, J., Robertson, J. H., Trueblood, K. N., Prosen, R. J. & White, J. G. (1955) The crystal structure of the hexacarboxylic acid derived from B12 and the molecular structure of the vitamin, *Nature.* **176**, 325-8.

95. Deisenhofer, J., Epp, O., Miki, K., Huber, R. & Michel, H. (1985) Structure of the protein subunits in the photosynthetic reaction centre of Rhodopseudomonas viridis at 3A resolution, *Nature.* **318**, 618-24.

96. Abrahams, J. P., Leslie, A. G., Lutter, R. & Walker, J. E. (1994) Structure at 2.8 A resolution of F1-ATPase from bovine heart mitochondria, *Nature.* **370**, 621-8.

97. Kobilka, B. K. (2007) G protein coupled receptor structure and activation, *Biochimica et biophysica acta.* **1768**, 794-807.

98. Bingel-Erlenmeyer, R., Olieric, V., Grimshaw, J. P. A., Gabadinho, J., Wang, X., Ebner, S. G., Isenegger, A., Schneider, R., Schneider, J., Glettig, W., Pradervand, C., Panepucci, E. H., Tomizaki, T., Wang, M. & Schulze-Briese, C. (2011) SLS crystallization platform at beamline X06DA—A fully automated pipeline enabling in situ X-ray diffraction screening, *Crystal Growth & Design.* **11**, 916-923.

99. Duke, E. M. H. & Johnson, L. N. (2010) Macromolecular crystallography at synchrotron radiation sources: current status and future developments, *Proceedings of the Royal Society A: Mathematical, Physical and Engineering Sciences.* **466**, 3421-3452.

100. Garman, E. F. & Schneider, T. R. (1997) Macromolecular cryocrystallography. **30**, 211-237.

101. Pflugrath, J. W. (2004) Macromolecular cryocrystallography—methods for cooling and mounting protein crystals at cryogenic temperatures, *Methods.* **34**, 415-423.

102. Pflugrath, J. W. (2015) Practical macromolecular cryocrystallography, *Acta crystallographica Section F, Structural biology communications.* **71**, 622-42.

103. McPherson, A. & Gavira, J. A. (2014) Introduction to protein crystallization, *Acta crystallographica Section F, Structural biology communications.* **70**, 2-20.

104. Hyde, A. M., Zultanski, S. L., Waldman, J. H., Zhong, Y.-L., Shevlin, M. & Peng, F. (2017) General principles and strategies for salting-out informed by the Hofmeister series, *Organic Process Research & Development.* **21**, 1355-1370.

105. Bailey, K. (1945) Proteins, amino-acids and peptides as ions and dipolar ions, *Nature.* **156**, 405-406.

106. Kunz, W., Henle, J. & Ninham, B. W. (2004) 'Zur Lehre von der Wirkung der Salze' (about the science of the effect of salts): Franz Hofmeister's historical papers, *Current Opinion in Colloid & Interface Science.* **9**, 19-37.

107. Zhou, H.-X. & Pang, X. (2018) Electrostatic interactions in protein structure, folding, binding, and condensation, *Chem Rev.* **118**, 1691-1741.

108. McPherson, A., Jr. (1976) Crystallization of proteins from polyethylene glycol, *The Journal of biological chemistry.* **251**, 6300-3.

109. Patel, S., Cudney, B. & McPherson, A. (1995) Polymeric precipitants for the crystallization of macromolecules, *Biochemical and biophysical research communications.* **207**, 819-28.

110. Ingham, K. C. (1990) Precipitation of proteins with polyethylene glycol, *Methods in enzymology.* **182**, 301-6.

111. Israelachvili, J. (1997) The different faces of poly(ethylene glycol), *Proceedings of the National Academy of Sciences of the United States of America.* **94**, 8378-8379.

112. McPherson, A., Malkin, A. J. & Kuznetsov, Y. G. (1995) The science of macromolecular crystallization, *Structure (London, England : 1993).* **3**, 759-68.

113. Watts, A. (1993) Crystallization of nucleic acids and proteins. A practical approach. **319**, 283-284.

114. Chayen, N. E., Shaw Stewart, P. D. & Blow, D. M. (1992) Microbatch crystallization under oil — a new technique allowing many small-volume crystallization trials, *Journal of Crystal Growth.* **122**, 176-180.

115. Chayen, N. (1998) Comparative studies of protein crystallization by vapour-diffusion and microbatch techniques, *Acta Crystallographica Section D.* **54**, 8-15.

116. Chayen, N. E. (1997) The role of oil in macromolecular crystallization, *Structure (London, England : 1993).* **5**, 1269-74.

117. Sarwate, V. (1993) *Electromagnetic fields and waves*, bohem press.

118. Murray, J. W., Garman, E. F. & Ravelli, R. B. G. (2004) X-ray absorption by macromolecular crystals: the effects of wavelength and crystal composition on absorbed dose, *Journal of Applied Crystallography.* **37**, 513-522.

119. Nave, C. (1995) Radiation damage in protein crystallography, *Radiation Physics and Chemistry.* **45**, 483-490.

120. Dauter, Z., Jaskolski, M. & Wlodawer, A. (2010) Impact of synchrotron radiation on macromolecular crystallography: a personal view, *J Synchrotron Radiat.* **17**, 433-444.

121. Phillips, J. C., Wlodawer, A., Yevitz, M. M. & Hodgson, K. O. (1976) Applications of synchrotron radiation to protein crystallography: preliminary results, *Proceedings of the National Academy of Sciences of the United States of America.* **73**, 128-32.

122. Uruga, T. (2017) Synchrotron-radiation sources, X-ray optics and beamlines in *XAFS Techniques for Catalysts, Nanomaterials, and Surfaces* (Iwasawa, Y., Asakura, K. & Tada, M., eds) pp. 53-62, Springer International Publishing, Cham.

123. Taylor, G. (2003) The phase problem, *Acta Crystallographica Section D.* **59**, 1881-1890.

124. Rossmann, M. (1990) The molecular replacement method, *Acta Crystallographica Section A.* **46**, 73-82.

125. Patterson, A. L. (1934) A Fourier series method for the determination of the components of interatomic distances in crystals, *Physical Review.* **46**, 372-376.

126. Kleywegt, G. J. & Alwyn Jones, T. (1997) [11] Model building and refinement practice in *Methods in enzymology* pp. 208-230, Academic Press.

127. Alsarraf, H. M., Laroche, F., Spaink, H., Thirup, S. & Blaise, M. (2011) Purification, crystallization and preliminary crystallographic studies of the TLDc domain of oxidation resistance protein 2 from zebrafish, *Acta crystallographica Section F, Structural biology and crystallization communications.* **67**, 1253-6.

128. Baginski, E. S., Foa, P. P. & Zak, B. (1967) Microdetermination of inorganic phosphate, phospholipids, and total phosphate in biologic materials, *Clinical chemistry.* **13**, 326-32.

129. Charoensutthivarakul, S., David Hong, W., Leung, S. C., Gibbons, P. D., Bedingfield, P. T. P., Nixon, G. L., Lawrenson, A. S., Berry, N. G., Ward, S. A., Biagini, G. A. & O'Neill, P. M. (2015) 2-Pyridylquinolone antimalarials with improved antimalarial activity and physicochemical properties, *MedChemComm.* **6**, 1252-1259.

130. David, G. & Perez, J. (2009) Combined sampler robot and high-performance liquid chromatography: a fully automated system for biological small-angle X-ray scattering

experiments at the Synchrotron SOLEIL SWING beamline, *Journal of Applied Crystallography.* **42**, 892-900.

131. Konarev, P. V., Volkov, V. V., Sokolova, A. V., Koch, M. H. J. & Svergun, D. I. (2003) PRIMUS: a Windows PC-based system for small-angle scattering data analysis, *Journal of Applied Crystallography.* **36**, 1277-1282.

132. Schneidman-Duhovny, D., Hammel, M., Tainer, J. A. & Sali, A. (2013) Accurate SAXS profile computation and its assessment by contrast variation experiments, *Biophysical journal.* **105**, 962-74.

133. Battye, T. G. G., Kontogiannis, L., Johnson, O., Powell, H. R. & Leslie, A. G. W. (2011) iMOSFLM: a new graphical interface for diffraction-image processing with MOSFLM, *Acta Crystallographica Section D.* **67**, 271-281.

134. Evans, P. R. & Murshudov, G. N. (2013) How good are my data and what is the resolution?, *Acta Crystallographica Section D.* **69**, 1204-1214.

135. Vagin, A. & Teplyakov, A. (2010) Molecular replacement with MOLREP, *Acta Crystallogr D Biol Crystallogr.* **66**, 22-5.

136. Emsley, P., Lohkamp, B., Scott, W. G. & Cowtan, K. (2010) Features and development of Coot, *Acta Crystallogr D Biol Crystallogr.* **66**, 486-501.

137. Murshudov, G. N., Skubák, P., Lebedev, A. A., Pannu, N. S., Steiner, R. A., Nicholls, R. A., Winn, M. D., Long, F. & Vagin, A. A. (2011) REFMAC5 for the refinement of macromolecular crystal structures, *Acta Crystallogr D Biol Crystallogr.* **67**, 355-367.

138. Trott, O. & Olson, A. J. (2010) AutoDock Vina: improving the speed and accuracy of docking with a new scoring function, efficient optimization, and multithreading, *J Comput Chem.* **31**, 455-461.

139. Grosdidier, A., Zoete, V. & Michielin, O. (2011) SwissDock, a protein-small molecule docking web service based on EADock DSS, *Nucleic acids research.* **39**, W270-7.

140. Pettersen, E. F., Goddard, T. D., Huang, C. C., Couch, G. S., Greenblatt, D. M., Meng, E. C. & Ferrin, T. E. (2004) UCSF Chimera--a visualization system for exploratory research and analysis, *J Comput Chem.* **25**, 1605-12.

141. Ovchinnikov, S., Kamisetty, H. & Baker, D. (2014) Robust and accurate prediction of residue-residue interactions across protein interfaces using evolutionary information, *eLife.* **3**, e02030.

142. Crooks, G. E., Hon, G., Chandonia, J. M. & Brenner, S. E. (2004) WebLogo: a sequence logo generator, *Genome research.* **14**, 1188-90.

143. Taylor, J. C., Takusagawa, F. & Markham, G. D. (2002) The active site loop of S-adenosylmethionine synthetase modulates catalytic efficiency, *Biochemistry.* **41**, 9358-9369.

144. Fernandez-Irigoyen, J., Santamaria, E., Chien, Y. H., Hwu, W. L., Korman, S. H., Faghfoury, H., Schulze, A., Hoganson, G. E., Stabler, S. P., Allen, R. H., Wagner, C., Mudd, S. H. & Corrales, F. J. (2010) Enzymatic activity of methionine adenosyltransferase variants

identified in patients with persistent hypermethioninemia, *Molecular genetics and metabolism.* **101**, 172-7.

145. Quinlan, C. L., Kaiser, S. E., Bolanos, B., Nowlin, D., Grantner, R., Karlicek-Bryant, S., Feng, J. L., Jenkinson, S., Freeman-Cook, K., Dann, S. G., Wang, X., Wells, P. A., Fantin, V. R., Stewart, A. E. & Grant, S. K. (2017) Targeting S-adenosylmethionine biosynthesis with a novel allosteric inhibitor of Mat2A, *Nature chemical biology.* **13**, 785-792.

146. Firestone, R. S. & Schramm, V. L. (2017) The transition-state structure for human MAT2A from isotope effects, *Journal of the American Chemical Society.* **139**, 13754-13760.

147. Mudd, S. H. (2011) Hypermethioninemias of genetic and non-genetic origin: A review, *American journal of medical genetics Part C, Seminars in medical genetics.* **157c**, 3-32.

148. Gahl, W. A., Bernardini, I., Finkelstein, J. D., Tangerman, A., Martin, J. J., Blom, H. J., Mullen, K. D. & Mudd, S. H. (1988) Transsulfuration in an adult with hepatic methionine adenosyltransferase deficiency, *The Journal of clinical investigation.* **81**, 390-7.

149. Gaull, G. E., Tallan, H. H., Lonsdale, D., Przyrembel, H., Schaffner, F. & von Bassewitz, D. B. (1981) Hypermethioninemia associated with methionine adenosyltransferase deficiency: clinical, morphologic, and biochemical observations on four patients, *The Journal of pediatrics.* **98**, 734-41.

150. Chamberlin, M. E., Ubagai, T., Mudd, S. H., Thomas, J., Pao, V. Y., Nguyen, T. K., Levy, H. L., Greene, C., Freehauf, C. & Chou, J. Y. (2000) Methionine adenosyltransferase I/III deficiency: novel mutations and clinical variations, *American journal of human genetics.* **66**, 347-55.

151. Mudd, S. H., Levy, H. L., Tangerman, A., Boujet, C., Buist, N., Davidson-Mundt, A., Hudgins, L., Oyanagi, K., Nagao, M. & Wilson, W. G. (1995) Isolated persistent hypermethioninemia, *American journal of human genetics.* **57**, 882-92.

152. Ubagai, T., Lei, K. J., Huang, S., Mudd, S. H., Levy, H. L. & Chou, J. Y. (1995) Molecular mechanisms of an inborn error of methionine pathway. Methionine adenosyltransferase deficiency, *The Journal of clinical investigation.* **96**, 1943-7.

153. Chien, Y. H., Chiang, S. C., Huang, A. & Hwu, W. L. (2005) Spectrum of hypermethioninemia in neonatal screening, *Early human development.* **81**, 529-33.

154. Couce, M. L., Boveda, M. D., Castineiras, D. E., Corrales, F. J., Mora, M. I., Fraga, J. M. & Mudd, S. H. (2008) Hypermethioninaemia due to methionine adenosyltransferase I/III (MAT I/III) deficiency: diagnosis in an expanded neonatal screening programme, *Journal of inherited metabolic disease.* **31 Suppl 2**, S233-9.

155. Couce, M. L., Boveda, M. D., Garcia-Jimemez, C., Balmaseda, E., Vives, I., Castineiras, D. E., Fernandez-Marmiesse, A., Fraga, J. M., Mudd, S. H. & Corrales, F. J. (2013) Clinical and metabolic findings in patients with methionine adenosyltransferase I/III deficiency detected by newborn screening, *Molecular genetics and metabolism.* **110**, 218-21.

156. Martins, E., Marcao, A., Bandeira, A., Fonseca, H., Nogueira, C. & Vilarinho, L. (2012) Methionine adenosyltransferase I/III deficiency in Portugal: high frequency of a dominantly inherited form in a small area of Douro high lands, *JIMD reports.* **6**, 107-12.

157. Hazelwood, S., Bernardini, I., Shotelersuk, V., Tangerman, A., Guo, J., Mudd, H. & Gahl, W. A. (1998) Normal brain myelination in a patient homozygous for a mutation that encodes a severely truncated methionine adenosyltransferase I/III, *American journal of medical genetics.* **75**, 395-400.

158. Kido, J., Sawada, T., Momosaki, K., Suzuki, Y., Uetani, H., Kitajima, M., Mitsubuchi, H., Nakamura, K. & Matsumoto, S. (2019) Neonatal methionine adenosyltransferase I/III deficiency with abnormal signal intensity in the central tegmental tract, *Brain & development.* **41**, 382-388.

159. Tada, H., Takanashi, J., Barkovich, A. J., Yamamoto, S. & Kohno, Y. (2004) Reversible white matter lesion in methionine adenosyltransferase I/III deficiency, *AJNR American journal of neuroradiology.* **25**, 1843-5.

160. Sen, K., Felice, M. D., Bannick, A., Colombo, R. & Conway, R. L. (2019) Mild persistent isolated hypermethioninemia identified through newborn screening in Michigan, *Journal of pediatric genetics.* **8**, 54-57.

161. Nagao, M., Tanaka, T. & Furujo, M. (2013) Spectrum of mutations associated with methionine adenosyltransferase I/III deficiency among individuals identified during newborn screening in Japan, *Molecular genetics and metabolism.* **110**, 460-4.

162. Chadwick, S., Fitzgerald, K., Weiss, B. & Ficicioglu, C. (2014) Thirteen patients with MAT1A mutations detected through newborn screening: 13 Years' Experience, *JIMD reports.* **14**, 71-6.

163. Chamberlin, M. E., Ubagai, T., Mudd, S. H., Levy, H. L. & Chou, J. Y. (1997) Dominant inheritance of isolated hypermethioninemia is associated with a mutation in the human methionine adenosyltransferase 1A gene, *American journal of human genetics.* **60**, 540-6.

164. Bottiglieri, T. (2002) S-adenosyl-l-methionine (SAMe): from the bench to the bedside—molecular basis of a pleiotrophic molecule, *The American Journal of Clinical Nutrition.* **76**, 1151S-1157S.

165. Chien, Y. H., Abdenur, J. E., Baronio, F., Bannick, A. A., Corrales, F., Couce, M., Donner, M. G., Ficicioglu, C., Freehauf, C., Frithiof, D., Gotway, G., Hirabayashi, K., Hofstede, F., Hoganson, G., Hwu, W. L., James, P., Kim, S., Korman, S. H., Lachmann, R., Levy, H., Lindner, M., Lykopoulou, L., Mayatepek, E., Muntau, A., Okano, Y., Raymond, K., Rubio-Gozalbo, E., Scholl-Burgi, S., Schulze, A., Singh, R., Stabler, S., Stuy, M., Thomas, J., Wagner, C., Wilson, W. G., Wortmann, S., Yamamoto, S., Pao, M. & Blom, H. J. (2015) Mudd's disease (MAT I/III deficiency): a survey of data for MAT1A homozygotes and compound heterozygotes, *Orphanet journal of rare diseases.* **10**, 99.

166. Perez Mato, I., Sanchez del Pino, M. M., Chamberlin, M. E., Mudd, S. H., Mato, J. M. & Corrales, F. J. (2001) Biochemical basis for the dominant inheritance of hypermethioninemia associated with the R264H mutation of the MAT1A gene. A monomeric methionine adenosyltransferase with tripolyphosphatase activity, *The Journal of biological chemistry.* **276**, 13803-9.

167. Reczkowski, R. S., Taylor, J. C. & Markham, G. D. (1998) The active-site arginine of S-adenosylmethionine synthetase orients the reaction intermediate, *Biochemistry.* **37**, 13499-506.

168. Nagao, M. & Oyanagi, K. (1997) Genetic analysis of isolated persistent hypermethioninemia with dominant inheritance, *Acta paediatrica Japonica : Overseas edition.* **39**, 601-6.

169. Linnebank, M., Lagler, F., Muntau, A. C., Roschinger, W., Olgemoller, B., Fowler, B. & Koch, H. G. (2005) Methionine adenosyltransferase (MAT) I/III deficiency with concurrent hyperhomocysteinaemia: two novel cases, *Journal of inherited metabolic disease.* **28**, 1167-8.

170. Nashabat, M., Al-Khenaizan, S. & Alfadhel, M. (2018) Methionine adenosyltransferase I/III deficiency: beyond the central nervous system manifestations, *Therapeutics and clinical risk management.* **14**, 225-229.

171. Guo, D.-c., Gong, L., Regalado, E. S., Santos-Cortez, R. L., Zhao, R., Cai, B., Veeraraghavan, S., Prakash, S. K., Johnson, R. J., Muilenburg, A., Willing, M., Jondeau, G., Boileau, C., Pannu, H., Moran, R., Debacker, J., GenTac Investigators, N. H. L., Blood Institute Go Exome Sequencing, P., Montalcino Aortic, C., Bamshad, M. J., Shendure, J., Nickerson, D. A., Leal, S. M., Raman, C. S., Swindell, E. C. & Milewicz, D. M. (2015) MAT2A mutations predispose individuals to thoracic aortic aneurysms, *American journal of human genetics.* **96**, 170-177.

172. Ferrier, D. R. (2017) Enzymes in *Biochemistry*, Wolters Kluwer, Philadelphia

173. Peng, H., Dara, L., Li, T. W., Zheng, Y., Yang, H., Tomasi, M. L., Tomasi, I., Giordano, P., Mato, J. M. & Lu, S. C. J. H. (2013) MAT2B-GIT1 interplay activates MEK1/ERK 1 and 2 to induce growth in human liver and colon cancer. **57**, 2299-2313.

174. Peng, H., Li, T. W., Yang, H., Moyer, M. P., Mato, J. M. & Lu, S. C. (2015) Methionine adenosyltransferase 2B-GIT1 complex serves as a scaffold to regulate Ras/Raf/MEK1/2 activity in human liver and colon cancer cells, *The American journal of pathology.* **185**, 1135-44.

175. Ramani, K., Mato, J. M. & Lu, S. C. (2011) Role of methionine adenosyltransferase genes in hepatocarcinogenesis, *Cancers.* **3**, 1480-97.

176. Murray, B. (2015) *Structural and functional studies of human methionine adenosyltransferases*, University of Liverpool.

177. Hoefen, R. J. & Berk, B. C. (2006) The multifunctional GIT family of proteins, *Journal of cell science.* **119**, 1469-75.